Microfluidic Genetic Analysis: Tools for Pharmacogenomics and Cell Sorting

Brian Lawrence Poe
Charlottesville, Virginia

B.S. in Biochemistry, Virginia Polytechnic Institute and State University, 2006
B.S. in Biological Sciences, Virginia Polytechnic Institute and State University, 2006

A Dissertation presented to the Graduate Faculty
of the University of Virginia in Candidacy for the Degree of
Doctor of Philosophy

Department of Chemistry
University of Virginia
May, 2014

Acknowledgements

I would like to start by thanking my advisor, Prof. James Landers, for the opportunity to conduct this research. Prof. Landers' cogent vision for microfluidic technologies has been a constant inspiration to me. When major events in my life challenged my scientific endeavors, Prof. Landers provided support and the opportunity to complete this doctorate. I am grateful to Dr. Jerome Ferrance for his guidance, wisdom, and technical assistance. I would also like to thank the members of the Landers Group for their mentorship, collaboration and camaraderie over the years: Dr. Dan Marchiarullo, Dr. Lindsay Legendre, Dr. Jessica Norris, Prof. Ling Huang, Prof. Alison Dewald, Dr. Erkin Şeker, Dr. Dan Leslie, Dr. Kristin Hagan, Dr. Carmen Reedy, Dr. Jenny Lounsbury, Dr. Jingyi Li, Kerui Xu, Dr. Yiwen Ouyang, Dr. Briony Strachan, Dan Nelson, Qian Liu, Dr. Kyudam Oh, Hillary Sloane, Kim Jackson, Brandon Thompson, Jacquelyn DuVall, Shannon Kraus, and future students who will continue our research and make it their own. I would like to thank Prof. Chris Easley and Prof. James Karlinsey for developing microfluidic technologies vital to my doctoral research, and for leaving an inspiring codebase of software for controlling microfluidic systems. Furthermore, I am grateful to Prof. Murali Ghatkesar, Prof. Francisco Lara, Dr. Carol Price, Prof. Gabriela Duarte, Prof. Brian Augustine, Prof. Chris Deppmann, Mr. Chris Dawson, Prof. Cameron Mura, and Prof. Doris Haverstick for sharing their experience and for their collaboration. I am grateful for the support and consideration of members of my PhD exam committee: Prof. B. Jill Venton, Prof. Timothy Macdonald, and Prof. Richard Price. I would also like to thank Michael Do, Jonathan Armstrong, and Dr. Sonia Taneja for their dedication and camaraderie as my undergraduate advisees during their time at UVA, and for their work which has been included in this thesis. Moreover, I would like to thank Kimberly Jackson for her help in achieving ultrasound-mediated PCR. I was very fortunate to receive the

hospitality and training of Prof. Johan Nilsson, Prof. Tomas Laurell, Dr. Per Augustsson, Dr. Björn Hammarström, Maria Nordin, and all other members of the Laurell and Nilsson research groups at Lund University, Sweden. My time working at MicroLab Diagnostics was formative for me, and I am grateful for the mentorship and camaraderie of Dr. Brian Root, Dr. Orion Scott, Mr. Jeff Hickey MFS, Ms. AnChi Tsui, Mr. Lawrence Dirks, Mr. Robert Lovaglio, Dr. Carmen Reedy of MicroLab, and Dr. Joan Bienvenue, Mike Egan, and Darren Albert of Lockheed Martin Inc. During my graduate career the support and friendship of Joe Jablonski, Chris Jacobs, Dan Leslie, Jenny Lounsbury, Briony Strachan, Trisha Vickrey, Lynn Mandeltort, and Bill and Jenn Peairs was essential to my success and sanity. I would like to thank my parents, Diane Poe and David Poe, for their love and support as I began this journey and for their advocacy and dedication to my education and wellbeing that made it possible. I am grateful to my brother, Nathan Poe, for love and camaraderie through hard times, and his persistent belief in my ability to earn this degree. I also want to thank my grandfather, Harvey Poe, and my extended family for their love and support. I am truly fortunate to have a wonderful family-in-law, and this degree definitely wouldn't have been possible without the members of the Jones Family: Don Jones, Trudi Jones, Christy and Christopher. I am grateful to my daughter, Eva Diane Poe, who gave my life (and my research) a new dimension of purpose. Lastly, I would like to thank my wife, Erica Jones Poe, for her love, honesty, and support during this journey.

Table of Contents

1 Introduction

1.1 Bioanalytical Microfluidics

Analytical chemistry performed on biological systems (i.e., bioanalytical chemistry) is used to derive information vital for improving human health and solving crime. Such information is obtained by determining the presence, quantity, and/or quality of components of a biological system. Bioanalysis is extensively applied in medical and forensic settings, as well as in basic biological research, to improve human health, facilitate justice, and elucidate truths of biological systems for greater understanding of our own biology and the biosphere in which we live. Bioanalytical testing is traditionally performed using small volumes of liquid in test tubes, and testing requires performing many operations on these tubes. Shrinking these test tubes down to sub-millimeter length scales, and connecting them together, is a conceptual framework for microfluidic devices. Microfluidic devices offer significant improvements in sample and reagent economy, substantial reductions in assay duration, multiplex capability, and portability of testing instrumentation. Furthermore, the unique properties of micro-scale fluid handling have been used to study biological systems in ways that were previously impossible.

Fluid containers with sub-millimeter dimensions demonstrate a distinctive set of physical phenomena. The size scales for microfluidic devices are depicted in Figure 1.1A. Microfluidic channels and chambers have high surface area to volume ratios (SA:V), which scale nonlinearly with length dimensions Figure 1.1B. At sub-millimeters length scales, the surface tension and contact angle of microchannels become the dominant

forces, as opposed to gravitational forces which generally dominate fluid localization at the macroscale. Due to the high SA:V, adsorption of important macromolecules can substantially deplete those species from the liquid, and compensation strategies such as surface passivation may be required to maintain adequate concentration of essential reagents. Bubbles are stabilized by the dominance of surface tension forces, and bubbles are often confined within microfluidic architectures, causing problems such as obstructed flow and damage to living cells. Another consequence of the large SA:V is that heat transport between the liquid and the substrate is dramatically increased (heat flux is proportional to the contact area),. This makes rapid thermal modulation possible[1] and enables more extreme operation of heat-generating processes, such as electrophoresis, possible without detrimental overheating. Moreover, the well-defined dimensions of microfluidic systems often allow for precise introduction of external forces (including electromagnetic radiation, electrical fields, acoustic fields, magnetic fields). Liquid within microfluidics also falls into the laminar flow regime, where layers of fluid can flow together without turbulent, convective mixing. These are just a few of the characteristic physical phenomena that must be accounted for, and often utilized, when working with microfluidic systems.

Traditional substrates for microfluidic technologies were silicon and glass, due to the well-established micropatterning techniques available through the microelectronics industry.[2]. Photolithography and wet chemical etching have been extensively applied to microfluidic device fabrication. While the properties of silicon and glass are often desirable (e.g., high thermal and acoustic conductivity, excellent optical properties (glass), mechanical strength of microchannels, etc.), the cost of the materials and the fabrication

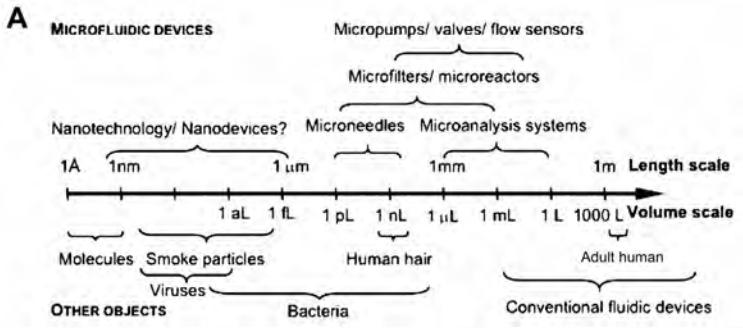

B

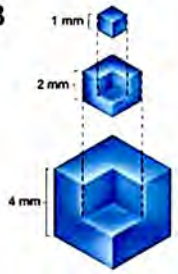

Side length	Surface area	Volume	Surface area/ volume ratio
1 mm	6 mm^2	1 mm^3 = 1 μL	6:1
2 mm	24 mm^2	8 mm^3 = 8 μL	3:1
4 mm	96 mm^2	64 mm^3 = 64 μL	3:2

Figure 1.1: Length scales and volumes of microfluidic technology. A. Logarithmic chart of liquid volumes and associated sizes B. Study of the relationship between surface area and volume.

facilities required for these microfluidic substrates has led to a large-scale movement to develop microfluidic devices in polymeric substrates. Polymers such as -polydimethylsiloxane (PDMS), polymethylmethacrylate (PMMA), and cyclo-olefin copolymer (COC) have seen extensive use due to their low cost, favorable optical properties, and the variety of methods[3] in which micro-scale channels and features can be formed in these materials.

1.2 Commercialization of Microfluidic Technologies

Bioanalytical microfluidics have matured significantly in the past 15 years and commercialization has put microfluidic devices in the hands of end users[4][5][6][7][8][9]. Bioanalytical microfluidics is a deeply interdisciplinary field where experts from cell biology, electrical and computer engineering, mechanical

engineering, analytical chemistry, clinicians, and biologists meet. Microfluidic systems offer both improvements of traditional methods as well as enabling new techniques that would not otherwise be possible. After a surge of commercialization efforts for bioanalytical microfluidic devices, such as the widely successful Agilent 2100 Bioanalyzer and Abbott iSTAT platforms in the early 2000s, commercialization and adoption of bioanalytical microfluidics have been modest but steady while the technology was refined. Note that in some cases, the primary selling point for microfluidic technologies was the improved performance versus conventional methods afforded by the unique physics of microfluidic devices (e.g., for the Agilent 2100, Figure 1.2A). In other cases, the primary selling points have been portability and multiplex capabilities that offer logistical improvements over existing methods despite analytical performance equal to or lower than conventional methods (e.g., the Abbott iSTAT product line[10][11] (Figure 1.2). The Agilent 2100 instrument was used extensively by this author in the proceeding chapters.

Literature suggests that microfluidic devices have generally performed well for early adopters, but perhaps haven't yet made a transformative impact on bioanalytical testing. One reason for this is may be that microfluidic products have been (naturally) implemented first in operational bioanalytical labs for evaluation. In this setting performance gains may have been seen as incremental (as opposed to enabling disruptive change) because the conventional techniques were readily available to these early adopters. Arguably[12], the external hardware and technical expertise required to operate microfluidic devices have been the most significant obstacle to deployment of microfluidic technology in the field and at the point-of-care, although refinements in microfluidic

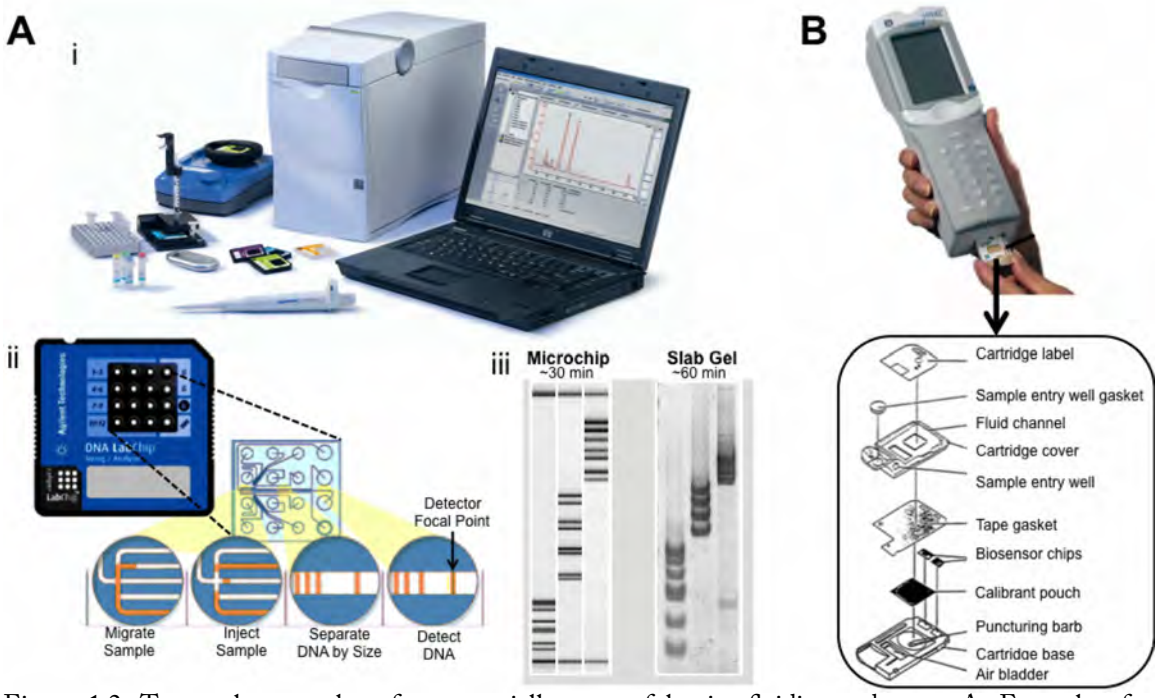

Figure 1.2: Two early examples of commercially successful microfluidic products. A. Example of a commercial microfluidic product that offers better performance than traditional methods. (i) The Agilent 2100 Bioanalyzer instrument and accessories. (ii) The DNA 1000 microfluidic devices utilizes the rapid heat dissipation of glass and the reduced joule heating of micro-scale channels to perform rapid separations of DNA fragments. (iii) Comparison of electrophoretic data in 2D slab gel format demonstrates the enhanced resolution of the microfluidic DNA separation versus a traditional polyacrylamide slab gel show superior resolution and turn-around time for the microfluidic method. B. Example of a commercial microfluidic product (Abbott Laboratories iSTAT) that specializes in improved portability and multiplex testing.

device design and instrumentation are making significant strikes towards overcoming these obstacles. The potential benefits and impact of microfluidic technology have not changed, and have almost certainly increased with the proliferation of microfluidic techniques in the literature.

Several complex, and challenging hurdles lie between a proof of principle microfluidic technology and a commercially available system with demonstrated utility. One significant challenge is the technical achievement of a practical microfluidic diagnostic device because integrating disparate bioanalytical processes on a single microfluidic device technology poses a complex landscape of engineering and logistical

challenges. (There are a host of issues in the business development side of microfluidic diagnostic device commercialization, yet these are beyond the scope of this thesis and the reader is directed to recent reviews on this topic [5,6].) Technical considerations for microfluidic device development include bioanalytical assay considerations (assay suitability for target application, operability on microfluidic platforms, and ease of integration with upstream and downstream processes), engineering considerations for the microfluidic device and its associated hardware (microstructure manufacturing decisions, cost and performance tradeoffs for associated instrumentation, etc.)The inter-relatedness of design and production challenges for bioanalytical testing was recently summarized by Ríos *et al.* [12], as seen in Figure 1.3.

More involved bioanalytical processes, especially analysis of nucleic acids, have created a need for microfluidic devices capable of integrating several separate processes in one device to yield meaningful data. Early drivers in point-of-care nucleic acid testing were actually methods for detection of biowarfare agents funded by the United States Defense Advanced Research Projects Agency (DARPA)[13] and this patronage continues to this day (e.g., [14]). Rapid genetic analysis for the purpose of forensic human identification is an application that has seen intense interest[15–17][le Roux et al. 2014, in prep]. Biomedical applications have included microfluidic handling of rare cells[18], such as circulating tumor cells

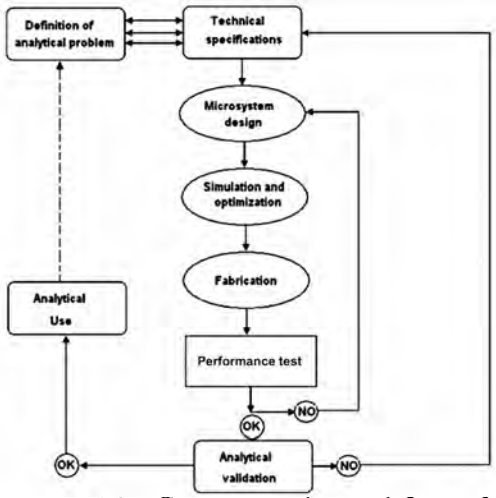

Figure 1.3: Conceptual workflow for development of bioanalytical microfluidic systems. (Adapted from [9])

(CTCs) or fetal cells in maternal blood, has also resulted in significant research efforts and the release of commercial products such as the Veridex Cell Search instrument which has gained US FDA approval for the isolation of CTCs bearing epithelial cell surface antigens. Integrated biomedical testing has been commercialized by Cepheid and others to combine several bioanalytical steps into one integrated device (Figure 1.4). The microfluidic diagnostic test market is currently a burgeoning field, crowded with industry giants as well as many promising startups[19][5,20].

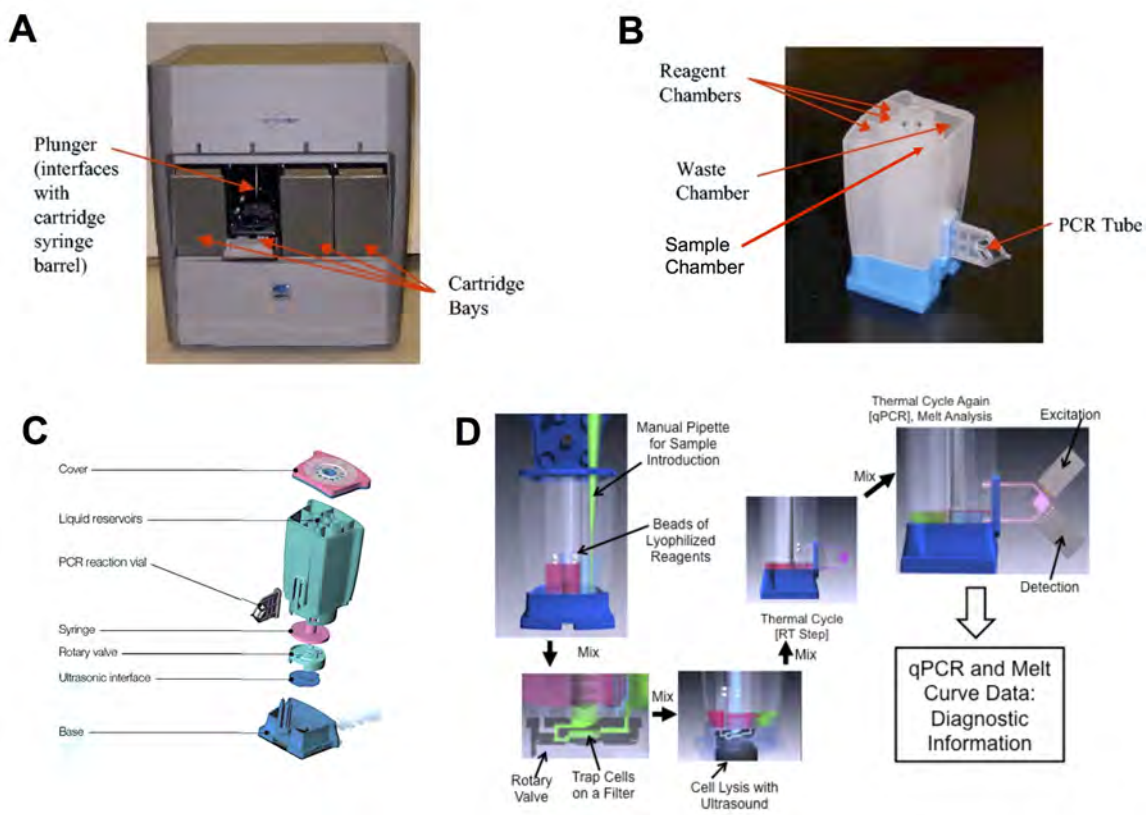

Figure 1.4: Conceptual overview of a commercial integrated microfluidic platform for RT-qPCR molecular diagnostics. A. The GeneXpert series instruments (produced by Cepheid Inc.) are bench-top devices. B. Disposable cartridge for integrated molecular diagnostics. C. Exploded view of cartridge. D. Process flow for generation of diagnostic information from raw samples containing cells of interest. (A and B adapted from [21], C and D adapted from materials provided by Cepheid [https://www.youtube.com/watch?v=mIsBLmjus6Q])

1.3 Concluding Remarks and Preface for Upcoming Chapters

Various aspects of bioanalytical microfluidic technology development are described in the chapters that follow. In particular, development of microfluidic devices for analysis of nucleic acids (the steps of which are diagrammed in Figure 1.5) has been the primary end goal for all of the research efforts in this thesis. With the pharmacogenomic genotyping project described in Chapter 2, we sought to improve medical care by putting out an inexpensive, rapid testing method for an application where the acquisition of genetic information is time sensitive[Epstein] (thus utilizing a key strength of bioanalytical microfluidics: accomplishing a conventional laboratory procedure in less time). Compatibility with microfluidic platforms was considered from the inception of this assay development. The bulk of the complexity for this multiplex genotyping assay was derived from careful choice of nucleic acid sequences, and this "bioinformatics engineering" reduced the cost of reagents (e.g., simple unmodified oligonucleotides were used), required less complex of instrumentation (e.g., single-color electrophoresis versus multiple-color detection methods), and paved the way for integration on a single microfluidic substrate by reducing the number of steps needed (e.g., avoided complicated multi-step workflows of other SNP typing methods) and increasing the compatibility with upstream and downstream bioanalytical processes. Chapter 3 describes practical implementation and upkeep of systems for microchip electrophoresis (ME) and laser induced fluorescence (LIF). ME-LIF methods offer fast and high resolution separations of biomolecules by taking advantage of microfluidic attributes (e.g., microscale channels for rapid heat dissipation). This instrumentation can be combined with microfluidic devices for a variety of bioanalytical purposes that include DNA separations, DNA melt

curve analysis, fluorescence emission spectral analysis, flow cytometry, fluorescence-based thermometry. Chapter 4 describes microchip fabrication via laser ablation for rapid prototyping of microfluidic devices. Primary goals of this work were to find methods that were both easy to implement and accessible to a wide variety of researchers (due to the increasing availability of laser engraving instruments and the widespread availability of the commercial glass cover slips and PDMS sheets that were used). With the acoustic trapping work in Chapter 5, we tried to apply acoustic trapping methods for the trapping and enrichment of pathogenic bacteria to prepare samples for subsequent genetic analysis.

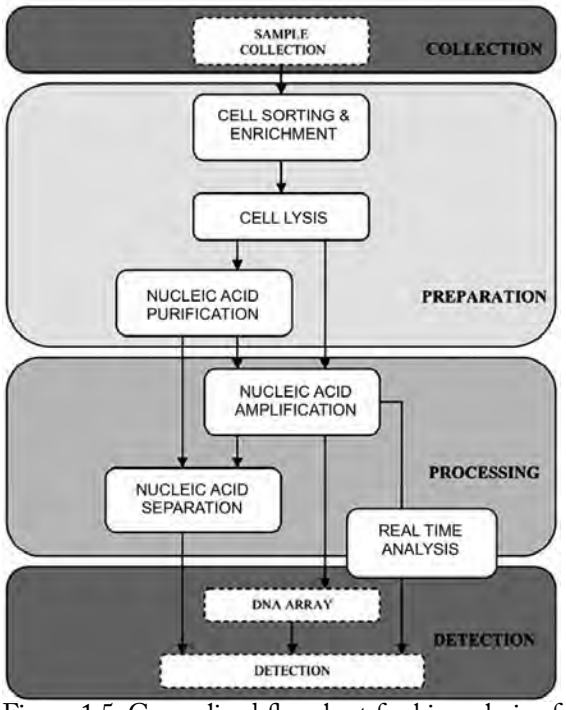

Figure 1.5: Generalized flowchart for bioanalysis of nucleic acids. (Adapted from [19])

Chapter 6 covers the combination of acoustic trapping and ultrasound-mediated heating for bioanalytical processes related to mammalian cells (e.g., circulating tumor cells). Design, fabrication, and evaluation was conducted for 2 major types of printed circuit board-mounted ultrasonic transducers capable of acoustic trapping. The complexities of heating with resonant ultrasound were empirically deduced and applied for controlled heating within microfluidic chambers. A thermophilic protease was utilized for thermally-switchable cell lysis to achieve in situ integration of acoustic cell trapping

and cell lysis. The effects of ultrasound on DNA aggregation were explored, and ultrasound-mediated compaction of condensed DNA states were observed. Heating with resonant ultrasound was applied for conducting PCR and a product specific to the genome of *E. coli* was successfully amplified.

1.4 References

[1] V. Miralles, A. Huerre, F. Malloggi, M.-C. Jullien, A Review of Heating and Temperature Control in Microfluidic Systems: Techniques and Applications, Diagnostics. 3 (2013) 33–67. doi:10.3390/diagnostics3010033.

[2] K. Ren, J. Zhou, H. Wu, Materials for microfluidic chip fabrication., Acc. Chem. Res. 46 (2013) 2396–406. doi:10.1021/ar300314s.

[3] H. Becker, C. Gärtner, Polymer microfabrication technologies for microfluidic systems., Anal. Bioanal. Chem. 390 (2008) 89–111. doi:10.1007/s00216-007-1692-2.

[4] I. Oita, H. Halewyck, B. Thys, B. Rombaut, Y. Vander Heyden, D. Mangelings, Microfluidics in macro-biomolecules analysis: macro inside in a nano world., Anal. Bioanal. Chem. 398 (2010) 239–64. doi:10.1007/s00216-010-3857-7.

[5] C.D. Chin, V. Linder, S.K. Sia, Commercialization of microfluidic point-of-care diagnostic devices., Lab Chip. 12 (2012) 2118–34. doi:10.1039/c2lc21204h.

[6] J.M. Walker, Microfluidic Diagnostics, Humana Press, Totowa, NJ, 2013. doi:10.1007/978-1-62703-134-9.

[7] T. Robinson, P.S. Dittrich, Microfluidic technology for molecular diagnostics., Adv. Biochem. Eng. Biotechnol. 133 (2013) 89–114. doi:10.1007/10_2012_139.

[8] E.K. Sackmann, A.L. Fulton, D.J. Beebe, The present and future role of microfluidics in biomedical research, Nature. 507 (2014) 181–189. doi:10.1038/nature13118.

[9] A. Ríos, M. Zougagh, M. Avila, Miniaturization through lab-on-a-chip: utopia or reality for routine laboratories? A review., Anal. Chim. Acta. 740 (2012) 1–11. doi:10.1016/j.aca.2012.06.024.

[10] J.N. Murthy, J.M. Hicks, S.J. Soldin, Evaluation of i-STAT portable clinical analyzer in a neonatal and pediatric intensive care unit., Clin. Biochem. 30 (1997) 385–9.

[11] F.S. Apple, M.M. Murakami, R.H. Christenson, J.L. Campbell, C.J. Miller, K.G. Hock, et al., Analytical performance of the i-STAT cardiac troponin I assay., Clin. Chim. Acta. 345 (2004) 123–7. doi:10.1016/j.cccn.2004.03.010.

[12] Á. Ríos, M. Zougagh, Sample preparation for micro total analytical systems (μ-TASs), TrAC Trends Anal. Chem. 43 (2013) 174–188. doi:10.1016/j.trac.2012.12.009.

[13] G.M. Whitesides, The origins and the future of microfluidics., Nature. 442 (2006) 368–73. doi:10.1038/nature05058.

[14] www.ecbc.army.mil, Detection Connection-Partnerships, Innovation help develop Army-specific CB Smartphone detector, (2014).

[15] A. Hopwood, C. Hurth, J. Yang, Z. Cai, Integrated Microfluidic System for Rapid Forensic DNA Analysis: Sample Collection to DNA Profile, Anal. Chem. 82 (2010) 6991–6999.

[16] J. Yang, C. Brooks, M.D. Estes, C.M. Hurth, F. Zenhausern, An integratable microfluidic cartridge for forensic swab samples lysis., Forensic Sci. Int. Genet. 8 (2014) 147–58. doi:10.1016/j.fsigen.2013.08.012.

[17] T. Geng, R. Novak, R.A. Mathies, Single-Cell Forensic Short Tandem Repeat Typing within Micro fl uidic Droplets, (2014).

[18] Y. Chen, P. Li, P.-H. Huang, Y. Xie, J.D. Mai, L. Wang, et al., Rare cell isolation and analysis in microfluidics., Lab Chip. 14 (2014) 626–45. doi:10.1039/c3lc90136j.

[19] L. Malic, M. Herrmann, X. Hoa, M. Tabrizian, Current State of Intellectual Property in Microfluidic Nucleic Acid Analysis, Recent Patents Eng. 1 (2007) 71–88. doi:10.2174/187221207779814680.

[20] B.H. Park, Y.T. Kim, J.H. Jung, T.S. Seo, Integration of sample pretreatment, μPCR, and detection for a total genetic analysis microsystem, Microchim. Acta. (2013). doi:10.1007/s00604-013-1128-y.

[21] S. Raja, J. Ching, L. Xi, S.J. Hughes, R. Chang, W. Wong, et al., Technology for automated, rapid, and quantitative PCR or reverse transcription-PCR clinical testing., Clin. Chem. 51 (2005) 882–90. doi:10.1373/clinchem.2004.046474.

2 Warfarin Genotyping in a Single PCR Reaction for Microchip Electrophoresis

2.1 Introduction:

The anticoagulant medication warfarin has been the leading oral anticoagulant for the past several decades[1,2]. Unfortunately, warfarin can also cause unsafe bleeding events, and it has been identified as the second leading cause of drug related emergency room visits[3]. Initiation of warfarin therapy is complicated by many factors, including a narrow therapeutic index, drug interactions with a wide range of pharmaceutical and dietary compounds, and substantial inter-patient variability in warfarin sensitivity. This inter-patient variability is due, in part, to genetic factors. Warfarin is metabolized by cytochrome P_{450} variant 2C9 (CYP2C9), and the *2 and *3 single nucleotide polymorphisms (SNPs) of *CYP2C9* result in impaired clearance of warfarin[1]. These 3 pharmacogenetic targets are illustrated in Figure 2.1. A major haplotype of the pharmacological target of warfarin, Vitamin K Epoxide Reductase, Complex 1 (VKORC1), is predictive of increased sensitivity to warfarin, as determined by SNPs 6853 (-1639A>G) or 6484 (1173C>T) [4,5] (Figure 2.2). Other SNPs evaluated for predicting warfarin sensitivity include *CYP2C9* *4 and *5, *APOE *E4* and *GGCX*, but their predictive value has been modest and inconsistent between patient populations[6]. A high-dose genotype, *CYP4F2 (rs2108622; p.V433M)*, has recently been identified[7], but this SNP does not impart sensitivity to warfarin. Furthermore, non-(dose-related) SNPs have been found to affect bleeding while in target INR[8], possibly warranting their incorporation into pharmacogenetic profiling in the future. Substantial portions of

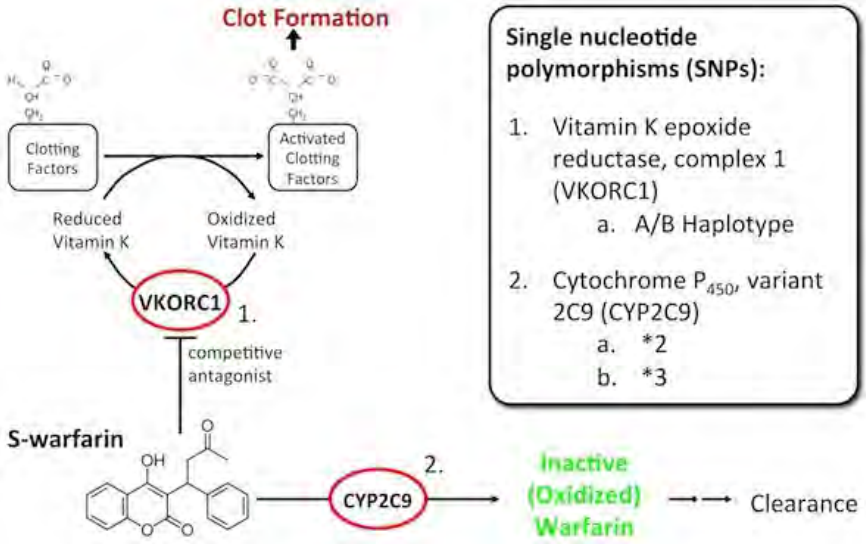

Figure 2.1. Genetic factors related to warfarin sensitivity in the pharmacological target and clearance pathway of warfarin.

many patient populations carry genetic factors conferring warfarin sensitivity[9][10], and a summary of allele variants in the US population from Schwarz *et al.[10]* is reproduced in Table 1. The *CYP2C9* and *VKORC1* genetic factors account for between 40% of inter-patient warfarin dosing variability in typical clinical setting[1,11], and a recent study in healthy control subjects found that approximately 62% of the variability in stable warfarin dose was explained by genotype[12], as shown in Figure 2.3.

An ongoing controversy exists over the clinical utility of warfarin genotyping[13,14], but recent prospective clinical trials have shown statistically significant improvement in patient outcomes when genotyping was performed prior to warfarin dosing[11,15,16]. In a recent study by Epstein *et al.* knowledge of the *CYP2C9* and *VKORC1* genotype was found to reduce hospitalizations from bleeding or thromboembolism by 43% versus non-genotyped control groups[11]. Importantly, genotyping was most useful prior to initial dosing because its clinical utility decreased

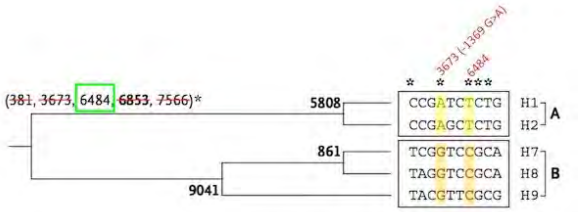

Figure 2.2. Linkage analysis of VKORC1 SNPs by Rieder et al. revealed 5 SNPs that were discriminatory for the VKORC1 haplotype. Of the 5 discriminatory SNPs, 4 were found to be unsuitable for TARMS by either bioinfomatics analysis or empirical testing (for 6853). Figure adapted from Rieder *et al. [4]*.

Table 2. Frequency of the *VKORC1* Haplotype and the *CYP2C9* Genotype, According to Race.*

Variant	Frequency in American Population		
	White	Black	All Patients†
	number (percent)		
VKORC1 haplotype			
Non-A/non-A	114 (43.2)	21 (72.4)	135 (45.6)
Non-A/A	119 (45.1)	8 (27.6)	129 (43.6)
A/A	31 (11.7)	0	32 (10.8)
Total	264 (100.0)	29 (100.0)	296 (100.0)
CYP2C9 genotype			
*1/*1	176 (66.7)	27 (96.4)	204 (69.4)
*1/*2 or *1/*3	77 (29.2)	1 (3.6)	79 (26.9)
*2/*2, *3/*3, or *2/*3	11 (4.2)	0	11 (3.7)
Total	264 (100.0)	28 (100.0)	294 (100.0)

Table 1. The frequency of alleles related to warfarin sensitivity in the US population was evaluated by Schwartz et al.[Schwartz], and their findings are reproduced here for demonstration purposes. (Source: Schwarz *et al.* [10])

once monitoring of INR had begun and dose adjustment was performed empirically. Many testing methodologies (but certainly not all, see Table 2) have a lengthy turn-around time that precludes pre-dosing genotyping in emergency cases. Assays with rapid turn-around times are key to maximizing the utility of warfarin genotyping.

In the past few years some new oral anticoagulants (e.g., dabigatran (Pradaxa®), rivaroxaban (Xarelto®), and apixaban (Eliquis®))[17] have come to market. Current dosing trends show a slow adoption of these new drugs[18], perhaps due to medication cost considerations (only branded formulations are available) or due to physician caution given the death of phase 4 safety and efficacy data. For the near term, warfarin will continue to be the

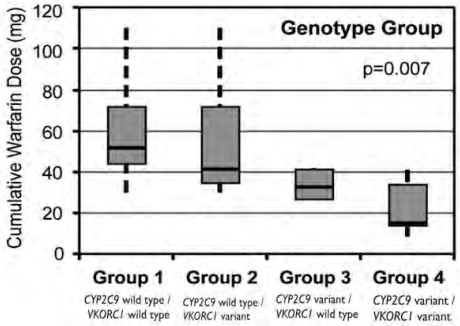

Figure 2.3. Warfarin dosing was correlated with genotype by Kadian-Dodov *et al.[12]*. The necessary cumulative dose of warfarin needs to reach 2 consecutive days within a target INR between 2 and 3. Lower cumulative doses are indicative of greater sensitivity to warfarin. (Source: [[12]Table 1 and Figure 2.)

predominant oral anticoagulant, and maximizing the safety and efficacy of warfarin dosing through pharmacogenetics remains important.

Cost considerations also impact the feasibility of routine warfarin genotyping. Tests for warfarin genotyping currently cost on average USD 250[19,20], and many insurers will not reimburse at this price[11,15]. Further complicating matters is that many pharmacogenetic tests do not have a defined insurance billing code[21], but instead depend on generic laboratory testing codes. Cost considerations for warfarin genotyping platforms include the cost of reagents and consumables, up-front instrumentation costs, and the amount of handling required[22]. The economics of warfarin pharmacogenetic

	Verigene	eSensor	Luminex	Invader	Multiplexed warfarin T-ARMS
SNP Detection Methology	Gold nanoparticle hybridization assay	Electrochemical hybridization assay	Multiplex PCR and allele-specific primer extension	Flap endonuclease	*Taq* polymerase base pairing selectivity
Instrumentation Required	Verigen Processor and Reader	Themocycler, eSensor modular detection tower	Thermocycler, Luminex Detection System	Thermocycler, 96well plate fluorimeter	Thermocycler (conventional or microchip), Agilent 2100
Instrument Cost	$55,000 USD	--	$45,000	$12,000	$12,200
Reagents Cost per Single Analysis	$72	$263	$347	$230	$26
Turn Around Time (hours)	1.7	2.8	5.5	2.6	1.25 (conv. PCR, 1.0(microchip PCR)
Lab Footprint	9383 cm	1741 cm	15834 cm	2338 cm	1720 cm^3
Minimum DNA per Reaction	2500 ng	10 ng	15 ng	50 ng	10 ng
PCR Step Required	No	Yes	Yes	Yes	Yes
Alleles Tested	*2, *3; 1173C>T	*2, *3; -1639G>A	*2, *3, *4, *5, *6; -1639G>A, +85G>T, 121G>T, 134T>C, 172A>G, 1331G>A, 3487T>G	*2, *3; -1639G>A	*2, *3; 1173C>T
Number of pipetting steps per single sample run	2	18	63	71	20 (2 for PCR, 18 for ME*)
Relevant Reviews	Maurice, Lefferts, Ryan	Maurice, Babic	Maurice, Johnson	Maurice, Lefferts, Langley	

Table 2. Comparison of commercial warfarin genotyping products with the assay described in this paper. Characteristics of the four commercial systems were derived from summary information in the reviews cited in the last row of the table. [*for manual loading of the chip for microchip electrophoresis (ME)] (Reproduced from [43])

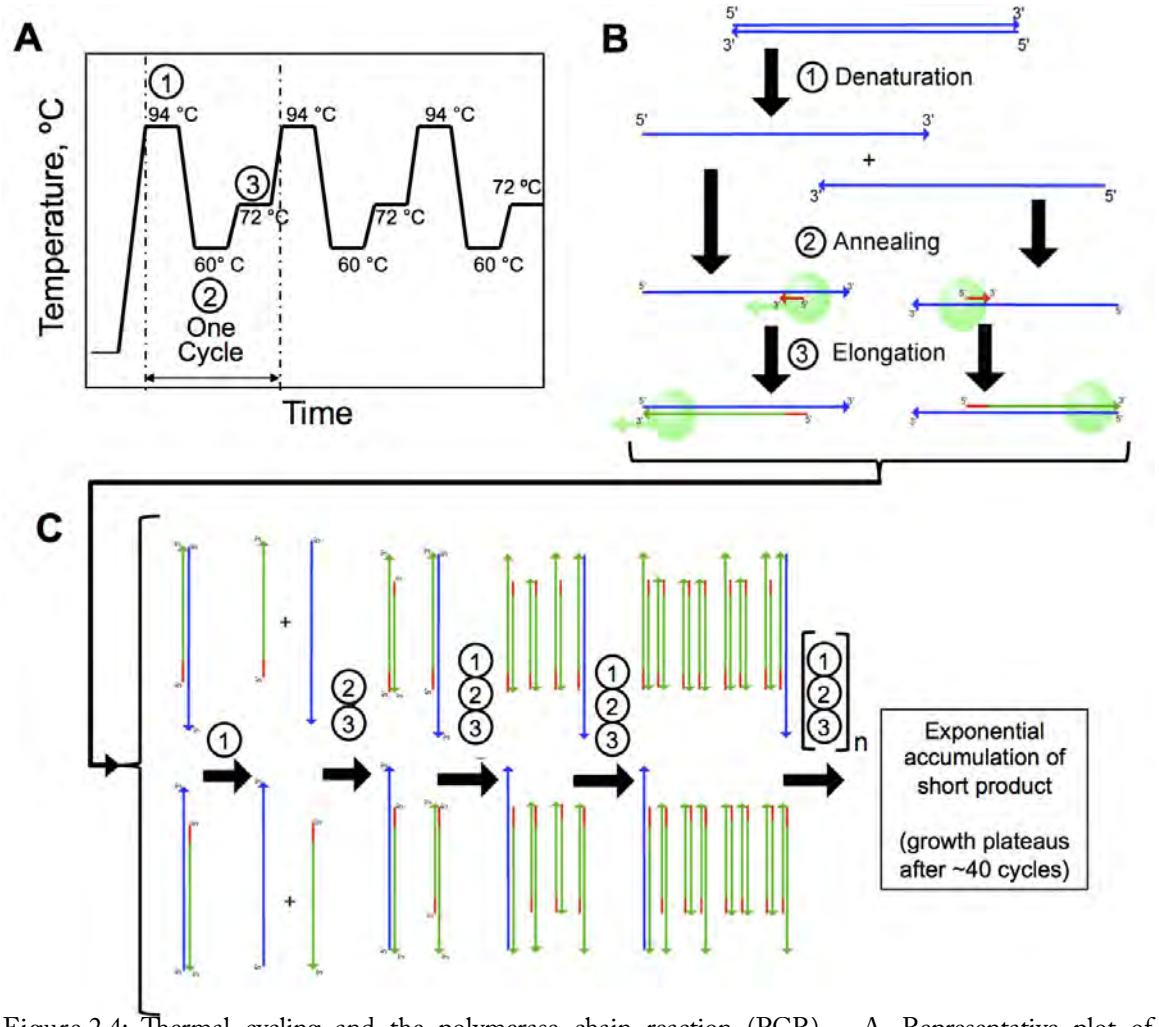

Figure 2.4: Thermal cycling and the polymerase chain reaction (PCR). A. Representative plot of temperature versus time annotated with DNA denaturation (1), primer-template annealing (2), and DNA fragment extension (3). B. Diagram of the first cycle in PCR. Template DNA strands are shown in blue, primers are shown in red, and newly-synthesized DNA is shown in green. Taq polymerase is represented by the green sphere in (2) and (3). C. Diagram of subsequent PCR cycles leading to amplification of the original template sequence.

testing create a demand for low-cost genotyping, with low instrumentation costs and good economy for a relatively low volume of samples.

To address both cost and turn around time concerns, we set out to design an assay that would use widely available reagents, widely available laboratory equipment, and rapid microchip gel electrophoresis instrumentation. The polymerase chain reaction (PCR) is

diagrammed in Figure 2.4. Published methods for warfarin genotyping include allele-specific PCR [23][24], PCR with ligation [10], single base extension [25], PCR with restriction digestion [26][27], pyrosequencing[27], melt analysis [28], and quantitative PCR [29,30]. Despite the wealth of published genotyping methods, either multiple PCR reactions are required, dedicated equipment is needed, or the assays call for sample clean-up steps that complicate analyses. In particular, we sought a genotyping method that required only a single PCR amplification followed by microchip electrophoresis, as this would be well suited to an integrated microfluidic device [31]. One such method is the amplification refractory mutation system (ARMS) [32] where primers anneal to the SNP site at their 3' end. Under optimal conditions, *Taq* polymerase will not extend a primer that does not exhibit canonical Watson-Crick base pairing with the SNP site base of the DNA template [33]. ARMS assays provide a digital 'yes/no' answer for one allele based on the presence or absence of the allele-specific amplicon. When two pairs of ARMS primers are applied to one SNP, unambiguous genotyping of bi-allelic SNPs is achieved, in what is called tetra-primer ARMS (T-ARMS) [34][35][36]. Both ARMS [23], and T-ARMS [24,37] have been applied to pharmacogenetic testing, but a fully-multiplexed T-ARMS assay for warfarin genotyping has not been described. Recently, guidelines were published for optimizing T-ARMS assays[38], and several of these principles were independently implemented in this work. This chapter describes steps taken to multiplex three T-ARMS primer sets together for definitive determination, in one PCR reaction, of *CYP2C9* *2, *3, and *VKORC1* genotypes utilized in warfarin dosing algorithms.

2.2 Materials and Methods

2.2.1 Assay Scheme

The allele-specific ARMS SNP typing method was chosen initially due to its compatibility with microfluidic PCR. The ARMS scheme for genotype a single locus is shown in Figure 2.5, where 2 allele-specific primers bind to the same site on the same template strand. The allele-specific primers were to be differentiated by fluorescent labels or electrophoretic mobility modifiers. This assay scheme was used to initially genotype a small cohort of 4 samples. However, a genotyping methodology was sought that would diminish the demands on the microchip gel electrophoresis detection system to a single laser-induced fluorescence color.

A novel multiplex T-ARMS assay was envisioned to allow single-reaction genotyping for the 3 SNPs using a conventional thermocycler and the popular Agilent 2100 microchip gel electrophoresis platform. The multiplex T-ARMS scheme is diagrammed in Figure 2.6. As with the ARMS assay, allele specificity is derived from the primers (Figure 2.6A). Either of two "inner" allele-specific PCR products maybe formed

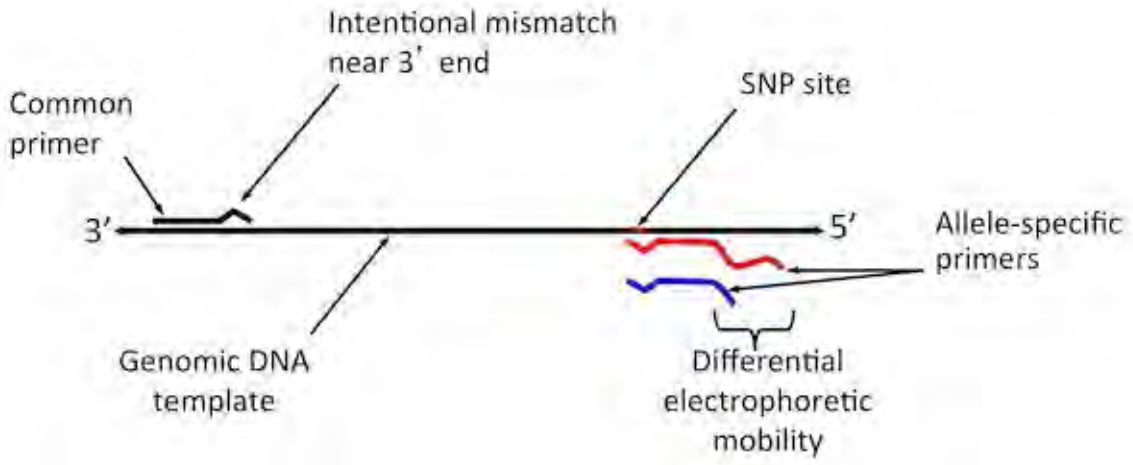

Figure 2.5. The amplification refractory mutation system (ARMS) for a single SNP site.

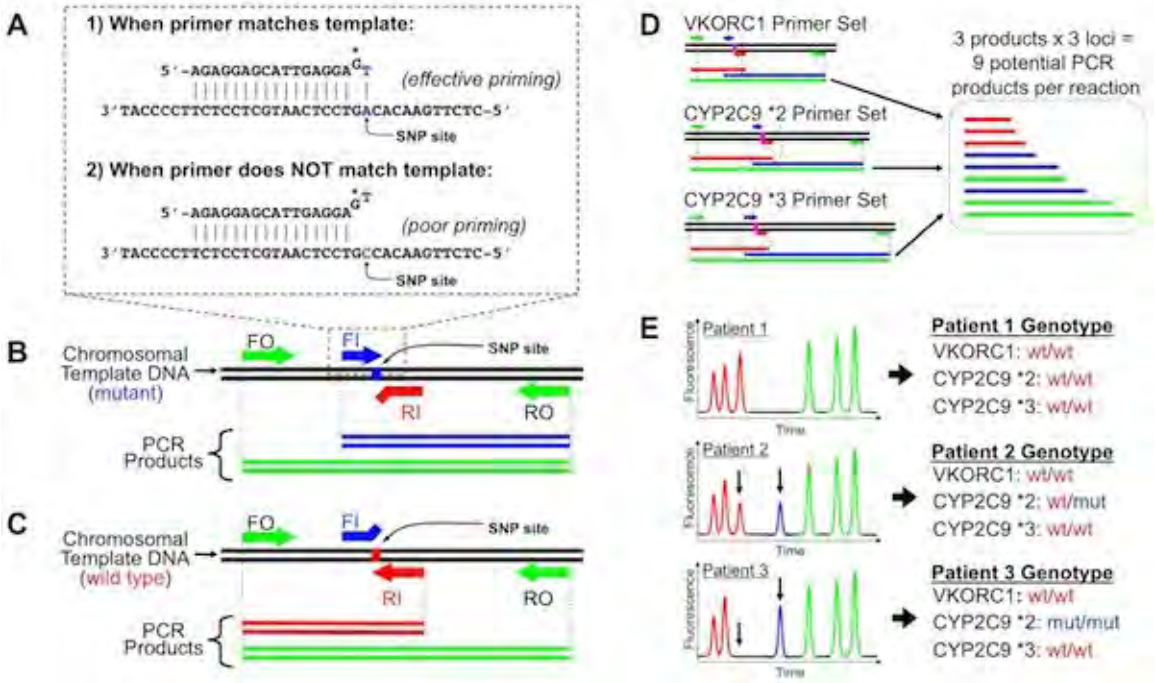

Figure 2.6. A. The assay utilizes the high selectivity of Taq polymerase for allele-specific amplification of PCR primers. B,C. Four primers are needed per locus, forming 1 or 2 allele-specific products and a control product. D. Three SNPs are simultaneously genotyped by multiplexing three primer sets. E. Mock electropherograms depict how genotype data is derived from the electrophoretic data (arrows indicate the CYP2C9 *2 specific product). Figure reproduced from [43].

along with an "outer" PCR product as an internal positive control (Figure 2.6B and C). Three SNP sites were genotyped by developing non-overlapping T-ARMS PCR products (Figure 2.6D). When the PCR products were separated by size via microchip electrophoresis, each genotype generated a characteristic pattern of peaks (Figure 2.6E).

2.2.2 Sequence Analysis, Primer Design, and PCR Simulation

Sequences for the single nucleotide polymorphisms were obtained from the National Center for Biotechnology Information (NCBI, Bethesda, MD, USA): *CYP2C9* *2 (430C>T; rs1799853), *CYP2C9* *3 (1075A>C; rs1057910), VKORC1 6853 (1542G>C; rs8050894), and *VKORC1* 6484 (1173C>T, rs9934438). Comparisons to homologous sequences were made with the NCBI basic local alignment search tool (BLAST)[39] for

nucleic acid sequences. The annotated BLAST alignments provided in Figure 2.7 and Figure 2.8. show regions of the nucleotide sequence dissimilarity between *CYP2C* subtype 9 versus homologous subtypes. BLAST alignments for 2 SNPs of the VKORC1 haplotype are given in Figure 2.9 and Figure 2.10. Outer primers for the *VKORC1* 6484 primer set were designed using the Primer3 online primer design tool [40]. PCR was simulated *in silico* with AmplifX (Jullien N. AmplifX version 1.44. 2007) and Amplify 3X

Figure 2.7. CYP2C9 *2 BLAST alignment. Significant homology was found with the closely-related genes CYP2C19, CYP2C18, and CYP2C8 and a homologous pseudogene.

Figure 2.8. CYP2C9 *3 BLAST alignment. Various iterations of primers are also shown aligned to the sequence.

(Engels B. Amplify 3X for Mac OS X. 2005) as exemplified by the screenshot in Figure 2.11.

To apply the T-ARMS assay methodology to warfarin pharmacogenetic testing, 3 compatible primer sets were designed to determine the genotypes of the *CYP2C9* *2, *3,

Figure 2.9. VKORC1 6853 (1542G>C) BLAST alignment.

and *VKORC1* loci in a single multiplexed PCR reaction. Highly homologous genes (*CYP2C19*, *CYP2C8*, *CYP2C18*) necessitate *CYP2C9* subtype-specific outer primers as well. A library of potential primers was generated from the multiple candidate primer

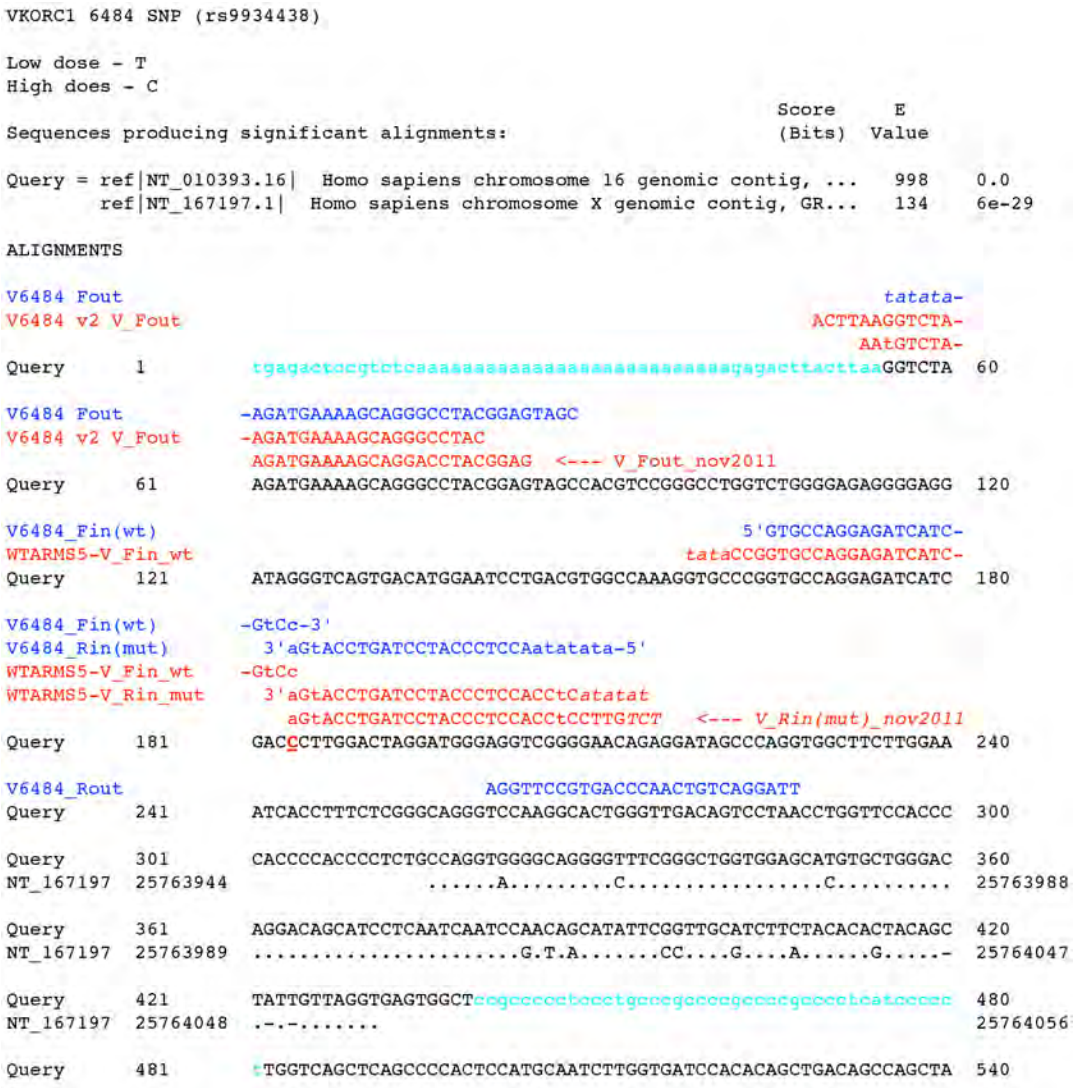

Figure 2.10. VKORC1 6484 (1542G>C) BLAST alignment.

binding sites (see Figure 2.12). Then within this library of potential primers the exact lengths were carefully chosen both to normalize the predicted T_m values of the primers relative to each other, and to find compatible theoretical amplicon sizes. T-ARMS primer sets consisting of 2 outer primers and 2 inner primers were chosen for each of the 3 SNP loci. Priority was given to primers that yielded products with unique sizes within the assay so PCR products were identifiable by size via microchip electrophoresis.

To enhance allele- or subtype-specificity, primers were given an intentional

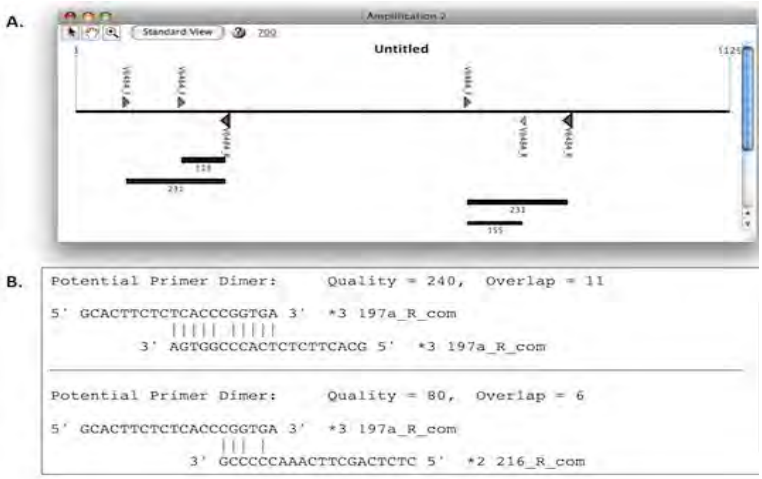

Figure 2.11. PCR reactions were simulated in the Amplify3X program. First the target sequence and primer sequences were specified, then the program produced graphical summaries of predicted PCR products- a screenshot of which is shown here (A.). Simulations also produced text-based sequence and primer-dimer information such as primer dimer predictions (B.).

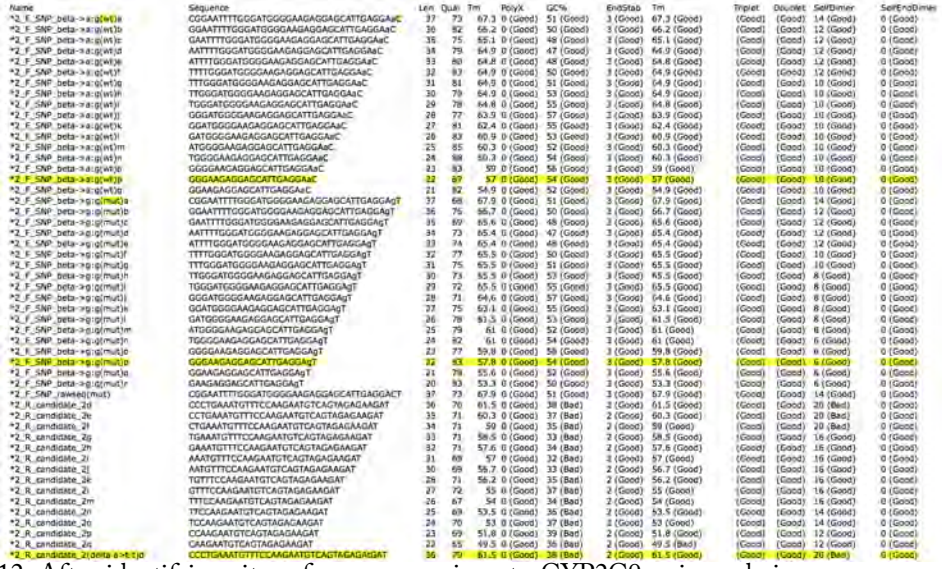

Figure 2.12. After identifying sites of sequence unique to CYP2C9, primer design was accomplished by manually screening primers based on their metrics reported by the AmplifX program.

mismatch to destabilize the 3' end to ensure that effective priming would only occur if the terminal base matched the template. The thermodynamic stabilities of mismatched bases (e.g. A:A, A:C, A:G) are not uniform [41], and thus the position and base of the intentional mismatches were selected to normalize the stability of the 3' ends of the primers. Primer dimers predicted to be very stable were averted by adding an additional

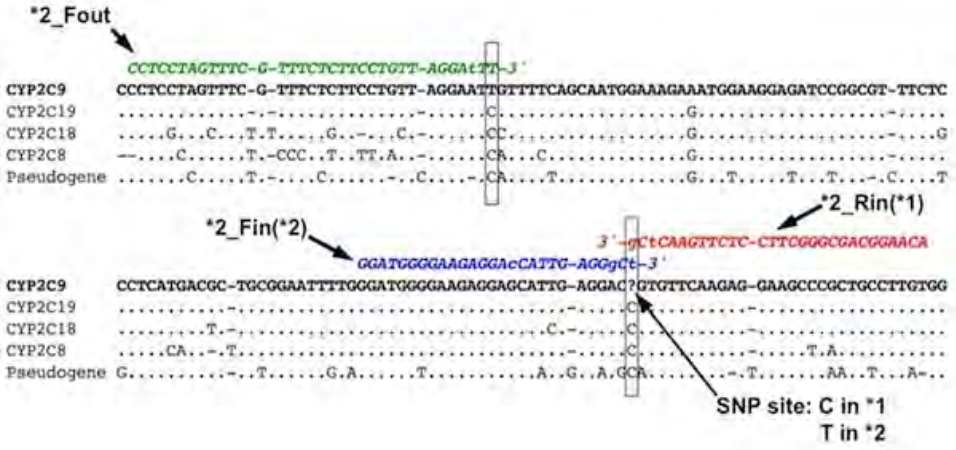

Figure 2.13. BLAST alignment of a portion of the CYP2C9 *2 SNP showing the placement and sequence of select primers. Dots indicate there is no difference in sequence, dashes indicate insertions or gaps relative to the CYP2C9 sequence, and letters indicate base substitutions. Note that the *2 reverse outer primer is not shown in this view. Reproduced from [43].

intentional mismatch in the middle of the primer where dimerization would have occurred. To avoid overlapping product sizes, the lengths of the *VKORC1* products were increased by adding a string of poly-AT bases at the 5' end of the primers. Finally, the length of each primer was adjusted to yield primers with compatible annealing temperatures (T_m's). One example of a *CYP2C9*-specific primer binding site found through these computational studies is shown in Figure 2.13. The final set of primers is shown in Table 3.

Table 3. Primers for warfarin multiplexed T-ARMS assay. Lowercase letters in primer sequences indicate intentional mismatches versus the genomic template. Primer melting temperatures were calculated without factoring in the effect of mismatches versus the template. Reproduced from [Poe 2012].

Primer Name	Sequence	Final Conc. (μM)	T_m (°C)	Product Size (bp)	
CYP2C9*2 Fout	CCTCCTAGTTTCGTTTCTCTTCCTGTTAGGAtTT	0.20	61.2	154	307
CYP2C9*2 Rin(*1)	ACAAGGCAGCGGGCTTCCTCTTGAACtCg	0.16	67.6		
CYP2C9*2 Fin(*2)	GGATGGGGAAGAGGAcCATTGAGGgCt	0.16	65.0	206	
CYP2C9*2 Rout	CCGCTTCACATaAGCTAACAACCAGaACTCAT	0.20	62.4		
CYP2C9*3 Fout	CAGAAACCGGAGCaCCTGCATGtAA	0.20	61.5	110	340
CYP2C9*3 Rin(*1)	CATGGGGCAGGCTGGTGGtGAGAAGGTCtAT	0.16	67.5		
CYP2C9*3 Fin(*3)	TGTGGTGCAgGAGGTCCAGAGATgCc	0.20	65.7	286	
CYP2C9*3 Rout	CCAGACACTAGGACCTcTTACAAACCTTTATtGC	0.20	61.9		
VKORC1 6484 Fout	ACTTAAGGTCTAAGATGAAAAGCAGGGCCTAC	0.30	61.5	170	235
VKORC1 6484 Rin(B)	TCCTCTGTTCCCCCACCTCCCATCCTtGTCCAAtA	0.40	68.2		
VKORC1 6484 Fin(A)	tataCCGGTGCCAGGAGATCATCGtCc	0.16	63.1	133	
VKORC1 6484 Rout	TTAGGACTGTCAACCCAGTGCCTTGGA	0.30	63.1		

2.2.3 Primer Preparation and Conventional PCR

Primers were synthesized by Eurofins MWG Operon (Eurofins MWG Operon, Huntsville, AL, USA); lyophilized primers were suspended in de-ionized water and working stocks were prepared at 20 μM in diH_20 or 100 μM tris pH 8.0 and stored at -20 °C. Tris buffer, deoxynucleotide triphosphates (dNTPs) and bovine serum albumin (BSA) were obtained from Fisher BioReagents (Fisher Scientific, Pittsburgh, PA, USA). AmpliTaq Gold polymerase, GeneAmp PCR Buffer II, and 25 mM $MgCl_2$ were purchased from Applied Biosystems (Life Technologies Corporation, Carlsbad, CA, USA). SpeedSTAR polymerase was obtained from Takara Bio Inc. (Shiga, Japan). Cheetah Taq hot start polymerase was obtained from Biotium (Biotium Inc., Hayward, CA, USA). Conventional PCR reactions were performed in a Bio-Rad MyCycler thermal cycler (Bio-Rad, Hercules, CA, USA). As with all rapid PCR assays, thermal cyclers should be validated for rapid thermal cycling [Kim 2008] prior to use for this assay because non-ideal thermal cycling may adversely affect the specificity and yield. Post-PCR samples were analyzed by microchip gel electrophoresis using the Agilent 2100 Bioanalyzer DNA 1000 Series II kits and instrumentation (Agilent Technologies, Santa Clara, CA, USA).

Primers were tested in conventional PCR amplification reactions at increasing levels of multiplexing – first in pairs, then the 4 primers of each SNP site, then all 12 primers together. Samples of known genotype were used as template to verify the allele-specificity of the inner primers. The closely related genes (*CYP2C19*, CYP2C18, and *CYP2C8*) contain a wild type base in the site homologous to the *CYP2C9* *2 and *3 SNPs,

and thus verification of the *CYP2C9* subtype specificity was possible because only a mutant CYP2C9 sequence would generate a mutant-specific amplicon.

To streamline analyses, an algorithm was written for the Agilent 2100 Expert software (and a custom LabVIEW program was developed) (Figure 2.15) to interpret the pattern of PCR product peaks and automatically report the genotyping results in standard notation. Data was processed in batch mode to perform genotype calling on many samples at once. Automated interpretation of raw detector data is an essential step for useful point-of-care testing technologies, and setting up 2100 expert or utilizing the custom LabVIEW program significantly simplified the process of interpreting the pattern of peaks in a given electropherogram.

Extensive parameter optimization studies were conducted during development of this assay. For example, Figure 2.14 shows the experimental plan for a multi-parameter optimization study. Several performance metrics were evaluated, including PCR efficiency (peak height), inner product to outer product balance, primer dimerization, *CYP2C* subtype specificity, and allele specificity. Optimized thermal cycling conditions were: 2 min @ 95 °C, 10 x [5 s @ 95 °C, 5 s @ 62 °C, 5 s @ 72 °C], 25 x [5 s @ 95 °C, 5 s @ 60 °C, 5 s @ 72 °C], 2 min @ 72 °C. The optimized reaction composition was found to be: 1X GeneAmp PCR Buffer II, 3 mM $MgCl_2$, 0.075 μg/μl BSA, 0.2 mM each dNTP, 1 ng/μL hgDNA, primers in concentrations listed in Table 3 and 0.05 U/μL of Cheetah Taq polymerase in a total volume of 20 μL.

2.2.4 Microchip PCR

The PCR microdevices used in this work were fabricated in borofloat glass, and the

Warf T-ARMS - *2/*3 multiplex series: ext temp, [MgCl2], [buffer]

This experiment will test three conditions that may improve the performance of the inner primers: 1) 1.5 and 3 mM $MgCl_2$, 2) lower extension temperatures, and 3) 1X and 2X buffer concentration. These ideas came from reviewing the multiplex PCR paper by Henegariu et al (BioTechniques 23:504-511, 1997) and the Joseph Warren's PowerPoint presentation on PCR Generalities. Each condition will be tested with two replicates, and I will forgo NTCs. This will be the first time that the *2 and *3 primer sets will be multiplexed in their entirety, but the results on page 175 are promising.

	[Stock]	Stock ID	Vol. (µL)	[Final]	MM1	Vol (µL)	MM2
Water	n/a	PCR grade water	8.080	n/a	**67.333**	6.580	**54.833**
10X PCR Buffer II	10x	Applied Bio, Lot KP6784	1.500	1X or 2X	**12.500**	3.000	**25.000**
MgCl2 + water	25 mM	Applied Bio, Lot KP0119	1.800	1.5 or 3 mM	--	--	--
dNTPs	2.5 mM ea	(new aliq.) 11Mar2009	1.200	200 µM ea	--	--	**10.000**
***2 Fout**	20 µM	03Aug2009 prep, BLP1-159	0.150	0.2 µM	--	--	**1.250**
***2 Rin(wt)**	20 µM		0.300	0.4 µM	--	--	**2.500**
***2 Fin (mut)**	20 µM		0.300	0.4 µM	--	--	**2.500**
***2 Rout**	20 µM		0.150	0.2 µM	--	--	**1.250**
***3 Fout**	20 µM		0.150	0.2 µM	--	--	**1.250**
***3 Rin(wt)**	20 µM		0.300	0.4 µM	--	--	**2.500**
***3 Fin(mut)**	20 µM		0.300	0.4 µM	--	--	**2.500**
***3 Rout**	20 µM		0.150	0.2 µM	--	--	**1.250**
hgDNA	3 ng/µL	BLP1-page29-line01	0.500	1 ng/µL	--	--	**4.167**
AmpliTaq Gold	5 U/µL	Appl. Bio, KP5386, op:05Aug2009	0.120	0.04 U/µL	--	--	**1.000**
			15.000	8.3333	**110.000**	15.000	**110.000**

Thermal Cycling Program

Initial Denature – 10 min @ 95 °C
Thermal Cycle x 10:
Denature – 30 sec @ 95 °C
Anneal – 30 sec @ 60 °C
Extend – 30 sec @ 72/68 °C
Thermal Cycle x 30:
Denature – 30 sec @ 95 °C
Anneal – 30 sec @ 52 °C
Extend – 30 sec @ 72/68 °C
Final Extension – 7 min @ 72 °C
Hold indefinitely @ 4 °C

8.3333	1.5mM	3mM
Water	7.500	0.000
$MgCl_2$	7.500	15.000
Total	**15.000**	**15.000**

	Reps
MM	13.2
$MgCl_2$	1.8
Total:	**15.0**

(Notebook Reference: BLP1-pg176)

Figure 2.14. A sample PCR worksheet from a parameter optimization study during warfarin mutliplex T-ARMS assay development.

fabrication and operation processes have been previously described in greater detail[42]. The PCR reaction mixture was identical to that described in the previous section, except for higher concentrations of BSA (0.4 µg/µL) and *Taq* polymerase (0.1 U/µL). Microchip PCR reactions required 4 µL of total volume to fill the microfluidic architecture, with a PCR chamber volume of less than 1 µL.

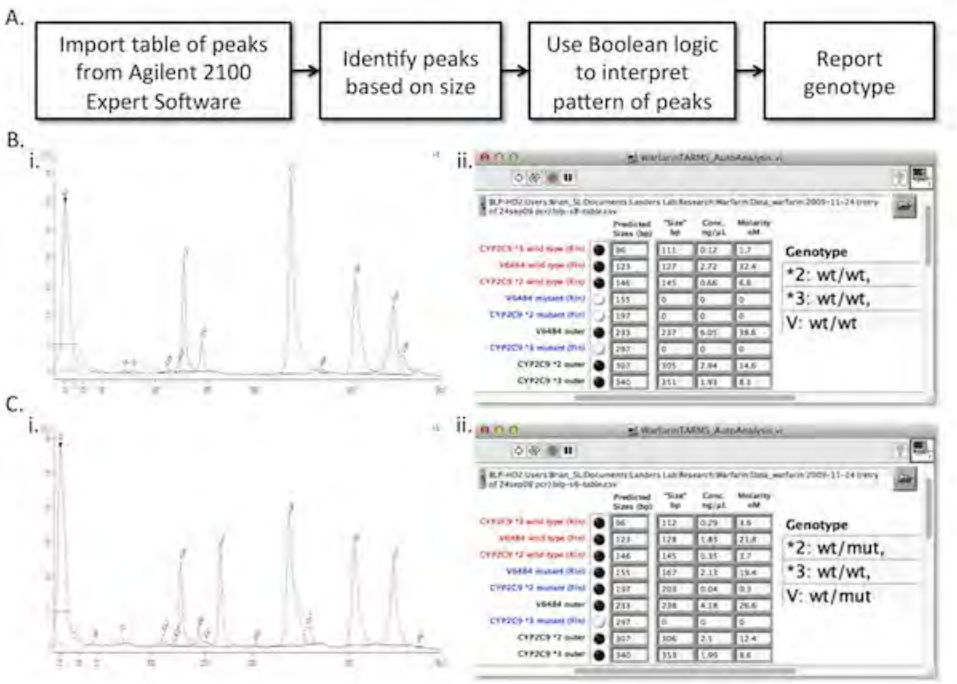

Figure 2.15. Custom software was developed to interpret the pattern of peaks in Agilent 2100 run data and call a genotype. A. The algorithm, shown here in flowchart form, was implemented in LabVIEW. B,C. Two examples of interpretation of electropherogram peaks (i.) to produce a genotype (ii.).

The dual modular microfluidic apparatus consisted of an infrared-mediated PCR system and the Agilent 2100 Bioanalyzer microchip electrophoresis system (Figure 2.17). The hardware of IR-PCR system has been described previously [42], but this was the first implementation of thermal cycling with multiple annealing temperatures on this system. Glass microfluidic devices (Figure 2.16) were fabricated via photolithography and wet chemical etching.

2.2.5 Patient Samples

Clinical samples of pre-purified human genomic DNA (hgDNA) from 10 de-identified individuals were obtained from the University of Virginia Pathology Department and the Mayo Clinic. Some samples were split and blinded to the experimenter to assess

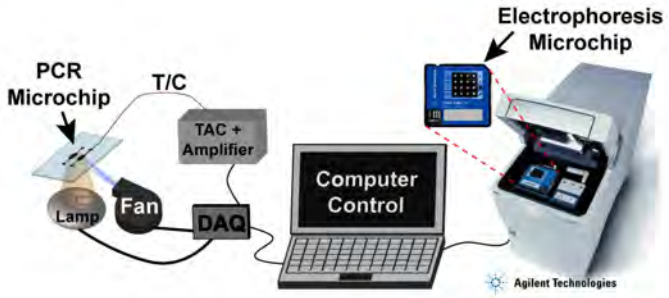

Figure 2.17. Modular microfluidic platform for warfarin genotyping consisted of 2 separate instruments: an infrared-mediated microchip PCR system (left) and Agilent 2100 Bioanalyzer microchip electrophoresis instrument (right). (Abbreviations: T/C (thermocouple), TAC (thermocouple to analog converter), DAQ (data acquisition card). Reproduced from [43]

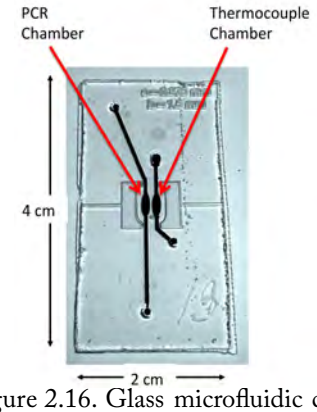

Figure 2.16. Glass microfluidic chips for infrared-mediated PCR were fabricated via traditional photolithography and wet chemical etching. The microdevice is shown filled with black ink for contrast.

reproducibility. The *CYP2C9* genotypes of the samples were determined using the Invader® assay (UVA Pathology samples) or by an allele-specific PCR assay (Mayo Clinic samples). The *VKORC1* genotype at the 6484 locus was determined by bi-directional sequencing of PCR products encompassing the SNP site. Thirteen samples of de-identified hgDNA were prepared from buccal swabs, evaluated with the T-ARMS assay while genotypes were unknown, then genotyped at all three loci by Sanger sequencing. Some samples were obtained from patients already undergoing warfarin genotyping, and therefore the population probably contained a high proportion of warfarin sensitive genotypes relative to the general population. One dual heterozygote was encountered (*1*2/AB) and readily genotyped by the T-ARMS assay, but other compound heterozygotes were not part of this sample set. This collection of genotypes had at least one homozygote for both wild type and mutant alleles and a heterozygote for each locus, thus allowing verification of allele specificity at each of the three SNP sites.

2.3 Results

The results of this study were initially computational, and a substantial amount of *in silico* optimization was performed on a library of potential primers, followed by synthesis and *in vitro* testing and optimization. A set of twelve primers, along with specific PCR reaction conditions, was empirically identified for accurate and reproducible genotyping of clinical samples. Following optimization in conventional equipment, this assay was adapted to a dual microchip apparatus for more rapid analysis. Blinded samples of diverse genotypes were genotyped by this method.

2.3.1 Study of SNP Site Suitability for T-ARMS Assay

The sequences surrounding the *2 and *3 *CYP2C9* SNP sites and five SNPs comprising the *VKORC1* haplotype were analyzed to find primer sequences with the subtype specificity, allele specificity, and product sizes required for this unique, single-tube T-ARMS assay. The sequence flanking the *CYP2C9* *2 and *3 SNPs contained a few regions unique to the *CYP2C9* subtype, and some of these were exploited as subtype-specific outer priming sites. Sequence analysis of 5 *VKORC1* SNPs diagnostic of the low or high dose haplotype [4] revealed that 4 out of 5 sites (381, 3673, 6853, and 7566) contained repetitive sequence elements problematic for a T-ARMS primer binding arrangement. The *VKORC1* 6484 (1175C>T) SNP site was found to lack repetitive sequence or highly homologous sequence within the footprint of the T-ARMS binding sites. The linkage of SNPs between the two dosing-relevant haplotypes of the *VKORC1* is shown above in Figure 2.2. The suitability of the *VKORC1* 6484 site is opportune because the 6484 site (like its counterparts 3673 and 6853) serves as a discriminatory

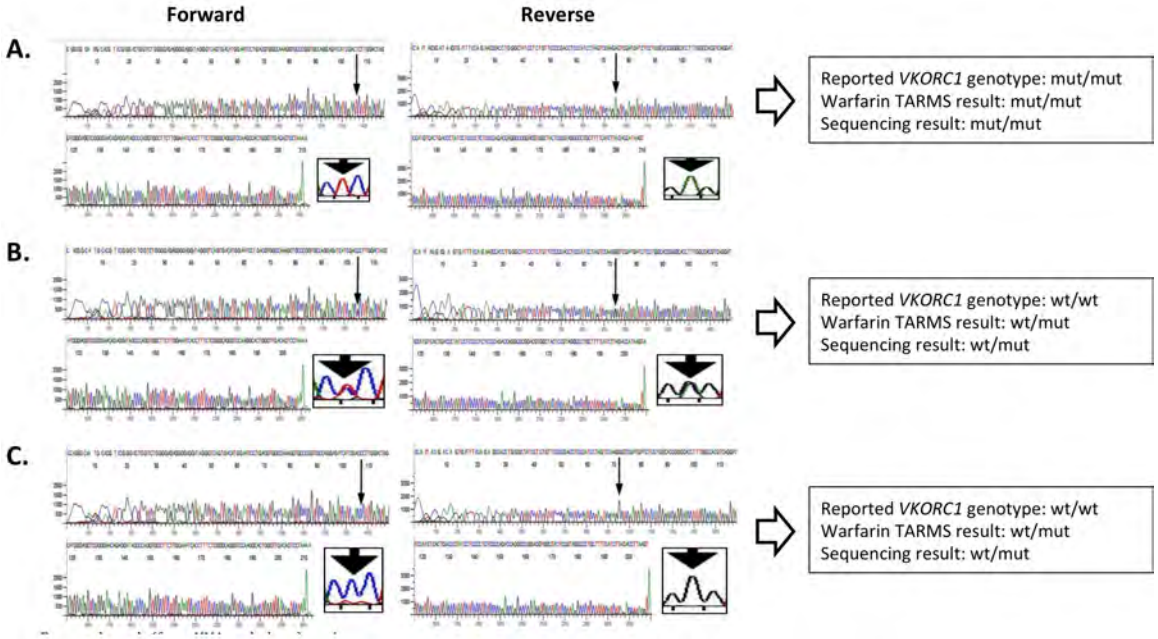

Figure 2.18. Bi-directional sequencing (using either Forward and Reverse primers) was utilized to unambiguously determine the genotype of samples at the VKORC1 4684 SNP site. Three example analyses are shown here for samples: A.) a homozygous mutant sample with fully concordant test results, B,C.) putatively homozygous wild type samples that were revealed by TARMS and sequencing to be heterozygous.

SNP for assigning the *VKORC1* haplotype.

2.3.2 VKORC1 SNP Site Cross-Validation

The results of several T-ARMS genotyping attempts were inconsistent with the *VKORC1* type reported by the source institutions of the human genomic DNA. To determine the genotypes at the *VKOCR1* 6484 locus for certain, bi-directional sequencing was conducted on the *VKORC1* 6484 outer T-ARMS PCR products. Three representative sequencing analyses are shown in Figure 2.18. The T-ARMS genotyping calls were actually vindicated by the Sanger sequencing results. Reasons for the discrepancy are unknown, but could include a rare recombination event between the *VKORC1* SNPs in those samples, and/or a false negative for the *VKORC1* mutant allele.

2.3.3 Assay Troubleshooting and Optimization

Even after careful computational design, significant empirical optimization was required. Each of the nine PCR products comprising this assay were successfully amplified individually, and samples of homozygous mutant and wild type genotypes were used to verify allele specificity of all products, and in the case of *CYP2C9* sites, subtype specificity as well. Where a wild type background would be expected from non-subtype-specific amplification, conditions were identified that gave no callable product by microchip electrophoresis of the incorrect *CYP2C9* subtype or incorrect genotype. The

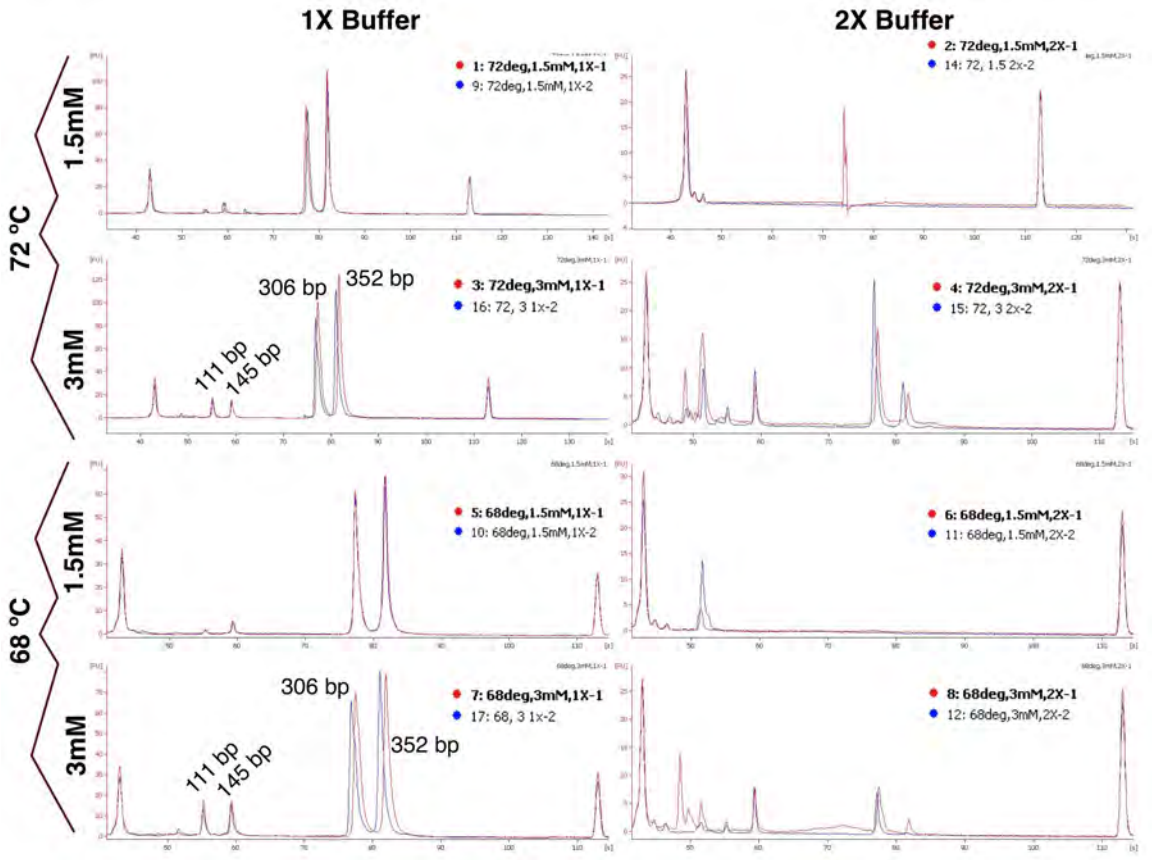

Figure 2.19. Parameter optimization experiment on a draft version of the warfarin multiplex TARMS assay (using only the CYP2C9 *2 and *3 primer sets). Parameters studied were extension step temperatures (72˚C vs. 68˚C), MgCl2 concentration (1.5 mM vs. 3 mM), and ionic strength via buffer concentration (1X vs. 2X final dilution). Amplification performance metrics included PCR efficiency (peak height), inner to outer balance, primer dimerization, and allele specificity (all samples wt/wt genotype, 111 bp and 145 bp are wt-specific inner products. Replicates of the various conditions (n=2 each) showed nearly identical amplification performance to each other as judged from the overlaid, aligned electropherograms.

VKORC1 was similarly assessed for allele-specificity. Several rounds of optimization experiments, such as Figure 2.19, were carried out until adequate amplification efficiency and peak balance were achieved to preclude false positive and false negative test results. To expedite analysis, faster polymerases were evaluated to replace AmpliTaq Gold. The SpeedSTAR polymerase gave reaction high efficiency but was unsuitable for this assay because the 3'>5' exonuclease activity degraded the allele-specific ends of the primers. Finally, Cheetah Taq was selected for a 5-fold reduction in the initial denature time (from 10 to 2 minutes) while maintaining subtype- and allele-specificity.

In some cases the efficiency or specificity of a specific product was suboptimal and targeted troubleshooting was required. Primer redesign was needed when, for example, a prototype of the *1-specific inner primer at the *3 site proved to be stable against *3 template due to relatively stable G:G mismatches. This stable mismatch resulted in nonspecific amplification of the *1-specific product (indicated with dashed box in Figure 2.20**)** to render a false *1/*3 result on a *3/*3 template. However, selection of a different intentional mismatch resolved this problem, and produced acceptable allele-specificity as seen in Figure 2.20. Furthermore, lowering the annealing temperatures led to enhancements in larger product formation, as shown in the dashed boxes in Figure 2.20.

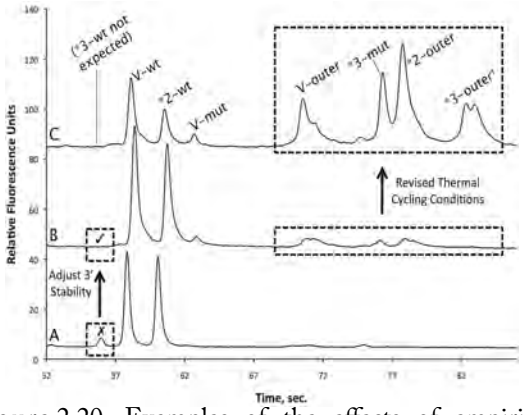

Figure 2.20. Examples of the effects of empirical troubleshooting steps required for the multiplexed TARMS CYP2C9 *2/*3, VKORC1 assay. †The shape of *3 outer peak is reproducible in all *3 homozygous mutant samples. Reproduced from [43].

The *CYP2C* subtype specificities of the *CYP2C9* *2 and *3 outer primers were also assayed using a restriction endonuclease digestion. Bioinformatics tools were used to generate the sequence of PCR products that would arise from the other *CYP2C* subtypes if the specificity for *CYP2C9* was low. NCBI BLAST was used to align the sequences between the primers, and alignments were found: *CYP2C9* *2 site showed homology with *CYP2C19, CYP2C8*, and a pseudogene; *CYP2C9* *3 site showed homology with *CYP2C19* and *CYP2C18*. The primer sequences were then prepended and appended to the aligned sequences to generate the putative sequences for amplicons generated by the *2 and *3 outer primers. Restriction sites between the putative products were compared using the program EnzymeX (http://www.mekentosj.com/enzymex/, supported by the

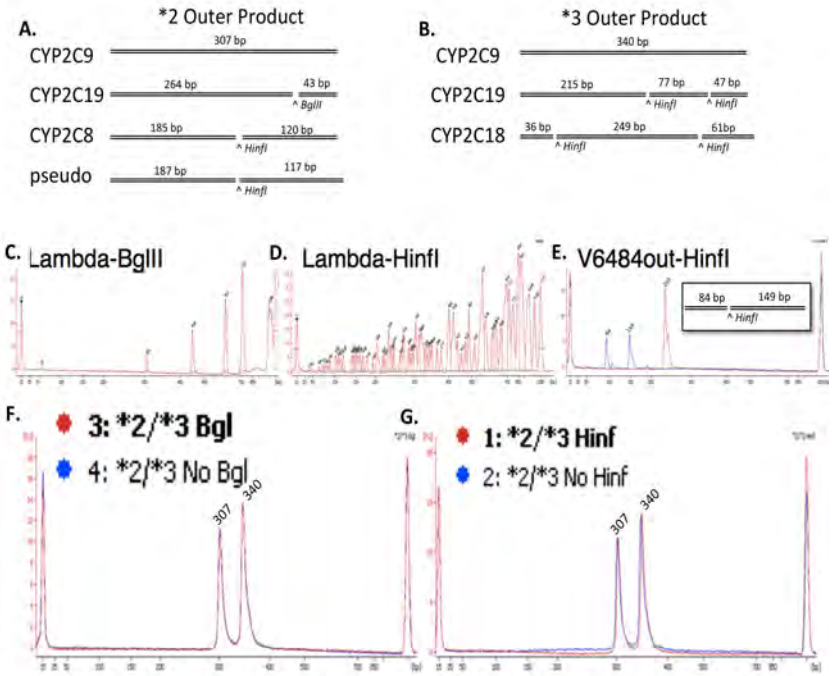

Figure 2.21. Use of bioinformatics and restriction endonuclease digestion to probe CYP subtype specificity. A,B. Restriction site map of the outer products and putative amplicons from homologous sequences in other subtypes for the CYP2C9 *2 primer set (A) and the CYP2C9 *3 primer set (B). C. Electropherogram of digestion of lambda phage genome with BglII to confirm enzyme activity. D. Electropherogram of digestion of lambda phage genome with HinfI to confirm enzyme activity. E. Electropherogram of digestion of a different PCR product (VKORC1 outer) with HinfI to confirm enzyme activity on PCR products. The inset box shows the restriction map for this PCR product. F. Electropherogram of *2 and *3 outer products with and without BglII digestion. G. Electropherogram of *2 and *3 outer products with and without HinfI digestion.

Netherlands Cancer Institute, Version 3.1) and Microsoft Excel. Restriction sites unique to the putative non-specific products were identified and the enzymes *HinfI* and *BglII* were chosen, with maps from restriction sites shown in Figure 2.21A,B. Enzyme activity was confirmed for the lambda phage genome Figure 2.21(C, D) and for an unrelated PCR product (the *VKORC1* 4684 outer product) Figure 2.21E. Digestion reactions were conducted to assay for non-subtyped-specific amplification of the *CYP2C9* *2 and *3 outer primer pairs. Individually amplified *2 outer and *3 outer PCR products were combined (ratio 1:1) then digested with *BglII* Figure 2.21F or *HinfI* Figure 2.21G. The restriction digestion results were in concordance with the observed lack of wild-type allele seen in homozygous mutant patient samples. No digestion was observed: none of the predicted digested products were observed and the product peak heights did not decrease following digestion. The restriction digest study indicated that the *CYP2C9* subtype-specific ARMS outer primers were indeed specific to *CYP2C9*.

Next the primer sets were multiplexed together first by locus, then the complete ensemble and troubleshooting continued. Competition between primers was problematic because unbalanced early proliferation of one product stunted the formation other products (especially for products sharing a common primer such as the *2 inner product and the *2 outer product). To offset competition effects, the relative primer concentrations were empirically-adjusted to those listed above in Table 2.

As proof-of-principle for microchip PCR, 2 of the pre-genotyped samples were amplified on the microchip format, and full profiles were generated with the correct genotype. A representative thermal cycling temperature profile and electropherogram of

the microchip PCR product are shown in Figure 2.22. For this assay, the time required for thermocycling was reduced from 45 minutes in a bench-top thermal cycler (of which ~70% is ramping time) to 30 minutes in a microchip (of which ~30% is ramping time). At excessively low annealing temperatures, a non-specific 400 bp peak was observed, but the robust peak sizing capability of the microchip electrophoresis instrument allowed for reproducible peak identification and genotype calls. Assay conditions were determined that gave a mean signal-to-noise ratio (S/N) for undesired allele- or subtype-nonspecific peaks of 3.62 ± 0.45 relative fluorescence units (RFU), and for allele-specific peaks ("products of the inner primers") a minimum S/N of 52.6 ± 7.82 RFU and a maximum S/N of 414 ± 67.2 RFU. The turn around time for a single sample of hgDNA was as little as 75 minutes for conventional PCR and ME, and 60 minutes for the microchip PCR and ME setup. Given that 12 conventional PCR reactions may be analyzed on one Agilent 2100 microchip, batches of 12 samples were run with increases in processing time due only to additional pipetting. Fourteen samples of known genotype were tested with the full complement of primers and, after a period of empirical optimization, 100% agreement was observed between the predetermined genotypes and experimental assay results.

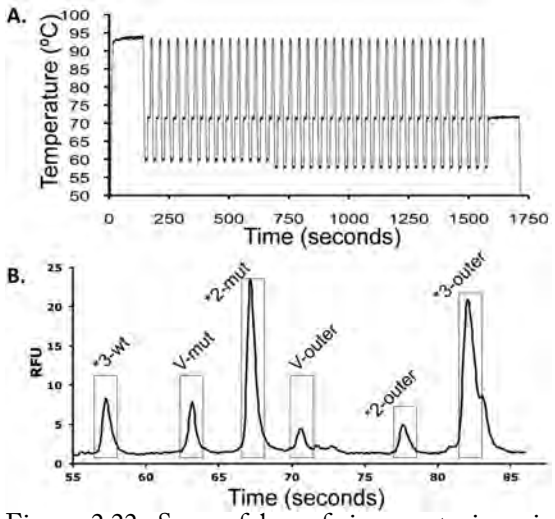

Figure 2.22. Successful warfarin genotyping via microchip PCR. A.) Temperature versus time profile for an IR-PCR run, and B.) The electropherogram of the PCR product extracted from the microchip. Reproduced from [43].

2.3.4 Analysis of Blinded Samples

After troubleshooting and optimization, the new assay was further validated by the analysis of 21 blinded samples (8 split samples, 17 unique genomes in all). Genotyping results were concordant with previously determined patient sample genotypes. Of the 35 genotype determinations attempted, 100% were found to be concordant with other validated methods (e.g., Sanger sequencing of an additional assay validation cohort: Appendix Figure 2.25, Appendix Figure 2.26). Analysis of the blinded, split samples showed complete agreement of peak patterns between split samples. When taken together with the unblinded samples, our multiplex T-ARMS assay correctly and reproducibly genotyped 35 clinical samples (23 unique donors) of following genotypes: *1*1/AA (21.7%), *1*1/BB (21.7%), *1*1/AB (13%), *1*3/BB (8.7%), *3*3/AB (8.7%), *1*2/AB (4.3%), *2*2/AA (4.3%), *2*2/AB (4.3%), *2*2/BB (4.3%), *3*1/AA (4.3%), and *3*1/BB (4.3%). Figure 2.23 summarizes the electrophoretic data of our assay validation cohort, and it shows 35 samples that were genotyped with this assay. Degraded template DNA has been shown to reduce the intensity of the outer

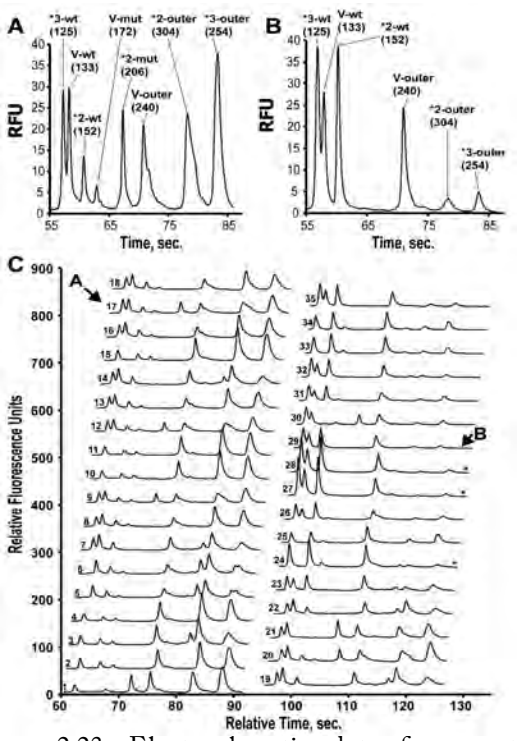

Figure 2.23. Electrophoretic data for genotype determination. A,B) Two annotated electropherograms corresponding to *1/*2, A/B (panel A) and *1*1/AB (panel B) genotypes. Numbers below peak designate the amplicon sizes in bp. C) Stacked electropherograms of 35 samples genotyped with the multiplexed T-ARMS CYP2C9/VKORC1 genotyping assay. Samples marked with * were scaled by a factor of 2 to highlight outer products. *Reproduced from [43]

products (Figure 2.23 samples 23-35), but the allele-specific inner products show ample intensity for accurate genotype calls. The genotypes of all samples of this study are summarized in Figure 2.24 and the genotypes are grouped according to the criteria of Kadian-Dodov *et al.[12]* (with dose correlations shown above in Figure 2.5). Optimized conditions and preparation of reagents in advance allowed for batch genotyping via conventional thermal cycling in 45 minutes and single-sample microchip electrophoresis analysis in 30 minutes, or approximately 90 minutes for 12 samples.

	Sample	Genotype	Count	Group
1	DonA	*1*1/AA	5	Group 1
2	L2	*1*1/AA		
3	L3	*1*1/AA		
4	L6	*1*1/AA		
5	L9	*1*1/AA		
6	UVA2	*1*1/AB	3	Group 2
7	L5	*1*1/AB		
8	L8	*1*1/AB		
9	UVA4	*1*1/BB	5	
10	L7	*1*1/BB		
11	L10	*1*1/BB		
12	L11	*1*1/BB		
13	M4	*1*1/BB		
14	9947A	*3*1/AA	1	Group 3
15	M2	*2*2/AA	1	
16	UVA3	*1*2/AB	1	Group 4
17	UVA1	*1*3/BB	2	
18	M3	*1*3/BB		
19	L1	*3*1/BB	1	
20	M5	*3*3/AB	2	
21	M6	*3*3/AB		
22	L4	*2*2/AB	1	
23	M1	*2*2/BB	1	

Genotype	Count	Percent
*1*1/AA	5	21.7%
*1*1/AB	3	13.0%
*1*1/BB	5	21.7%
*1*2/AB	1	4.3%
*1*3/BB	2	8.7%
*2*2/AA	1	4.3%
*2*2/AB	1	4.3%
*2*2/BB	1	4.3%
*3*1/AA	1	4.3%
*3*1/BB	1	4.3%
*3*3/AB	2	8.7%
	23	100%

Figure 2.24. Grouped genotype information for all of the deidentified samples of human genomic DNA used to validate the warfarin multiplex T-ARMS assay. The genotypes were grouped into the same categories as Kadian-Dodov et al. [12] (refer to {dose vs. genotype} for the correlation that study found between genotype category.

2.4 Discussion

In response to the economics and time sensitivity of warfarin pharmacogenetic testing, we developed a simple PCR-based *CYP2C9/VKORC1* genotyping assay and implemented it on a microchip platform for rapid testing. A system of 12 primers was designed *de novo* to unambiguously determine a patient's genotype at the *CYP2C9* *2, *3 and *VKORC1*

6484 (1173CT) SNP sites in a single, multiplexed PCR reaction. To our knowledge, this was the first instance of three separate T-ARMS assays conducted in a single reaction. Since the publication of the work in this chapter[43], the TARMS assay has continued to garner attention for its low-cost and uncomplicated assay procedure. For instance, a new online design tool[44], assay development guidelines (independently verifying the optimization strategy above)[38] have been released, and the PCR additive betaine was shown to improve multiplex TARMS performance[45]. Nonetheless, the method described in this chapter was the first single-reaction PCR-based genotyping method with single color microchip electrophoresis for the simultaneous determination of wild type, heterozygote, or mutant genotypes at the *CYP2C9* *2, *3 and *VKORC1* 1173CT SNPs. TARMS assays are an attractive method for genotyping a small number of high value SNPs because these simple yet powerful assays leverage built-in complexity gained through upfront bioinformatics engineering to genotype with inexpensive reagents on ubiquitous laboratory equipment.

Following optimization of the assay in conventional tube PCR with ME, proof of principle experiments were conducted on a dual microchip platform for improvements in speed and reagent consumption. The combined analytical process time from hgDNA sample input to genotyping result for a single sample was 75 minutes for conventional PCR with ME, and 60 minutes for the modular microfluidic IR-PCR and ME platform. This assay was validated for 35 patient samples expressing a range of *CYP2C9*/*VKORC1* genotypes, with 100% concordance with other validated genotyping methods. This multiplex PCR assay is compatible with equipment already commonplace in clinical

laboratories, and as such it is already a rapid, low-cost option for warfarin genotyping.

2.5 Acknowledgements

The author gratefully acknowledges the many people who helped make this work possible: Agilent for providing of the DNA 1000 kits used in this work; Steve Monson of the Mayo Clinic and their patients for providing de-identified clinical samples; the UVA Pathology Dept. and their patients for providing genotyped, de-identified DNA samples; Dr. Yongde Bao of the UVA Sequencing Facility for assistance with Sanger sequencing; Dr. Dan Marchiarullo, Dr. Daniel Leslie, Dr. Alison Dewald, Dr. Sonia Taneja, Dr. Jenny Lounsbury, Dr. Jane Juusola, Dr. Jerome Ferrance, all Landers Group members for helpful conversation on this work; Profs. Cafiso, Mura, and Macdonald for serving on the candidacy exam committee for this project; Jeff Hickey MFS, Dr. Carmen Reedy, *et al.* at MicroLab Diagnostics and Lockheed Martin Company for providing cross-validation between the Agilent 2100 and the MicroLab Beta unit; as well as Prof. Dede Haverstick, and Prof. James Landers for their constant guidance and advice.

2.6 References

[1] B.F. Gage, L.J. Lesko, Pharmacogenetics of warfarin: regulatory, scientific, and clinical issues., J. Thromb. Thrombolysis. 25 (2008)45–51. doi:10.1007/s11239-007-0104-y.

[2] D. a Flockhart, D. O'Kane, M.S. Williams, M.S. Watson, B.F. Gage, R. Gandolfi, et al., Pharmacogenetic testing of CYP2C9 and VKORC1 alleles for warfarin., Genet. Med. 10 (2008) 139–50. doi:10.1097/GIM.0b013e318163c35f.

[3] D.S. Budnitz, D. a Pollock, K.N. Weidenbach, A.B. Mendelsohn, T.J. Schroeder, J.L. Annest, National surveillance of emergency department visits for outpatient adverse drug events, JAMA. 296 (2006) 1858–66. doi:10.1001/jama.296.15.1858.

[4] M.J. Rieder, A.P. Reiner, B.F. Gage, D. a Nickerson, C.S. Eby, H.L. McLeod, et al., Effect of VKORC1 haplotypes on transcriptional regulation and warfarin dose., N. Engl. J. Med. 352 (2005) 2285–93. doi:10.1056/NEJMoa044503.

[5] N.A. Limdi, M. Wadelius, L. Cavallari, N. Eriksson, D.C. Crawford, M.-T.M. Lee, et al., Warfarin pharmacogenetics: a single VKORC1 polymorphism is predictive of dose across 3 racial groups., Blood. 115 (2010) 3827–34. doi:10.1182/blood-2009-12-255992.

[6] M. Wadelius, L. Chen, The largest prospective warfarin-treated cohort supports genetic forecasting, …. 113 (2009) 784–792. doi:10.1182/blood-2008-04-149070.

[7] R. Liang, C. Wang, H. Zhao, J. Huang, D. Hu, Y. Sun, Influence of CYP4F2 genotype on warfarin dose requirement-a systematic review and meta-analysis., Thromb. Res. 130 (2012) 38–44. doi:10.1016/j.thromres.2011.11.043.

[8] S.H. An, K.E. Lee, B.C. Chang, H.S. Gwak, Association of gene polymorphisms with the risk of warfarin bleeding complications at therapeutic INR in patients with mechanical cardiac valves., J. Clin. Pharm. Ther. (2014) 1–5. doi:10.1111/jcpt.12143.

[9] S.A. Scott, R. Khasawneh, I. Peter, R. Kornreich, R.J. Desnick, Combined CYP2C9, VKORC1 and CYP4F2 frequencies among racial and ethnic groups., Pharmacogenomics. 11 (2010) 781–91. doi:10.2217/pgs.10.49.

[10] U.I. Schwarz, M.D. Ritchie, Y. Bradford, C. Li, S.M. Dudek, A. Frye-Anderson, et al., Genetic determinants of response to warfarin during initial anticoagulation., N. Engl. J. Med. 358 (2008) 999–1008. doi:10.1056/NEJMoa0708078.

[11] R.S. Epstein, T.P. Moyer, R.E. Aubert, D.J. O Kane, F. Xia, R.R. Verbrugge, et al., Warfarin genotyping reduces hospitalization rates results from the MM-WES (Medco-Mayo Warfarin Effectiveness study)., J. Am. Coll. Cardiol. 55 (2010) 2804–12. doi:10.1016/j.jacc.2010.03.009.

[12] D.L. Kadian-Dodov, S. a van der Zee, S. a Scott, I. Peter, S. Martis, D.O. Doheny, et al., Warfarin pharmacogenetics: a controlled dose-response study in healthy subjects., Vasc. Med. 18 (2013) 290–7. doi:10.1177/1358863X13503193.

[13] L.M. Hynicka, W.D. Cahoon, B.L. Bukaveckas, Genetic testing for warfarin therapy initiation., Ann. Pharmacother. 42 (2008) 1298–303. doi:10.1345/aph.1L127.

[14] D. a Garcia, Warfarin and pharmacogenomic testing: the case for restraint., Clin. Pharmacol. Ther. 84 (2008) 303–5. doi:10.1038/clpt.2008.131.

[15] M.H. Eckman, J. Rosand, S.M. Greenberg, B.F. Gage, Annals of Internal Medicine Article Cost-Effectiveness of Using Pharmacogenetic Information in Warfarin, (2009).

[16] Y. Caraco, S. Blotnick, M. Muszkat, CYP2C9 genotype-guided warfarin prescribing enhances the efficacy and safety of anticoagulation: a prospective randomized controlled study., Clin. Pharmacol. Ther. 83 (2008) 460–70. doi:10.1038/sj.clpt.6100316.

[17] W.I. Gonsalves, R.K. Pruthi, M.M. Patnaik, The new oral anticoagulants in clinical practice., Mayo Clin. Proc. 88 (2013) 495–511. doi:10.1016/j.mayocp.2013.03.006.

[18] Y. Xu, A. Holbrook, Prescribing patterns of novel oral anticoagulants following regulatory approval for atrial fibrillation in Ontario, Canada: a population-based descriptive analysis, Can. Med. Assoc. J. 1 (2013) 115–119. doi:10.1503/cmaj.20130032.

[19] C.B. Maurice, P.K. Barua, D. Simses, P. Smith, J.G. Howe, G. Stack, Comparison of assay systems for warfarin-related CYP2C9 and VKORC1 genotyping., Clin. Chim. Acta. 411 (2010) 947–54. doi:10.1016/j.cca.2010.03.005.

[20] C.R. King, R.M. Porche-Sorbet, B.F. Gage, P.M. Ridker, Y. Renaud, M.S. Phillips, et al., Performance of commercial platforms for rapid genotyping of polymorphisms affecting warfarin dose., Am. J. Clin. Pathol. 129 (2008) 876–83. doi:10.1309/1E34UAPR06PJ6HML.

[21] K.J. Yeo, N. Babic, A.H.B. Wu, Issues in Translation of Pharmacogenomics into Clinical Practice, in: A.H.B. Wu, K.-T.J. Yeo (Eds.), Pharmacogenomic Test. Curr. Clin. Pract., Humana Press, Totowa, NJ, 2011. doi:10.1007/978-1-60761-283-4_1.

[22] V.A. Joshi, E. Duffy, B.H. Funke, L.M. Farwell, D. Mancini-Dinardo, R.S. Kucherlapati, Platform evaluation for rapid genotyping of CYP2C9 and VKORC1 alleles, Per. Med. 6 (2009) 449–457. doi:10.2217/PME.09.8.

[23] J. Zhu, W. Zhang, Y. Li, W. Zhang, H. Wang, W. Zheng, et al., ARMS test for diagnosis of CYP2C9 and VKORC1 mutation in patients with pulmonary embolism in Han Chinese., Pharmacogenomics. 11 (2010) 113–9. doi:10.2217/pgs.09.138.

[24] G. Spohn, C. Geisen, B. Luxembourg, K. Sittinger, E. Seifried, H. Bonig, Validation of a rapid and inexpensive allele-specific amplification (ASA)-PCR genotyping assay for vitamin K antagonist pharmacogenomics., Mol. Diagn. Ther. 15 (2011) 13–9. doi:10.2165/11588300-000000000-00000.

[25] A.J. Rai, N. Udar, R. Saad, M. Fleisher, A Multiplex Assay for Detecting Genetic Variations in CYP2C9, VKORC1, and GGCX Involved in Warfarin Metabolism, Clin. Chem. 55 (2009) 823–826. doi:10.1373/clinchem.2008.118497.

[26] A.K. Daly, C.P. Day, G.P. Aithal, CYP2C9 polymorphism and warfarin dose requirements, Br J Clin Pharmacol. 53 (2002) 403.

[27] C.L. Aquilante, M.T. Lobmeyer, T.Y. Langaee, J.A. Johnson, Comparison of Cytochrome P450 2C9 Genotyping Methods and Implications for the Clinical Laboratory, Pharmacotherapy. 24 (2004) 720–726.

[28] N. Crews, C.T. Wittwer, J. Montgomery, R. Pryor, B. Gale, Spatial DNA melting analysis for genotyping and variant scanning., Anal. Chem. 81 (2009) 2053–8. doi:10.1021/ac801495w.

[29] S.-W. Huang, H.-S. Chen, X.-Q. Wang, L. Huang, D.-L. Xu, X.-J. Hu, et al., Validation of VKORC1 and CYP2C9 genotypes on interindividual warfarin maintenance dose: a prospective study in Chinese patients., Pharmacogenet. Genomics. 19 (2009) 226–34. doi:10.1097/FPC.0b013e328326e0c7.

[30] T. Aomori, K. Yamamoto, A. Oguchi-Katayama, Y. Kawai, T. Ishidao, Y. Mitani, et al., Rapid single-nucleotide polymorphism detection of cytochrome P450 (CYP2C9) and vitamin K epoxide reductase (VKORC1) genes for the warfarin dose adjustment by the SMart-amplification process version 2., Clin. Chem. 55 (2009) 804–12. doi:10.1373/clinchem.2008.115295.

[31] C.J. Easley, J.M. Karlinsey, J.M. Bienvenue, L. a Legendre, M.G. Roper, S.H. Feldman, et al., A fully integrated microfluidic genetic analysis system with sample-in-answer-out capability., Proc. Natl. Acad. Sci. U. S. A. 103 (2006) 19272–7. doi:10.1073/pnas.0604663103.

[32] C.R. Newton, A. Graham, L.E. Heptinstall, S.J. Powell, C. Summers, N. Kalsheker, et al., Analysis of any point mutation in DNA. The amplification refractory mutation system (ARMS), Nucleic Acids Res. 17 (1989) 2503–2516. doi:10.1093/nar/17.7.2503.

[33] M.M. Huang, N. Arnheim, M.F. Goodman, Extension of base mispairs by Taq DNA polymerase: implications for single nucleotide discrimination in PCR., Nucleic Acids Res. 20 (1992) 4567–73.

[34] S. Ye, S. Dhillon, X. Ke, a R. Collins, I.N. Day, An efficient procedure for genotyping single nucleotide polymorphisms., Nucleic Acids Res. 29 (2001) E88–8.

[35] P. Piccioli, M. Serra, V. Gismondi, S. Pedemonte, F. Loiacono, S. Lastraioli, et al., Multiplex tetra-primer amplification refractory mutation system PCR to detect 6 common germline mutations of the MUTYH gene associated with polyposis and colorectal cancer., Clin. Chem. 52 (2006) 739–43. doi:10.1373/clinchem.2005.060137.

[36] N. Okayama, K. Fujimura, J. Nakamura, Y. Suehiro, Y. Hamanaka, Y. Hinoda, Evaluation of a new efficient procedure for single-nucleotide polymorphism genotyping: tetra-primer amplification refractory mutation system-polymerase chain reaction., Clin. Chem. Lab. Med. 42 (2004) 13–6. doi:10.1515/CCLM.2004.004.

[37] D.K. Toubanaki, T.K. Christopoulos, P.C. Ioannou, A. Gravanis, Visual genotyping of SNPs of drug-metabolizing enzymes by tetra-primer PCR coupled with a dry-reagent DNA biosensor., Pharmacogenomics. 10 (2009) 495–504. doi:10.2217/14622416.10.3.495.

[38] R.F.V. Medrano, C.A. de Oliveira, Guidelines for the Tetra-Primer ARMS-PCR Technique Development., Mol. Biotechnol. (2014). doi:10.1007/s12033-014-9734-4.

[39] Z. Zhang, S. Schwartz, L. Wagner, W. Miller, A greedy algorithm for aligning DNA sequences., J. Comput. Biol. 7 (n.d.) 203–14. doi:10.1089/10665270050081478.

[40] S. Rozen, H. Skaletsky, Primer3 on the www for general users and for biologist programmers, Bioinforma. Methods Protoc. (1999).

[41] J. SantaLucia, D. Hicks, The thermodynamics of DNA structural motifs., Annu. Rev. Biophys. Biomol. Struct. 33 (2004) 415–40. doi:10.1146/annurev.biophys.32.110601.141800.

[42] C.J. Easley, J.A.C. Humphrey, J.P. Landers, Thermal isolation of microchip reaction chambers for rapid non-contact DNA amplification, J. Micromechanics Microengineering. 17 (2007) 1758–1766. doi:10.1088/0960-1317/17/9/002.

[43] B.L. Poe, D.M. Haverstick, J.P. Landers, Warfarin genotyping in a single PCR reaction for microchip electrophoresis., Clin. Chem. 58 (2012) 725–31. doi:10.1373/clinchem.2011.180356.

[44] A. Collins, X. Ke, Primer1: primer design web service for tetra-primer ARMS-PCR, Open Bioinforma. J. 44 (2012) 55–58.

[45] B. Lajin, A. Alachkar, A. Alhaj Sakur, Betaine significantly improves multiplex tetra-primer ARMS-PCR methods., Mol. Biotechnol. 54 (2013) 977–82. doi:10.1007/s12033-013-9651-y.

2.7 Appendix: Raw Data for Assay Cross-Validation with Sequencing

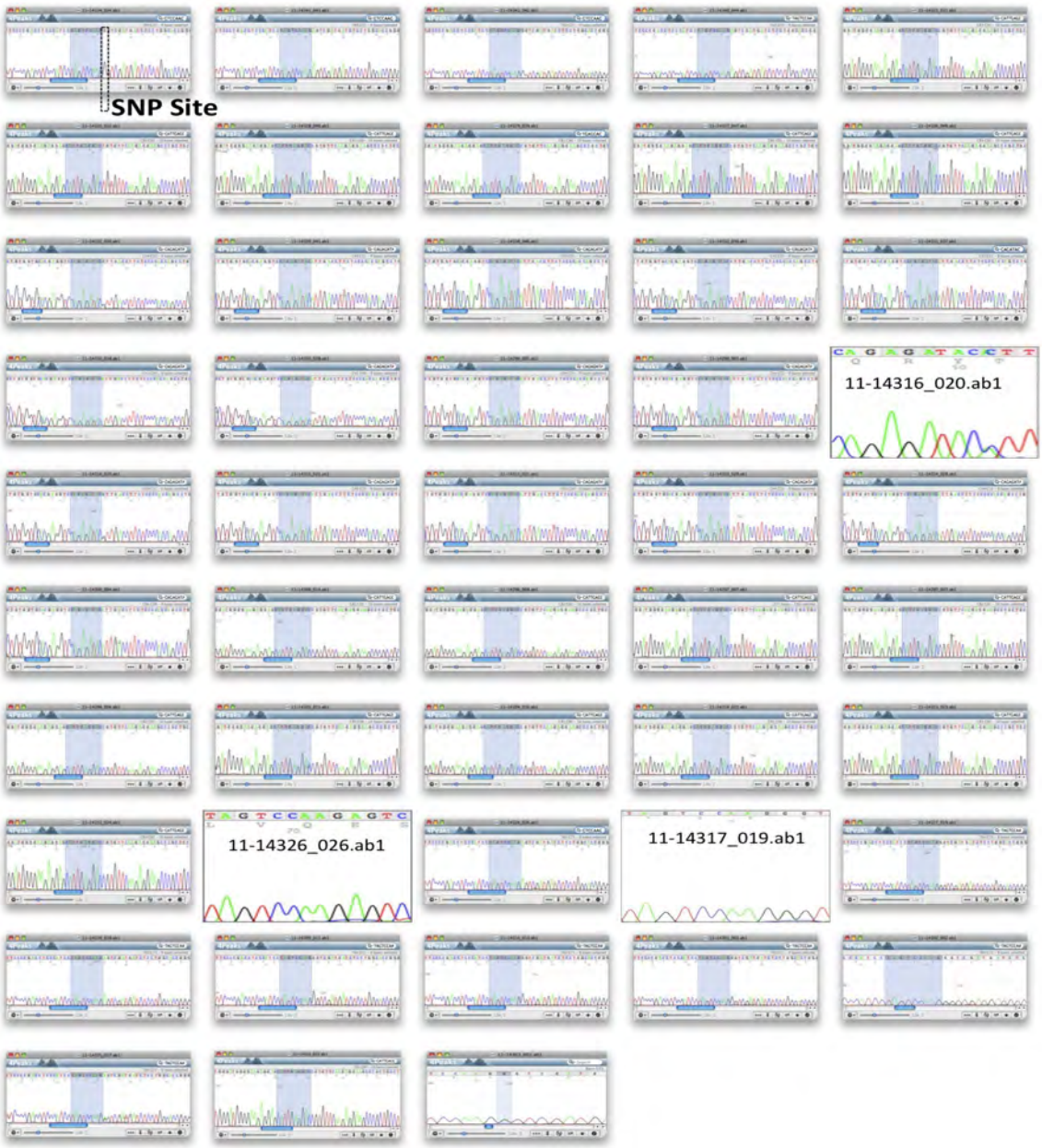

Figure 2.25. Full electropherograms for each of the three loci for all of the samples in the second validation cohort of human genomic DNA samples. Electropherograms were manually inspected in a blinded fashion to identify the genotype in each electropherogram. See Figure 2.26 for a cross-reference between the electropherogram (timestamp/injection number) and the locus and sample to which they correspond.

ABI	Base Call
1	G/A
2	G/A
3	G/G
4	A/A
5	A/A
6	C/C
7	C/C
8	C/C
10	G/G
11	G/G
12	A/A
13	A/A
14	C/C
15	C/C
16	C/C
18	A/A
19	G/A
20	C/A
21	A/A
22	C/C
23	C/C
24	C/C
26	A/A
27	G/A
28	A/A
29	A/A
30	C/A
31	C/C
32	T/T
34	G/G
35	G/G
36	C/C
37	A/A
38	A/A
39	C/C
40	C/C
42	G/G
43	A/A
44	A/A
45	A/A
46	A/A
47	C/C
48	C/C

ABI	Sample ID	Sample	Loc	Base Call	
47	***2out-9947A**	9947A	*2	C/C	*1/*1
6	***2out-DonorA**	DonA	*2	C/C	*1/*1
8	***2out-L1**	L1	*2	C/C	*1/*1
31	***2out-L10**	L10	*2	C/C	*1/*1
39	***2out-L11**	L11	*2	C/C	*1/*1
16	***2out-L2**	L2	*2	C/C	*1/*1
24	***2out-L3**	L3	*2	C/C	*1/*1
32	***2out-L4**	L4	*2	T/T	*2/*2
40	***2out-L5**	L5	*2	C/C	*1/*1
48	***2out-L6**	L6	*2	C/C	*1/*1
7	***2out-L7**	L7	*2	C/C	*1/*1
15	***2out-L8**	L8	*2	C/C	*1/*1
23	***2out-L9**	L9	*2	C/C	*1/*1
22	***2out-M5**	M5	*2	C/C	*1/*1
20	***3out-9947A**	9947A	*3	C/A	*3/*1
28	***3out-DonorA**	DonA	*3	A/A	*1/*1
30	***3out-L1**	L1	*3	C/A	*3/*1
4	***3out-L10**	L10	*3	A/A	*1/*1
12	***3out-L11**	L11	*3	A/A	*1/*1
38	***3out-L2**	L2	*3	A/A	*1/*1
46	***3out-L3**	L3	*3	A/A	*1/*1
5	***3out-L4**	L4	*3	A/A	*1/*1
13	***3out-L5**	L5	*3	A/A	*1/*1
21	***3out-L6**	L6	*3	A/A	*1/*1
29	***3out-L7**	L7	*3	A/A	*1/*1
37	***3out-L8**	L8	*3	A/A	*1/*1
45	***3out-L9**	L9	*3	A/A	*1/*1
36	***3out-M5**	M5	*3	C/C	*3/*3
34	**Vout-9947A**	9947A	V	G/G	A/A
42	**Vout-DonorA**	DonA	V	G/G	A/A
44	**Vout-L1**	L1	V	A/A	B/B
18	**Vout-L10**	L10	V	A/A	B/B
26	**Vout-L11**	L11	V	A/A	B/B
3	**Vout-L2**	L2	V	G/G	A/A
11	**Vout-L3**	L3	V	G/G	A/A
19	**Vout-L4**	L4	V	G/A	A/B
27	**Vout-L5**	L5	V	G/A	A/B
35	**Vout-L6**	L6	V	G/G	A/A
43	**Vout-L7**	L7	V	A/A	B/B
2	**Vout-L8**	L8	V	G/A	A/B
10	**Vout-L9**	L9	V	G/G	A/A
1	**Vout-M5**	M5	V	G/A	A/B

Figure 2.26. Each electropherogram was coded with an injection identifier that did not identify the sample source. Electropherograms were first evaluated in a blinded fashion (left table) by finding the SNP sites in the electropherograms. Following interpretation of all electropherograms, samples were decoded to reveal the genotype at all 3 loci for each sample (right table).

3 Capillary and Microchip Electrophoresis

3.1 Introduction

3.1.1 Surface Chemistry in Capillary and Microchip Electrophoresis

Capillary electrophoresis (CE) is an analytical chemistry technique that produces fast, high-resolution analyses by exploiting charge and size differences between analytes. Separations are conducted by applying an electric field to exert force on charged particles that causes them to migrate. Such migration is opposed by viscous drag, however, and the balance of forces results in a characteristic mobility for each analyte. CE can effectively separate a wide variety of analytes, from single ions to colloidal particles, and it is particularly useful for analysis of complex mixtures such as biological samples.

The small dimensions of CE are key to its function, but the high surface area to volume ratio makes surface effects a vital concern. CE utilizes high voltages to accentuate slight differences in analyte electrophoretic mobility, but it produces significant amount of heat in the process that could hamper analysis. Capillaries feature a very high surface area to volume ratio that is key to managing heat production. Furthermore, charged surfaces are never naked in aqueous media, but instead attract a layer of ions that complicates both electrophoretic mobility and bulk flow in capillaries. Since CE is a microscopic world of charged surfaces, from the capillary wall to charged analytes, electrical forces are key players in capillary electrophoresis.

3.1.2 Instrumentation

High voltages yield superior analytical performance, but advanced instrumentation is required to manage components and deal with heat production. Heat arises from

intermolecular collisions as ions are propelled through solution, a phenomenon called Joule heating[1]. Typical electrical field strengths for CE are on the order of hundreds of volts per centimeter[2], which is at least an order of magnitude higher than other electrophoresis techniques such as slab gel electrophoresis[3]. Since Joule heating is a major limiting factor, overcoming this obstacle permits CE to outperform many comparable techniques.

The small dimensions of capillaries minimize the amount of heat generated as well as effectively dissipate what heat is generated. Typical CE capillaries are manufactured from fused silica, with an outer diameter of ~375 μm and an internal diameter ranging 20-200 μm (Figure 3.1A and B)[3]. The narrow internal diameters of such capillaries result in significant electrical resistance that permits less current for a given applied voltage. Thus, a relatively low amount of heat is generated for a given electric field strength because of the capillary's small internal dimensions. Furthermore, the heat generated can then be effectively dissipated through the thin walls of the capillary.

There are other consequences of the microscopic dimensions of CE capillaries. The short optical path length of a capillary can limit optical detection, and high intensity lasers are often required for adequate sensitivity. The high surface area to volume ratio accentuates the problem of adsorption to the capillary wall, and a variety of preventative measures can be taken such as polymer wall coatings or covalent surface modifications[4]. Given the importance of the capillary surface, most methods require preconditioning with acidic or basic solutions[3]. Surface effects aside, the small volumes of the capillary lumen offer inherently low reagent consumption (often ≤ μL). Such considerations are not insurmountable, and capillary electrophoresis has proven to be a powerful analytical tool.

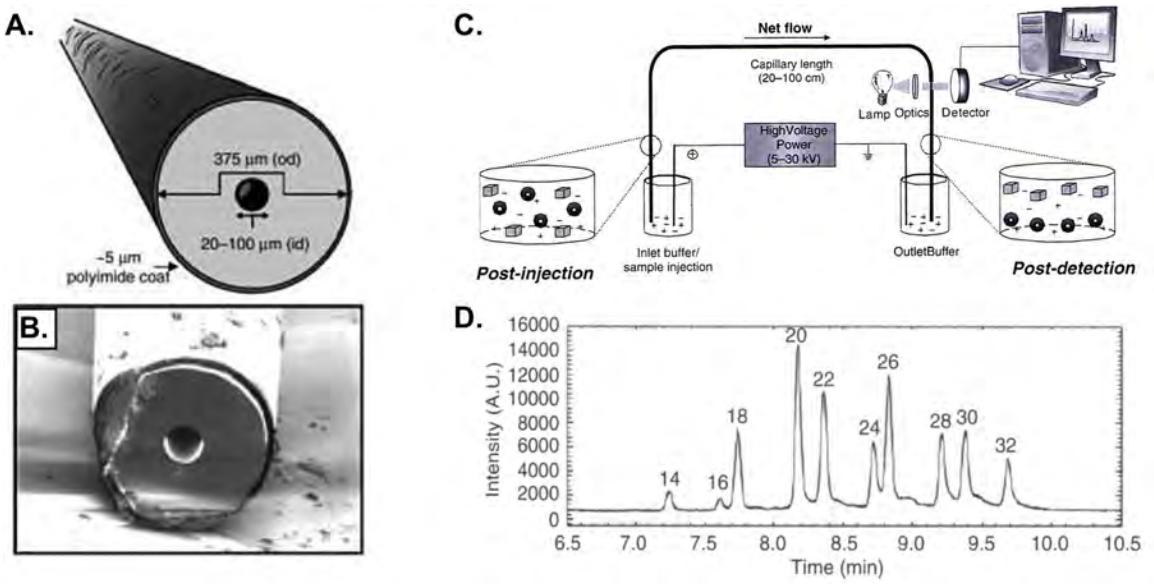

Figure 3.1: Capillary electrophoresis instrumentation and data. An analytical capillary is depicted in A and an actual scanning electron micrograph is shown in B. Panel C shows how the functional elements of a typical CE instrument are arranged. Panel D shows an electropherogram demonstrating effective separation of different oligonucleotides; peak labels are number of DNA bases. (Content adapted from [3]).

Commercial CE instruments are equipped to maneuver the capillary, apply hydrostatic pressures and voltages, and detect optical signals during separations. A basic CE setup is diagramed in Figure 3.1C. The capillary itself is often housed in a cartridge for easier handling, and liquid coolant is circulated within the cartridge to regulate temperature. A robotic assembly brings vials into contact with the capillary ends, and most models permit extensive automation. During electrophoretic separations, optical detection methods such as UV-visible absorbance spectroscopy or laser induced fluorescence (LIF) collect data in real time. Many commercial CE instruments can apply between 5 and 30 thousand volts[3] (which is much higher than other electrophoresis methods, such as slab gel electrophoresis that is run at ~100 V).

Representative data from capillary electrophoresis is shown in Figure 3.1D, wherein a mixture of oligonucleotides are separated. A plot of detector signal intensity

versus time is referred to as an electropherogram, and ideally the analytes are separated (resolved) into individual peaks. Adequate separation occurs if and only if the various analytes travel down the capillary at different rates.

3.1.3 Theoretical Basis of Capillary and Microchip Electrophoresis

The driving force behind electrophoretic separations is the fact that electric fields apply a force to charged particles. This force can be described mathematically by equation (Eq. 3.1), which shows that the force the particle feels is proportional both to its effective charge, *q*, and the strength of the applied electric field, *E (Eq. 3.2)*. The effective charge of an ion can be complicated by interaction with other ions (discussed below), but as a frame of reference, the effective charge of a small ion at infinite dilution can be described by equation (Eq. 3.3). Higher voltages yield larger electrical driving forces, and fast separations result because charged analytes can traverse the length of the capillary in less time.

(Eq. 3.1) $$F_{el} = qE$$

where F_{el} – electrostatic force
q – effective charge of particle
E – electric field strength

(Eq. 3.2) $$E = \frac{\text{applied voltage}}{\text{capillary length}}$$

(Eq. 3.3) $$q = ze^-$$

where z – valence of a small ion
e^- – charge of an electron

As electrical forces propel charged particles through a fluid continuous phase, a viscous drag force opposes their motion. This force, F_{drag}, is the result of intermolecular interactions, but it can be generally described by equation (Eq. 3.4). The magnitude of

the frictional coefficient, f, is a function of the particle size and shape as well as the viscosity of the continuous phase. The Stokes-Einstein equation, (Eq. 3.5), describes the friction coefficient for a hard spherical particle, and it correlates well with empirical data when the particles are much larger than the continuous phase molecules [5] Almost immediately after an electric field gradient is established, F_{el} and F_{drag} reach equilibrium and particles reach a terminal velocity. This situation, shown in equation (Eq. 3.6), yields a general description of electrophoretic velocity as a function of particle effective charge, q, and its characteristic frictional coefficient, f.

(Eq. 3.4) $F_{drag} = f v_i$ where F_{drag} – viscous drag force
f – frictional drag coefficient
v_i – velocity of particle i

(Eq. 3.5) $f = 6\pi\eta R_s$ where η – viscosity of continuous phase
R_s – radius of hard spherical particle

(Eq. 3.6) $$F_{el} = F_{drag} \longrightarrow v_i = \frac{qE}{f}$$

Since both F_{el} and F_{drag} are a function of electric field strength, the electrophoretic velocity may be described independently of electric field strength by a single coefficient called the electrophoretic mobility, μ. Electrostatic and viscous drag factors describe the electrostatic component of electrophoretic mobility, μ_{el}. For now electrophoretic mobility shall be described in empirical terms as apparent electrophoretic mobility, μ_{app}, to acknowledge that particles can move by bulk flow as well. Electrophoretic mobility is very important because different analyte species can only be adequately separated if they have different electrophoretic mobilities.

(Eq. 3.7) $$v_i = \mu_{app} E$$ where v_i – velocity of species i
μ_{app} – apparent electrophoretic mobility

Charged surfaces, be they the capillary wall or colloidal analytes, can complicate

the picture of electrophoretic mobility because they attract a "cloud" of oppositely charged ions known as the electrical double layer (EDL). Electrostatic attraction and repulsion act to draw counterions toward a charged surface while thermal motion tends to dissipate them. Consequences of the EDL in capillary electrophoresis include screening of analyte charge and a type of non-separative flow called electroosmotic flow (EOF).

The electrical potential near a charged surface can be represented as a function of distance using the Poisson equation, (Eq. 3.8), for a continuous phase of given electrical permittivity and local charge density ρ^*. When the EDL is thin relative to its charged surface, such as a capillary wall, it is reasonable to use a flat planar surface as a limiting condition. Only the *x*-direction term remains with this assumption, and equation (Eq. 3.9) results. Charge density may be related to the ion content of bulk solution, which is accounted for by ionic strength as defined in (Eq. 3.10). Furthermore, (Eq. 3.9) can be stated more succinctly by using a cluster of constants called the Debye length, κ^{-1} (or alternatively λ_D) as defined in (Eq. 3.11). The Debye length is important because it characterizes how ions screen the electric field of a charged surface. High salt

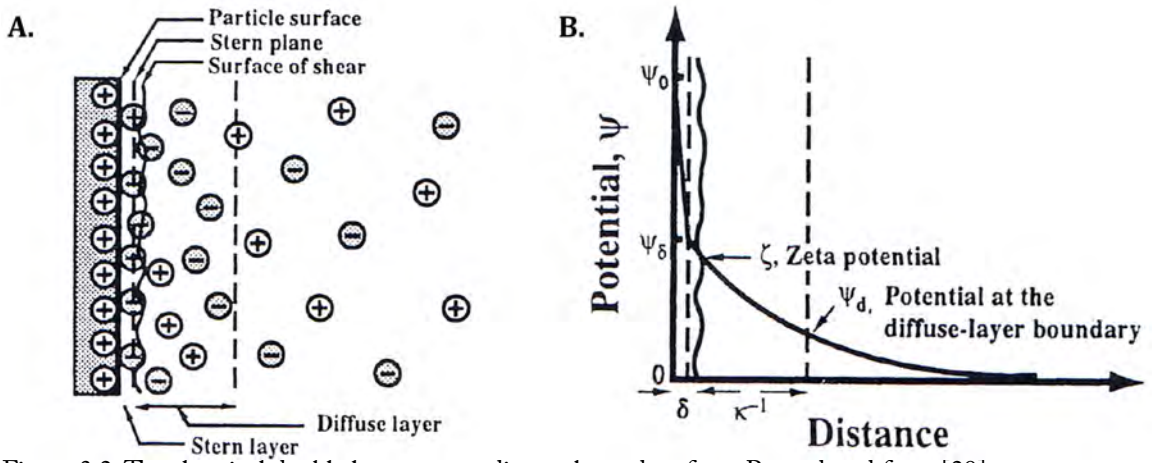

Figure 3.2: The electrical double layer surrounding a charged surface. Reproduced from [29].

concentration and/or high ion valency results in a smaller Debye length, which means surface charge is cancelled out relatively close to a charged surface. The Debye length in typical capillary electrophoresis conditions range from ~1-10 nm[2].

(Eq. 3.8) $$\left(\frac{\partial^2\psi}{\partial x^2}\right)+\left(\frac{\partial^2\psi}{\partial y^2}\right)+\left(\frac{\partial^2\psi}{\partial z^2}\right)=-\left(\frac{\rho^*}{\varepsilon_r\varepsilon_0}\right)$$

where ρ^* – charge density
ψ – electrostatic potential
ε_r – relative permittivity
ε_0 – vacuum permittivity

(Eq. 3.9) $$\left(\frac{d^2\psi}{dx^2}\right)=\left[\left(\frac{e^2}{\varepsilon_r\varepsilon_0 k_B T}\right)\sum_i z_i^2 c_{i_{(bulk)}}\right]\psi=\kappa^2\psi$$

where e – charge of an electron
z_i – valence of ion i
$c_{i(bulk)}$ – bulk conc. of i

(Eq. 3.10) $$I=\frac{1}{2}\sum_i z_i^2 c_{i_{(bulk)}}$$

where I – ionic strength

(Eq. 3.11) $$\kappa^{-1}=\sqrt{\frac{\varepsilon_r\varepsilon_0 k_B T}{2N_A e^2 I}}$$

where κ^{-1} – Debye length

(Eq. 3.12) $$\psi(x)=\psi_\delta\cdot\exp\left(-\frac{x}{\kappa^{-1}}\right)$$

where
$\psi(x)$ – electric potential at distance x from a flat surface.
ψ_δ – electric potential at the Stern layer

The layer of cations directly adjacent to the silica surface is so strongly adsorbed that they are practically immobilized. This layer of tightly bound counterions is called the Stern layer and is shown diagrammatically in Figure 3.2A. Since the Stern layer adsorbs so strongly, it is useful to account for it and establish a baseline potential at the Stern layer, ψ_δ, which is also shown in Figure 3.2B. The first layer of ions to move independently from the Stern layer is called the shear surface, and the electrostatic potential at which this slippage occurs is termed the ζ (zeta) potential. Zeta potential has theoretical and experimental significance because it provides a link between theoretical predictions and empirical observations. For instance, bare silica capillary features silanol

groups with pK_a values of approximately 4 - 6 [3] that are negatively charged at neutral pH and above. Indeed, the ζ potential of the silica capillary wall is between -50 to -100 mV for most CE applications[2].

For charged spherical particles, the electrophoretic mobility may be described mathematically as a function of the Debye length, spherical radius, and zeta potential. Two limiting cases are important: the Huckel approximation wherein the electrical double layer is large compared to the particle radius (Figure 3.3A), and the Helmholtz-Smoluchowski approximation that assumes that the Debye length is small compared to the particle radius (Figure 3.3B). While many analytes fall between these two extremes, the Huckel and Helmholtz-Smoluchowski approximations describe small charged analytes and large colloidal particles, respectively.

An important feature of both equations (Eq. 3.13) and (Eq. 3.14) in Figure 3.3 is that electrophoretic mobility does not depend on the particle radius. Equation (Eq. 3.6) shows that the electrophoretic mobility of a species depends on the ratio of charge to

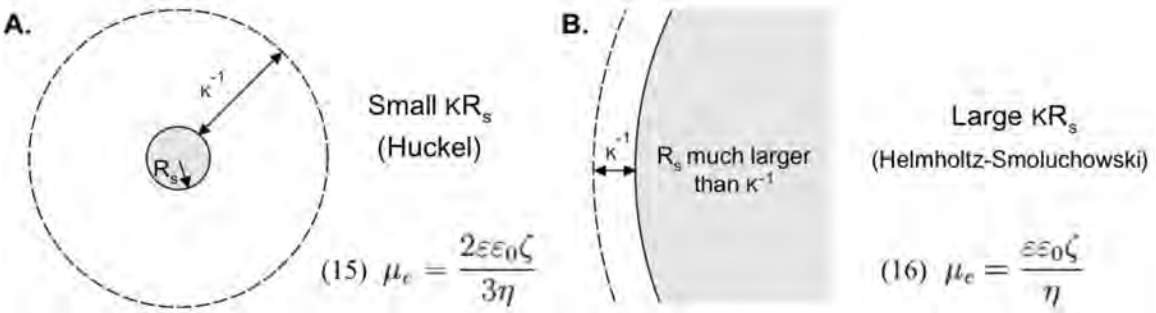

Figure 3.3: Two models of electrophoretic mobility of charged colloidal particles. (Adapted from [29] (A) and [30] (B))

viscous drag. Adequate separation of requires dissimilar electrophoretic mobilities, so separation of analytes with a similar charge-to-mass ratio can be challenging. While

many ions and small molecules migrate at very different rates through solution, all DNA molecules will electrophoretically migrate through free solution at the same rate regardless of how large they are. For such cases, the medium may be modified to create a greater size-dependent variation in viscous drag[3] – such as when a polymer sieving matrix is used in DNA separations[6,7][8]

Figure 3.4 depicts a diagram of forces acting on an electrophoretically migrating particle. The interaction of the applied electric field with counterions in the EDL around a charged particle results in two additional forces called electrophoretic retardation and relaxation, which both oppose the driving electrostatic force. Electrophoretic retardation arises from the force that the applied electric field exerts on the counterions, and net effect opposes the driving force applied to the charged particle, F_{el}, by virtue of opposite charge polarity. Furthermore, the applied electric field distorts the otherwise spherical EDL, and this deviation from spherical geometry results in a force called the relaxation effect. Capillary electrophoresis experiments have demonstrated that the relaxation effect can result in electrophoretic mobilities that do not depend on zeta potential, particularly at very low ionic strengths (large Debye lengths) [9].

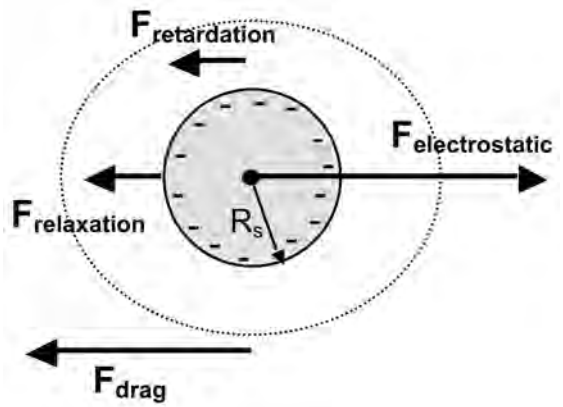

Figure 3.4: Free body diagram of the EDL around a charged particle. Dashed line represents EDL distortion from external electric field. (Adapted from [30] and [3])

Electrical double layer considerations extend beyond electrophoretic mobility of analytes to include a type of non-separative bulk flow called electroosmotic flow (EOF). The applied electric field exerts a force on ions in the

EDL at capillary surface, causing surface-bound ions to migrate laterally down the length of the capillary. These migrating, surface-associated ions form a mobile sheath lining the capillary surface that drags the bulk solution along with it. Volumetric flow from EOF can be roughly calculated using equation (Eq. 3.15). The magnitude of EOF is directly related to zeta potential of the capillary wall and the electric field strength, so controlling it requires modulating one or the other. One feature of EOF noteworthy for separations is that a relatively flat fluid plug forms (whereas pressure-driven flow has a parabolic flow profile that can cause dispersion). EOF can potentially hide differences in electrophoretic mobility, but it can also extend CE's usefulness to all species, regardless of electrophoretic mobility, because everything is eventually carried past the detector.

(Eq. 3.15) $$V_{eof} = \frac{\varepsilon_r \varepsilon_0 \xi E(\pi R_c^2)}{\eta}$$

where V_{eof} – volumetric flow rate of eof
ε_0 – permittivity of free space
ε_r – relative permittivity of medium
R_c – capillary radius

(Eq. 3.16) $\mu_{app} = (\mu_{el} + \mu_{eof})$

where μ_{el} – electrostatic component of electrophoretic mobility

(Eq. 3.17) $$v_i = (\mu_{el} + \mu_{eof})E$$

μ_{eof} – electroosmotic flow component of electrophoretic mobility

Apart from electrokinetic phenomena, adsorption driven by van der Waals forces can be a significant complication in CE separations. Much effort has been devoted to reducing adsorption including covalent surface modifications (e.g. covalent coatings[3,4]), adsorbed polymer coatings (e.g. coatings of ionic polymers[10]), and buffer additives (e.g. 1,4 diaminobutane[3,11]) While a detailed discussion on adsorption is not presented here, van der Waals interactions and adsorption are important considerations when developing CE/ME methods, and adsorption has been reviewed recently by [12].

3.1.4 Applications of CE

The most basic CE implementation is called capillary zone electrophoresis (CZE), where an open tubular capillary has been used to separate ions, small molecules, peptides, carbohydrates, and even colloidal particles [3,9] into spatially distinct bands or zones. Non-polar, electrophoretically-immobile analytes can also be separated by CE when ionic surfactant micelles are used to create a mobile hydrophobic phase in a technique called micellar electrokinetic chromatography (MEKC) [3]. The last major mode of CE is called capillary gel electrophoresis (CGE) because it employs a sieving polymer gel to effectively separate nucleic acids by length for forensic and medical applications.

3.1.5 Microchip Electrophoresis

The fast, high-resolution separations possible with CE are ultimately limited by the fact that one capillary can only do so much. One way to circumvent this bottleneck is to implement an array of capillaries to perform many simultaneous separations[13]. Another major development in capillary electrophoresis is, ironically, the abandonment of the capillary for micro-fabricated channels in glass or plastic for what is called microchip electrophoresis (ME)[3,14]. ME separations can be 10 times faster than standard CE with comparable resolution[15]. As seen in Figure 3.5, ME channels can be co-fabricated with other architectures to permit integration of ME with other analytical steps such as DNA purification [3,15–17]. As miniaturization of analytical instrumentation continues, the surface chemistry phenomena discussed in this paper will become more and more important.

Significant effort has been spent developing polymeric, disposable microdevices for electrophoretic separations. This chapter describes separations on polyester-toner

(PeT) microdevices that were fabricated from overhead transparencies and laser printer toner[18–20]. PeT devices are capable of many analytical processes performed in more expensive glass or silicon devices but they can be rapidly fabricated from low cost materials, allowing for completely disposable microdevices. Another polymeric ME device used in the work described here was developed by MicroLab Diagnostics LLC and related entities for a prototype integrated genetic analysis instrument[21,22]. While many findings are proprietary, separations performed on the MicroLab instruments produced data that was processed to yield performance metrics for new formulations of a proprietary polymer sieving matrix. Software was developed for analyzing the separation quality of ME data, and this is described below.

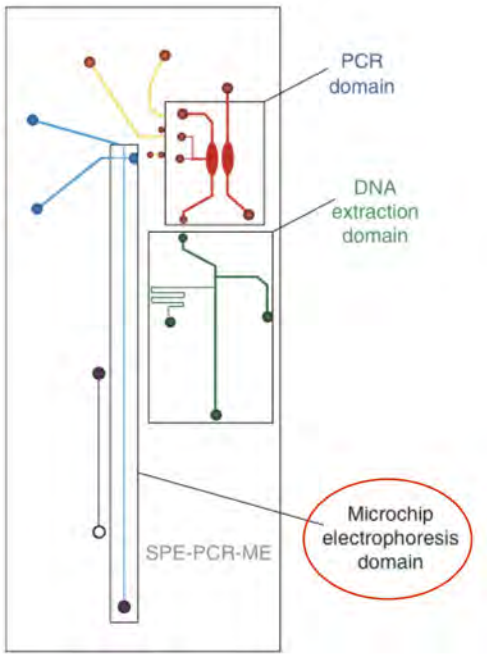

Figure 3.5: An integrated microchip device featuring ME. Chip dimensions: 30.0 by 63.5 mm, with a total solution volume <10 μL. (Reproduced from [15], adapted from [31].)

3.2 Materials and Methods

3.2.1 Capillary Electrophoresis

3.2.1.1 Separation of Ovalbumin Glycoforms

Separations of ovalbumin were performed as a model for separation of immunoglobulin glycoforms following the method of Morbeck *et al. [23].* Separations were conducted in an 87 cm bare silica capillary (50 μm i.d., Polymicro Technologies) in a Beckman P/ACE

MDQ_CE instrument. Detection was via UV detection module (λ = 200 nm) at 80 cm effective capillary length. Working stocks of ovalbumin protein (Sigma, A7641) were prepared at 1.0 mg/mL in 100 mM borate buffer (EM Science) at pH 9 with 1 mM 1-4 diaminobutane (Aldrich, D13208). All buffers and samples were filtered through 0.22 μm syringe filters prior to use. Dimethyl-sulfoxide (Fisher) (DMSO) was used as an EOF marker. Samples were hydrodynamically injected for 3 seconds at 0.5 psi, then separated at 25 kV for 30 minutes at 28 °C.

3.2.1.2 Separation of PCR Products

Capillary electrophoresis was used to analyze PCR products and DNA fragments according to the method described by Sanders *et al.[6]* and Marchiarullo[24]. Hydroxypropylcellulose sieving medium was prepared at a concentration of 3.5 % w/v in a 80 mM MES/40 mM Tris buffer. Prior to separation of PCR products, a fresh 1 mL aliquot of polymer was spiked with 1 μL of stock YO-PRO intercalating dye (Molecular Probes (Invitrogen)), vortexed thoroughly, and centrifuged to remove bubbles that might be introduced to the capillary. Prior to separations the capillary (50 μm I.d., 30 cm length, operated with an effective capillary length from sample to detector of 10 cm, fused silica capillary from Polymicro Inc.) 1 M HNO_3 was injected for 30 minutes. Samples were electrokinetically injected for 5 seconds at 10 kV, then 8 kV were applied for separation. Detection was via laser-induced fluorescence with 488 nm Argon laser-generated excitation and emission collected with a 20 nm bandpass filter centered at 520 nm.

3.2.2 AOTF ME-LIF System

DNA separations were performed on a microchip electrophoresis system with 5 color laser-induced fluorescence (LIF) detection as described previously [24–26]. The detection scheme employed an acousto-optical tunable filter (AOTF) to selectively defract light of a desired wavelength onto a photomultiplier tube detector(Figure 3.6A,B). The optics system is shown in Figure 3.6B with the protective light-proof housings removed from the beam path. In this way, 5 separate fluorescent dyes could be detected in rapid succession. Commerical PCR-based human identification kits were used (AmpFℓSTR® Identifiler®, Applied Biosystems) kit, which consisted of a multiplex PCR reaction to determine a subject's genotype as 16 short tandem repeat (STR) loci. A combination of poly-N-hydroxy-ethyl-acrylamide (pHEA) and poly-N,N-dimethyl-acrylamide (pDMA) were used as adsorptive surface modifiers and a sieving media, respectively[27]. Previously fabricated microfluidic devices[26] with 10 cm long separation channels (50 μm deep and 75 μm wide) were used for microfluidic STR separations. A proprietary polymeric microfluidic device with a proprietary polymer sieving matrix[21] was also used for separations.

3.2.2.1 Troubleshooting and Repair of AOTF ME-LIF Hardware

The laser for the ME-LIF apparatus (a multiline argon laser, LS200A, Dynamic Laser Inc.) was frequently cutting off unexpectedly during normal operation. Upon disassembly of the laser housing (with the unit unplugged for safety) the air cooling fins were found to be completely blocked by dust and debris. The cloth light-proofing material used in the laboratory environment generated a large amount of dust, and this dust had clogged the cooling fins. Removal of debris from the air cooling fins by vacuum and then an 80 psi

compressed nitrogen line successfully cleared the debris. Following this operation, the laser did not overheat or turn off unexpectedly during microchip electrophoresis even after several hours of use. The LIF system was aligned as previously described [24]. To comply with revised UVA Environmental Health and Safety requirements, a new light-proof housing was built for the entire optics system using black foam core board.

3.2.2.2 Bypass of Faulty Relay Driver in High Voltage Power Supply

Troubleshooting using a high voltage probe (Pintek, HVP-40) revealed that the relay driver circuitry in the existing high voltage power supply unit was faulty. By splicing into

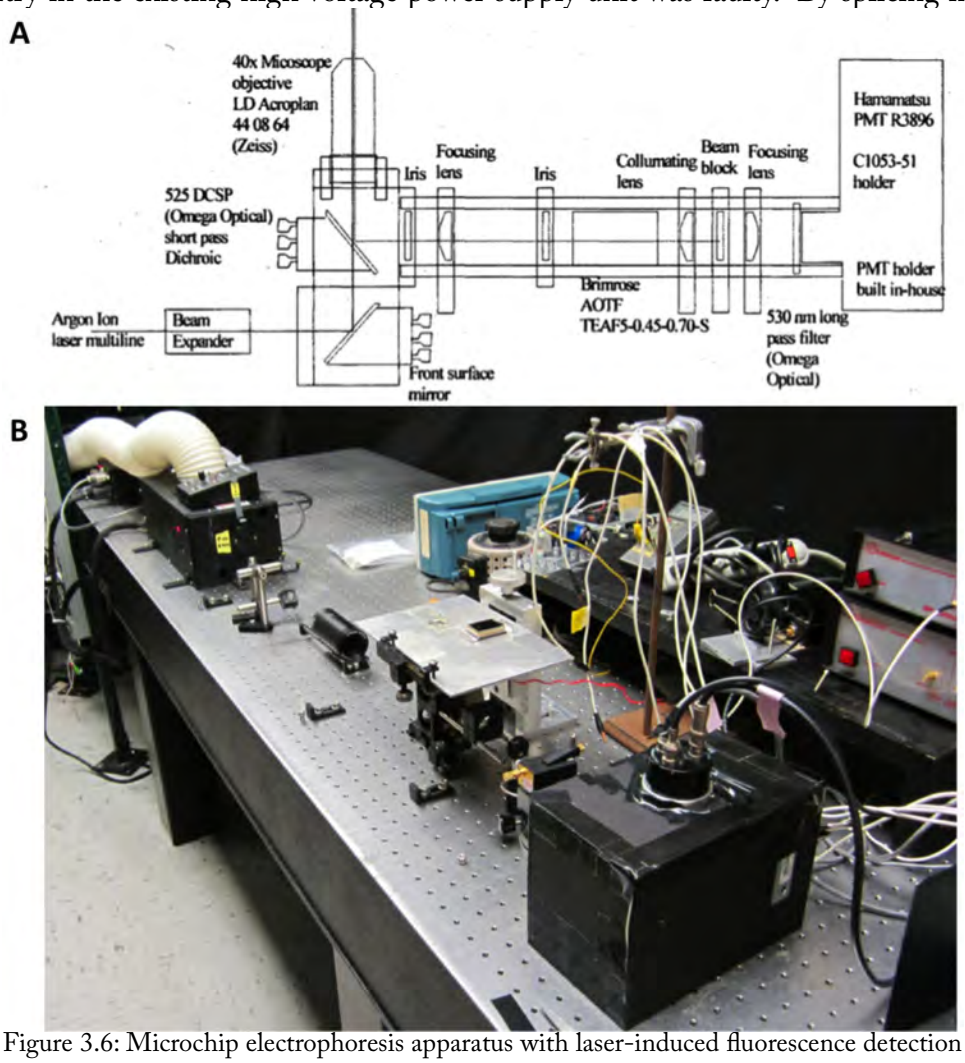

Figure 3.6: Microchip electrophoresis apparatus with laser-induced fluorescence detection with acousto-optical tunable filter (AOTF). A. Optical configuration and component details (reproduced from [Marchiarullo thesis]). B. Photograph of the apparatus.

the ribbon cable of the existing digital out DAQ card, the relay controls were bypassed, and replaced with a standalone relay driver circuit. The standalone relay driver was based on the UC3702N integrated circuit (Texas Instruments) under control of the digital I/O lines of a USB-6008 DAQ card (National Instruments). The LabVIEW software for apparatus control and data acquisition was amended to include control via the additional DAQ device.

3.2.2.3 Troubleshooting Brimrose AOTF Drivers

The device that generated the AC driving signal to control the AOTF for wavelength selection, the AOTF driver (Brimrose, model SPFII) was found to be faulty. The output signal equipment with an oscilloscope (Tektronics, TDS2024), an older AOTF driver (Brimrose, model SPS) was substituted in, and the LabVIEW code was updated to control the system. The RS232 serial communication settings had to be reconfigured and recoded in LabVIEW. The electrical output of the driver was verified, and optimal flatness of the AOTF driver signal versus frequency was found when the lock-in amplifier was removed.

3.2.2.4 Development of Improved Electrode Housings

The previous apparatus configuration featured loose electrical leads for insertion of electrodes into the microchip fluidic reservoirs. While the loose leads provided flexibility, the tension in the wires would frequently dislodge electrodes from the reservoirs slowly over time. New platinum electrode housings were developed that secured the platinum electrodes to the device reservoirs to both prevent evaporation and hold the electrodes securely in contact with the liquid within. Mini banana plugs were fitted with soldered-in platinum wire, and these plugs were fitted into plastic caps fashioned from diced P-1000

pipette tips with parafilm gaskets.

3.2.2.5 Validation of Spectrometer Calibration

The reproducibility and accuracy of the AOTF driver signal frequency to observed optical wavelength was validated using a multi-line mercury-argon lamp (HG-1, Ocean Optics) and solutions of organic fluorescent dyes (e.g., fluorescein in diH_2O). The known emission lines of the mercury-argon lamp were used to generate calibration curves between AOTF driving frequency and optical wavelength.

3.2.3 Compact ME-LIF System

3.2.3.1 Characterization and Refurbishing of a Compact ME-LIF Apparatus

A compact ME-LIF system consisted of a relatively simple combination of a dual high-voltage power supply and a single-color laser-induced fluorescence detection scheme. The optics system consisted of a 473 nm diode laser system (Roithner Lasers, 20 mW, model RLTMBL-473-20), passed through a 5X beam expander (Edmund Optics), onto a dichroic mirror (XB22, Omega Optical), through a 16X objective (Edmund Optics), and into the microfluidic device; backscattered fluorescence emissions passed through the dichroic mirror, through a tube lens (Edmund Optics), onto a flat front mirror (Edmund Optics), through a pinhole spatial filter (Thor Labs), through a 530 nm band pass filter (Omega Optical) and onto the sensor of a photomultiplier tube (PMT) (Hamamatsu H5784). A custom multi-function power supply device (built by Larry St. John, UVA Physics Electronics Shop) was used to power the PMT, collect the PMT signal, filter the PMT signal (Avens AMLP8B-15Hz filter module), as well as control 2 high voltage DC to DC converters (Ultravolt 4A12-P or –N4) using high-voltage relays (Kilovac model

k81c). The system was retrofitted with shielded cabling to reduce noise in the analog signal acquisition system. Current was monitored manually using 2 digital multimeters (BK Precision, BK2405a). The system was controlled, and data was collected, using a USB-6229 DAQ device (National Instruments) controlled by software written in-house in LabVIEW (National Instruments).

3.2.3.2 PeT ME Devices and Separations

Electrophoretic microdevices were fabricated from commercial overhead transparencies (3M, CG5000) and laser printer toner (HP Laserjet 4000) using laser ablation as described previously[28]. Briefly, microfluidic devices were patterned using CO_2 laser ablation (VLS350, Universal Laser Systems). After carefully aligning the layers the devices were bonded using the heated rollers of an inexpensive laminating machine. For separations in PT microchips, 0.5% hydroxy-propyl-cellulose was used spiked with 0.1X EvaGreen intercalating dye (Biotium Inc.) or YO-PRO (Molecular Probes Inc.) intercalating dye. Typical separation conditions consisted of a 30 second injection (Buffer and Buffer Waster reservoirs electrically floating, -100 V applied to the Sample reservoir, +100 V applied to the Sample Waste reservoir) followed by a 300 second separation (-125 V at Buffer reservoir, +500V at Buffer Waste reservoir, with the Sample and Sample Waste electrodes grounded to generate a pull-back current).

3.2.4 Software Development for MicroLab Diagnostics LLC et al.

Prototype microfluidic genetic analyzer equipment was developed by MicroLab Diagnostics LLC and associated entities. The integrated microfluidic genetic analysis instrument was described in two recent patents [21,22] and in a forthcoming

publication (Le Roux, D. *et al.*, Submitted, Lab on a Chip). Remaining details are proprietary and may not be disclosed here. Custom data analysis software was developed using the LabVIEW Professional Development System (versions 2009 and 2012, National Instruments Inc.).

3.3 Results and Discussion

3.3.1 Capillary Electrophoresis

3.3.1.1 Separation of Ovalbumin Glycoforms by CZE

Separations of ovalbumin were conducted using a borate buffer complex resulted in a partial separation of purified ovalbumin into several overlapping peaks and appreciable EOF (Figure 3.7A). The addition of the EOF modifier 1,4 diaminobutane resulted in longer residence time within the chamber and better resolution of the ovalbumin glycoforms (Figure 3.7B).

3.3.1.2 Separation of Multiplex PCR Products

CE was used as sample analysis method during early stages of the warfarin pharmacogenetic assay described in the previous chapter. Several PCR products from an ARMS reactions for the CYP2C9 *2, *3 and VKORC1 6853 SNPs were analyzed by CE (Figure 3.8). Injections of PCR products were preceded and followed by sizing standards. The PCR products revealed significant primer dimer formation. Precise sizing of the PCR products was difficult due to the lack of an internal size standard. The size standards may have migrated significantly differently due to greater sample stacking in the size standard injections due to their lower ionic strength relative to the raw PCR products. Ultimately, the commercial Agilent 2100 ME platform was chosen for analysis

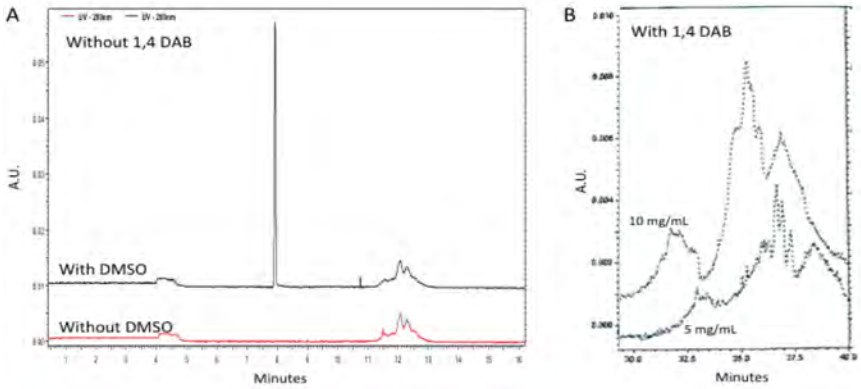

Figure 3.7: Resolution of ovalbumin glycoforms via capillary zone electrophoresis with borate and 1,4 diaminobutane buffer additives. A. In absence of the 1,4 diaminobutane (1,4 DAB) EOF modifier, the protein elutes in 12 minutes, and with EOF elution at 8 minutes as seen by dimethylsulfoxide (DMSO) EOF marker. B. The ovalbumin was resolvable into separate peaks corresponding to different glycoforms of ovalbumin when EOF was suppressed.

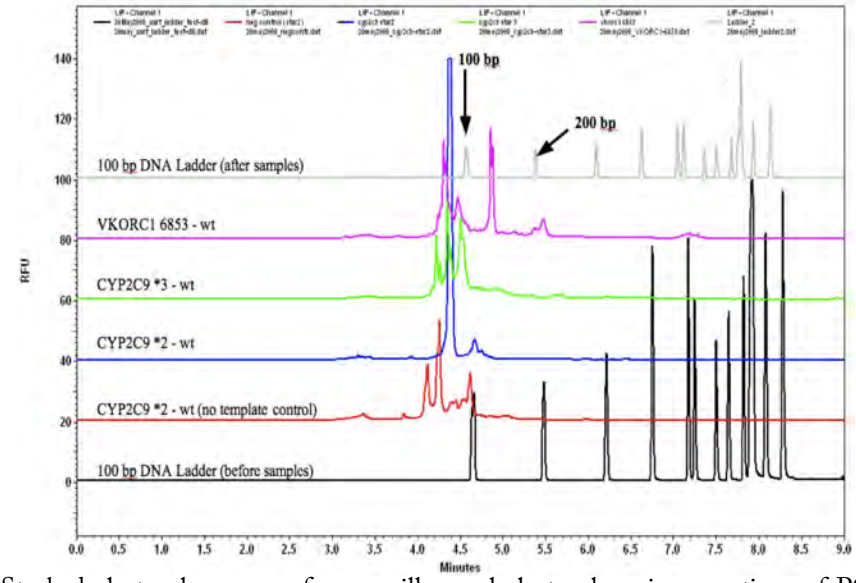

Figure 3.8: Stacked electropherograms from capillary gel electrophoresis separations of PCR products. Acronyms: Relative Fluorescence Units (RFU); Vitamin K Epoxide Reductase Complex 1 (VKORC1); Cytochrome P450, family 2, subfamily C, polypeptide 9 (CYP2C9).

of PCR products instead of CE, but the CE separations served as a useful conceptual prototype for understanding subsequent ME separations.

3.3.2 AOTF-based ME-LIF System

The apparatus for multi-color ME separations using the AOTF optical filter, was

serviced as described in the Materials and Methods section (and diagrammed above in Figure 3.6A). With the improved electrode housings (Figure 3.9), the length of time that a microfluidic device could be on the heated stage at 60 ºC was increased from approx. 20 minutes to well over an hour to provide for a more robust experimental workflow. Fluorescein (shown a tube for effect in (Figure 3.10A) has an emission spectrum that is partially truncated by the optics of the AOTF-based ME-LIF system (Figure 3.10B). Repeated spectral scans of fluorescein (Figure 3.10C,D) were evaluated to verify the accuracy of the correlation between AOTF driver frequency and the observed optical emission signals.

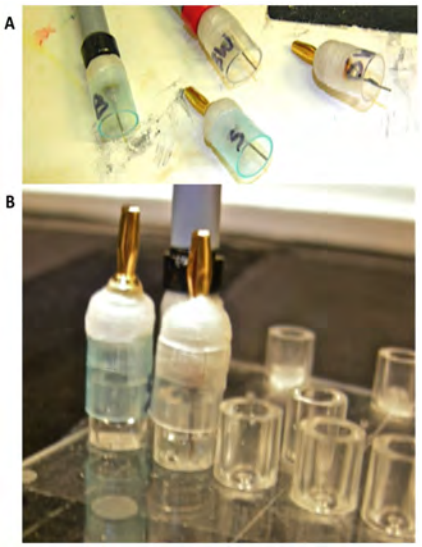

Figure 3.9: Improved electrode housings for microchip electrophoresis. A. Housings labeled with corresponding microchip reservoir. B. Close-up view of electrode housings fitted to microfluidic reservoirs.

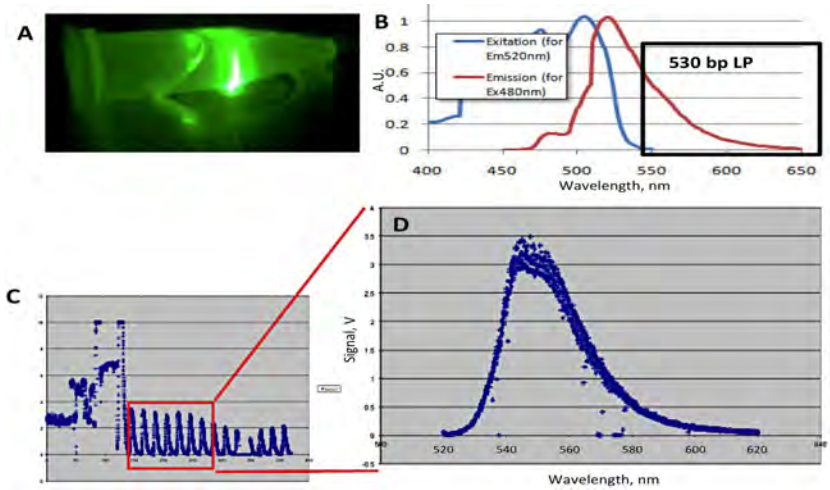

Figure 3.10: Validation of AOTF spectral calibration using an organic fluorescent dye. A. Microcentrifuge tube of 1 x 10-4 M fluorescein placed above the objective lens. B. Spectrum of fluorescein with annotated region of detectable light (Source [Wikimedia Commons, Fluorescein]). C. Plot of raw data collected during alignment and spectral sweeping of a dye stock solution. D. Plot of signal versus wavelength for several sweep replicates.

3.3.3 Compact ME-LIF System

The compact ME-LIF system (Figure 3.11A-C) was refurbished and restored to functionality. The user interface of the custom control software is shown in Figure 3.12, and this software allowed for automated application of voltages and collection of detector signals. The electrical control module was repaired and calibrated; for example, the high voltage DC to DC converters were calibrated Figure 3.13 to ensure safety and accuracy of the high voltage power supplies.

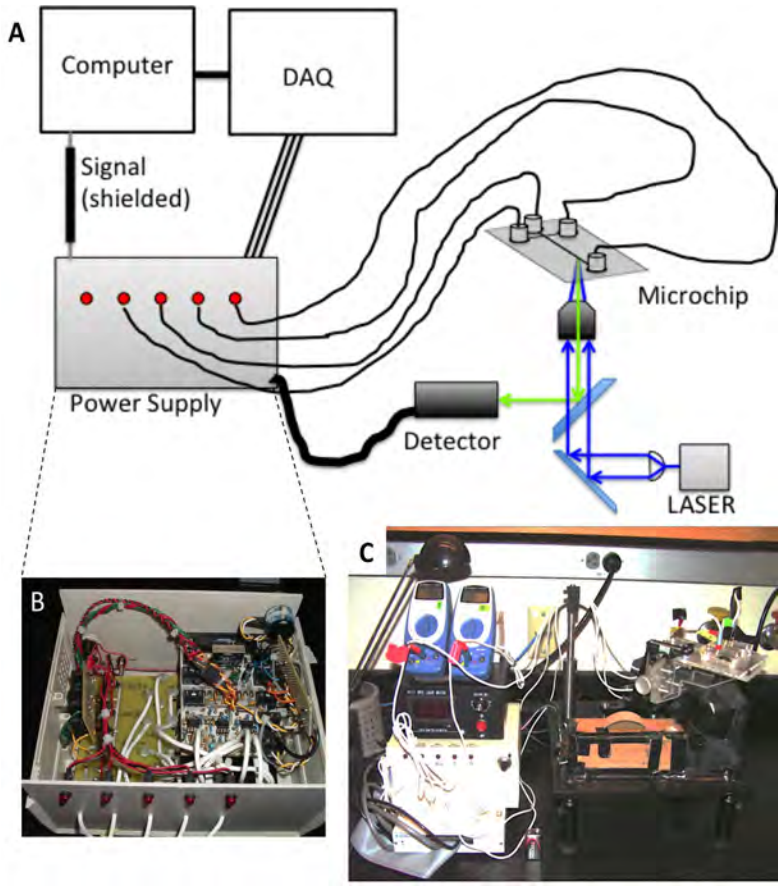

Figure 3.11: Compact ME-LIF apparatus. A. Diagram of system components with electrical and optical paths represented. B. Photograph of the interior of the ME-LIF control box. C. Photograph of compact ME-LIF apparatus.

Figure 3.12: User interface for the custom ME-LIF control software.

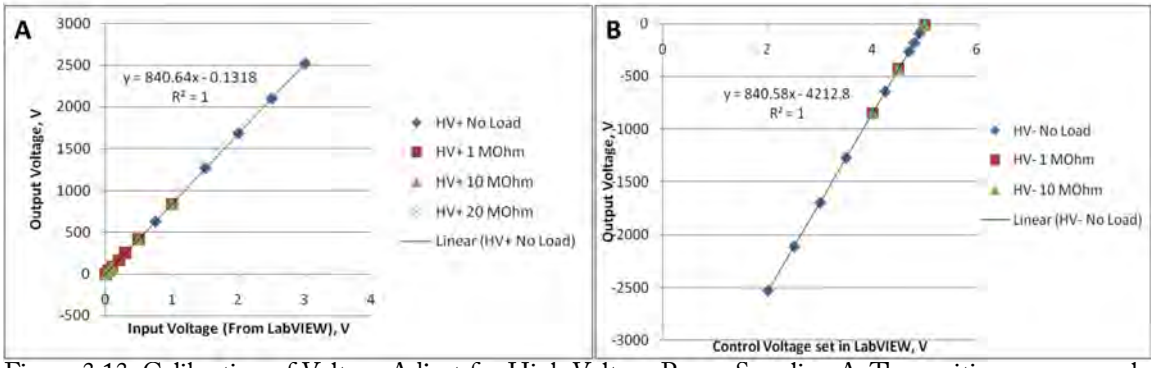

Figure 3.13: Calibration of Voltage Adjust for High Voltage Power Supplies. A. The positive power supply responded to positive control voltages. B. The negative power supply responded only to negative control voltage, presenting a potential safety hazard in the event of DAQ failure or improper system initialization.

3.3.4 PeT Microfluidic Devices for Electrophoresis

Layered PeT microdevices (Figure 3.14) were used for separations of fluorescent organic dyes and PCR products. Imaging of the "cross t" region of the microdevice revealed mobilization of fluorescent sample Figure 3.15A-B, injection of a sample plug down the separation channel (Figure 3.15C), and application of pull-back currents to prevent sample leakage during separation (Figure 3.15D). Gated injections of fluorescein (Figure

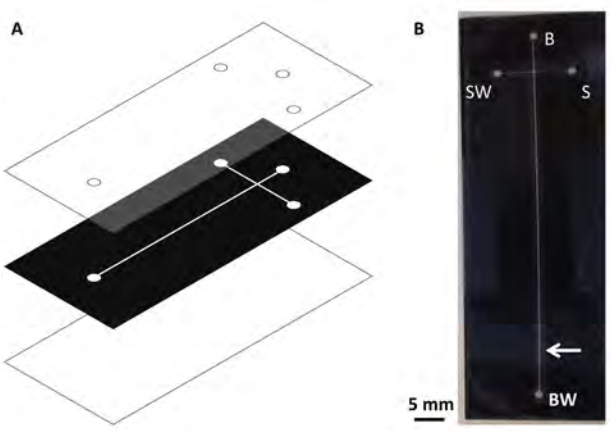

Figure 3.14: Diagram and photograph of three layer polyester-toner (PeT) microdevice. A. The device consists of three layers of polyester film. The middle layer is coated with toner on both sides to serve as glue and the top layer has hole cut to access the channels. All features are cut with a CO2 laser engraving/cutting machine. B. Photograph of a 3-layer PeT device for ME-LIF. Reservoirs are labeled (in clockwise order): Buffer (B), Sample (S), Buffer Waste (BW), and Sample Waste (SW). The approximate location of the LIF detector focal point is indicated by the white arrow.

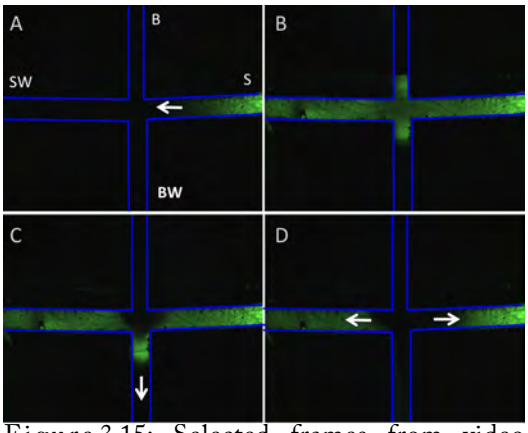

Figure 3.15: Selected frames from video microscopy of electrokinetic injection of 1 x 10-3 M fluorescein in a PeT microfluidic device. The orientation of the reservoirs is indicated by the reservoir labels in A. A. Initial stage of sample injection across the cross t intersection. B. Late stage of sample injection. C. Initial gated inject of a sample plug down the separation channel. D. Demonstration of sample pullback to prevent leakage of sample down the separation channel.

3.16A) and PCR products stained with the fluorescent intercalating dye EvaGreen (Figure 3.16B) were injected and separated in the PeT microfluidic device.

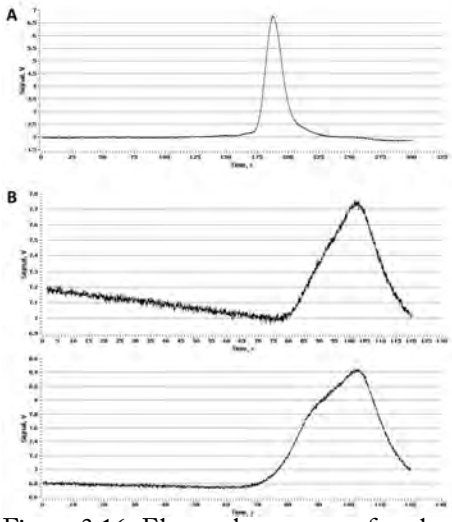

Figure 3.16: Electropherograms of analyte injections using the compact ME-LIF setup and PeT microfluidic devices. A. Fluorescein injection, and B. Replicate injections of 500 bp PCR product generated from the λ phage genome.

3.3.5 Software Development for Processing and Analysis of ME Data

3.3.5.1 Improved Methods for AOTF ME-LIF Data Visualization

A LabVIEW program was created to simplify and improve upon the data analysis process following

each AOTF ME-LIF run. Prior to this program, data was processed manually in Microsoft Excel, and analysis of a single data file would require at least 10 minutes. As depicted in Figure 3.17 the program read in raw five-color electrophoretic data and sorted by wavelength. Once colors were separated, data was smoothed by applying a low-pass (Butterworth) filter to reduce noise. Next, the spectral overlap between the different fluorescent dyes may be subtracted out by a process called matrix deconvolution. Once processed, data is then displayed on five linked XY-graphs so the user can dynamically scale and zoom the data plots to clearly visualize the electrophoretic data.

3.3.5.2 Development of ME Performance Evaluation Software

During my tenure as a consult with MicroLab Diagnostics LLC and related entities, I generated several data sets on an integrated microfluidic platform for forensic DNA

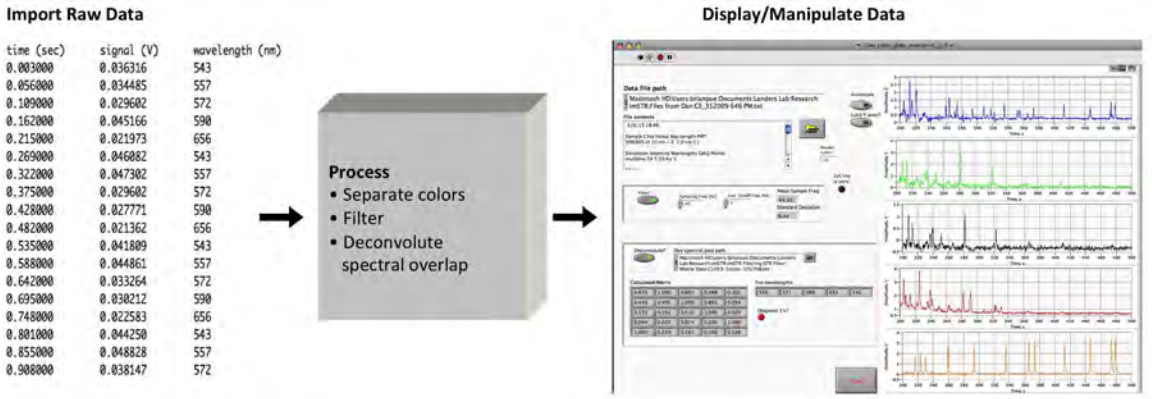

Figure 3.17: Workflow diagram of data processing from interleaved, raw data to five-color plots of data. Screenshot of the actual LabVIEW program is shown on the far right.

analysis that combined DNA extraction, PCR, and microchip electrophoresis . The first prototype genetic analyzer (Figure 3.18A) was capable of multicolor microchip gel electrophoresis separations. The multi-color data viewer application described above was revamped for a new storage format for electrophoretic data (Figure 3.18B). Then a new

module was developed to analyze the quality of ME separations according to well-established[5] chromatographic characterizations (e.g., peak full width at half maximum, resolution, mobility, etc). A typical run analysis workflow was as follows: First the program extracted relevant subsets of data from files of electrophoretic data to yield 5 sets of fluorescence intensity vs. time data (Figure 3.18C); Next it allowed the user to adjust the temporal region of interest, apply spectral matrix de-convolution, and then apply a low-pass filter to smooth and baseline-subtract the data; The analysis module allowed the user to identify the internal size standard peaks, fit each peak to a Gaussian curve Figure

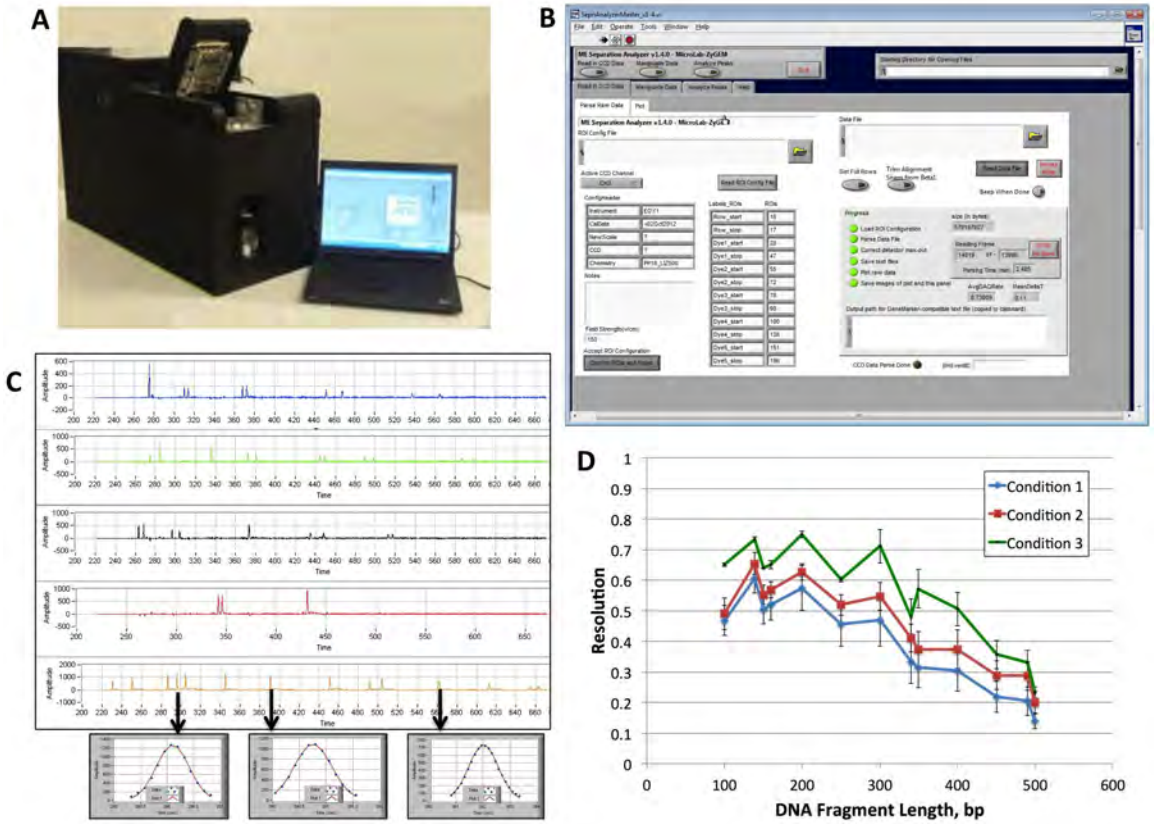

Figure 3.18: Overview of software developed to microchip electrophoresis data on the prototype genetic analyzer developed by MicroLab Diagnostics and associated entities. A. Photograph of the prototype genetic analyzer (reproduced from [Lounsbury thesis]). B. Screenshot of the software user interface during data import. C. Stacked 5-color electropherogram of an ME STR analysis. Peaks within the data were fitted to Gaussian curves (insets). D. Example comparison of ME performance for 3 different experimental conditions.

3.18C insets), and calculate chromatographic figures of merit; Finally, a data aggregation module facilitated simple statistical analysis of replicate tests and comparison between test conditions. Resolution data (e.g., as in Figure 3.18D) was used to assess the quality of various experimental separations. Propriety formulations of ME sieving polymer were prepared and evaluated, related reagent quality control experiments were performed. Additional software was written to facilitate calibration and alignment of optical detection equipment. Relative to prior methods, the ME separation analysis software accelerated the data extraction and analysis processes. Faster data processing allowed for timelier and less costly evaluation of experimental data for ME performance optimization.

3.4 Conclusions and Future Directions

Electrophoretic separations are an essential process in many bioanalytical applications, and one in which capillary microfluidic technologies have proven especially useful. Capillary-based separations were conducted for protein analyses and analysis of PCR products. These CE-based methods are illustrative of techniques essential for clinical and forensic bioanalysis. Furthermore, 3 different platforms for microchip electrophoresis were investigated, repaired, and utilized: an early large prototype ME apparatus with an AOTF filter, a compact ME setup with single color detection, and an advanced commercial prototype genetic analysis instrument. Custom software was written and maintained for operation and data management. Operational parameters of the system were determined to be suitable for electrophoretic separation of DNA. In summary, this work demonstrates a detailed understanding of the physics, engineering, and logistics of

ME instrumentation. The majority of the experiments described above were procedural or proprietary, but in light of the author's efforts the methods and apparatus described above are ready for future applications.

3.5 Acknowledgements

This work wouldn't have been possible with the help of individuals including Dr. Dan Marchiarullo for training on the AOTF ME-LIF system; Drs. Brian Root, Orion Scott, and Jess Norris for training on the MicroLab AOTF Beta Unit in 2009; Dr. Jerome Ferrance for building the compact ME-LIF and explaining its working principles; Prof. Gabriela Duarte for collaboration on PeT microfluidic devices; Dr. Brian Root *et al.* at MicroLab Diagnostics LLC and its subsequent entities for the opportunity to train and work on the MicroLab Beta systems and software.

3.6 References

[1] M. Geiger, A.L. Hogerton, M.T. Bowser, Capillary electrophoresis., Anal. Chem. 84 (2012) 577–96. doi:10.1021/ac203205a.

[2] S. Ghosal, ELECTROKINETIC FLOW AND DISPERSION IN CAPILLARY ELECTROPHORESIS, Annu. Rev. Fluid Mech. 38 (2006) 309–338. doi:10.1146/annurev.fluid.38.050304.092053.

[3] J.P. Landers, ed., Handbook of Capillary and Microchip Electrophoresis and Associated Microtechniques, 3rd ed., CRC Press, 2007.

[4] E.A.S. Doherty, R.J. Meagher, M.N. Albarghouthi, A.E. Barron, Microchannel wall coatings for protein separations by capillary and chip electrophoresis., Electrophoresis. 24 (2003) 34–54. doi:10.1002/elps.200390029.

[5] J. Giddings, Unified Separation Science, Wiley, New York, 1991.

[6] J.C. Sanders, M.C. Breadmore, Y.C. Kwok, K.M. Horsman, J.P. Landers, Hydroxypropyl cellulose as an adsorptive coating sieving matrix for DNA separations: artificial neural network optimization for microchip

analysis., Anal. Chem. 75 (2003) 986–94.

[7] C.P. Fredlake, D.G. Hert, T.P. Niedringhaus, J.S. Lin, A.E. Barron, Divergent dispersion behavior of ssDNA fragments during microchip electrophoresis in pDMA and LPA entangled polymer networks., Electrophoresis. 33 (2012) 1411–20. doi:10.1002/elps.201100686.

[8] B.C. Durney, J.A. Lounsbury, B.L. Poe, J.P. Landers, L.A. Holland, A thermally responsive phospholipid pseudogel: tunable DNA sieving with capillary electrophoresis, Anal. Chem. 85 (2013) 6617–6625.

[9] M.A. Rodriguez, D.W. Armstrong, Separation and analysis of colloidal/nano-particles including microorganisms by capillary electrophoresis: a fundamental review, J. Chromatogr. B. 800 (2004) 7–25. doi:10.1016/j.jchromb.2003.09.060.

[10] H. Katayama, Y. Ishihama, N. Asakawa, Stable Cationic Capillary Coating with Successive Multiple Ionic Polymer Layers for Capillary Electrophoresis, Anal. Chem. 70 (1998) 5272–5277. doi:10.1021/ac980522l.

[11] C.A. Lucy, A.M. MacDonald, M.D. Gulcev, Non-covalent capillary coatings for protein separations in capillary electrophoresis., J. Chromatogr. A. 1184 (2008) 81–105. doi:10.1016/j.chroma.2007.10.114.

[12] I. Wong, C.-M. Ho, Surface molecular property modifications for poly(dimethylsiloxane) (PDMS) based microfluidic devices., Microfluid. Nanofluidics. 7 (2009) 291–306. doi:10.1007/s10404-009-0443-4.

[13] C.R. Forest, B. Woodruff, D. Buckley, W.G. Thilly, I.W. Hunter, Assembly and constraint technology for large arrays of capillaries, Precis. Eng. 33 (2009) 275–283. doi:10.1016/j.precisioneng.2008.08.002.

[14] R. Sinville, S. a Soper, High resolution DNA separations using microchip electrophoresis., J. Sep. Sci. 30 (2007) 1714–28. doi:10.1002/jssc.200700150.

[15] A.H. Dewald, B.L. Poe, J.P. Landers, Electrophoretic microfluidic devices for mutation detection in clinical diagnostics, Expert Opin. Med. Diagn. 2 (2008) 963–977. doi:10.1517/17530059.2.8.963.

[16] S. Brunklaus, T.E. Hansen-Hagge, J. Erwes, J. Höth, M. Jung, D. Latta, et al., Fast nucleic acid amplification for integration in point-of-care

applications., Electrophoresis. 33 (2012) 3222–8. doi:10.1002/elps.201200259.

[17] V.N. Hoang, G. V Kaigala, A. Atrazhev, L.M. Pilarski, C.J. Backhouse, Strategies for enhancing the speed and integration of microchip genetic amplification., Electrophoresis. 29 (2008) 4684–94. doi:10.1002/elps.200800351.

[18] C.L. do Lago, H.D.T. da Silva, C.A. Neves, J.G.A. Brito-Neto, J.A.F. da Silva, A dry process for production of microfluidic devices based on the lamination of laser-printed polyester films., Anal. Chem. 75 (2003) 3853–8.

[19] G.R.M. Duarte, C.W. Price, B.H. Augustine, E. Carrilho, J.P. Landers, Dynamic solid phase DNA extraction and PCR amplification in polyester-toner based microchip., Anal. Chem. 83 (2011) 5182–9. doi:10.1021/ac200292m.

[20] Y. Ouyang, S. Wang, J. Li, P.S. Riehl, M.R. Begley, J.P. Landers, Rapid patterning of "tunable" hydrophobic valves on disposable microchips by laser printer lithography., Lab Chip. 13 (2013) 1762–71. doi:10.1039/c3lc41275j.

[21] Michael Egan, B. ROOT, O.N. Scott, D.J. South, J. Bienvenue, P. Kinnon, et al., Microfluidic cartridge, 2013.

[22] H.R. Bell, J. Bienvenue, J.W. Pettit, J.P. Landers, J. Norris, O. Scott, et al., Dna analyzer, US Pat. …. (2010).

[23] D.E. Morbeck, B.J. Madden, D.J. McCormick, Analysis of the microheterogeneity of the glycoprotein chorionic gonadotropin with high-performance capillary electrophoresis, J. Chromatogr. A. 680 (1994) 217–224. doi:10.1016/0021-9673(94)80070-7.

[24] D.J. Marchiarullo, Development of Microfluidic Technologies for On-site Clinical and Forensci Analysis: Extraction, Amplification, Separation, and Detection, 2009.

[25] J.M. Karlinsey, J.P. Landers, Multicolor fluorescence detection on an electrophoretic microdevice using an acoustooptic tunable filter., Anal. Chem. 78 (2006) 5590–6. doi:10.1021/ac0607358.

[26] J.M. Karlinsey, J.P. Landers, AOTF-based multicolor fluorescence

detection for short tandem repeat (STR) analysis in an electrophoretic microdevice., Lab Chip. 8 (2008) 1285–91. doi:10.1039/b801759j.

[27] C.R. Reedy, K. a Hagan, D.J. Marchiarullo, A.H. Dewald, A.E. Barron, J.M. Bienvenue, et al., A modular microfluidic system for deoxyribonucleic acid identification by short tandem repeat analysis., Anal. Chim. Acta. 687 (2011) 150–8. doi:10.1016/j.aca.2010.12.016.

[28] G.R.M. Duarte, W.K.T. Coltro, J.C. Borba, C.W. Price, J.P. Landers, E. Carrilho, Disposable polyester-toner electrophoresis microchips for DNA analysis., Analyst. 137 (2012) 2692–8. doi:10.1039/c2an16220b.

[29] P. Hiemenz, R. Rajagopalan, Principles of Colloid and Surface Chemistry, revised and expanded, CRC Press, 1997.

[30] H. Bruus, Theoretical Microfluidics, OUP Oxford, 2008.

[31] C.J. Easley, J.M. Karlinsey, J.M. Bienvenue, L. a Legendre, M.G. Roper, S.H. Feldman, et al., A fully integrated microfluidic genetic analysis system with sample-in-answer-out capability., Proc. Natl. Acad. Sci. U. S. A. 103 (2006) 19272–7. doi:10.1073/pnas.0604663103.

4 Techniques and Applications for Microfluidic Device Fabrication via CO_2 Laser Ablation

4.1 Introduction

4.1.1 CO_2 Laser Ablation Principles

CO_2 lasers typically contain a mixture of helium, nitrogen, and carbon dioxide within a sealed laser chamber. A radio-frequency electrical input excites the N_2 molecules that then transfer their excited state to CO_2 through inter-molecular collisions. CO_2 has several vibrational modes in the IR range, but there is a predominant vibration mode with emission at 10.6 μm that dominates the output spectrum for most CO_2 laser instruments[1][2]. The power output of the laser is modulated via pulse width modulation, and given the rise time of the laser module of approximately 100 μs[3] (due to both electronics delays and to gas diffusion), a continuous wave laser beam is effectively generated when the excitation pulse rate exceeds 200 kHz[1]. The laser used in this work was operated in a pulsed mode with synchronization between the laser beam steering system (described below) and the laser module. Mechanisms for removal of material during ablation include photochemical, thermal, and mechanical phenomena [4] with substantial differences between substrate materials.

The output of the CO_2 laser must be steered and focused in a controlled fashion to create patterns for microfluidic device fabrication. The instrument is diagrammed in Figure 4.1A and pictured in Figure 4.1B. The beam is steered by mirrors and focused by IR-transparent ZnSe lenses. These steering and focusing optics are mounted on an x-y motion system, which (in the system utilized for this work) consisted of 3 independent belt drive mechanisms driven by stepper motors. Features are created in the x-y plane in

one of 2 operational modes – vector movements (Figure 4.1C) or raster patterns (Figure 4.1D), and the relative operational specifics outlined in the user manual information for each mode must be taken into account when predicting the final ablation results. The lens assembly focused the material down to spot size of roughly 25 μm (Figure 4.1E), and this nearly diffraction-limited spot size typically creates feature sizes in the range of 150 μm in thermoplastics such as polymethylmethacrylate (PMMA). Recently, the use of metal masking patterns has overcome the spot size limitations of focus CO_2 lasers, and features sizes of 75 μm [5] down to 25 μm [6]. The resolution and fidelity of motion system translation, the aberration in beam steering/focusing, the focused spot size, and the material response to laser flux all determine the characteristics of the microstructures that can be produced.

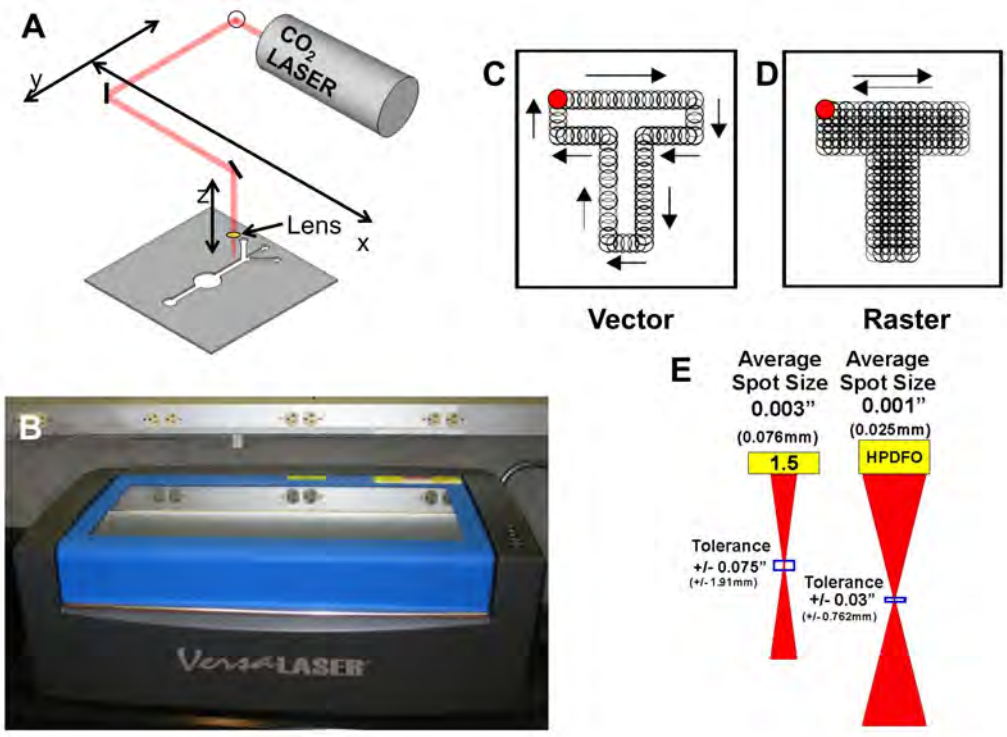

Figure 4.1. Overview of CO2 laser ablation instrument.

4.1.2 Substrates for Microfluidic Devices

4.1.2.1 PMMA

Microfluidic devices have been extensively fabricated in the thermoplastic PMMA in recent years (e.g., [7,8]). The quality of features are suitable for a variety of bioanalytical microfluidic applications. For instance, surface tension-mediated valving has been demonstrated in laser-ablated PMMA devices [9]. Microdevice assembly has been achieved by several methods, including thermal bonding [10] and chemical bonding [11][12]. The initial in-house validation of a laser fabrication method and thermal bonding method for PMMA microdevices is presented below.

4.1.2.2 Glass

Laser ablation of glass has been studied extensively due to the commercial and scientific importance of glass materials [13–17]. Traditional methods of microstructure fabrication in glass[18] are often superior to laser fabrication (e.g., Roper *et al.* recently compared the electrophoretic performance of laser-ablated glass channels to wet-etched channels and found that wet etched channels were superior for ME[19]). However, the low cost and facile fabrication workflow of laser ablation warrants a sustained effort to implement this fabrication method. Cracking during laser ablation of glass is a critical concern, but strategies such as heating the glass to ~350 ^{o}C to relieve thermal stress[19], water immersion[15], and polymeric overlays[20] have been proven to reduce bulge and crack suppression. A method of crack suppression method is presented below wherein a ubiquitous and low cost commercial pressure sensitive adhesive was used to protect thin glass plates during ablation of holes.

4.1.2.3 Fluorocarbons

Despite the exceptional chemical stability of fluorocarbons such as polytetrafluoroethylene (PTFE), it is possible to still modify it via laser ablation. Note that caution is warranted when cutting halogen-containing polymers via CO_2 laser ablation, because some such polymers (e.g., polyvinyl chloride) will evolve toxic and corrosive chlorine gas upon laser irradiation. Studies of PTFE modification by CO_2 laser ablation have revealed that small scale ablation was harmless with adequate engraver ventilation. PTFE microstructuring via CO_2 laser ablation was found to produce microscale mesh of 5-20 μm fibers is formed[21]. Recently Zestos *et al.* (including this author) used laser ablation of PTFE to create microscale molds for crafting microelectrodes[22].

4.1.2.4 PDMS and Glass-PDMS-Glass Hybrid Devices

Laser ablation and modification of poly(dimethyl)-siloxane (PDMS) has been widely studied for microfluidic applications [23][24–27]. PDMS itself is a remarkable polymer that finds use in nearly every sector of manufacturing, consumer products, and industry[28]. PDMS is a hydrophobic polymer that is gas permeable, optically transparent, swells in hydrophobic solvents, acts as a solid solvent for a wide variety of small hydrophobic molecules, features low surface energy for high hydrophobicity and high biocompatibility, elastomeric for active fluid control methods, and relatively low cost. PDMS is structured by CO_2 ablation by photothermal effects of melting and oxidation of methyl groups from the PDMS backbone[23][26]. This ablation produces a substantial amount of debris (depleted in carbon, indicative of more SiO_2-like character [25]) that must be removed following laser ablation because it interferes with downstream bonding

to other parts of microfluidic devices[26].

The combination of glass and (PDMS) in microdevices has been in practice since the inception of PDMS-based microfluidics[29]. The marriage of these two materials is due in large part to the inherent compatible chemistry between glass (SiO_2) and PDMS ($(C_2H_6OSi)_n$) available through (Si-O-Si) bonds. In particular, devices fabricated by multiple layers have proven particularly useful due to the complimentary mechanical strength of glass to the versatility of PDMS. Such layered devices have been fabricated by various means (e.g., dry reactive ion etching[Oh 2008], addition of a polymeric vapor barrier to PDMS [30], templated microblasting[31], and soft lithography[32] or manual cutting and assembly with clamping[33]). The fabrication and assembly methods presented in this chapter were extended from these works to streamline the device fabrication process and validate an in-house fabrication method using the laser engraving instrumentation that had been newly acquired by our laboratory.

4.1.2.5 Developments in Post-Ablation Processing and Assembly

The traditional method of bonding the layers of these glass-PDMS-glass devices is plasma bonding, where an O_2 plasma is used to modify the surfaces so they bond instantly and permanently upon contact[34]. While this process gives strong bond, the cleaning and alignment steps have a high failure rate and the process is time consuming. A facile method of assembling these devices was developed that uses alcohol-assisted relaxation and dynamic alignment of layers to achieve a high-quality bond without plasma bonding. Next, ethanol was added between the layers so they can slide past each other. This step lets the deformable PDMS fluidic layer relax (for faithfully preserved channel dimensions) and then the layers can be slid past each other to line up the access holes

with channels. As the ethanol evaporates the layers form a reversible bond of a large area of van der Waals interactions. Devices fabricated in this manner were shown to have reproducible inter- and intra-device features. The PDMS and glass layers were cleaned after laser ablation with mechanical removal of the micro- and nano-particulate ablation debris. Moreover, a novel chemical treatment of concentrated NaOH was developed that etched some of the silica ablation debris, and more importantly, facilitated the unique property of silicones to recombine at a molecular level [35][36] to spread the PDMS bulk back over the ablation debris and possibly reestablish covalent bonds with the debris. The base treatment of PDMS also creates a temporary hydrophilic layer that is useful for electrophoretic applications[37].

4.1.3 Design Elements of Microfluidic Devices

4.1.3.1 Neurochips

PDMS microfluidics have enabled a new direction of research for neuroscience by facilitating studies on individual cell or even sub-components of cell (e.g., neuron axons) [38]. While soft lithography has been the predominant method for fabricating PDMS device for cell culture, the development method of direct (maskless) fabrication of PDMS microchips for this purpose is described below. Careful optimization of laser ablation parameters identified settings that produced thin cross-channels for guiding axon growth in neuron culture. Prototype devices were fabricated and evaluated for culturing primary rat neuronal stem cells.

4.1.3.2 GPG Chip Adaptations for High Temperature Operation

Another extension of our glass-PDMS-glass (GPG) technology is the addition of fluidic

architectures to enable extended high temperature of GPG devices. PDMS is an elastomeric material that is both gas and water permeable, and these features normally cause excessive bubble formation and dehydration of microchamber contents upon heating to PCR-relevant temperatures (e.g. 95 ^{o}C). PDMS without a glass casing must be modified to limit dehydration[30], but the devices described here are predominantly enclosed by glass, which has the benefit of dramatically limiting the diffusive path out of the microchamber. Even with the glass enclosure, a set of engineered solutions such as guard channels, vacuum chamber degassing, and in-plane thermocouple insertion need to effectively prevent evaporation of the chamber contents during PCR thermal cycling.

4.1.3.3 GPG Chip Fabrication and Function (Valving)

Added functionality to the three-layer microfluidic devices fabricated from glass (typically microscope coverslips) and PDMS silicone. In addition to using the CO_2 laser-engraving machine for cutting channels and access holes, a 3D sculpting method was developed to fashion monolithic valves and pumps in pre-fabricated, commercial sheets of PDMS. Traditional methods of forming these fluidic control elements typically require a cleanroom and a time consuming process of generating a mold via photolithography then casting liquid PDMS onto the mold. Multi-step soft lithography was used to create 3D fluidic architectures in PDMS [39]. The method described below can fabricate functional valving structures directly into PDMS. A valve membrane is formed via a 2-step laser ablation process to form a valve that is normally open when no pressure is applied.

4.2 Materials and Methods

4.2.1 GPG Layer Preparation and Device Assembly

Laser ablation steps were performed on a VersaLaser 350 fitted the high power density focusing optic (HPDFO) lens assembly (both manufactured by Universal Laser Systems Inc.). Prior to CO2 laser processing, the tuning value (motion system compensation factor) as optimize according to manufacturer protocols; for the devices use in this work, a value of +2 yielded the best alignment of subsequent laser passes.

Fluidic/spacer layers were fabricated from thin PDMS sheets (HT6240, Stockwell Elastomerics). In the ULS driver within CorelDRAW, vectors were rendered using "sort only" and not "enhance" (to avoid loss of microstructure detail). Settings and order of sequential processing for vector ablation operations on PDMS were as follows: {red (through-cut channels): 3% power, 2% speed, 1000PPI; blue (etched channels): 1% power, 2% speed, 1000 PPI; green (through-cut chip perimeter): 15% power, 10% speed, 1000PPI}. Monolithic valves were etched as above, with the addition of step to flip the PDMS part over, relax its structure again, and perform a second laser ablation step.

The upper layer of the GPG trapping devices were fabricated from coverslip glass (#2, FisherBrand 12-540-B) were covered in Scotch Magic Tape (3M Industries), then holes were ablated in the glass with two sequential passes (separate by a few seconds for cooling) at 65% power, 20% speed, 500 PPI. Following ablation, any residual material in the holes was removed by gently pressing on the material with the point of a thumbtack until it snapped out. Next the tape support layers were removed by softening the tape adhesive using liberal amounts of methanol and manually peeling of the tape in a direction parallel to the glass surface to minimize bending stress on the glass.

The bottom (carrier layer, contacting the transducer) was made using coverslips (#1, VWR Cat 48366067). PDMS was cleaned by wiping with an IPA-soaked swab then blotting dry to pull the debris/IPA away from the surface. Prior to chip assembly, PDMS parts were cleaned by wetting the PDMS surfaces with ethanol then slowly blowing the ethanol away (using compressed air line at 20 psi or canned duster (e.g., Maxell, Item#190025)) to drag dust and debris away with the receding ethanol interface. PDMS was placed on a thin (2 mil. thickness) film of fluorinated ethylene propylene (FEP) (DuPont Inc.), which was supported by a more rigid material - the backing from the HT-6240 PDMS sheets. The FEP film was chosen to aid plasma bonding via better release during the first plasma bonding step. PDMS parts were floated with a small amount of ethanol underneath so the fluidic architecture could relax to avoid deformations of the PDMS layer.

Parts to be bonded were exposed to RF-excited rarefied air plasma for 45 s (with periodic valve opening/closing to maximize plasma brightness) in a plasma cleaner (PDC-32G, Harrick Scientific, Pleasantville, NY). After plasma bonding the chip was placed in an oven maintained at 50 ºC for at least one hour (with additional time preferable, e.g., overnight). with a little bit of weight on it (brass parts from machine shop class) and allowed to sit for 30 minutes.

4.2.2 NaOH Treatment

NaOH Treatment: base-mediated hydrolysis/repolymerization of laser ablation ejecta on PDMS was performed by immersing the PDMS parts in 5 M sodium hydroxide for at least 1 hour. Fluorocarbon labware (Fluoroware) was used for testing the

surface treatment, but equally good results were obtained using common low density polyethylene plastic containers. Parts were immersed in the alkaline solution for at least one hour, rinsed with diH2O, and submerged (if possible) or floated in fresh diH2O. Digital photographs were taken of 3 replicate PDMS parts and 3 initially identical parts that were only treated with water.

4.2.3 SEM Imaging

Samples of laser-etched PDMS were mounted on 2.5 cm diameter aluminum pedestals using conductive carbon tape as the base layer. Carbon and gold conducting layers were sputtered onto the specimens with a Gaton Model 682 Precision Etching Coating System. Sputtering was performed with the following settings: 10 keV, deposition rate of 1.75 Angstroms/s for 3 minutes, approx. 200 μA, 2,5 Torr foreline, 1 x 10-4 Torr in the sputtering chamber; rock angle 30º, rock rate 16 º/s, rotate at 30 rpm. Approximately 60 nm of Au deposited on top of previously sputtered carbon. Scanning electron microscopy (SEM) imaging was performed using a JOEL JSM-6700F, Gaton MonoCl, 10 kV, 5 μA instrument.

4.2.4 Fabrication of PMMA Microfluidic Devices

The etched PMMA layer was placed onto the hot plate and the other PMMA layer was placed over the top of the etched layer. These two PMMA layers were sandwiched between PDMS pieces to evenly distribute the force of the weights. Using the equation Pressure = Force/Area, the appropriate set of weights was determined. The previously reported[40] bonding pressure of 200 kPa, or 1.97 atm, was achieved by loading the structure with a known mass of material. The chip dimensions were 2.5 x 2.5 cm.

Knowing this information, in addition to the fact that the gravitational constant g = 9.8 m/s2, the desired weight was found to be 1.275 kg. However, a precisely 1.275 kg weight was not available, so various weights that sum up to 1.275 kg were stacked on top of the PMMA chip. Temperature was measuring using a miniature type T thermocouple (M240C, Physitemp Inc.) placed in the stack adjacent to the PDMSlayer contacting the PMMA part to be bonded. The layer was then heated at 165˚C on the hot plate (determined to be dial setting 7 out of 10) for 30 minutes and cooled to 80 ˚C (dial setting 4.5 out of 10) for another 20-30 minutes. Once removed, the PMMA chip should be tightly bonded with few air bubbles present.

4.2.5 Fluidic Interfacing

Basic fluidic interconnections with GPG chips were made from 3 mm o.d., 1 mm i.e. silicone tubing (Cole Palmer) glued in place with silicone sealant (Permatex 81730). Clamping gasket manifolds were constructed from laser etched PMMA layers bonded together using ARseal double-sided pressure sensitive adhesive (Adhesives Research). Magnetic fluidic connectors were constructed from toroidal magnets (Emovendo Inc) fitted with the same silicone tubing (Cole Palmer), a thin PDMS membrane as a gasket against the glass microchip surface, and silicone adhesive to bond the parts together. Thin sheets of PTFE fluoropolymer were used a non-stick surface during gluing so that a second magnet could be applied to clamp the connector in its intended final configuration.

4.3 Results and Discussion

4.3.1 PDMS Etching and Post-Ablation Removal of Debris

Despite the relative abundance of published reports on laser fabrication of PDMS microdevices, there is enough variation between individual laser engraving machines (and intra-instrument variation over time) that quality control of ablated microstructures was a routine practice. The drive system of the instrument experience wear and changes over time, the beam steering mirrors may fall out of alignment with prolonged system vibration and motion, and the laser module output slowly declines with use (for instance, when the instrument was first installed in 2008 the output power was measured to be 67.2 W, but had dropped to 58 W when serviced again in 2011). Moreover, the variation in beam alignment between one region of the 12 in. x 24 in. cutting bed was found to vary substantially at the microscale, with both alignment and power differences. Therefore, reported correlations between fabrication figures of merit (e.g., etch depth) and operation parameters (e.g., power and speed values), while useful, should always be verified at the time of device fabrication.

An unexpected phenomenon was discovered when debris from ablation was deposited on the uncut material ahead of the laser beam. When the laser beam rastered the debris-covered PDMS, the laser power was used to etch through both material and debris and shallower etches resulted. The net effect of this was a significant loss of quality for deeply ablated regions longer than approximately a millimeter in the y direction. Irregular debris deposition resulted in heterogeneity of etch depth in the x direction within the footprint of the raster as well. When the cutting direction was reversed to traverse the table from bottom to top, this effect was alleviated because debris was

deposited asymmetrically around the cut site and moving away from the majority of the debris deposition resulted in the highest quality raster etchings.

Following laser ablation of PDMS microfluidic layer, a multi step post-processing workflow was developed to ensure the PDMS surfaces were free from debris that interfered with bonding. In the first step of microdevice fabrication, Figure 4.2A, an aluminum slab was used as a solid support for a thin sheet of PDMS what was laser ablated as described above. The vector-based 2D design of the device is shown in Figure 4.2B. Post-ablation processing was performed on the solid support, where swabs mechanically removed debris with the aid of alcohol surfactants (Figure 4.2C). As the photographic data in Figure 4.2D show, the majority of the ablation debris was removed in this first manual step. Note the improved optical clarity between the top image of Figure 4.2D and the 2 bottom images. When compared directly, isopropyl alcohol outperformed ethanol for debris removal. With most of the debris cleared, the ablated PDMS structure was be removed from the slab with forceps (Figure 4.2E), leaving any cut out material behind.

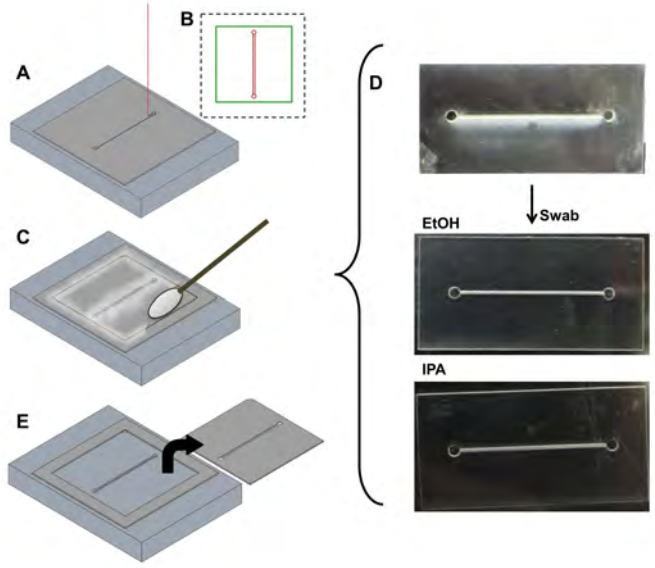

Figure 4.2. Mechanical removal of ablation debris.

4.3.2 Base-Mediated Clean Up of Laser Ablation Debris on PDMS

The NaOH clean up procedure proved to be an effective method for improving the optical clarity of laser-ablated PDMS. Immediately after laser ablation, all pieces appeared like those in Figure 4.3A. The side facing up during laser ablation was very hydrophilic (a thin film of water or NaOH would remain on the surface), but the pristine PDMS side would de-wet immediately (i.e., a meniscus would form and spread until PDMS-air interface replaced the PDMS-NaOH(aq) inferface). SEM imaging of unmodified PDMS (Figure 4.3B) revealed a close up view of the fine powder debris. Following an hour incubation in 5 M NaOH, the PDMS test pieces were noticeably more transparent (Figure 4.3C). Moreover, both sides of the PDMS parts were very hydrophobic following NaOH treatment. Note that the mechanical swabbing step was omitted for Figure 4.3A and Figure 4.3C to isolate the effect of the NaOH treatment. SEM imaging of a PDMS surface following both the swabbing and NaOH treatment

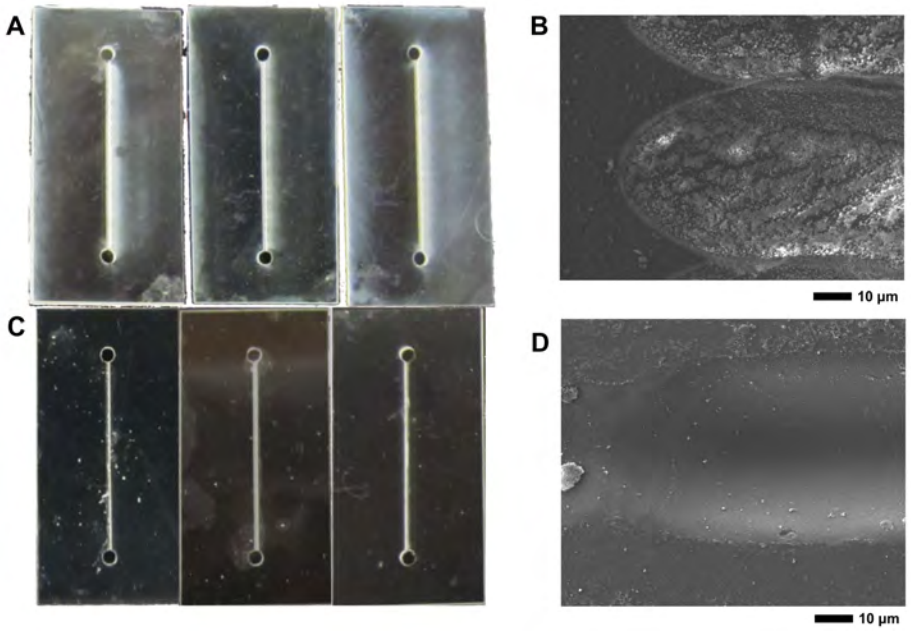

Figure 4.3. Chemical reduction and clarification of ablation debris.

revealed a visibly cleaner surface (Figure 4.3D). The water-only controls recovered their hydrophobicity in spite of the debris. The removal/clarification of ablation on debris by NaOH treatment was an effective means of improving the appearance and optical clarity of the PDMS parts.

4.3.3 Laser Ablation of Holes in Glass.

The glass top layers of microfluidic devices were modified with access holes for interfacing with the microfluidic architecture in the PMS layer. Cracking in the glass from ablation was suppressed by contacting both sides of the glass with common office tape prior to laser processing, and removing it with alcohol immediate following ablation (Figure 4.4A). Imaging of the posts appellation holes in glass by SEM (Figure 4.4B)

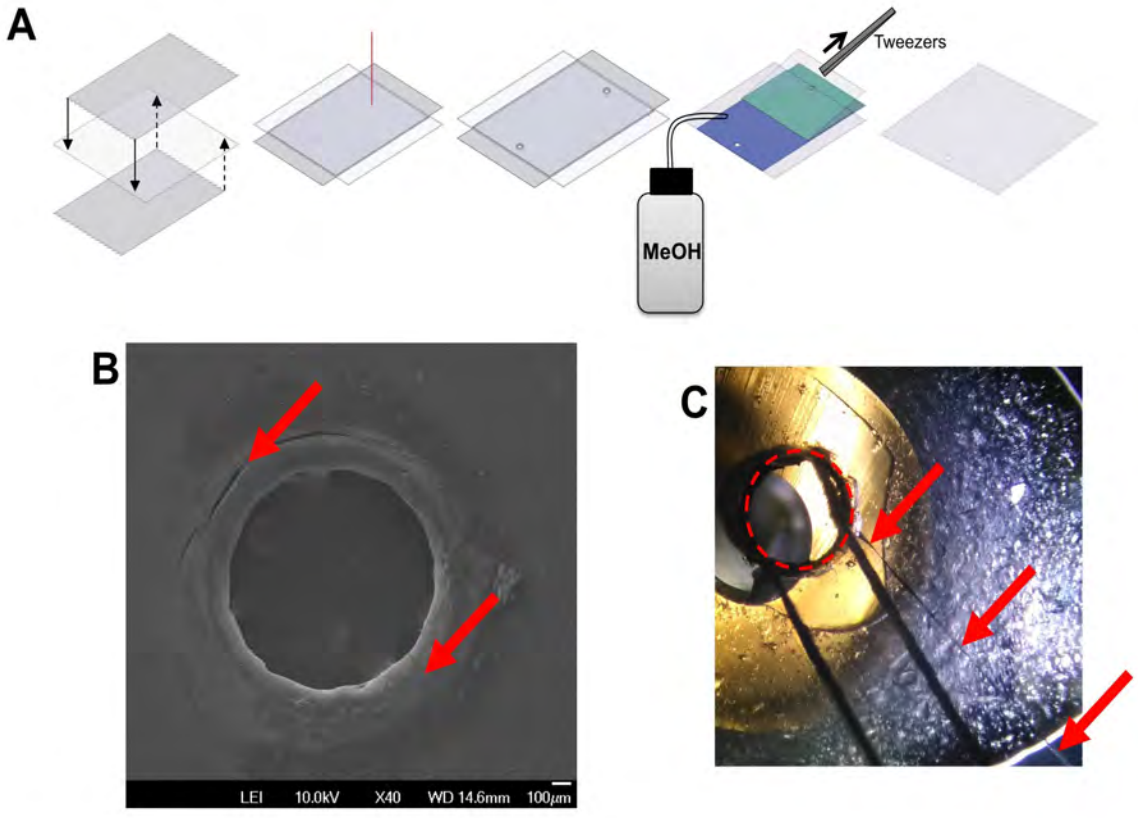

Figure 4.4. Method and outcome of laser ablation for creating holes in thin glass plates.

revealed that small cracks were often still present. Comparison of the crack pattern with the tape versus without revealed that the cracks were less radial than when tape was not used (data not shown), and the likelihood of crack propagation (ruining the part) was reduced when tape reinforcement was used. Nonetheless, the glass holes were still the weakest point in the microfluidic device, which is unfortunate because the fluidic inlets are subjected to the most stress. For instance, applying excessive pressure to the GPG device shown in Figure 4.4C resulted in crack propagation. Until a satisfactory improvement in the hole forming method is validated, caution must be used to prevent cracks from forming and propagating into the rest of the microchip.

4.3.4 Glass-PDMS-Glass Assembly Strategies.

Two methods of device assembly that were developed are represented in Figure 4.5A and B. The more traditional approach for device assembly utilized plasma activation of both the glass and PDMS surfaces to form permanent bonds between the layers. A separate strategy was validated wherein "reversible" bonds between the layers were established after aligning and annealing the layers together. A vital step for both methods was the use of a readily-evaporated surfactant (i.e., alcohol) to allow the planar PDMS structures to float and relax so that deformations could be relaxed by the elastomeric properties of the PDMS. The bond achieved by both methods was strong enough for applications of pressures as high as 10 psi above ambient, at which weakness in the glass holes was the typical failure point. As recently rediscovered and reproved by McCarthy et al., PDMS will readily undergo recombination between polymer chains[36], so prolonged annealing at elevated temperature may have somewhat equalized the bonding strength between

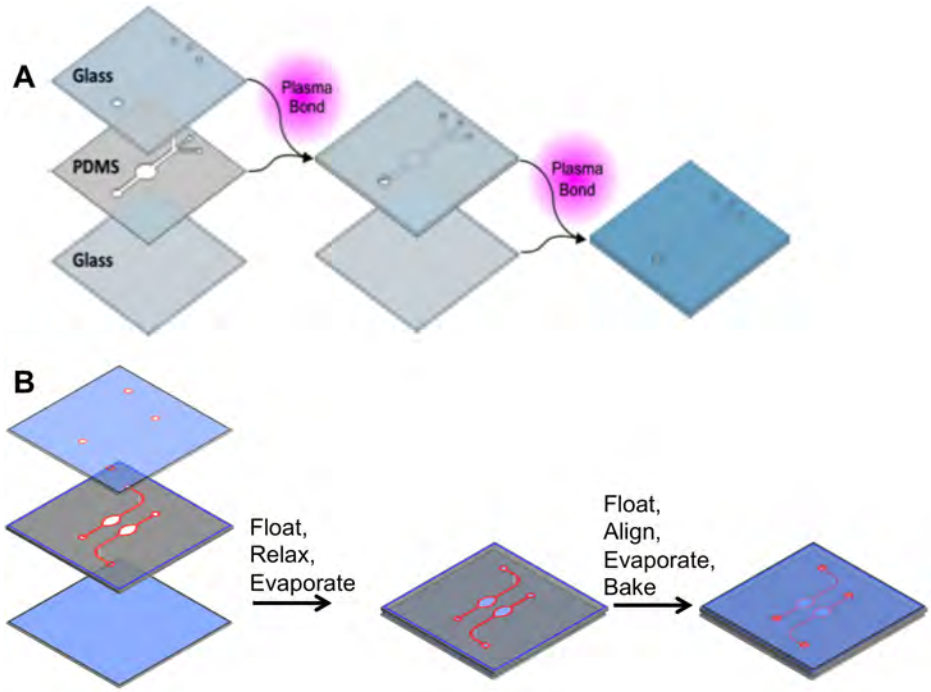

Figure 4.5. Assembly methods for glass-PDMS-glass microfluidic devices.

these two methods. The close contact between the glass layers and the PDMS were likely the most critical factor.

4.3.5 Results of Fluidic Architecture Fidelity Testing.

The fidelity of reproduction of fluidic architecture from computer design to physical device was evaluated for the alcohol-assisted alignment and annealing method. To compare the performance between methanol and ethanol for relaxation and annealing (IPA was excluded due to its PDMS swelling properties), 6 replicate devices like those diagrammed in Figure 4.6A and B were constructed using either methanol or ethanol (3 devices each). Relaxation of a fluidic channel is diagrammed in Figure 4.6C, and a representative GPG device is shown in Figure 4.6D. The intra-device variation (i.e., a measure of deformation within each microchannel) is reported for 3 replicate devices

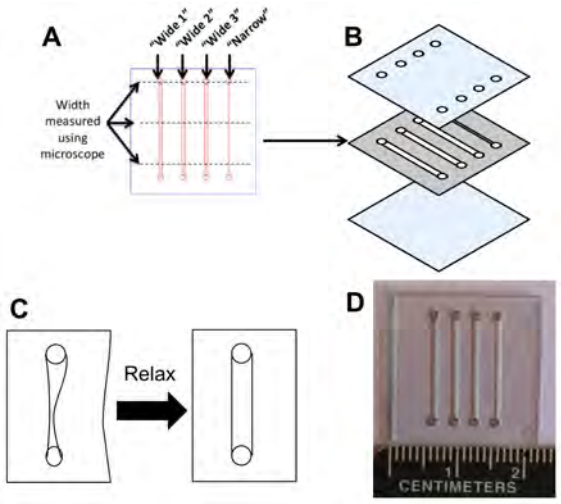

Figure 4.6. Microfluidic testing devices for evaluation of fabrication quality.

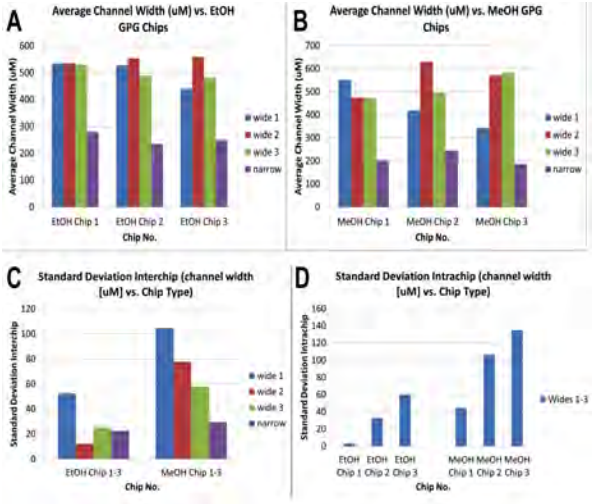

Figure 4.7. Comparisons of channel width within and between channels, replicate devices, and annealing solvents.

using ethanol Figure 4.7A) and methanol Figure 4.7B). Devices assembled using ethanol had a more uniform channel geometry than those with methanol, and this may be due to the longer evaporation time and greater surfactant properties of ethanol versus methanol. While methanol is desirable because it is least likely to swell PDMS, it also evaporated quickly which may not have allowed sufficient time, or adequate lubrication between the glass and PDMS, for the fluidic structures to relax to their original geometry as defined by the laser cutter before friction between the plates was restored. Moreover, the inter-device standard deviation per channel (i.e., comparing the same channel position between the 3 replicate devices) (Figure 4.7C) revealed a lower variability in the ethanol-assisted samples. Lastly, the 3 replicate channels within each device were compared to each other Figure 4.7D), and again, ethanol was preferable over methanol for alcohol-assisted relaxation and alignment of GPG devices.

4.3.6 Stencil method for creating closed-loop structures.

Many microfluidic architectures and two and three dimensions call for closed-loop

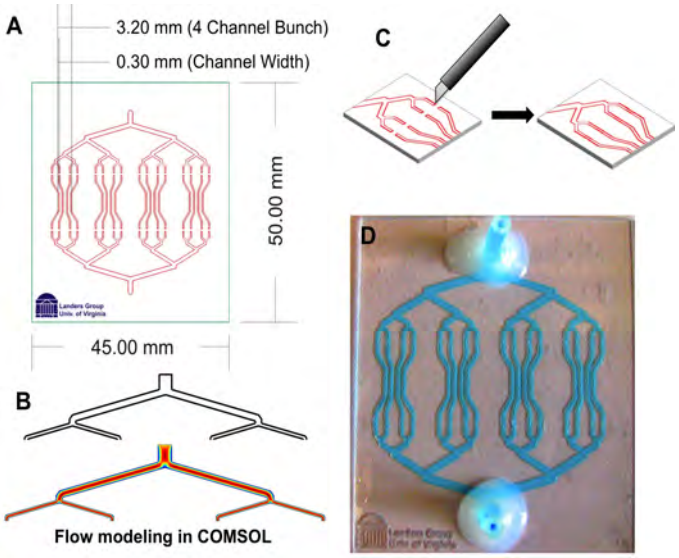

Figure 4.8. Stencil method for creating closed-loop fluidic architectures of constant channel cross section in planar PDMS layers.

structures that create islands of material when through-cutting a planar material. During GPG device assembly, PDMS layers are annealed to a flat carrier substrate (or to the bottom layer of glass) which will maintain that 2-D alignment of PDMS structures. Small segments of solid or lightly etched material were included in the paths of microchannel to hold together material that would otherwise be completely cut apart. While the PDMS was annealed to a solid support these small solid segments occluding the microchannels were manually removed with a surgical blade. The ablation pattern for a microdevice constructed with this technique is shown in Figure 4.8A. The microfluidic architecture for this multiple bifurcated design was initially modeled in COMSOL Multiphysics software (Figure 4.8B) to choose geometry that would minimize areas of stagnant flow[41] that may cause unintended adsorption of cells and microparticles. The stencil cutting step is diagrammed in Figure 4.8C. This method was laborious and subject to heterogeneous excision of material, but it allowed for rapid prototyping of closed-loop

GPG devices that would otherwise not be possible. One completed microdevice is pictured in Figure 4.8D with fluidic connections attached and filled with blue dye for contrast.

4.3.7 Measurements of Etch Depth in Elastomers with Optical Imaging.

Measuring the depth and morphology of laser ablation in PDMS is contemplated by the compressibility of PDMS (which precluded using a micrometer) and the high deformability of PDMS (which resulted in large distortions of cross-sectional dimensions). For optical measurement of laser ablation that GPG assembly method was modified such that the etched region extended beyond the edge of the glass layers. Careful alignment of glass layers generated a planar surface at their edges, and cutting along the glass edge plane (Figure 4.9A) with a sharp blade generated smooth and undistorted cross-sections of PDMS material (Figure 4.9B,C). The structures were then photographed through microscope, and the images were quantitated using the pixel to

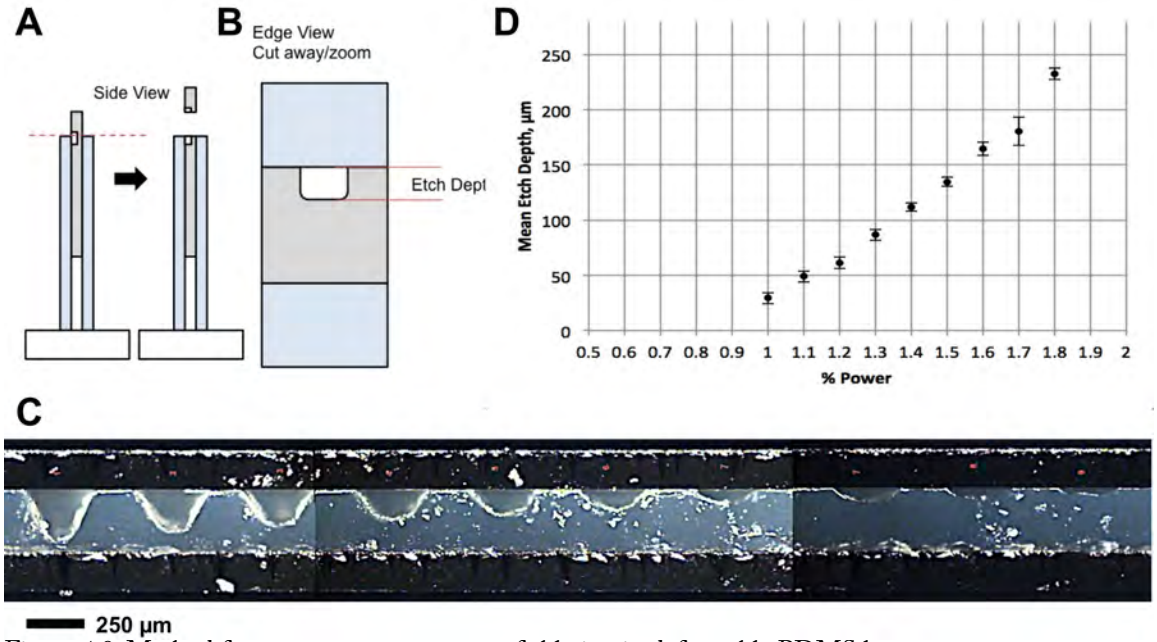

Figure 4.9. Method for accurate measurement of ablation in deformable PDMS layers.

size correlation attainable from the glass layer thickness. A representative study of laser power versus edge depth is shown in Figure 4.9D.

4.3.8 Fluidic interconnection with a gasket compression manifold.

Clamping manifolds were designed and built for making fluidic connections to GPG devices with compressible gaskets. A generalized diagram of this gasket arrangement is shown in cross-section in Figure 4.10A, and the resulting manifold is pictured in Figure 4.10B. The fragile glass access holes of GPG devices proved incompatible with most clamping manifolds, however, because devices would crack if either too much pressure was applied or if pressure was applied at a direction other than perfectly normal to the glass surface. This is because the compressible PDMS middle layer would allow the glass to flex enough to crack. After several iterations of clamping manifolds (as a graveyard of GPG devices), use of manifolds with compression gaskets was discontinued.

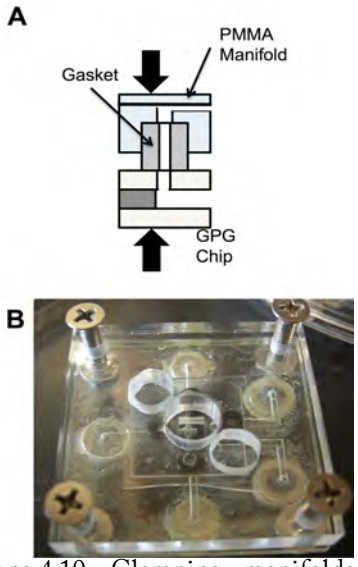

Figure 4.10. Clamping manifolds for fluidic and pneumatic connections to glass-PDMS-glass devices through compressible gaskets.

4.3.9 Closed-system thermal cycling in a glass-PDMS-glass microdevice.

The suitability of glass and PCR microdevices for PCR has been well documented, but the permeability of PDMS has been a reported source of dehydration of reaction liquid during high temperature holds. Some design modifications were required to adapt GPG devices to infrared mediated PCR technology previously developed in our laboratory.

While the glass top and bottom of the microfluidic device significantly limited dehydration (relative to the more common glass-PDMS device design), additional features had to be developed (Figure 4.11A). Micro-channels flanking the 2 heated chambers were added which, when filled with water, provided a vapor barrier against dehydration. Threading of the thermocouple into the heating reference chamber required in-plane channel extending out from the PDMS layer. When devices were left open to atmospheric pressure bubble expansion and dehydration or common. Vacuum degassing of GPG devices, along with plugging of the affixed tubing fluid connectors (Figure 4.11B) effectively pressurized the device to reduce bubble expansion. Ultimately, thermal cycling was achieved (Figure 4.11C), and this served as proof of principle for applications described in Chapter 6.

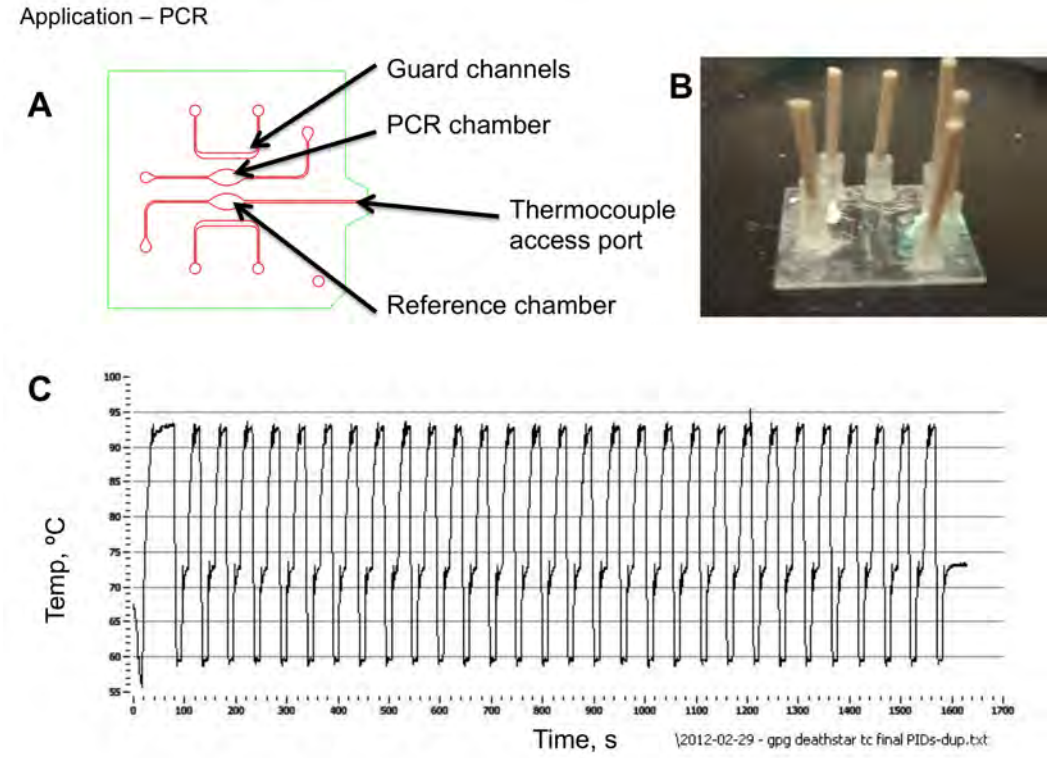

Figure 4.11. Preliminary evaluation of the compatibility between glass-PDMS-glass microfluidic device and infrared-mediated polymerase chain reaction thermal cycling.

4.3.10 Fluidic Interconnection with Magnetic Connections.

The reproducible and predictable directionality of magnetic forces was utilized for fluidic interconnections with GPG devices. As diagrammed in Figure 4.12A, toroidal magnets were fitted with silicone tubing and a thin silicone gasket. GPG devices were clamped between these magnetic fluidic connectors on additional solid support and a second magnet. This arrangement generated a compression force that was well distributed around holes in the glass and cracking was prevented. Moreover, the placement of the solid magnets could be constrained with a PMMA guide so that the magnets were perfectly aligned with the microfluidic device design. A close up view of a magnetic fluidic connector is shown in Figure 4.12B. An ancillary fluidic handling device, a pressurized micro centrifuge tube, is diagrammed in Figure 4.12C. This system of fluidic connections was successfully applied for rapid interfacing with GPG devices, obviating attachment of tubing to the devices with silicone adhesive. This development lowers the cost and time

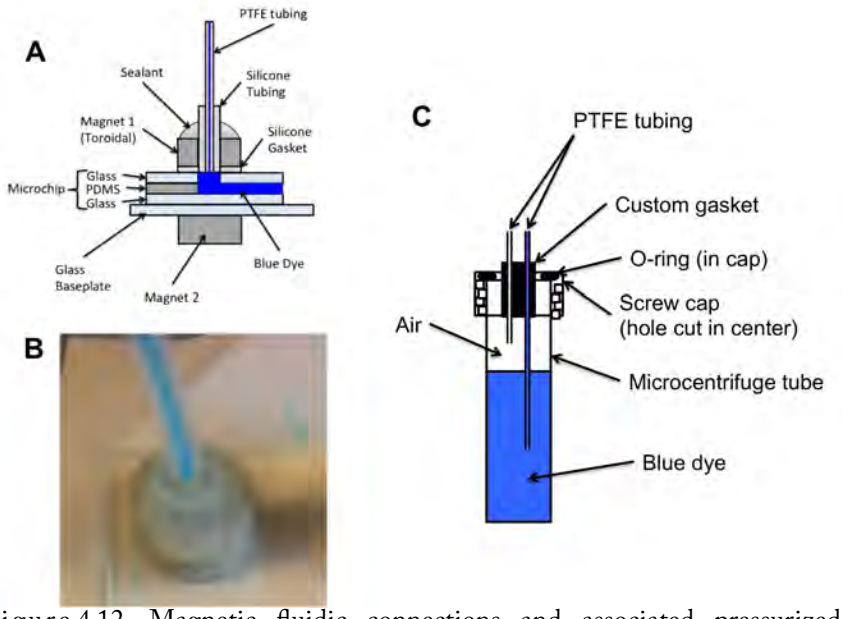

Figure 4.12. Magnetic fluidic connections and associated pressurized microcentrifuge tube device.

required for usable GPG device manufacturing, which is an important consideration for future device disposability.

4.3.11 Strategy for fabrication of PMMA microdevices.

This author, in collaboration with undergraduate researcher Michael Do, adapted a strategy of thermal PMMA bonding[40] that was suitable for device manufacturing using laser ablation. The temperature and applied force were optimized (Figure 4.13A) as prescribed in [40], but dust and debris would inevitably get trapped between the PMMA layers. This debris would cause un-bonded regions in the finished devices (Figure 4.13B). A grid-work pattern was then engraved along with the fluidic architecture (Figure 4.13C) to provide an escape path for trapped air and to allow greater flexing of the PMMA plate during bonding. This fabrication method was subsequently adopted, and further developed, by Lounsbury *et al.[8]* to conduct rapid forensic human identification via microfluidic PCR.

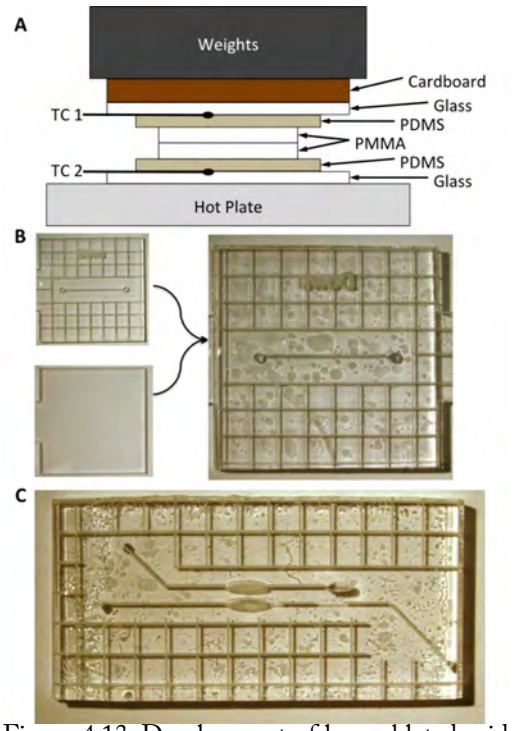

Figure 4.13. Development of laser ablated grid technique for improving thermal bonding of PMMA microfludic devices.

4.3.12 Rapidly Fabricated PDMS Devices for Neural Stem Cell Culture .

Laser ablation was investigated for creation of very narrow channels intended to guide axon growth in vitro. Conventional soft lithography methods are capable of feature sizes

on the order of a few microns Figure 4.14A, so it was unknown whether the somewhat larger channels formed by laser ablation would still adequately exclude neuron cell bodies from the narrow channels dividing 2 microchannels. Cross channels were ablated in the dividing wall between 2 chamber using a vector pattern (Figure 4.14B) or a raster pattern set to low vertical density (not shown). Early versions of the device were made using only the thin PDMS described thus far, but buckling was observed. Therefore, cast PDMS was incorporated in the fabrication scheme as diagrammed in Figure 4.14C. Surprisingly, the spacing fidelity of cross channels was better for raster patterns than for vector graphics. This is most likely due to slippage during abrupt movements of sequential vector etching as opposed to the more fluid raster pattern engraving where the y stepper motor was continuously engaged. Visual evaluations of etch depth were used to minimize etch depth while maximizing channel reproducibility. Subsequently, SEM imaging was performed (Figure 4.15) for more detailed characterization. Lastly, in vitro testing of prototype devices was conducted by Prof. Chris Deppmann and Mr. Chris Dawson, as shown in Figure 4.16. The laser fabricated devices did appear to exclude the neural cell bodies, but axons were not strictly guided down the channels due to incomplete bonding

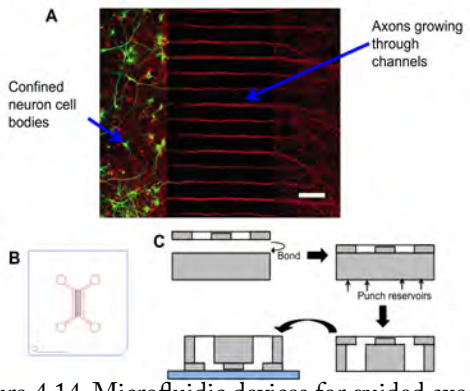

Figure 4.14. Microfluidic devices for guided axon growth.

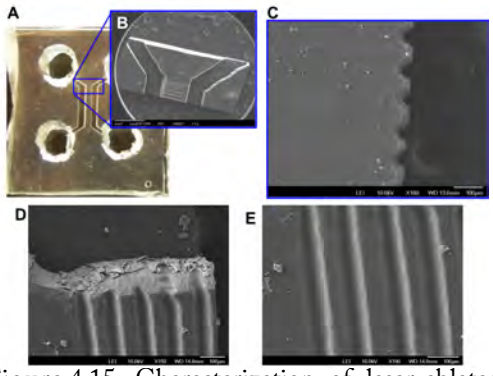

Figure 4.15. Characterization of laser-ablated devices for neuron culture using SEM imaging.

between the glass and PDMS. These studies constitute a potential path to rapid and very low cost manufacture of devices for microfluidic-enabled neurobiology research.

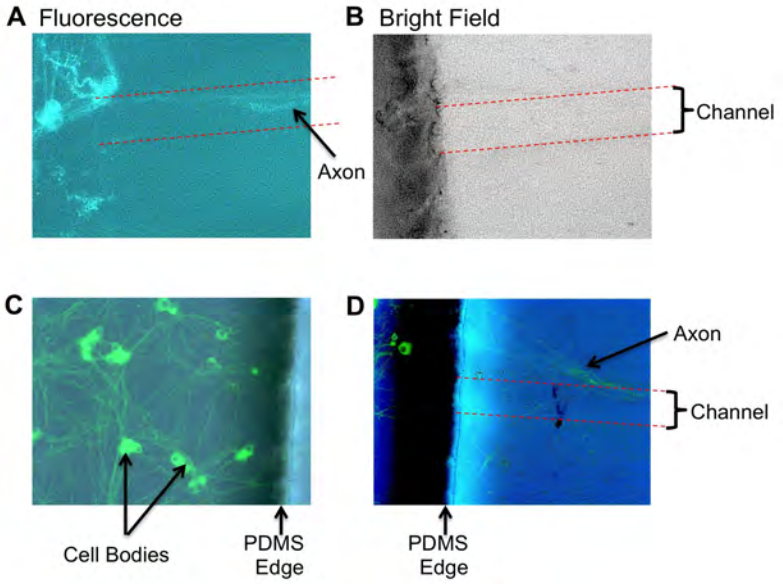

Figure 4.16. Culture of rat primary neuronal stem cells in laser-fabricatied microfluidic devices.

4.3.13 Diagram of laser ablated normally open valve.

The typical geometry of a "push-down" pneumatic microfluidic valve is shown in Figure 4.17. Rounded channels are required for these valves, wherein a semicircular channel is pushed down so it collapses against the channel floor and seals off the channel. These valves will not close completely when the channels are not rounded, such as in standard soft lithography (square channels) or standard laser ablation (parabolic channels), and thus valves with these sub-optimal geometry are leaky. Furthermore, the thickness of

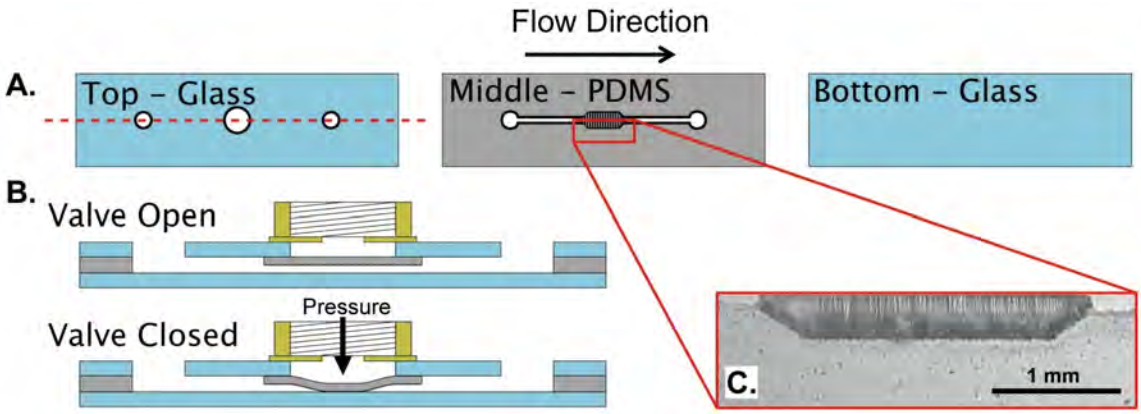

Figure 4.17. Operational principle for laser ablated push-down valve.

PDMS elastomer between the control and fluidic channels was critical because the pressure required to close the valve is prohibitively high if the membrane is too thick, and membrane failure with fluid leakage was observed if the membrane was too thin. To close the valve, the region above the membrane and fluidic channel was pressurized, and this causes the membrane to deflect downward and pinch off the microchannel.

4.3.14 Calculation of 3D Etching Settings for Laser Engraver Digitizer.

Fabrication of rounded microfluidic channels and a double-sided ablation procedure were developed via iterative design. The 3D engraving mode of the laser cutter was used to dynamically adjust the laser power during translation across the microvalve footprint, so a gradient of laser power was used to etch the valve channels. The edges of the valve channels were etched with lower laser power and the power was tapered up to a maximum in the center of the channel to produce a rounded channel of any width. Motion system non-idealities such as slippage and warped ablation lines were observed at speed settings above 2%.

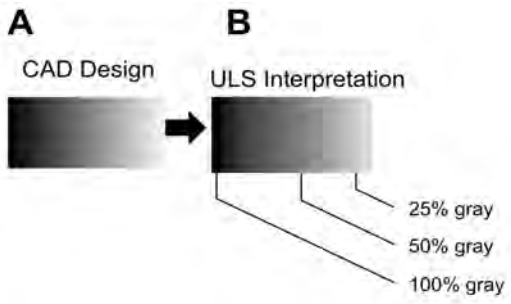

Figure 4.18. Illustration of digitization of grayscale color space.

Table 1. Optimized settings for ablation of PDMS using the 3D feature of the UniversalLaser Systems Advanced control software.

White:Black	Number	Percent Gray	Digitized Power Level
black	15	100.00	2
31:255	14	95.00	1.9
47:255	13	90.00	1.8
63:255	12	85.00	1.7
79:255	11	80.00	1.6
95:255	10	75.00	1.5
111:255	9	70.00	1.4
127:255	8	65.00	1.3
143:255	7	60.00	1.2
159:255	6	55.00	1.1
175:255	5	50.00	1
191:255	4	45.00	0.9
207:255	3	40.00	0.8
223:255	2	35.00	0.7
239:255	1	30.00	0.6
white	0		0

Reduction of laser debris was achieved by modification of the air assist cone with a custom extender to deliver greater gas flow to the ablation site. Using speed settings for optimal beam translation, the maximum power setting before completely burning through the PDMS material was 2%. Thus, the laser power was programmed by using different shades of gray in the CAD design (Figure 4.18A,B) in a descending series from 2% power. Unexpected bunching of etch depth were initially observed, which is hypothesized to a result of digitization errors in the laser engraver power modulation circuitry. That is, gray levels were constrained to 0.1% power steps, and interpretation of the continuous gradient CAD design resulted in large blocks of equal depth. To better control the spacing of power modulation steps, the engraver settings were adjusted to properly match up the shades of gray specified to the 0.1% power step size of the laser power digitizer (**Table 1)**.

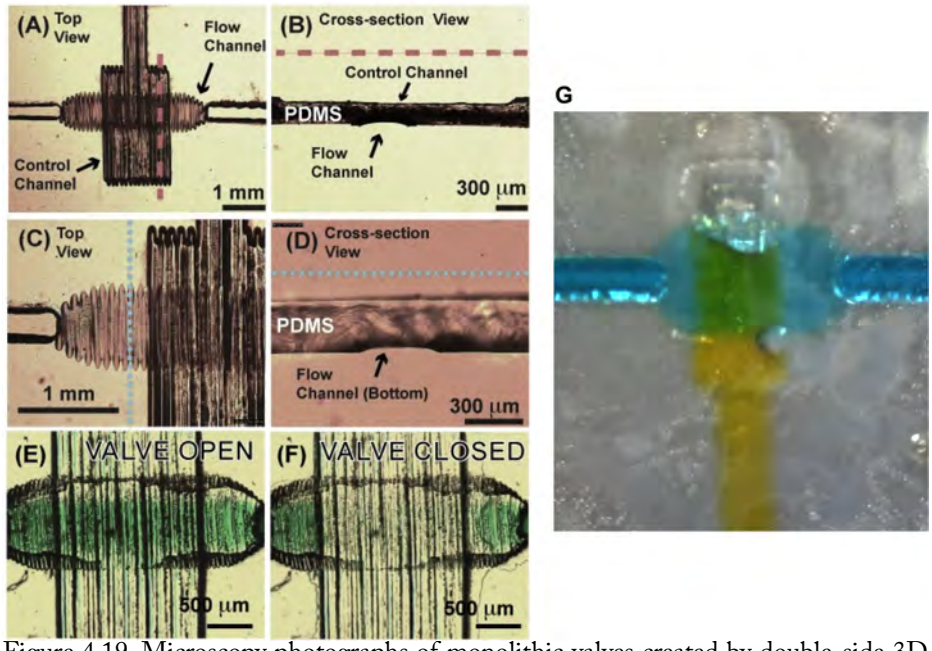

Figure 4.19. Microscopy photographs of monolithic valves created by double-side 3D laser ablation.

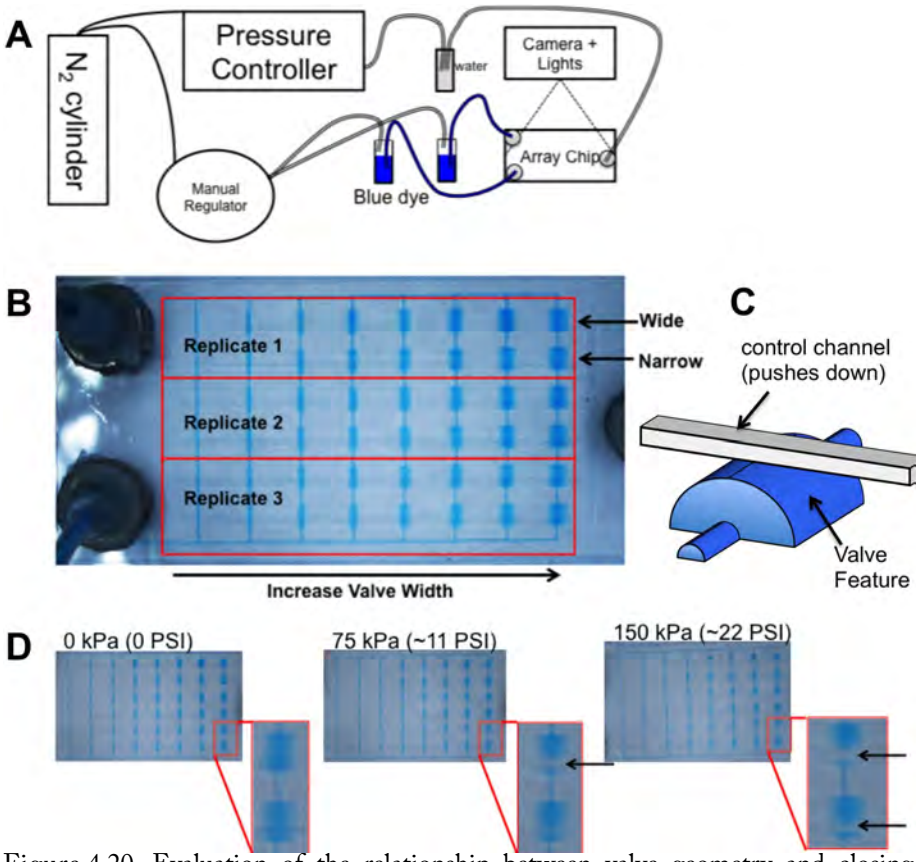

Figure 4.20. Evaluation of the relationship between valve geometry and closing pressures.

Initial characterization of the valve architecture are shown in Figure 4.19, but the possible range of deflections, volume, and control pressures of the valves was unknown. Computer modeling of structural dynamics in 3D elastomeric structures is notoriously difficult (due to complex 3D geometry and various non-linear phenomena), so an empirical testing strategy was devised to correlate microstructure geometry to valve performance. A range of valve and control channel geometries were simultaneously using the experimental setup diagrammed in Figure 4.20**A**. An array of 48 valves were fabricated on a 25 mm x 50 mm footprint Figure 4.20**B**, and. I found a trend in the pressures at which individual valves in the array would close. As shown in Figure 4.20**C**,

all valves were open when no pressure was applied, but as increasing amounts of pressure were applied valves can be seen to close (indicated by arrows in Figure 4.20**D** insets). Using these data on functional valve geometry, it will be now be possible to build the next generation of these devices and utilize their ability to precisely control movement of fluid in a microfluidic device.

4.4 Conclusions and Future Studies

Techniques for fabrication of microfluidic devices using CO_2 laser ablation were developed for multiple substrate materials and for multiple applications. These findings have significantly enabled research efforts described in the remaining chapters of this thesis, and the author hopes that public disclosure in scientific publications will allow a diverse set of researchers to utilize equipment already in place at their institutions to apply microfluidic technologies to research problems that benefit society at large.

4.5 Contributions

GPG fabrication and development: Michael Do

SEM imaging: Dr. Chris Jacobs (and Dr. Erkin Şeker, (data not shown))

Valve co-development: Murali Ghatkesar, Jon Armstrong

Teflon electrode fabrication: Alex Zestos, Dr. Chris Jacobs, et al.

Neurochip fabrication and development: Jon Armstrong; Neurochip evaluation with primary rat neuron cultures: Chris Deppmann, Chris Dawson

4.6 References

[1] R. Schaeffer, Fundamentals of Laser Micromachining, CRC Press, 2012.

[2] T. Chen, R.B. Darling, Fundamentals of Laser Ablation of the Materials Used in Microfluiducs, in: M. Kahrizi (Ed.), Micromach. Tech. Fabr. Micro Nano Struct.,

InTech, 2012. doi:10.5772/1364.

[3] I. Universal Laser Systems, Single-Resonator Lasers Spec Sheet (for ULR50), (n.d.).

[4] M.S. Brown, C.B. Arnold, Laser Precision Microfabrication, in: K. Sugioka, M. Meunier, A. Piqué (Eds.), Laser Precis. Microfabr., Springer Berlin Heidelberg, Berlin, Heidelberg, 2010: pp. 91–120. doi:10.1007/978-3-642-10523-4.

[5] C.K. Chung, S.L. Lin, On the fabrication of minimizing bulges and reducing the feature dimensions of microchannels using novel CO 2 laser micromachining, J. Micromechanics Microengineering. 21 (2011) 065023. doi:10.1088/0960-1317/21/6/065023.

[6] Y.C. Yap, R.M. Guijt, T.C. Dickson, A.E. King, M.C. Breadmore, Stainless steel pinholes for fast fabrication of high-performance microchip electrophoresis devices by CO2 laser ablation., Anal. Chem. 85 (2013) 10051–6. doi:10.1021/ac402631g.

[7] M.F. Jensen, M. Noerholm, L.H. Christensen, O. Geschke, Microstructure fabrication with a CO2 laser system: characterization and fabrication of cavities produced by raster scanning of the laser beam., Lab Chip. 3 (2003) 302–7. doi:10.1039/b308153b.

[8] J.A. Lounsbury, B.L. Poe, M. Do, J.P. Landers, Laser-ablated poly(methyl methacrylate) microdevices for sub-microliter DNA amplification suitable for micro-total analysis systems, J. Micromechanics Microengineering. 22 (2012) 085006. doi:10.1088/0960-1317/22/8/085006.

[9] M.I. Mohammed, M.P.Y. Desmulliez, The manufacturing of packaged capillary action microfluidic systems by means of CO2 laser processing, Microsyst. Technol. 19 (2013) 809–818. doi:10.1007/s00542-013-1792-1.

[10] Y. Sun, Y.C. Kwok, Polymeric microfluidic system for DNA analysis., Anal. Chim. Acta. 556 (2006) 80–96. doi:10.1016/j.aca.2005.09.035.

[11] V. Sunkara, D.-K. Park, H. Hwang, R. Chantiwas, S. a. Soper, Y.-K. Cho, Simple room temperature bonding of thermoplastics and poly(dimethylsiloxane), Lab Chip. (2011). doi:10.1039/c0lc00272k.

[12] K.S. Lee, R.J. Ram, Plastic-PDMS bonding for high pressure hydrolytically stable active microfluidics., Lab Chip. 9 (2009) 1618–24. doi:10.1039/b820924c.

[13] J. Ni, S. Shi, J. Gu, T. Yamabe, Fabrication quality of glass microfluidic chips, Inf. Autom. …. (2010) 1500–1503.

[14] C.K. Chung, Y.C. Sung, G.R. Huang, E.J. Hsiao, W.H. Lin, S.L. Lin, Crackless

linear through-wafer etching of Pyrex glass using liquid-assisted CO2 laser processing, Appl. Phys. A. 94 (2008) 927–932. doi:10.1007/s00339-008-4863-x.

[15] C.K. Chung, H.C. Chang, T.R. Shih, S.L. Lin, E.J. Hsiao, Y.S. Chen, et al., Water-assisted CO(2) laser ablated glass and modified thermal bonding for capillary-driven bio-fluidic application., Biomed. Microdevices. 12 (2010) 107–14. doi:10.1007/s10544-009-9365-x.

[16] G. a J. Markillie, H.J. Baker, F.J. Villarreal, D.R. Hall, Effect of vaporization and melt ejection on laser machining of silica glass micro-optical components., Appl. Opt. 41 (2002) 5660–7.

[17] J.-Y. Cheng, C.-J. Hsieh, Y.-C. Chuang, J.-R. Hsieh, Performing microchannel temperature cycling reactions using reciprocating reagent shuttling along a radial temperature gradient., Analyst. 130 (2005) 931–40. doi:10.1039/b501061f.

[18] J.P. Landers, ed., Handbook of Capillary and Microchip Electrophoresis and Associated Microtechniques, Third Edition, 3rd ed., CRC Press, 2007.

[19] C. a Baker, R. Bulloch, M.G. Roper, Comparison of separation performance of laser-ablated and wet-etched microfluidic devices., Anal. Bioanal. Chem. 399 (2011) 1473–9. doi:10.1007/s00216-010-4144-3.

[20] L.C. Ozcan, V. Treanton, R. Kashyap, L. Martinu, High-Quality Flat-Top Micromachining of Silica by a CW CO<formula formulatype="inline"><tex>$_{2}$</tex></formula> Laser, IEEE Photonics Technol. Lett. 19 (2007) 459–461. doi:10.1109/LPT.2007.893044.

[21] E.M. Tolstopyatov, Ablation of polytetrafluoroethylene using a continuous CO 2 laser beam, J. Phys. D. Appl. Phys. 38 (2005) 1993–1999. doi:10.1088/0022-3727/38/12/021.

[22] A.G. Zestos, M.D. Nguyen, B.L. Poe, C.B. Jacobs, B.J. Venton, Epoxy insulated carbon fiber and carbon nanotube fiber microelectrodes, Sensors Actuators B Chem. 182 (2013) 652–658. doi:10.1016/j.snb.2013.03.066.

[23] B. a Fogarty, K.E. Heppert, T.J. Cory, K.R. Hulbutta, R.S. Martin, S.M. Lunte, Rapid fabrication of poly(dimethylsiloxane)-based microchip capillary electrophoresis devices using CO2 laser ablation., Analyst. 130 (2005) 924–30. doi:10.1039/b418299e.

[24] L. Wang, R. Kodzius, X. Yi, S. Li, Y.S. Hui, W. Wen, Prototyping chips in minutes: Direct Laser Plotting (DLP) of functional microfluidic structures, Sensors Actuators B Chem. 168 (2012) 214–222. doi:10.1016/j.snb.2012.04.011.

[25] M. Li, S. Li, J. Wu, W. Wen, W. Li, G. Alici, A simple and cost-effective method for fabrication of integrated electronic-microfluidic devices using a laser-patterned PDMS layer, Microfluid. Nanofluidics. 12 (2011) 751–760. doi:10.1007/s10404-011-0917-z.

[26] H.-B. Liu, H.-Q. Gong, Templateless prototyping of polydimethylsiloxane microfluidic structures using a pulsed CO 2 laser, J. Micromechanics Microengineering. 19 (2009) 037002. doi:10.1088/0960-1317/19/3/037002.

[27] M.. T. Khorasani, H. Mirzadeh, P.. G. Sammes, Laser surface modification of polymers to improve biocompatibility: HEMA grafted PDMS , in vitro assay-III, Radiat. Phys. Chem. 55 (1999) 685–689. doi:10.1016/S0969-806X(99)00212-1.

[28] M.J. Owen, Why Silicones Behave Funny, Société royale de chimie, n.d.

[29] J.C. McDonald, G.M. Whitesides, Poly(dimethylsiloxane) as a material for fabricating microfluidic devices., Acc. Chem. Res. 35 (2002) 491–9.

[30] A. Ranjitprakash, S. Adamia, V. Sieben, P. Pilarski, L. Pilarski, C.J. Backhouse, Small volume PCR in PDMS biochips with integrated fluid control and vapour barrier, Sensors Actuators B Chem. 113 (2006) 398–409. doi:10.1016/j.snb.2005.03.049.

[31] A. Plecis, Y. Chen, Fabrication of microfluidic devices based on glass–PDMS–glass technology, Microelectron. Eng. 84 (2007) 1265–1269. doi:10.1016/j.mee.2007.01.276.

[32] D.W. Inglis, A method for reducing pressure-induced deformation in silicone microfluidics., Biomicrofluidics. 4 (2010) 1–8. doi:10.1063/1.3431715.

[33] J. Hultström, O. Manneberg, K. Dopf, H.M. Hertz, H. Brismar, M. Wiklund, Proliferation and viability of adherent cells manipulated by standing-wave ultrasound in a microfluidic chip., Ultrasound Med. Biol. 33 (2007) 145–51. doi:10.1016/j.ultrasmedbio.2006.07.024.

[34] K. Chau, B. Millare, A. Lin, S. Upadhyayula, V. Nuñez, H. Xu, et al., Dependence of the quality of adhesion between poly(dimethylsiloxane) and glass surfaces on the composition of the oxidizing plasma, Microfluid. Nanofluidics. 10 (2010) 907–917. doi:10.1007/s10404-010-0724-y.

[35] D. Hurd, R. Osthoff, M. Corrin, The Mechanism of the Base-catalyzed Rearrangement of Organopolysiloxanes1, … Am. Chem. Soc. 943 (1954) 9–12.

[36] J.W. Krumpfer, T.J. McCarthy, Rediscovering silicones: “unreactive” silicones react with inorganic surfaces., Langmuir. 27 (2011) 11514–9. doi:10.1021/la202583w.

[37] I. Hoek, F. Tho, W.M. Arnold, Sodium hydroxide treatment of PDMS based microfluidic devices., Lab Chip. 10 (2010) 2283–5. doi:10.1039/c004769d.

[38] A.K. Soe, S. Nahavandi, K. Khoshmanesh, Neuroscience goes on a chip., Biosens. Bioelectron. 35 (2012) 1–13. doi:10.1016/j.bios.2012.02.012.

[39] J.R. Anderson, D.T. Chiu, R.J. Jackman, O. Cherniavskaya, J.C. McDonald, H. Wu, et al., Fabrication of topologically complex three-dimensional microfluidic systems in PDMS by rapid prototyping., Anal. Chem. 72 (2000) 3158–64.

[40] Y. Sun, Y.C. Kwok, N.-T. Nguyen, Low-pressure, high-temperature thermal bonding of polymeric microfluidic devices and their applications for electrophoretic separation, J. Micromechanics Microengineering. 16 (2006) 1681–1688. doi:10.1088/0960-1317/16/8/033.

[41] V. Janakiraman, S. Sastry, J.R. Kadambi, H. Baskaran, Experimental investigation and computational modeling of hydrodynamics in bifurcating microchannels., Biomed. Microdevices. 10 (2008) 355–65. doi:10.1007/s10544-007-9143-6.

5. Ultrasonic Trapping and Analysis of Foodborne Pathogens

5.1. Abstract

In this work, bacterial foodborne pathogens (*Escherichia coli, Salmonella enterics serovar enteriditis*, and *Listeria monocytogenes*) were acoustically-trapped as an enrichment step prior to genetic analysis via the polymerase chain reaction (PCR). Acoustic trapping was performed in microfluidic devices capable of ultra-rapid infrared-mediated PCR, thereby demonstrating the multifunctionality of these devices. Low-cost, rapidly-fabricated microfluidic devices were also used for acoustic trapping. Miniaturized (1 mm^2) piezoelectric transducers were fabricated from widely-available and inexpensive materials in a simple bench-top method. Electrical characterization and computer modeling of the microfluidic acoustic trapping system was performed. Microbeads were used to assess trapping efficiency as a function of particle size and flow rate. Individually trapped microbeads were used to determine the maximum sustainable flow rate as a function of particle size. These developments lay the groundwork for a viable system for acoustic trapping of foodborne pathogens that could be incorporated into future microfluidic genetic analyzers for pathogen detection.

5.2. Introduction

The economic cost of food-borne illness in the United States alone was recently estimated at $51 to 77 billion dollars annually[1], and efforts for an international estimate are underway[2]. The medical expenses, lost productivity, and lost lives due to foodborne illness are a major societal problem, so technologies that prevent outbreaks of food-borne pathogens are in high demand. Polymerase chain reaction (PCR) assays offer specific and sensitive detection of bacterial pathogens like *Escherichia coli O157:H7*, but they are dependent upon upstream sample concentration steps[3]. Microfluidic devices are an attractive platform for genetic analysis because they offer reduced reagent consumption, facile optical access, reduced instrumentation footprint, and integration of multiple analytical processes. Conventional cell concentration processes such as centrifugation and filtration are hard to implement in microfluidic systems due to physical and logistical limitations. Conversely, the unique physics of microsystems opens new avenues for microparticle trapping. Acoustofluidic handling of micron-sized species is a promising method because micron-scale particles are vital to many biotechnology applications, and this report describes the development of such a system [4].

Microfluidic-based microparticle trapping methods are an active area of research because the unique physics of microfluidic system enables a range of novel techniques. Conventional methods of cell and microparticle handling such as centrifugation, filtration, and magnetic manipulation are powerful and convenient in traditional lab settings. However, these methods can become cost- and time-prohibitive in emerging bioanalytical settings such as on-site testing when large equipment are required or many

manual steps are required[5,6].

A variety of microfluidic cell/microparticle trapping methods have been developed, including dielectrophoresis[7], functionally-coated magnetic beads[8], optical tweezers[9], hydrodynamic[10], centrifugal forces[11], and acoustofluidic manipulation[12,13]. The optimal trapping solution depends on the desired application, and a more detailed review of microfluidic cell trapping methods was recently published by Gao *et al. [14]*. Acoustic trapping is attractive for a number of reasons including non-destructive handling of cells, lack of consumable filters, and straightforward integration with advanced techniques such as fluorescence microscopy[15] and MADLI-TOF[16].

Microfluidic devices can serve as acoustic resonators when they are actuated with MHz range ultrasound. Ultrasonic standing waves (USW) can be established in water-filled cavities when the wavelength of the ultrasound excitation corresponds to a multiple of the half-wavelength of sound in the liquid medium (Figure 5.1A-G). For example, the speed of sound in water is roughly 1500 m/s, so a 6 MHz sound wave will have a wavelength (λ) of 250 μm, and thus, a 125 μm tall ($\lambda/2$) water filled cavity will resonate at ~6 MHz. Particles within an acoustic field will experience a force axial to the direction of sound propagation known as the primary acoustic radiation force, F_{prf}. As presented in [17], and shown in Eq. 5.1, this force will cause microparticles that are denser and/or less compressible than the surrounding medium (typically the case for cells and microspheres) will experience a force towards the pressure nodes within an ultrasonic standing wave. Gradients of pressure amplitude orthogonal to the axis of beam propagation often arise when localized or focused transducers are used, and these lateral gradients give rise to a trapping force[18], F_{Lat} (Eq. 5.2). Microparticles that are co-trapped in the same pressure

nodal plane will experience secondary acoustic forces that attract the particle towards each other, F_{Sec} (Eq. 5.3). This attractive force holds particles to the particle aggregate, thereby increasing the effective volume of the trapped particle (and thus the primary and

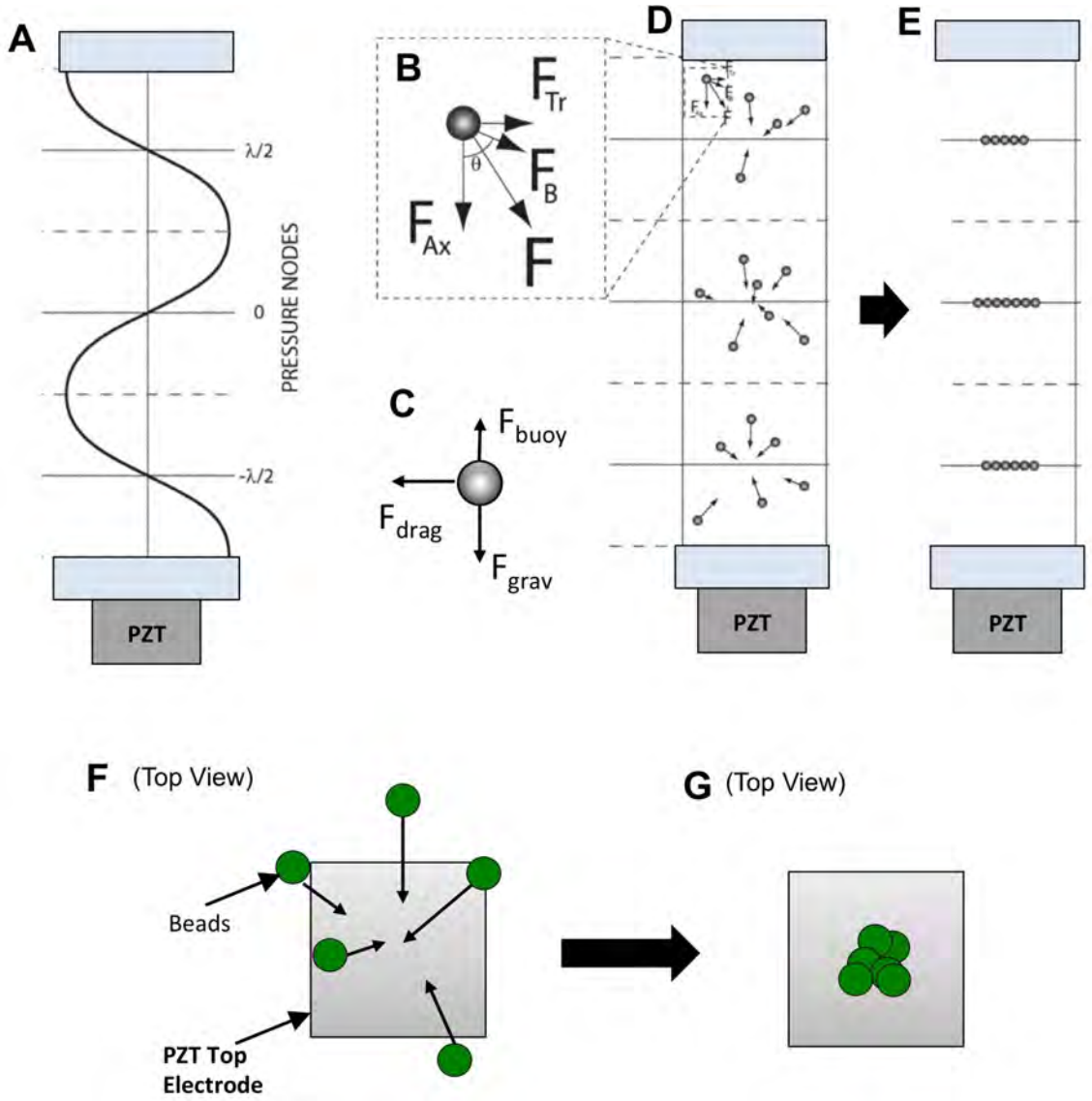

Figure 5.1: Sinusoidal representation of an ultrasonic standing wave. B. Free body diagram for a microparticle in the beginning stages of acoustic trapping. F = sum of forces on particle (F_{AX} = acoustic radiation force along propagation axis of the standing wave; F_{Tr} = Transverse (lateral) trapping forces; F_B = inter-particle (Bjerknes) forces) C. Additional, non-acoustic forces acting on particles (F_{grav} = gravitational force, F_{buoy} = buoyant force, F_{drag} = viscous drag force) D,E. The initiation of acoustic trapping is diagramed here in side view (C). The spacing of the nodal planes in the ultrasonic standing wave correspond to multiples of one half the wavelength the ultrasonic standing wave. F,G. A simplified diagram of the trapping process as viewed from above (i.e., as viewed through a microscope). (Panels A,B, D and E adapted from [70].)

lateral acoustic forces) and makes trapped particles less prone to loss by viscous drag. Moreover, additional incoming particles are trapped more strongly than they would be without these attractive secondary forces. Continuous application of ultrasound in microfluidic devices has been shown to induce steady state circular flows[19]. These gyres can either aid trapping by increasing the residence time of microparticles as the traverse the ultrasonic trap, or they can hinder trapping by carrying away particles when acoustic forces are too weak. Trapping occurs when the combination of forces directing particles toward the pressure nodes of the acoustic trap exceed the Stokes drag force, F_{Drag} (Eq. 5.4) of the flowing sample medium. Retaining particles against flow is the basis of acoustic trapping performed here, and accumulation of particles over time can concentrate particles. Acoustic forces scale with the particle volume (i.e., radius^3) while viscous drag scales with the radius, and therefore smaller particles (especially sub-μm) are more difficult to trap using acoustic forces.

Piezoelectric transducers, such as those made from lead zirconium titanate (PZT) have been patterned into small footprints[20] or diced from larger PZT discs [21–23]. Transducers may be permanently glued to microfluidic devices (e.g., [23]), or reversibly coupled to microdevices [24]. The manufacture of miniature transducers has typically been conducted in cleanroom environments, yet a bench-top fabrication method is described here. Piezoelectric elements for ultrasound emission are driven by an oscillating signal in the MHz range that is generated by an electronic waveform generator. The driving voltage applied to transducers can be increased for greater output of acoustic energy, yet increased voltage results in greater heat generation that can become problematic. Effective acoustic trapping has been achieved in systems where the

transducer comprised part of the microfluidic channel (e.g. [20,25–27]. Another acoustic trapping method wherein the microfluidic device contents directly contact the transducer is in surface acoustic waves (SAW) trapping systems; while SAW devices have been demonstrated as an effective particle manipulation strategy[28], this technique is sufficiently different to lie outside the scope of this paper. Transducers that are exposed to the sample present difficulties with sample carry-over contamination. Small, localized transducers are often incorporated into a printed circuit boards for support and electrical connections. In this report, we describe a PCB transducer that is compact and capable or precise positioning to make contact with microfluidic device.

Fully-enclosed microfluidic devices are ideal for preventing sample carry-over, but the ultrasound must travel through an intermediate layer (often call the carrier layer) between the transducer and the water-filled cavity. Glass is a popular material because it has low acoustic impedance, optical clarity, generally low cost, and well-established microfabrication methods. Optimal transfer of acoustic energy has been the subject of modeling and experimentation, and a thin layer of glass that is $\lambda/4$ has been shown to be optimal[23,29,30][31]. It should be noted however that acoustic trapping is still possible if the $\lambda/4$ resonance condition is not met in the carrier layer, but the strength of the resonance for the whole system is decreased[31]. Glass capillaries are excellent devices for acoustic trapping (e.g., [24,32,33],) because they have thin glass walls and are inexpensive. Freestanding bridge structures within a glass microfluidic device[34] are a good analog to capillaries in vertical resonance, with the additional possibility of confocal chambers and facile monolithic integration with other microfluidic architecture. Confocal resonators have been shown to be an effective trapping geometry[35,36].

Layered acoustic resonators have also been developed with the inexpensive silicone elastomer polydimethylsiloxane (PDMS) as a spacing layer [27,37,38]. PDMS is a good interlayer because it bonds well to glass [39], and because microfluidic architecture can be readily created in PDMS by soft lithography [40] or etching channels into featureless PDMS by methods including computer controlled cutting[38] and laser ablation(e.g., [41]and **Chapter 4**). PDMS can be used for active fluidic control via valves and pumps(e.g., [42] and **Chapter 4**), which could facilitate integration between acoustic trapping and other microfluidic functions. As a bulk material, PDMS is prone to solvent-induced swelling [43], so care must be taken to avoid swelling-inducing solvents. The thermal expansion of the PDMS[44] interlayer is predicted to be on the order of a micron for a PDMS part that is 230 μm thick 25 °C to 40 °C, which is manageable at a steady state temperature. PDMS is also gas-permeable, which can be exploited to actually remove air bubbles through the PDMS bulk[45]. Most importantly though, glass-PDMS-glass (GPG) layered acoustic resonators are effective for acoustic trapping.

Where piezoelectric elements convert mechanical energy to and from electrical potential, electrical characterization by measuring the admittance as a function of frequency can reveal important information about both the transducer and the acoustic resonator system as a whole[46]. Measurement of the transfer function versus frequency identifies system resonances at characteristic frequencies, and the strength of these resonances can be determined by their Q factors, a quantitative evaluation of resonance. In most cases a narrow, high magnitude resonance peak (i.e., a high Q value) is desirable because the high amplitudes should be achievable when the system is driven precisely at its resonant frequency. Conversely, a broader resonance peak, while having a lower Q

value, is less sensitive to deviations between the driving frequency and the resonance peak maximum frequency. The most efficient transfer of energy to the water-filled cavity will occur when the cavity's resonant frequency is close to (but not identical to) the resonance of the transducer [47].

Microfluidic acoustic resonators must be driven at specific frequencies for optimal performance, and methods such as electrical characterization, finite element modeling, and empirical testing of microparticle manipulation all contribute to effective system characterization. Resonant frequencies of the system can be roughly predicted using 1D modeling of the resonances or more precisely using 2D finite element analysis modeling[48][31]. Empirical trapping of microbeads is another vital tool for characterizing an acoustic trapping systems. The arrangement of beads maps out the pressure nodes of the acoustic field, discernible either by direct microscopic observation or advanced techniques such as particle image velocimetry [49] or optical focus analysis[50]. Furthermore, microbeads can be used to determine performance metrics such as trapping efficiency and sample throughput capability. To characterize this acoustic trapping system we used electrical analysis, modeling, and observation of bead behavior in the acoustic trap.

While the physical dimensions of a single microfluidic acoustic trap are small (~10-100 μm across, as discussed in **Chapter 1**), several techniques exist for parallel or expanded trapping for increased sample throughput and/or greater control over trap contents. Perhaps the most direct approach to parallel acoustic trapping is to have multiple separate transducers [51] or array controlled [52,53]. Despite the utility of such arrays of active trapping sites, practical limitations on driving power and resonance

matching can be non-trivial difficulties. Another strategy increasing the number of trapping sites within a given volume of fluid is to use higher order harmonic modes with multiple nodes across the fluidic channel[54] or phase modulation to set up complex patterns of multiple trapping sites [55]. The trapping devices described here were typically operated in the first harmonic mode with two vertical nodes spanning the fluidic channel. In this report we describe another method of acoustic trapping in parallel where several parallel channels in a GPG microdevices were excited by a strip of PZT. The differences in sound propagation between water and the PDMS channels were predicted to allow for water-centered vertical trapping nodes for parallel acoustic trapping.

Several authors have reported that trapping efficiencies of microparticles decrease rapidly below approximately 1 μm (e.g., [49][56]. The acoustic forces scale with particle volumes while viscous drag scales with radius, and at particle dimensions on the order of a micron these forces are believed to cancel out and preclude trapping. Nonetheless, a number of reports have described ultrasound-mediated accretion of bacteria in multi-wavelength resonators [57,58]. Recently, Hammarström, Laurell and Nilsson demonstrated that sub-micron particles, including *E. coli* cells, could be readily trapped using 4 MHz ultrasound and *E. coli* concentrations above 5 x 10^4 cells/μL (and at significantly lower concentrations when larger seed particles were used)[32]. It has also been reported that at higher frequencies (and, coincidentally, with more standing nodes) the acoustic trapping of 400 nm particle transitioned from a streaming-dominated regime at 2.11 MHz to an acoustic force-dominated regime at 7.21 MHz where aggregation in pressure nodes was apparent[19]. In this work we show that bacterial foodborne pathogens were acoustically trapped.

Eq. 5.1

$$F_{\mathrm{Axi}} = -V_{\mathrm{p}} \cdot E_{\mathrm{ac}} \cdot k \cdot \Phi \cdot \sin(2kx)$$

$V_p = (4/3)\pi(r_p)^3$

$$\Phi = \left(\frac{3(\rho_p - \rho_m)}{\rho_m + 2\rho_p} + \frac{\beta_m - \beta_p}{\beta_m} \right)$$

Eq. 5.2

$$F_{\mathrm{Lat}} = V_{\mathrm{p}} \nabla E_{\mathrm{ac}} \left(\frac{3(\rho_p - \rho_m)}{\rho_m + 2\rho_p} \cos^2(kx) - \frac{\beta_m - \beta_p}{\beta_m} \sin^2(kx) \right)$$

Eq. 5.3

$$F_{\mathrm{Sec}} = 4\pi a^6 \left\{ \frac{(\rho_p - \rho_m)^2 (3\cos^2\theta - 1)}{6\rho_m d^4} v^2(x) - \frac{\omega^2 \rho_m (\beta_p - \beta_m)^2}{9d^2} p^2(x) \right\}$$

Eq. 5.4

$F_{drag} = 6\pi\mu\upsilon rp$

5.3. Materials and Methods

5.3.1. Ultrasonic Transducer Fabrication and Characterization

Transducers were fashioned from lead-ziconate-titanate (PZT) piezoelectric ceramic disks with thickness resonance at either 6 MHz (PZ26, Ferroperm Piezoceramics, Kvistgaard, Denmark). The piezoelectric disks were manually cleaved into roughly 1 mm^2 pieces by scoring with a razor blade and carefully snapping apart the pieces. The small pieces were then mounted to stock printed circuit board (PCB) with copper-ringed holes, which also provided the PZT elements with an air backing. Conductive epoxy adhesive (MG Chemicals, type 8331-14G) was used to secure the PZT to the PCB, and also to create an electrical connection to adjacent holes where wire leads were soldered. The PZT was clamped to the PCB before the epoxy cured so that the PZT was flat against the PCB surface. Once the electrical contact to the bottom electrode of the PZT was cured, non-conducting epoxy (DevCon 5-min epoxy) was spread thinly over the board to electrically isolate the bottom and sides of the PZT (but leaving the other wire lead

uncovered). Conductive epoxy was then applied from the top electrode of the PZT to the other wire lead. More non-conducting epoxy was applied to the PCB to insulate most of the second coat of conductive epoxy. Once all epoxy was cured, the PCBs were inspected and the epoxy was carefully sanded so that the PZT was the tallest feature on the PCB (to ensure proper contact with the microfluidic devices).

Completed ultrasonic transducers were characterized by transfer function spectra analysis[46]. An Agilent 8753D network analyzer was used to measure the S_{11} (reflected power/incident power) and the S_{21} (transmitted power/incident power) over a range of frequencies. Microfluidic devices were placed in contact with the actuator mounted transducers, and spectra were obtained for empty microchannels and then for water-filled microchannels. A custom application was developed in LabVIEW (National Instruments) to take data from the network analyzer and calculate the Q factor (by finding the -3 dB values) for specific resonance peaks.

Manifolds for supporting the actuator-mounted transducers and the microfluidic devices were machined from 0.25 inch thick cast polymethylmethacrylate (PMMA) (McMaster-Carr, product number 8560K355). Manifold parts were cut out via CO_2 laser ablation on a VersaLaser 350 laser engraving machine (Universal Laser Systems) using manufacturer recommended settings for PMMA, and threaded holes were tapped by hand. The pivoting actuator heads were constructed from additional laser-sculpted PMMA, nylon washers, and 8-32 machine screws. The PCB-mounted transducers were affixed to the actuator heads using epoxy (DevCon 5 Minute Epoxy).

During trapping experiments, microfluidic chips were secured to a PMMA baseplate and the actuator-mounted transducers were manually lowered into contact with

the microfluidic device. Glycerol was applied between the microfluidic device and the transducer surface to exclude air and ensure maximal transmission of acoustic energy.

5.3.2. Modeling Microfluidic Acoustic Resonators

Modeling of microfluidic acoustic resonators was utilized for both predictive power and explanative power. Simple 1D modeling of the water-filled chamber where the speed of sound, C_L = 1500 m/s and the equation $C_L = \lambda/f$ to solve for conditions where chamber height was $n*\lambda/2$. Finite element analysis modeling was conducted in the COMSOL Multiphysics package (version 4.2) using eigenfrequency studies within the Pressure Acoustics module. Cross-sectional geometries of microfluidic devices were given soft sound boundaries because the glass layers were thin [59]. For glass-PDMS-glass devices where significant material existed to either side of the water-filled channel, a subsection of the cross-sectional area was used with a plane wave boundary condition precluding reflection from the boundary that was contiguous with several millimeters of additional material and clamps. Built in material properties were used where available (using borofloat glass, silicone, and water), and the speed of sound in PDMS was given as 1020 m/s[60]. The transducer itself or a localized source of acoustic energy was not included in modeling. Meshing was set to a maximum of 10 μm to allow for adequate sampling across the acoustic wavelength in water (e.g. ~250 μm at 6 MHz). Surface plots of the total acoustic pressure were used to identify resonant modes with potential for acoustic trapping.

5.3.3. Microfluidic Device Designs and Fabrication

5.3.3.1. Low thermal mass glass microdevices

Glass confocal acoustic resonators were fabricated in borofloat glass via photolithography and isotropic chemical etching. Devices fabricated by Easley *et al.[34]* were repurposed in this work to serve as acoustic resonators. These devices feature dual chambers within a freestanding bridge structure designed to have low thermal mass for rapid heating and cooling. The bridge region (3.375 mm wide) was the point of contact for the transducer. Chambers were 1 mm across at their widest point, and 115 μm deep with 115 μm of glass above and below. Chamber depths were confirmed by extrinsic Fabry-Perot interferometry[61,62] prior to acoustic trapping studies. The elliptical shape was designed to minimize sharp geometrical features to minimize bubble nucleation sites. These devices were designed for rapid infrared-mediated polymerase chain reaction (IR-PCR), which is a low-flow application, so these devices were adapted as acoustic resonators by adding fluidic connections for syringe pump driven flow. Silicone tubing (3 mm o.d., 1.02 mm i.d., Cole Palmer, Cat No. 07625-28) was affixed with silicone adhesive (Wacker, Elastosil A-07) over the channel access holes. Low retention TFE Teflon® tubing (1.58 mm (1/16 in.) o.d., 0.3 mm i.d., Supelco, Cat. No. 58698-U) was used in all experiments to minimize microparticle losses to adsorption. The TFE fluidic tubing was pressed into the silicone tubing, held in place by constriction of the silicone tubing, and no leaking was observed during pressure-driven flow.

5.3.3.2. Rapidly fabricated glass-PDMS-glass microdevices

Laser fabrication of microfluidic architecture was investigated as a more rapid and cost effective fabrication methodology than photolithography and wet chemical etching.

Hybrid devices consisting of a polymer fluidic layer sandwiched between two glass reflectors were developed. Sheets of the silicone elastomer polydimethylsiloxane (PDMS) were purchased in thicknesses of 230 μm (nominal thickness 0.01 inches, Rogers HT-6240, Stockwell Elastomerics Inc., USA). Fluidic channels and chambers were through-cut using a CO_2 laser etching/cutting machine (VersaLaser 350, Universal Laser Systems Inc) as described in **Chapter 4**. Freshly cut devices were first cleaned with ethyl alcohol and 5 M sodium hydroxide prior to bonding. The devices were assembled using oxygen plasma activation of the PDMS surface to achieve permanent bonding to the glass acoustic reflecting layers. The carrier glass layer (between fluid and the transducer) was microscope cover glass (Fisher Finest Brand, #1.5 or #1, Fisher Scientific). The reflector glass layer was made from 0.7 mm thick borofloat glass (Schott). Access vias were drilled into this layer using a diamond tipped drill bit (Triple Ripple, C.R. Laurence Co., Inc). For some GPG devices, the glass above the trapping sites was etched down to 0.4 mm thickness using HF to improve the optical and acoustic properties of the trapping site. As described in Chapter 4, some devices were fabricated from 2 layers of coverslip glass and in that case no HF etching was required. Macro-to-micro fluidic connections were made from silicone tubing affixed with silicone adhesive.

Microfluidic architectures for trapping at a single site featured a trifurcated inlet for hydrodynamic flow focusing, and a trapping chamber that opened gradually to minimize sharp corners that could act as bubble nucleation sites (or acoustic streaming sites[19]). The wider width of the trapping chamber relative to access channels also served to slow the translational motion of the sample fluid as it passed over the trapping site, and we believe this reduced the viscous drag experienced by particles in that region.

Two schemes for multiples trapping sites in GPG devices were also tested. First, a dual chamber device was constructed with 2 isolated microfluidic domains identical to the trifurcated GPG design described above. Alternatively, a GPG device with 6 parallel microfluidic channels was tested, and the closely-spaced channels were actuated by a single long transducer. Multiple syringes were used in both cases, using a multiple syringe pump to synchronize flow across multiple trapping sites.

5.3.4. Reagents

5.3.4.1. Fluorescent microspheres

Fluorescent microspheres of various diameters were used to characterize the acoustic trapping system. All microparticles used in this work were yellow-green fluorescent microspheres of the following diameters: 2 μm (FluoSpheres, Invitrogen, F8853), 6 μm (Polysciences Inc, 17156-2), 10 μm (Spherotech, FP-10052-2), and 20 μL (Spherotech, FP-20052-5). Microspheres were typically diluted to working stocks in 0.01% TWEEN 20 (Sigma, P5927). A small magnetic stirring disc (V&P Scientific, VP724F) was placed inside the syringes containing the microsphere suspensions, and settling was counteracted by periodic manual agitation the solution with a permanent magnet.

5.3.4.2. Bacterial cell trapping studies

Escherichia coli K12 cells with plasmid-derived ampicillin resistance were cultured on agar plates at 37 ºC. For *E. coli* trapping experiments, 2-3 mm diameter colonies were swabbed from an agar plate and briefly incubated in fresh LB medium. The cells were then pelleted (90s @ 9000 rpm), washed with 1X PCR buffer, pelleted again, and resuspended in 1X PCR buffer with 0.01% v/v TWEEN for acoustic trapping. One

milliliter of this suspension was spiked with 1 μL of 5 M Syto® 11 cell-permeable fluorescent DNA-intercalating dye (Invitrogen, S7573), and spiked with 2 μm fluorescent beads (final conc. of approx. 3 beads/μL). The Syto® 11 dye caused cells to emit green light after excitation with blue light, and FITC filter sets were used for microscopy.

Acoustic trapping parameters were optimized empirically at the time of trapping and conditions are described in the results section. Samples for PCR analysis were generated by infusing the bead/cell suspension through the acoustic trap for 10 minutes at 1 μl/min and collecting the effluent. Then the transducer was turned off, and sample was infused for 1 minute at 10 μl/min while the effluent was collected into a clean microcentrifuge tube. Control samples without acoustic trapping were collected by flowing the sample through at 10 ul/min for 1 min while collecting the effluent. The dead volume from the microchamber center to the PTFE tubing outlet was ~8 μL.

Bacterial cells recovered after ultrasonic trapping were lysed and used as template material for PCR reactions. *E. coli* trapping samples were lysed by hypotonic and thermal stress during the 10 minute pre-denaturation stage of PCR. PCR primers targeting the *LamB* (*maltoporin*) gene in the *E. coli* genome (forward 5'CTG-ATC-GAA-TGG-CTG-CCA-GGC-TCC-3', reverse 5'CAA-CCA-GAC-GAT-AGT-TAT-CAC-GCA-3')[63] were used to generate an *E. coli*-specific 365-bp product. For PCR analysis of post-trapping samples, 1 μL of well-vortexed trap effluent was mixed with 9 μL of PCR master mix (1.1X PCR Buffer II (Applied Biosystems), 2 mM $MgCl_2$, 0.2 mM each dNTPs, 0.3 μg/μl BSA, 0.2 μM each forward and reverse primers, 0.1 U/μL AmpliTaq Gold Polymerase (Applied Biosystems)). Thermocycling was performed in a Bio-Rad MyCycler thermal cycler. The PCR program consisted of (1x10 min. at 95 ^{o}C; 30x(10

sec. at 95 °C, 10 sec. at 55 °C, 10 sec. at 72 °C); 1x3 min at 72 °C). Post-PCR analyses were performed via microchip gel electrophoresis using the DNA 1000 kit for the Agilent 2100 Bioanalyzer.

Cultures of inactivated *Listeria monocytogenes* and *Salmonella enterica (subspecies enterica serovar enteriditis)* were kindly provided by Prof. Ian Glomski and Prof. Sanford Feldman, respectively. *Listeria* were cultured overnight, pelleted by centrifugation, and resuspended in phosphate buffered saline at a final concentration of ~2 x 10^{10} cells/mL. *Salmonella* were cultured overnight in Kreb's Ringers buffer for a cell concentration of ~1.5 x 10^{8} cells/mL. Samples of foodborne pathogens were heat-killed at 56 °C for 60 minutes[64] prior to use in trapping experiments. Bacterial cultures were stored at 2-8 °C following heat inactivation and used within 12 hours to preserve cellular integrity. Suspensions of *Listeria* and *Salmonella* were prepared by spiking 1 μL of culture and 1 μL of 5 M Syto 11 dye into 1 mL of 0.01% TWEEN 20, with a final cell concentration of ~2 x 10^{7} cells/mL (*Listeria*) and ~1.5 x 10^{5} cells/mL (*Salmonella*). Bacterial cell suspensions were incubated in the dark for 30 minutes for fluorescence staining then slowly aspirated into 1 mL glass syringes (SGE inc.). Protocols for acoustic trapping are described below.

Listeria and *Salmonella* trapping samples were lysed using the prepGEM Bacteria DNA extraction kit (ZyGEM, Inc). PCR typing of foodborne pathogens was accomplished using published PCR primers specific for the *invA (invasion protein A*) gene for S. enterica[65], the prfA (transcriptional activator of the virulence factor) gene for L. monocytogenes. A custom Plexor® (Promega) multiplex PCR reaction was designed; Listeria-specific primers were labeled with CAL Fluor® Orange 560 and *Salmonella*-specific primers were labeled with CAL Fluor® Red 610. Amplification reactions were

set up according to manufacturer protocols. Purified DNA from *L. monocytogenes* and *S. enterica* (purchased from American Type Culture Collection) were used to verify the inter-species specificity of the multiplex PCR reaction. The Plexor® quantitative PCR (qPCR) reaction operates by the progressive quenching of the fluorescent reporters as the species-specific PCR products are created and thus the fluorescence signal decreases as product accumulates. Thermal cycling was performed in a BioRad iQ5 with the PCR program (2 mins. At 95 °C; 40x(5 sec. at 95 °C, 35 sec. at 60 °C)). Following PCR, the amplification products were subjected to melting temperature analysis (range: from 60 °C to 95 °C) to further assess the specificity of the amplification products.

5.3.5. System hardware

The driving signal for the ultrasonic transducers was produced by an arbitrary waveform generator (Agilent, model 33220A) connected to a custom 5X amplifier[66], and the peak-to-peak voltage of the output signal was measured with an oscilloscope (Tektronix TDS1002). A 50-ohm BNC terminator was connected in parallel to suppress both 60 Hz line noise and a higher harmonics of the WFG signal. A fluorescence microscope (Zeiss Axioscope A1 with X-CITE 120Q light source; 2X, 5X, or 10X objective lens; Filter Set 10) was used to visually monitor the trapping process, and microscope images and videos were captured with a color CMOS camera (PixeLink, PL-B681) or color CCD camera (Hitachi, KP-D20; with USB frame grabber). Temperature readings were obtained by placing a fine gauge thermocouple (Physitemp Inc., model T240M) in the glycerol surrounding the transducer, and the thermocouple was read with an electrically isolated thermocouple-to-analog converter (Omega Engineering, TAC-80B) and digital

multimeter. Samples were infused using either a NeMesys dosing module (Cetoni), WPI SP101, or WPI SP230iw syringe pump (World Precision Instruments). In some cases, a flow selector valve (Rheodyne Inc) was used to switch the input flow stream between the cell or microbead suspension and clean run buffer.

5.3.6. Experimental procedures for ultrasonic trapping

5.3.6.1. Microparticle trapping efficiency

Suspensions of 2 μm and 6 μm diameter particles were infused through the GPG device at varying flow rates while the liquid stream coming out of the chip was collected as several sequential fractions in 0.7 mL microcentrifuge tubes. The aggregates of trapped particles were observed via video microscopy. Fluorescent microspheres in pre- and post-trapping samples were counted using Glasstic hemocytometer slides (Kova, Glastic 87144), and the ImageJ software suite (National Institutes of Health, USA) was utilized to facilitate bead counting. Trapping efficiency, T_{eff}, was calculated from the average bead concentration with ultrasound turned off, C_{off}, and the average bead concentration of fractions collected while ultrasound was applied, C_{on}, using the formula $T_{eff} = (C_{off} - C_{on})/C_{off}$. The microparticle concentrations were normalized to the average C_{off} to facilitate data comparisons. Trapping efficiencies were determined at a range of flow rates ($n \geq 3$ each) for both 2 μm and 6 μm diameter beads.

5.3.6.2. Single microparticle retention against flow

Single fluorescent microparticles of various sizes were loaded into the single chamber GPG acoustic trap by flowing a dilute microparticle suspension through the device until a single bead was held in the USW. Once a microparticle was trapped, the input stream

was switched to clean run buffer (0.1% TWEEN). Microparticles were then monitored by video. The input flow rate was increased in small increments, and the maximum flow rate before particles were dislodged from the trap was recorded.

5.3.6.3. Acoustic trapping of bacterial foodborne pathogens

3.6.3.1. Trapping of E. coli in glass ellipsoid microchambers

Suspensions of nonpathogenic live E. coli (described above) were infused in the glass ellipsoid microfluidic device via syringe pump. Prior to trapping bacteria against flow, the actuation frequency was scanned from 6 to 8 MHz, and 6.69 MHz was selected for bacterial trapping experiments. Bacterial cells were trapped by flowing sample through the activated ultrasonic trap for 10 minutes at 1 μl/min. Then ultrasound was turned off and sample was infused at 10 μl/min for 1 minute while collecting the effluent in a clean microcentrifuge tube. Control samples (no trapping) were collected by flowing the sample through at 10 μl/min for 1 minute while collecting the effluent in a tube. The trapping apparati and work area were decontaminated with 70% ethanol after trapping experiments with live bacteria.

3.6.3.2. Trapping of foodborne pathogens in GPG trapping chambers

Acoustic trapping of heat-killed foodborne pathogens (either *Listeria monocytogenes* or *Salmonella enterica*) was conducted in the single chamber GPG microfluidic device. The trapping frequency was empirically adjusted from nominal values of 7.1 MHz or 6.2 MHz. Suspensions of bacterial cell were infused at 1 μL/min without hydrodynamic flow focusing. Video microscopy was used to monitor the formation of trapped aggregates of cells. Trapping was conducted for 15 minutes (until visible aggregates of cells accumulated). To recover the trap contents the input flow was switched from sample to

clean 0.01% TWEEN solution. The flow rate was set to 10 µl/min and the effluent was collected for 1.5 minutes into microcentrifuge tubes.

5.4. Results and Discussion

5.4.1. Transducer Characterization

The miniaturized piezoelectric transducers were characterized electrically to determine their resonance characteristics. Dicing and mounting of a 6 MHz PZT to the PCB to create the miniature PZT assembly (Figure 5.2A-C) resulted in a drop of Q factor from 62.95 (6 MHz PZT with only soldered-on leads) to 19.79 ± 1.657 (N = 3 transducer assemblies) and shift in F_{max} from 6.30 MHz to 6.61 ± 0.0794 MHz. The reduction in observed Q factor indicates that the assembly process reduced the amplitude and decreased the bandwidth of the resonance peak of the transducers, but that the transducers were still functional because resonance peaks were clearly visible. Two of the transducer assemblies were selected for use in the trapping system. The shapes of the manually-cleaved PZT elements were slightly different (as is visible in micrographs of the trapping chambers), but the transducer assemblies showed similar electrical characterization results that are indicative of comparable performance. The electrical resistances between each wire lead to their respective PZT electrode surface were measured to be less than 1 ohm to minimize resistive losses. The PCB-mounted PZT assemblies were attached to a rotating, vertically adjustable positioner (Figure 5.2D,E) with a range of motion in the x, y, and z directions provided by a manifold assembly (Figure 5.2F,G) to precisely contact the delicate microfluidic devices. This transducer packaging method and interface with microfluidic devices were used for all studies in this

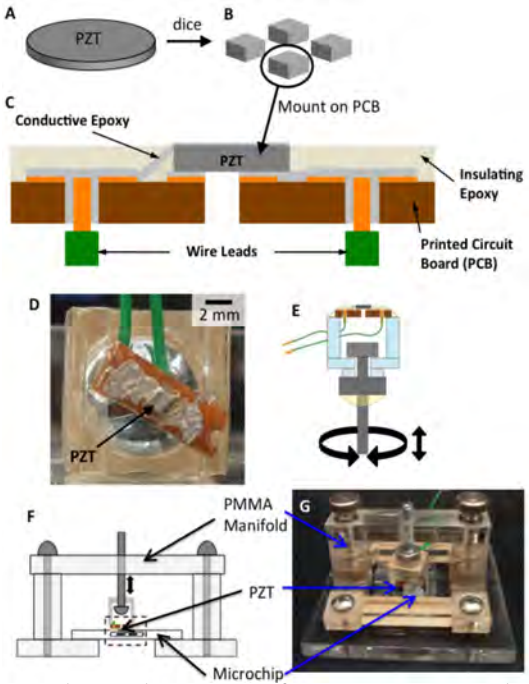

Figure 5.2: Fabrication of miniature piezoelectric transducers. Commercially available PZT discs (A) were manually diced into approximately 1 mm^2 pieces (B). The PZT fragments were mounted on ~(2.5 mm x 10 mm) pieces of printed circuit board (C), and insulating and conductive epoxies were used to fasten the PZT and make electrical connections to it. The completed transducer assemblies were mounted onto a positioning device (D, E) to facilitate precise mating of the transducer to microfluidic devices. A manifold (F,G) was used to position the parts relative to each other and hold them in place.

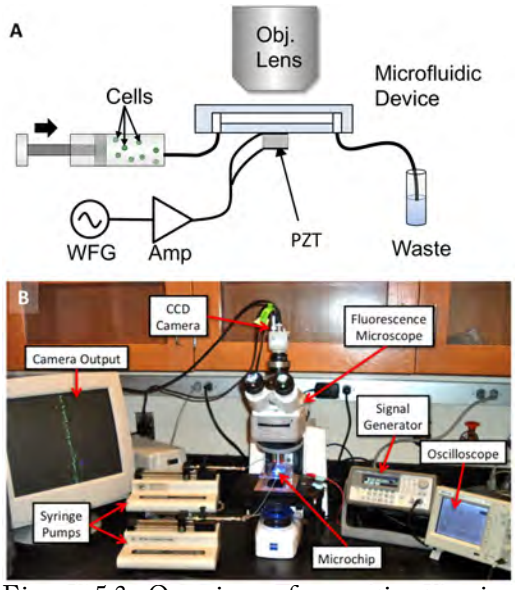

Figure 5.3 Overview of acoustic trapping apparatus. A. The apparatus for acoustic trapping consisted of a syringe pump for infusion of the microparticle/bacterial cell suspension, a layered glass-PDMS-glass microfluidic acoustic resonator, a waveform generator (WFG), amplifier (Amp), a maneuverable printed circuit board-mounted piezoelectric transducer, and an epifluorescence microscope for documentation of acoustic trapping. B. Photograph of the acoustic trapping apparatus used in this work.

chapter. The transducer and microchip were then connected to the other system components (Figure 5.3) to complete the apparatus.

5.4.2. Acoustic Trapping in Glass Ellipsoid Chambers

Acoustic trapping was performed in microfluidic devices with glass ellipsoid microchambers (Figure 5.4). Two operational modes were found at 2 specific frequencies. The first mode of operation depended on a multi-wavelength lateral resonance across the microchamber. Modeling of the microchamber cross-section (Figure 5.5A) indicated

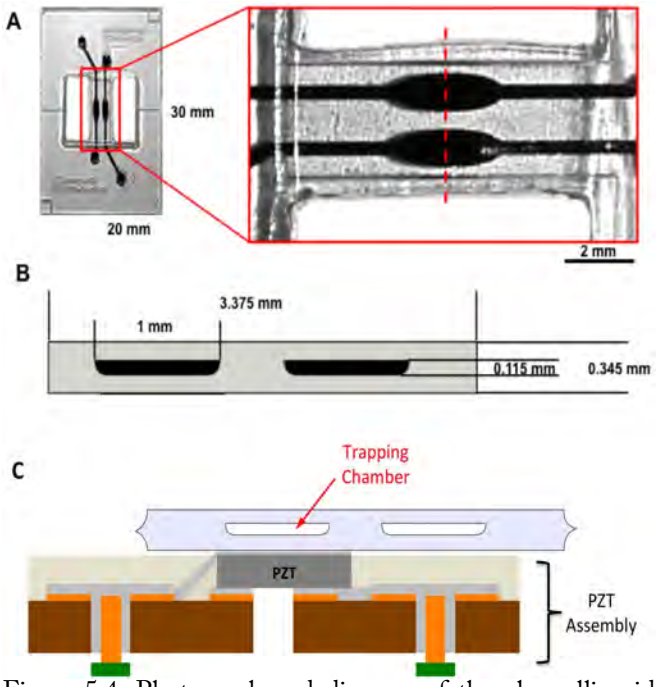

Figure 5.4: Photograph and diagram of the glass ellipsoid microfluidic acoustic resonator. (A) Microfluidic channels are shown filled with black ink for contrast. (B) Cross-sectional view (along the red dashed line in panel A inset) of bridge region of microfluidic device. (C) Arrangement of transducer assembly below the trapping microchamber.

that 8 nodes would span the widest part of the chamber, and 8 bands of beads were seen when ultrasound was applied a bead-filled chamber with no flow (Figure 5.5B). Trapping was initiated when this lateral focusing of beads transitioned to localized trapping. When bead aggregates reached ~20 μm in diameter, the secondary trapping forces were sufficient to force incoming beads onto the growing aggregate rather than exiting with the flow. Digital video shows that, for a flow rate of 2 μL/minute, nearly 100% of the incoming beads were retained once localized trapping initiated. Microsphere aggregates were also held against 4 μL/min. and 10 μL/min. albeit with lower trapping efficiency. Interestingly, the spacing between the various trapping sites corresponded to λ/2, or ~107 μm for 6.91 MHz (Figure 5.5C). Trapping was found to be strongest directly above the transducer, which is indicative of a minor vertical component in the coupling of acoustic energy from the transducer into the lateral resonance of the chamber.

The second operational mode of in the microfluidic devices with glass ellipsoid microchambers consisted of a vertically oriented pressure node in the microchamber and an ancillary lateral focusing within the inlet channel. Modeling predicted resonance with vertical character at 7.55 MHz (Figure 5.6A), and effective ultrasound-mediated particle

enrichment was observed at 7.545 MHz (Figure 5.6B). Lateral resonance within the inlet channel focused incoming particles into two nodal planes running along the length of the channel. As labeled in Figure 5.6B, spacing between the nodal planes in the inlet channel was measured as roughly λ/2 for 7.5 MHz (~99 μm) using the chamber width for scale. It should be noted that tight focusing in the inlet channel was relatively weak and only apparent at very slow flow rates (e.g., 0.1 μL/min). However, with future optimization (such as a longer inlet channel), this lateral pre-focusing could improve trapping

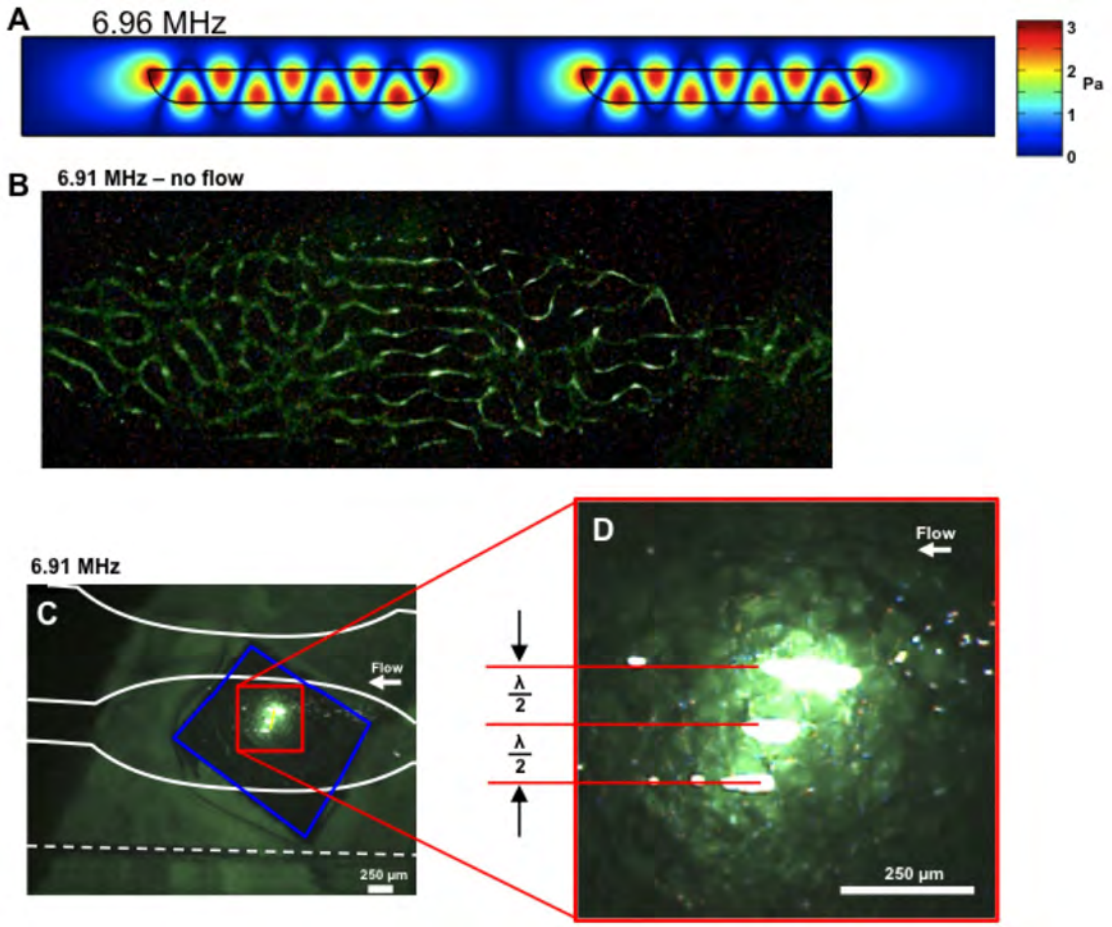

Figure 5.5: Computer modeling and empirical validation of a lateral acoustic trapping mode. (A) The absolute value of the total acoustic pressure is plotted over the cross-section of the trapping chambers. (B) This image from fluorescence microscopy shows the spontaneous arrangement of fluorescent microparticle when the glass ellipsoid trapping chamber was excited at resonance. (C,D) Still images from video microscopy documented trapping of incoming microparticles into nodal positions that matched the λ/2 condition for the the applied frequency. The microfluidic chamber walls are outlined in white, the PZT transducer is outlined in blue, and the edge of the glass bridge structure is indicated with the dashed white line.

performance by reducing positional heterogeneity and by moving microparticles away from the channel walls to reduce adsorptive losses. The main trapping site was a vertically oriented nodal plane, as shown both epifluorescence and brightfield lighting (Figure 5.6C). The combined lateral channel pre-focusing and in-chamber vertical resonance present an avenue for further optimization of this device.

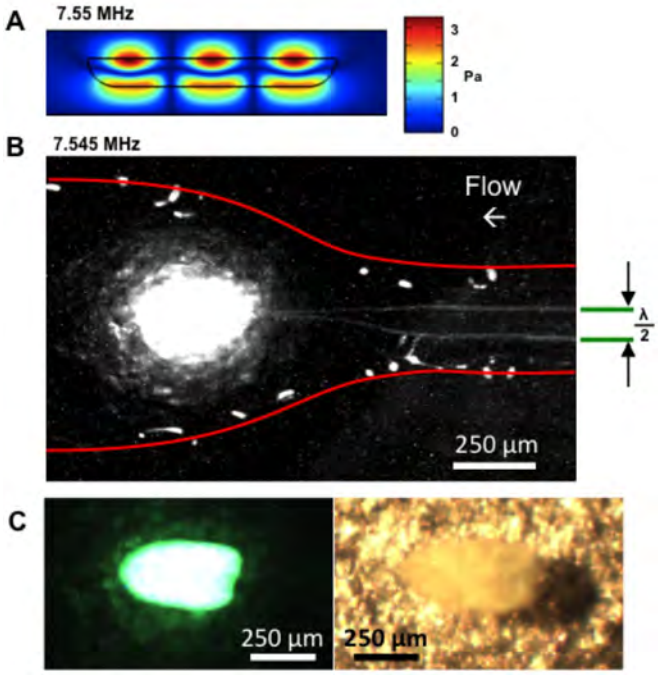

Figure 5.6: Computer modeling and empirical validation of a vertical acoustic trapping mode with lateral prefocusing upstream of the chamber. (A) The simulated absolute value of total acoustic pressure is shown for one of the trapping chambers, and a vertical mode is predominant. (B) Images of fluorescence microscopy of the chamber and inlet channel show two streams of prefocused microparticles. (C) An aggregate of fluorescent microparticles is shown under fluorescence (left) and brightfield illumination (right).

5.4.3. Acoustic Trapping in Glass-PDMS-Glass Layered Acoustic Resonators

The transducers and trapping apparatus was next applied to GPG acoustic resonators (Figure 5.7A,B). Computer modeling of the fluidic architecture predicted (Figure 5.7C,D), and observations confirmed (Figure 5.7E), that hydrodynamic focusing confined the microparticle-laden sample stream to the region above the trapping site while also slowing the linear flow rate to reduce hydrodynamic drag. Multiphysics simulations of acoustic resonance (Figure 5.8A,B) suggested that trapping nodes were centrally located within the chamber, and that two nodal planes were arranged vertically in the

microchamber (height = $2 \cdot \lambda/2$ for 6.34 MHz). The low acoustic impedance mismatch between water and PDMS resulted in suppressed lateral reflection of sound, so trapping nodes were predominantly arranged vertically. Bulk acoustic wave resonances of the water-filled channel were discernible in the transfer function spectra for the transducer-GPG microfluidic device (Figure 5.8C). Two peaks in the transmittance magnitude were seen at 6.14 MHz and 7.22 MHz, and these frequencies correlated well with empirically determined trapping modes. The vertical configuration of the trapping nodal planes was confirmed using translucent fluorescent particles that appear brighter where the two flat aggregates overlap (Figure 5.8F). Clusters of particles were seen to rotate independently of each other, providing further evidence of the dual arrangement of vertical trapping

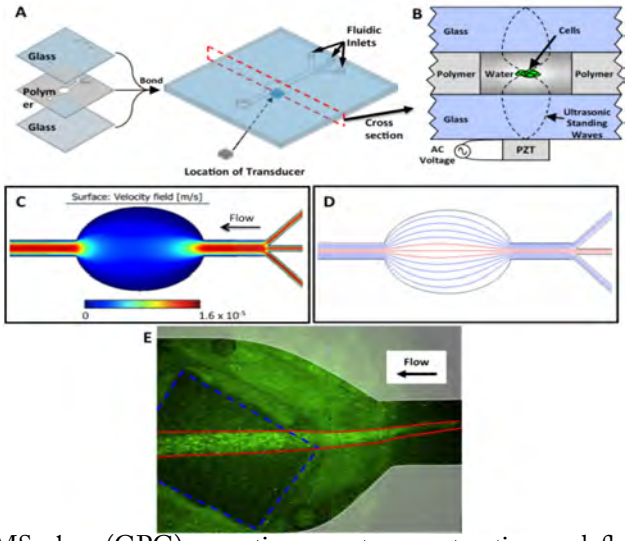

Figure 5.7: Glass-PDMS-glass (GPG) acoustic resonator construction and fluidic architecture. (A) Diagram of the construction process for layered microfluidic acoustic resonators for cell trapping. The middle and top layers were cut with a laser engraving machine. (B) Cross-sectional view of the trapping chamber when the ultrasound frequency creates a standing wave between the glass plates. This standing wave creates nodes where cells are trapped. (C) Modeling of the flow velocity reveals that flow is slowest in the center of the chamber (above the transducer). (D) Modeling of fluid lamina predicted that the center flow stream will be focused by the sheath flow. (E) Frame capture from video microscopy documenting hydrodynamic focusing of fluorescent microspheres. The fluid lamina containing fluorescent beads is outlined in red, the transducer is outlined in dashed blue, and the PDMS channel walls are shaded.

nodes.

Prominent acoustic streaming affected acoustic trapping in the GPG acoustic resonator. The rotational flows due to microstreaming were especially visible for small particles because of the size dependence in the contribution of F_{drag} relative to the sum of acoustic forces. The progression of acoustic trapping of 2 μm microspheres (Figure 5.9A-C) indicate that acoustic streaming played a significant role in directing microbeads towards the central trapping site. Furthermore, particle tracking analysis of digital video (Figure 5.9D,E) revealed curved trajectories due to influences of acoustic microstreaming.

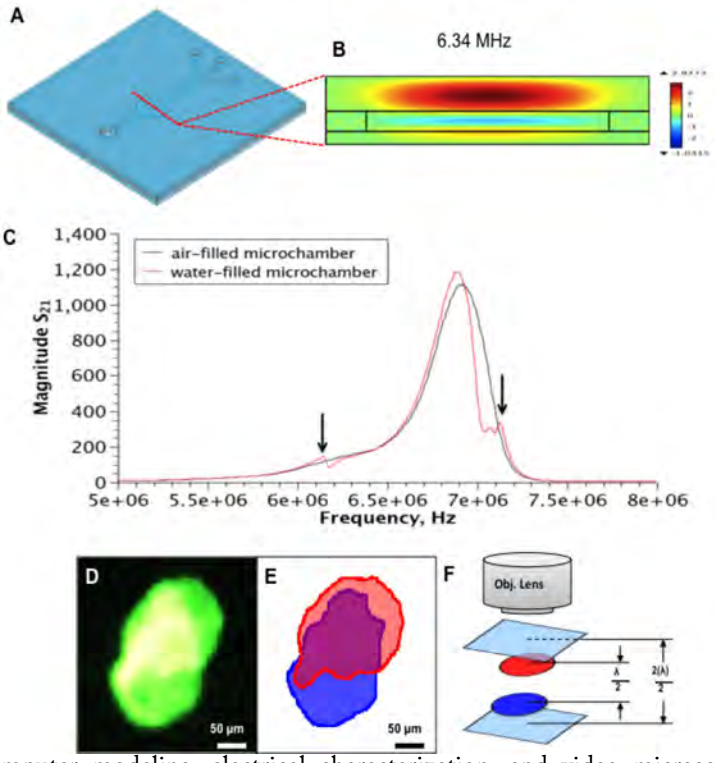

Figure 5.8: Computer modeling, electrical characterization, and video microscopy of a glass-PDMS-glass microfluidic acoustic resonator. (A,B) The microfluidic device is illustrated in isometric view (A) and a cross-section (along the red line in A.) was modeled in COMSOL and predicted to have vertically oriented resonance (B). (C) Admittance spectra were obtained for the microfluidic resonator in contact with the miniature ultrasonic transducer. When the microfluidic device was empty (air-filled), a gradual peak was observed, but additional resonance were observed when the microfluidic chamber was filled with water. Black arrows indicate frequencies at which trapping was observed empirically. (D) The vertical orientation and number of nodal planes is revealed by video microscopy where 2 flat aggregates were observed moving independently of each other. The fluorescence intensity was stronger where the two aggregates overlapped. (E) False color top-view image. (F) Isometric diagram of vertical spacing of flat aggregates within nodal planes of the standing wave.

The effective trapping zone was expanded for small particles because streaming vortexes prolonged the residence time of microparticles within the trapping chamber. These vortices tended to deliver particles to the trapping sites, thus allowing them to be pulled into the trapped aggregate by primary and secondary acoustic forces.

Quantitative evaluation of trapping performance was performed using fluorescent polymer microparticles. In some cases, direct analysis of digital video allowed for evaluation of trapping performance by counting individual beads (Figure 5.10A). The intensity of fluorescence emission of the microbeads, the sensitivity and frame rate of the camera, and linear velocity of the microparticle were the determining factors in whether individual particles could be tracked by digital video microscopy. Particle tracking was only possible when the particles were bright enough and moving slow enough to be

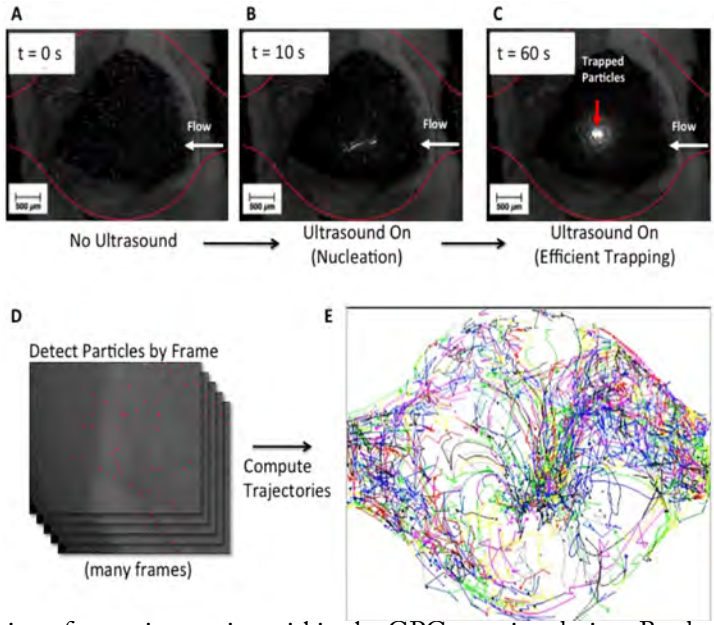

Figure 5.9: Progression of acoustic trapping within the GPG trapping device. Beads were initially evenly dispersed (A), but when the ultrasound was turned on the beads rapidly condensed in the center of the chamber (B). After 1 minute, a large aggregate was observed (C), and once the aggregate had formed all visible incoming beads were trapped. D,E. The motions of individual particles were tracked frame-by-frame (D) from digital video taken during microscopy to yield a rough population-level picture of bead trajectories (E). In E, note how most paths (especially those originating from the right side) end up in the center of the chamber.

distinctly visible in several successive frames of video. Despite loss of beads during the initiation of trapping, most of beads were retained once an aggregate was formed, for an overall trapping efficiency greater than 80% (Figure 5.10B).

Trapping efficiency was also determined by enumeration of microparticles in fluid recovered from the microfluidic device. The trapping efficiency was determined at a series of flow rates for both 2 μm and 6 μm polystyrene microspheres (Figure 5.11A). At low flow rates (2 μL/min), the trapping efficiency was nearly 80% for both bead sizes, which corroborated digital video-based counts. The terminal velocity of a microparticle is due to the balance of forces acting on it, and at low flow rates both the 2 μm and 6 μm particles had time to migrate into the acoustic trap before exiting the chamber. However, at higher

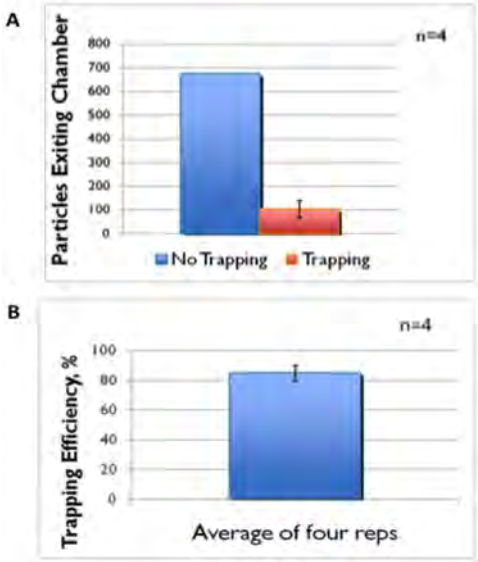

Figure 5.10: Results of manual counting of bead escape events in digital video of acoustic trapping. (A) Counts of escaping beads in digital video from 4 replicate acoustic trapping events compared to no trapping control. (B) Trapping efficiency for the counts in (A).

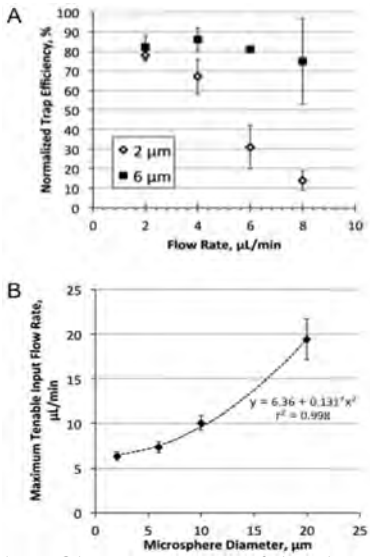

Figure 5.11: Characterization of the glass-PMDS-glass acoustic resonator through trapping of fluorescent microparticles. (A) The trapping efficiency (defined in section 2.6.1) showed that trapping efficiency showed size dependance, with high trapping efficiency for the 6 μm diameter microparticles. (B) Single microparticles were loaded individually into the acoustic trap and subjected to increasing flow rates until the maximum flow rate prior to escape was determined. (Compiled with additional data collection by Kerui Xu.)

flow rates the larger beads were trapped at greater efficiency due to the higher acoustic forces relative to viscous drag forces. A clear trend was discernible between the two sizes of microspheres. Under the conditions of this experiment, the trapping efficiency for the 2 μm beads declined from ~80% to ~15% when the flow rate was increased from 2 μL/min to 8 μm/min. The fact that the microparticle aggregate steadily grew in size over time definitively showed particle concentration enrichment within the acoustic trap.

To further investigate the relationship between microparticle size and trapping strength, individual polystyrene particles were loaded into the acoustic trap one at a time and subjected to increasing volumetric flow rates until dislodged by viscous drag forces (Figure 5.11B). While all particles could withstand 6 μL/min flow rates, size selectivity was achieved at progressively higher flow rates. For the largest diameter bead, 20 μm, particles were trapped until flow rates exceeded 19.4 ± 2.29 μL/min. The estimated trapping forces on individually trapped microbeads were calculated using the constants in Table 2 and the fitted equation in Figure 5.11B. Forces on the order of picoNewtons were calculated, which are similar to the range of 100-400 pN summarized by Nilsson *et al.* [4]. The complex microchamber geometry, variable vertical and horizontal positioning

Table 1: Physical constants used in calculations of trapping forces.

Dynamic viscosity of water (T=30 ºC)	0.798×10^{-3} kg/(m·s)
Chamber height	2.30×10^{-4} m
Chamber width at center	3.128×10^{-3} m

Table 2: Summary of single microbead trapping/drag forces.

Bead Diameter, μm	MTIFR, μL/min	F_{trap}, pN
2.0	6.36 ± 0.45	2.2 ± 0.16
6.0	7.34 ± 0.61	7.7 ± 0.64
10.0	10.07 ± 0.82	17.5 ± 1.4
20.0	19.39 ± 2.29	67.4 ± 8.0

of microspheres, gradients in flow velocity due to Poiseuille flow, and the presence of microstreaming could not be factored into the calculation of the linear flow velocity experienced by the particle, so the trapping forces listed in Table 2 may be viewed as a conservative lower limit of trapping forces.

5.4.4. Strategies for Multi-Site Acoustic Trapping

5.4.4.1. Simultaneous Operation of Multiple Isolated Trapping Sites

Since there are practical limits on throughput for any single trapping site, parallel device architectures were investigated to increase overall device throughput. The first multiplexed device was the dual GPG resonator depicted in Figure 5.12A, where two separate trapping sites were actuated and plumbed separately but simultaneously (Figure 5.12B). Trapping performances for the dual device were similar to the single chamber trapping after empirical tuning of each site. However, this arrangement was unwieldy in practice due to separate fluidic connections, PZT transducers, and driving electronics, as well as the large translation of the microscope stage. Fluorescent microbeads were retained against flow in both traps simultaneously (Figure 5.12C).

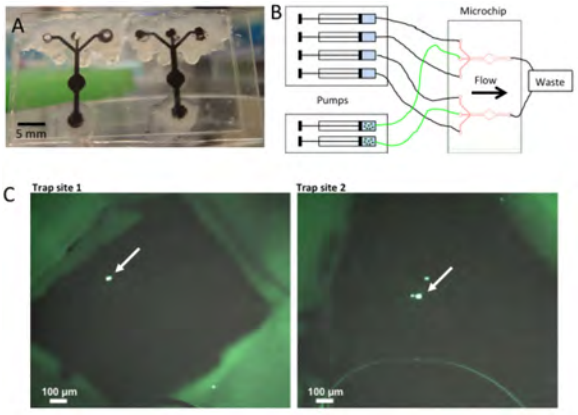

Figure 5.12. Parallel acoustic trapping in GPG devices. (A) Multiplexed trapping was performed in a GPG microdevice with 2 isolated domains driven by separate transducers with separate driving electronics. (B) Diagram of fluidic connections. (C) Video stills from simultaneous acoustic trapping of 2 µm fluorescent beads in 2 isolated domains. The aggregates of trapped microbeads are indicated with white arrows.

5.4.5. Multiple Parallel Microchannels Operated by a Single Transducer

A separate investigation into multi-site trapping featured a 6-channel GPG device (Figure 5.13A) where six separate channels were actuated by a common PZT to form trapping sites (Figure 5.13B,C). COMSOL modeling predicted several vertical modes isolated to the water channels, and the strongest, most balanced mode is shown in Figure 5.14. Localization of modes to the water-filled channels is due to differences in sound propagation through water versus PDMS. Digital video showed that ultrasound-induced aggregation and trapping of microbeads occurred in all 6 channels rapidly (in <30 sec.) and simultaneously (Figure 5.15A). Trapping was then conducted for a duration of 20 minutes, and digital video indicated that trapping efficiency for late-stage trapping was nearly 100% (Figure 5.15B middle). Secondary aggregation of microbeads on the channel walls was also observed, and this caused dispersion upon release of cells when ultrasound was turned off (Figure 5.15B right). Wall adsorption would be ameliorated by implementing established anti-fouling techniques such as passivation[67], use of low

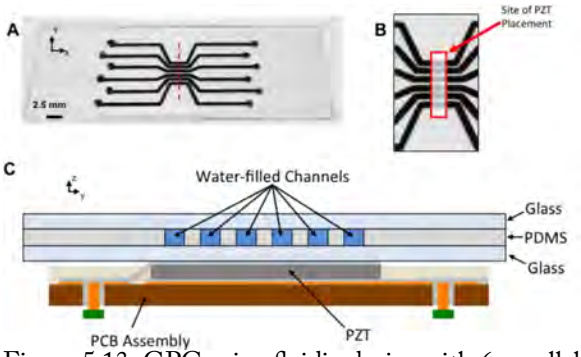

Figure 5.13: GPG microfluidic device with 6 parallel channels spanning a single transducer. (A) Photography of microfluidic device. (B) Close up of the trapping region with PZT position indicated. (C) Cross-sectional diagram (along the dotted line in panel A).

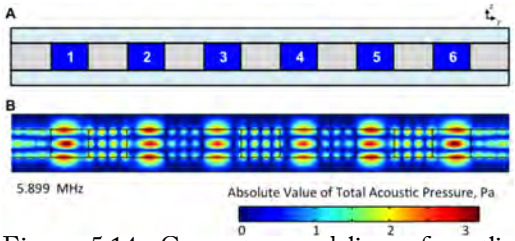

Figure 5.14: Computer modeling of mutli-channel, single transducer acoustic trapping device. (A) The geometry and materials of the device were used to create a model within the COMSOL Multiphysics software. The chambers were 1 mm wide, flanked by PDMS and separated by 1 mm regions of PDMS. The PDMS layer was 290 μm thick, and the glass plates were 150 μm thick. (B) Modeling results predicted a distributed trapping mode at 5.899 MHz.

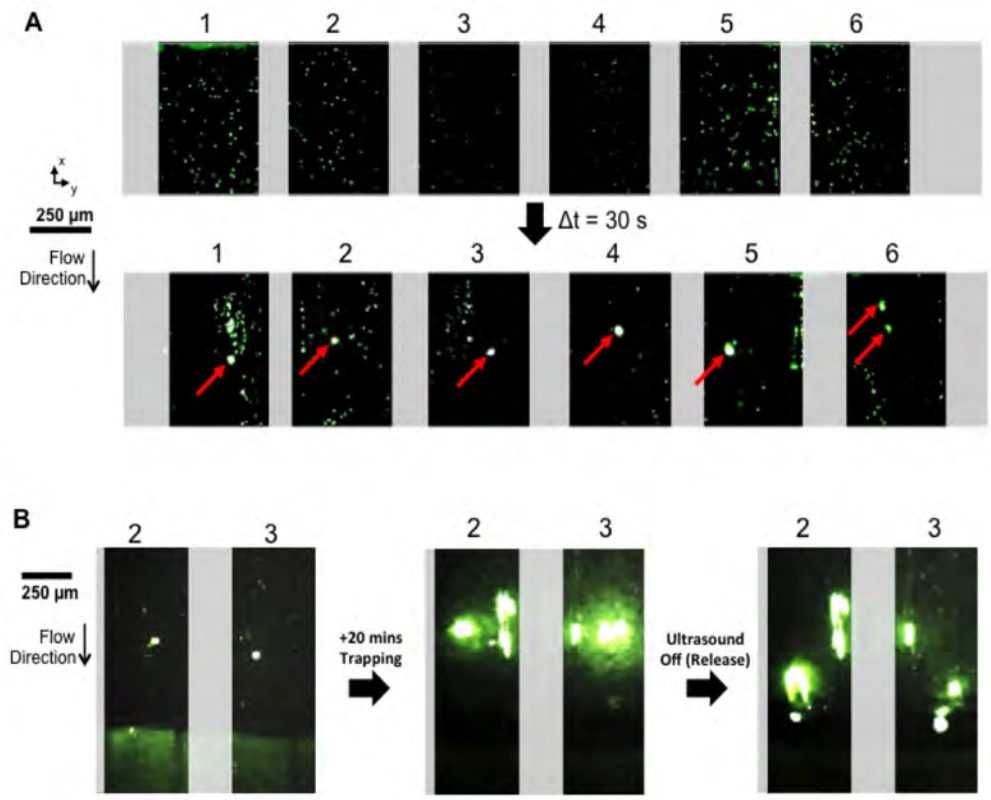

Figure 5.15: Mosaics of frames from video of simultaneous acoustic trapping in 6 parallel channels across a single transducer. (A) Initiation of trapping. PDMS chamber walls have been masked with translucent shapes to emphasize channels. Six channels were infused at 60 µL/hour per channel with a suspension of beads that were initially well distributed within the fluid (top), but after application of ultrasound (bottom) each of the channels had a visible aggregate of trapped beads (indicated by red arrows) and additional beads retained in streaming vortices. (B) Progression of prolonged acoustic trapping and subsequent release of microbeads. Initial aggregates (bottom left) grew to large accretions of beads (bottom middle). Discontinuation of ultrasonication (bottom right) showed a wall-adsorbed cluster and 2 free floating clusters per channel.

surface energy polymeric material[68], or rapid modulation of the driving signal to optimize trapping positions[69]. Nonetheless, these preliminary data clearly show that microparticle enrichment was performed in multiple channels simultaneously using a simple and low cost device.

5.4.6. Trapping of Foodborne Pathogens

Bacterial cells were acoustically trapped in the all-glass microdevice (described above in Figure 5.4) using the second operational scheme (~7.5 MHz, Figure 5.6).

Mixtures of live *E. coli* and microbeads were infused at 2 µl/min, and visible aggregates of cells/microbeads formed in the acoustic trap (Figure 5.16). Microbeads were originally added only as tracer particles, but we hypothesize that beads actively assisted the trapping process as described recently by Hammarström et al.[32]. Photobleaching of the fluorescently stained live bacteria was observed, and this hampered monitoring of the trapping progress via epifluorescence microscopy because prolonged illumination would cause trapped cells to fade and become invisible. Video microscopy showed the successful acoustic trapping and enrichment of E. coli cells within the trapping chamber.

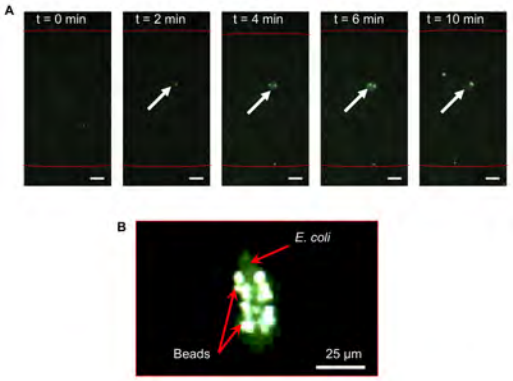

Figure 5.16: Video microscopy of acoustically trapped E. coli cells and fluorescent microbeads. (A) The size of the cell/bead aggregates were observed to increase in size, which is indicative of retention of incoming particles. The scale bars in panel A represent 100 µm. (B) A zoomed-in view of a typical cell/microparticle aggregate within the acoustic trap shows both fluorescently-stained cells and brighter fluorescent microparticles.

The contents of the acoustic trap were collected for three replicate *E. coli* trapping events, and these were used as template material for PCR *E. coli*-specific PCR reactions. First, the direct addition of intact cell to PCR reactions was validated for a serial dilution of *E. coli* cells (Figure 5.17A). Electropherograms of the processed post-trapping PCR samples are shown in Figure 5.17B. Two of the trapping samples produced the E. coli-specific PCR product. The third replicate trapping sample failed to produce the expected PCR product, and this may have been due to adsorption of the cell/bead aggregate to the microchannel wall instead of exiting the microfluidic device. Video microscopy collected during the 3rd trapping event clearly showed that acoustic trapping occurred (in fact, the

cell aggregate in Figure 5.16B, was from video of the 3rd trapping replicate). The infused, no-ultrasound control samples, as well as the unprocessed cell suspension itself, did not yield a PCR product. These results suggest that the minimum amount of starting genetic material was not present unless acoustic trapping-based enrichment was performed. The presence of the PCR product peaks in trapping samples confirmed that: 1) sufficient cells were collected to exceed the minimum amount of template DNA required, and 2) the DNA was from *E. coli* cells (by virtue of PCR primer specificity).

The GPG acoustic resonator was utilized to trap heat-killed foodborne pathogens. Stills from microscope video show the aggregation and trapping of *Listeria monocytogenes* cells (Figure 5.18A) and *Salmonella enterica* (Figure 5.18B). The acoustic trap was operated at either 7.088 MHz or 6.24 MHz, with a measured voltage of approximately 15 Vpp. These conditions led to heating of the transducer and microfluidic device, and a steady-state temperature of the glycerol surrounding the transducer was typically between 30-40 ºC. The fluorescence intensity of a growing aggregate of *S. enterica* cells was measured from the CMOS camera

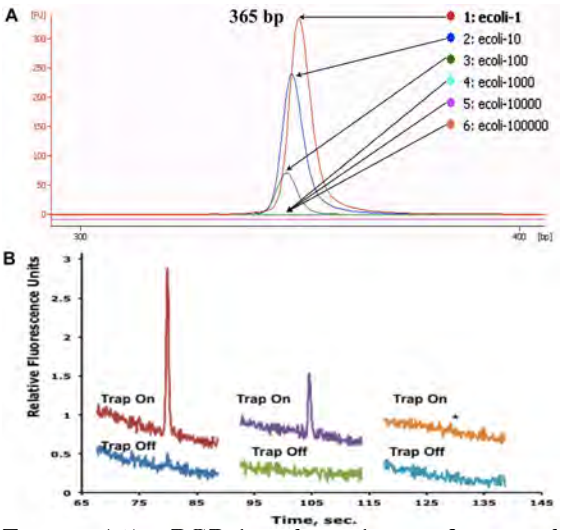

Figure 5.17: PCR-based analysis of trapped aggregates of E. coli cells and fluorescent microparticles. (A) Qualitative validation of direct PCR using intact E. coli cells as template without acoustic trapping or microfluidic handling. A single colony of day-old E. coli cells (on the order of 106 cells) was swabbed, serially diluted, and used as template for PCR reactions. Below 1000-fold dilution, PCR amplification was unsuccessful because insufficient numbers of cells were present. (B) Recovery, lysis, PCR, and microchip electrophoresis were performed on acoustic trap contents. E. coli-specific PCR peaks were observed in 2 of the trapping samples. (*) In the 3rd replicate, trapping was observed by video microscopy but post-processing (recovery, lysis, or PCR) yielded no peak. PCR product was not observed in any of the infused, no-ultrasound control samples.

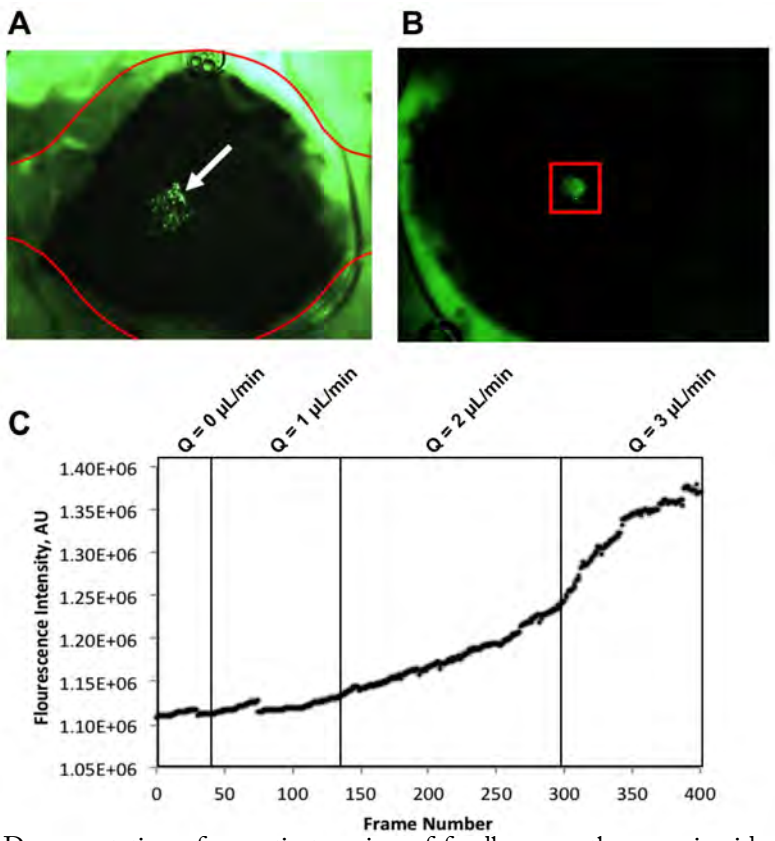

Figure 5.18: Documentation of acoustic trapping of foodborne pathogens via video microscopy. (A) Listeria monocytogenes and (B) Salmonella enterica were shown to form clusters that increased in size over time, indicating a net retention of cells. (C) The time course of fluorescence intensity during a Salmonella trapping experiment showed a net accumulation and retention of cells that was dependent on the rate at which cells were infused.

during the course of trapping (Figure 5.18C). The rate of increase in fluorescence was found to be roughly proportional to the flow rate (either 0, 1, 2, or 3 µL/min). While sample was infused at 3 µL/min. the aggregate reached a critical point where fluorescence intensity leveled off. At this point either hydrodynamic forces prevented further trapping and/or the build up of heat from the transducer was sufficient to change the resonant frequency of the acoustic trap and disrupt trapping. For both pathogen trapping experiments, the contents of the acoustic trap were collected and used as template material for multi-color multiplex qPCR reactions with specificity for pathogenic

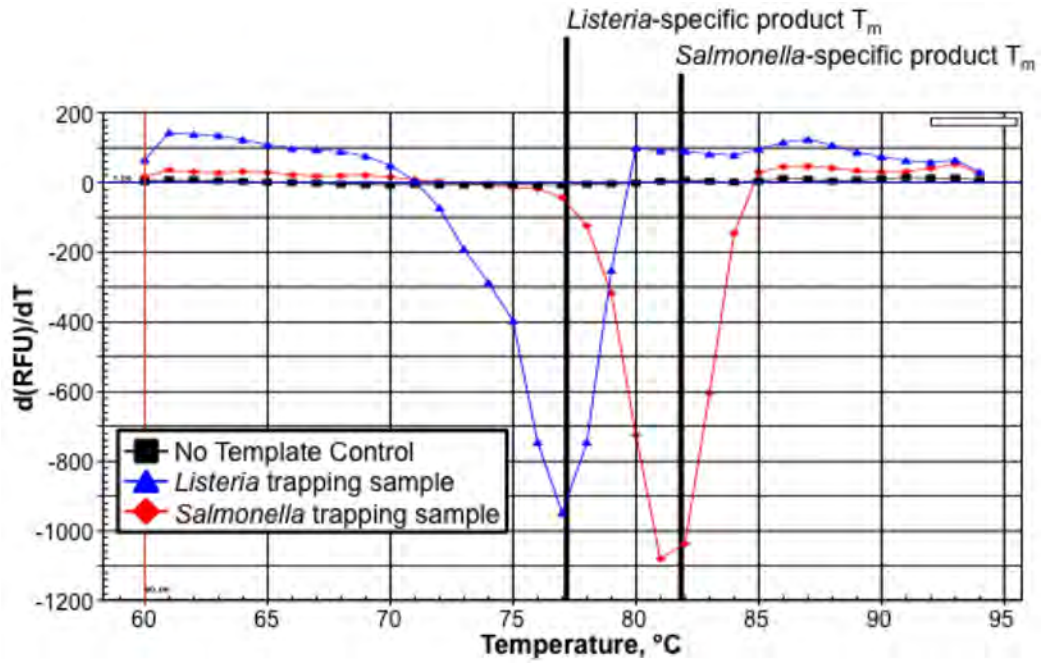

Figure 5.19: Genetic typing of cells recovered from the microfluidic acoustic trap demonstrated demonstrated suitability as template for downstream PCR. Melt curves were obtained following PCR amplification to achieve specific detection of foodborne pathogens.

Salmonella ssp. and *Listeria ss*p. The melt curve analysis of Figure 5.19 indicated that acoustically trapped foodborne pathogens were specifically detected via PCR. The combination of the visual evidence of cell concentration enrichment within the microchamber, and the specific detection of bacterial cells via PCR, indicated that acoustic trapping was a viable front-end enrichment process for genetic analysis of foodborne pathogens.

5.5. Conclusions

An entire system was developed for microfluidic acoustic trapping. Miniature transducers were built using low-cost materials in a typical laboratory setting (without a clean room). Transducers were characterized by transfer function spectral analysis to identify resonant modes. Microfluidic devices originally designed for ultra-rapid non-contact PCR were

shown to be capable of trapping microbeads and live E. coli cells. The dual functionality of this device has significant implications for the future integration of acoustic trapping and PCR in the same microdevice. Rapidly fabricated and low-cost glass-PDMS-glass microfluidic devices were characterized for their acoustic trapping ability through microparticle trapping studies. Bacterial cells were enriched in and successfully recovered from both microfluidic devices, and pathogen-specific PCR analysis was utilized for unambiguous detection of foodborne pathogens Listeria monocytogenes and Salmonella enterica. Bacterial enrichment is a vital process in bioanalytical testing, and the next generation of microfluidic genetic analyzers can incorporate the technologies described here for implementing acoustic trapping for sample enrichment.

5.6. Acknowledgements

This author would like to thank and acknowledge the following: Prof. James Landers for the opportunity and guidance during this project; Lockheed Martin Inc. for funding this research, Dr. Joan Bienvenue and Dr. Stephanie Groves of Lockheed Martin Inc. for project guidance and collaboration; the hospitality and training this author received from Prof. Thomas Laurell, Prof. Johan Nilsson, Dr. Per Augustsson, Dr. Björn Hammarström, and all other members of the Laurell and Nilsson research groups, as well as Prof. Francisco Lara for camaraderie during this training; Prof. Ian Glomski and Prof. Sandford Feldman of UVA for providing samples of inactivated foodborne pathogens; Prof. Chris Easley for constructing the all-glass acoustic resonators; and undergraduate researchers Jonathan Armstrong and Michael Do for their work on this project during their time at UVA.

5.7. References

[1] R.L. Scharff, Economic burden from health losses due to foodborne illness in the United States., J. Food Prot. 75 (2012) 123–31. doi:10.4315/0362-028X.JFP-11-058.

[2] A.H. Havelaar, A. Cawthorne, F. Angulo, D. Bellinger, T. Corrigan, A. Cravioto, et al., WHO Initiative to Estimate the Global Burden of Foodborne Diseases, Lancet. 381 (2013) S59. doi:10.1016/S0140-6736(13)61313-6.

[3] D. Rodríguez-Lázaro, B. Lombard, H. Smith, A. Rzezutka, M. D'Agostino, R. Helmuth, et al., Trends in analytical methodology in food safety and quality: monitoring microorganisms and genetically modified organisms, Trends Food Sci. Technol. 18 (2007) 306–319. doi:10.1016/j.tifs.2007.01.009.

[4] J. Nilsson, M. Evander, B. Hammarström, T. Laurell, Review of cell and particle trapping in microfluidic systems., Anal. Chim. Acta. 649 (2009) 141–57. doi:10.1016/j.aca.2009.07.017.

[5] V. Gubala, L.F. Harris, A.J. Ricco, M.X. Tan, D.E. Williams, Point of care diagnostics: status and future., Anal. Chem. 84 (2012) 487–515. doi:10.1021/ac2030199.

[6] M.L. Kovarik, D.M. Ornoff, A.T. Melvin, N.C. Dobes, Y. Wang, A.J. Dickinson, et al., Micro total analysis systems: fundamental advances and applications in the laboratory, clinic, and field., Anal. Chem. 85 (2013) 451–72. doi:10.1021/ac3031543.

[7] F.S.O. Fritzsch, K. Rosenthal, A. Kampert, S. Howitz, C. Dusny, L.M. Blank, et al., Picoliter nDEP traps enable time-resolved contactless single bacterial cell analysis in controlled microenvironments., Lab Chip. 13 (2013) 397–408. doi:10.1039/c2lc41092c.

[8] Q. Ramadan, M. a. M. Gijs, Microfluidic applications of functionalized magnetic particles for environmental analysis: focus on waterborne pathogen detection, Microfluid. Nanofluidics. 13 (2012) 529–542. doi:10.1007/s10404-012-1041-4.

[9] X. Ding, S.-C.S. Lin, B. Kiraly, H. Yue, S. Li, I.-K. Chiang, et al., On-chip manipulation of single microparticles, cells, and organisms using surface acoustic waves., Proc. Natl. Acad. Sci. U. S. A. 109 (2012) 11105–9. doi:10.1073/pnas.1209288109.

[10] C.M. Lin, Y.S. Lai, H.P. Liu, C.Y. Chen, A.M. Wo, Trapping of bioparticles via microvortices in a microfluidic device for bioassay applications., Anal. Chem. 80 (2008) 8937–45. doi:10.1021/ac800972t.

[11] R. Burger, D. Kirby, M. Glynn, C. Nwankire, M. O'Sullivan, J. Siegrist, et al., Centrifugal microfluidics for cell analysis., Curr. Opin. Chem. Biol. 16 (2012) 409–14. doi:10.1016/j.cbpa.2012.06.002.

[12] M. Evander, J. Nilsson, Acoustofluidics 20: Applications in acoustic trapping., Lab Chip. 12 (2012) 4667–76. doi:10.1039/c2lc40999b.

[13] A. Lenshof, C. Magnusson, T. Laurell, Acoustofluidics 8: applications of acoustophoresis in continuous flow microsystems., Lab Chip. 12 (2012) 1210–23. doi:10.1039/c2lc21256k.

[14] Y. Gao, W. Li, D. Pappas, Recent advances in microfluidic cell separations., Analyst. 138 (2013) 4714–21. doi:10.1039/c3an00315a.

[15] M. Wiklund, H. Brismar, B. Önfelt, Acoustofluidics 18: Microscopy for acoustofluidic micro-devices, Lab Chip. (2012) 3221–3234. doi:10.1039/c2lc40757d.

[16] B. Hammarström, H. Yan, J. Nilsson, S. Ekström, Efficient sample preparation in immuno-matrix-assisted laser desorption/ionization mass spectrometry using acoustic trapping., Biomicrofluidics. 7 (2013) 24107. doi:10.1063/1.4798473.

[17] H. Bruus, Theoretical Microfluidics, OUP Oxford, 2008.

[18] S. Woodside, B. Bowen, J. Piret, Measurement of ultrasonic forces for particle–liquid separations, AIChE J. 43 (1997).

[19] M. Wiklund, R. Green, M. Ohlin, Acoustofluidics 14: Applications of acoustic streaming in microfluidic devices., Lab Chip. 12 (2012) 2438–51. doi:10.1039/c2lc40203c.

[20] T. Lilliehorn, U. Simu, M. Nilsson, M. Almqvist, T. Stepinski, T. Laurell, et al., Trapping of microparticles in the near field of an ultrasonic transducer., Ultrasonics. 43 (2005) 293–303. doi:10.1016/j.ultras.2004.11.001.

[21] B. Hammarström, M. Evander, J. Wahlström, J. Nilsson, Frequency tracking in acoustic trapping for improved performance stability and system surveillance., Lab Chip. 14 (2014) 1005–13. doi:10.1039/c3lc51144h.

[22] M. Evander, L. Johansson, T. Lilliehorn, J. Piskur, M. Lindvall, S. Johansson, et al., Noninvasive acoustic cell trapping in a microfluidic perfusion system for online bioassays., Anal. Chem. 79 (2007) 2984–91. doi:10.1021/ac061576v.

[23] K.T. Son, C.C. Lee, Bonding and impedance matching of acoustic transducers using silver epoxy., Ultrasonics. 52 (2012) 555–63. doi:10.1016/j.ultras.2011.11.010.

[24] B. Hammarström, M. Evander, H. Barbeau, M. Bruzelius, J. Larsson, T. Laurell, et al., Non-contact acoustic cell trapping in disposable glass capillaries., Lab Chip. 10 (2010) 2251–7. doi:10.1039/c004504g.

[25] L. Johansson, M. Evander, T. Lilliehorn, M. Almqvist, J. Nilsson, T. Laurell, et al., Temperature control and resonance mode analysis of an acoustic trap for μTAS, (2008).

[26] J.V. Norris, M. Evander, K.M. Horsman-Hall, J. Nilsson, T. Laurell, J.P. Landers, Acoustic differential extraction for forensic analysis of sexual assault evidence., Anal. Chem. 81 (2009) 6089–95. doi:10.1021/ac900439b.

[27] S.S. Guo, L.B. Zhao, K. Zhang, K.H. Lam, S.T. Lau, X.Z. Zhao, et al., Ultrasonic particle trapping in microfluidic devices using soft lithography, Appl. Phys. Lett. 92 (2008) 213901. doi:10.1063/1.2937910.

[28] M. Gedge, M. Hill, Acoustofluidics 17: Theory and applications of surface acoustic wave devices for particle manipulation, Lab Chip. (2012) 2998–3007. doi:10.1039/c2lc40565b.

[29] M. Hill, The selection of layer thicknesses to control acoustic radiation force profiles in layered resonators, J. Acoust. Soc. Am. 114 (2003) 2654. doi:10.1121/1.1616581.

[30] M. Groschl, Ultrasonic Separation of Suspended Particles - Part II: Design and Operation of Separation Devices, Acoustica. 84 (1998) 632–642.

[31] P. Glynne-Jones, R.J. Boltryk, M. Hill, Acoustofluidics 9: Modelling and applications of planar resonant devices for acoustic particle manipulation., Lab Chip. 12 (2012) 1417–26. doi:10.1039/c2lc21257a.

[32] B. Hammarström, T. Laurell, J. Nilsson, Seed particle-enabled acoustic trapping of bacteria and nanoparticles in continuous flow systems., Lab Chip. 12 (2012) 4296–304. doi:10.1039/c2lc40697g.

[33] P. Glynne-Jones, C.E.M. Démoré, C. Ye, Y. Qiu, S. Cochran, M. Hill, Array-controlled ultrasonic manipulation of particles in planar acoustic resonator., IEEE Trans. Ultrason. Ferroelectr. Freq. Control. 59 (2012) 1258–66. doi:10.1109/TUFFC.2012.2316.

[34] C.J. Easley, J.A.C. Humphrey, J.P. Landers, Thermal isolation of microchip reaction chambers for rapid non-contact DNA amplification, J. Micromechanics Microengineering. 17 (2007) 1758–1766. doi:10.1088/0960-1317/17/9/002.

[35] J. Svennebring, O. Manneberg, P. Skafte-Pedersen, H. Bruus, M. Wiklund, Selective bioparticle retention and characterization in a chip-integrated confocal ultrasonic cavity., Biotechnol. Bioeng. 103 (2009) 323–8. doi:10.1002/bit.22255.

[36] a Lenshof, M. Evander, T. Laurell, J. Nilsson, Acoustofluidics 5: Building microfluidic acoustic resonators., Lab Chip. 12 (2012) 684–95. doi:10.1039/c1lc20996e.

[37] J. Hultström, O. Manneberg, K. Dopf, H.M. Hertz, H. Brismar, M. Wiklund, Proliferation and viability of adherent cells manipulated by standing-wave ultrasound in a microfluidic chip., Ultrasound Med. Biol. 33 (2007) 145–51. doi:10.1016/j.ultrasmedbio.2006.07.024.

[38] J.D. Adams, C.L. Ebbesen, R. Barnkob, A.H.J. Yang, H.T. Soh, H. Bruus, High-throughput, temperature-controlled microchannel acoustophoresis device made with rapid prototyping, J. Micromechanics Microengineering. 22 (2012) 075017. doi:10.1088/0960-1317/22/7/075017.

[39] J.C. McDonald, G.M. Whitesides, Poly(dimethylsiloxane) as a material for fabricating microfluidic devices., Acc. Chem. Res. 35 (2002) 491–9.

[40] P. Kim, K. Kwon, M. Park, S. Lee, S. Kim, K. Suh, Soft lithography for microfluidics: a review, 2 (2008) 1–11.

[41] H.-B. Liu, H.-Q. Gong, Templateless prototyping of polydimethylsiloxane microfluidic structures using a pulsed CO 2 laser, J. Micromechanics Microengineering. 19 (2009) 037002. doi:10.1088/0960-1317/19/3/037002.

[42] M. a. Unger, Monolithic Microfabricated Valves and Pumps by Multilayer Soft Lithography, Science (80-.). 288 (2000) 113–116. doi:10.1126/science.288.5463.113.

[43] J.N. Lee, C. Park, G.M. Whitesides, Solvent compatibility of poly(dimethylsiloxane)-based microfluidic devices., Anal. Chem. 75 (2003) 6544–54. doi:10.1021/ac0346712.

[44] Y.-H. Lin, S.-W. Kang, T.-Y. Wu, Fabrication of polydimethylsiloxane (PDMS) pulsating heat pipe, Appl. Therm. Eng. 29 (2009) 573–580. doi:10.1016/j.applthermaleng.2008.03.028.

[45] J. Monahan, a a Gewirth, R.G. Nuzzo, A method for filling complex polymeric microfluidic devices and arrays., Anal. Chem. 73 (2001) 3193–7.

[46] J. Dual, P. Hahn, I. Leibacher, D. Möller, T. Schwarz, Acoustofluidics 6: Experimental characterization of ultrasonic particle manipulation devices., Lab Chip. 12 (2012) 852–62. doi:10.1039/c2lc21067c.

[47] L. Johansson, M. Evander, T. Lilliehorn, M. Almqvist, J. Nilsson, T. Laurell, et al., Temperature and trapping characterization of an acoustic trap with miniaturized integrated transducers--towards in-trap temperature regulation., Ultrasonics. 53 (2013) 1020–32. doi:10.1016/j.ultras.2013.01.010.

[48] S.M. Hagsäter, a Lenshof, P. Skafte-Pedersen, J.P. Kutter, T. Laurell, H. Bruus, Acoustic resonances in straight micro channels: beyond the 1D-approximation., Lab Chip. 8 (2008) 1178–84. doi:10.1039/b801028e.

[49] P. Augustsson, R. Barnkob, S.T. Wereley, H. Bruus, T. Laurell, Automated and temperature-controlled micro-PIV measurements enabling long-term-stable microchannel acoustophoresis characterization., Lab Chip. 11 (2011) 4152–64. doi:10.1039/c1lc20637k.

[50] O. Dron, J.-L. Aider, Acoustic energy measurement for a standing acoustic wave in a micro-channel, EPL (Europhysics Lett. 97 (2012) 44011. doi:10.1209/0295-5075/97/44011.

[51] T. Lilliehorn, M. Nilsson, U. Simu, S. Johansson, M. Almqvist, J. Nilsson, et al., Dynamic arraying of microbeads for bioassays in microfluidic channels, Sensors Actuators B Chem. 106 (2005) 851–858. doi:10.1016/j.snb.2004.07.003.

[52] B. Vanherberghen, O. Manneberg, A. Christakou, T. Frisk, M. Ohlin, H.M. Hertz, et al., Ultrasound-controlled cell aggregation in a multi-well chip., Lab Chip. 10 (2010) 2727–32. doi:10.1039/c004707d.

[53] C. Demore, Y. Qiu, S. Cochran, P. Glynne-Jones, C. Ye, M. Hill, Transducer arrays for ultrasonic particle manipulation, 2010 IEEE Int. Ultrason. Symp. (2010) 412–415. doi:10.1109/ULTSYM.2010.5935702.

[54] J.J. Hawkes, S. Radel, Acoustofluidics 22: multi-wavelength resonators, applications and considerations., Lab Chip. 13 (2013) 610–27. doi:10.1039/c2lc41206c.

[55] J. Dual, P. Hahn, I. Leibacher, D. Möller, T. Schwarz, J. Wang, Acoustofluidics 19: ultrasonic microrobotics in cavities: devices and numerical simulation., Lab Chip. 12 (2012) 4010–21. doi:10.1039/c2lc40733g.

[56] M. Hill, N. Harris, Ultrasonic microsystems for bacterial cell manipulation, … Biosensors, Recognit. Recept. Microsystems. (2008). doi:10.1007/978-0-387-75113-9_35.

[57] M.S. Limaye, W.T. Coakley, Clarification of small volume microbial suspensions in an ultrasonic standing wave., J. Appl. Microbiol. 84 (1998) 1035–42.

[58] B. Lipkens, J. Dionne, M. Costolo, A. Stevens, E. Rietman, Separation of bacterial spores from flowing water in macro-scale cavities by ultrasonic standing waves., J. Acoust. Soc. Am. 128 (2010) 2338. doi:10.1121/1.3508271.

[59] H. Bruus, Acoustofluidics 2: Perturbation theory and ultrasound resonance modes., Lab Chip. (2011) 20–28. doi:10.1039/c1lc20770a.

[60] M. Sinha, D. Buckley, Acoustic Properties of Polymers, in: J. Mark (Ed.), Phys. Prop. Polym. Handb. SE - 60, Springer New York, 2007: pp. 1021–1031. doi:10.1007/978-0-387-69002-5_60.

[61] C.J. Easley, L. a Legendre, M.G. Roper, T. a Wavering, J.P. Ferrance, J.P. Landers, Extrinsic Fabry-Perot interferometry for noncontact temperature control of nanoliter-volume enzymatic reactions in glass microchips., Anal. Chem. 77 (2005) 1038–45.

[62] D.C. Leslie, E. Seker, L. a L. Bazydlo, B.C. Strachan, J.P. Landers, Platinum nanoparticle-facilitated reflective surfaces for non-contact temperature control in microfluidic devices for PCR amplification., Lab Chip. 12 (2012) 127–32. doi:10.1039/c1lc20779b.

[63] C. Ke, A.-M. Kelleher, H. Berney, M. Sheehan, A. Mathewson, Single step cell lysis/PCR detection of Escherichia coli in an independently controllable silicon microreactor, Sensors Actuators B Chem. 120 (2007) 538–544. doi:10.1016/j.snb.2006.03.019.

[64] D. a Drevets, P. a Campbell, Macrophage phagocytosis: use of fluorescence microscopy to distinguish between extracellular and intracellular bacteria., J. Immunol. Methods. 142 (1991) 31–8.

[65] A. Germini, A. Masola, P. Carnevali, R. Marchelli, Simultaneous detection of Escherichia coli O175:H7, Salmonella spp., and Listeria monocytogenes by multiplex PCR, Food Control. 20 (2009) 733–738. doi:10.1016/j.foodcont.2008.09.010.

[66] P. Augustsson, C. Magnusson, M. Nordin, H. Lilja, T. Laurell, Microfluidic, label-free enrichment of prostate cancer cells in blood based on acoustophoresis., Anal. Chem. 84 (2012) 7954–62. doi:10.1021/ac301723s.

[67] Y. Xia, Z. Hua, E. Gular, Minimizing the Surface Effect on PCR in PDMS-Glass Chips by Dynamic Passivation, 2005 Annu. …. (2005).

[68] W.H. Grover, M.G. von Muhlen, S.R. Manalis, Teflon films for chemically-inert microfluidic valves and pumps., Lab Chip. 8 (2008) 913–8. doi:10.1039/b800600h.

[69] P. Glynne-Jones, R.J. Boltryk, N.R. Harris, A.W.J. Cranny, M. Hill, Mode-switching: a new technique for electronically varying the agglomeration position in an acoustic particle manipulator., Ultrasonics. 50 (2010) 68–75. doi:10.1016/j.ultras.2009.07.010.

[70] T. Laurell, F. Petersson, A. Nilsson, Chip integrated strategies for acoustic separation and manipulation of cells and particles., Chem. Soc. Rev. 36 (2007) 492–506. doi:10.1039/b601326k.

6 Ultrasound-Mediated Heating for Cell Lysis and PCR

6.1 Abstract

The development of a platform for cell handling using resonant ultrasound will be described in this chapter. The ability to precisely (and gently) manipulate small populations of cells could be enormously useful for emergent biomedical techniques (e.g., gene therapy for cancer treatment[1,2]). When ultrasound is applied to a microfluidic device, the small water-filled chambers in the device can resonate and maintain a standing acoustic pressure wave[3]. Cells exposed to this acoustic field experience a force towards the nodes of the standing wave, and these acoustic forces can be used to trap and hold cells within a microfluidic chamber. Experimental results of acoustic trapping of bacterial pathogens and a cancer cell line will be presented. Moreover, the ultrasound intensity could be increased to induce heating by driving the system near its optimal resonance frequency. Ultrasound-induced heating was utilized both for cell lysis and for successful PCR amplification of a DNA template via thermal cycling. This multi-functional device for cell trapping, cell lysis, fluidic mixing, and PCR thermal cycling has the potential to simplify integration of bioanalytical processes need for a microfluidic genetic analysis system.

6.2 Introduction

Cell handling is an essential step in many bioanalytical and biological methods, and as described in the previous chapter, acoustic trapping is an attractive technology for non-contact manipulation of cells within a microfluidic device. Acoustic trapping is particularly well-suited to working with of small quantities of important or rare cells (e.g., circulating tumor cells). Determination of operational parameters for extended functionality (e.g., mixing of fluid lamina, simultaneous histological examination during acoustic trapping, thermally-activated cell lysis for preparation of cellular contents, thermal cycling for PCR, and even built-in thermometry) would add significant value to the acoustic trapping apparatus. Additionally, a demonstration of multi-functionality would provide a path for integration of multiple steps of a bioanalytical workflow on a single microfluidic device.

The objectives of this work were to improve all parts of the microfluidic acoustic trapping apparatus (Figure 6.1) introduced in the previous chapter. The quality of contact between the microfluidic device and the ultrasonic transducer is a key determinant of system performance. A new generation of printer circuit board-mounted ultrasonic transducers were developed in hopes of increasing the reproducibility of microfluidic device alignment and clamping. Excessive heat generation during acoustic trapping is a well-known problem in acoustofluidics because additional heat tends to destabilize the acoustic resonance and degrade cell handling performance. In fact, a number of cooling strategies for acoustofluidics have been described[4–6]. Given our research group's familiarity with PCR, instead of minimizing the generation of heat, we wondered if we

could control it, and even select for heat generation to achieve the high temperatures (i.e., near the boiling point of water) needed for PCR. Piezoelectric devices purpose-built for heat generation have been described for isolated transducers[7] and droplet-based surface acoustic wave technology[8], but a single device for both cell trapping and (intentional) ultrasonic heating for lysis and PCR has not yet been described elsewhere. As this chapter will show, the acoustic trapping system was actually a multi-functional unit, capable of cell trapping, microscopic cell analysis, microscale fluid mixing, bundling of genomic DNA into condensed cluster via acoustic microstreaming, single-cell and batch-mode cell lysis, and PCR amplification.

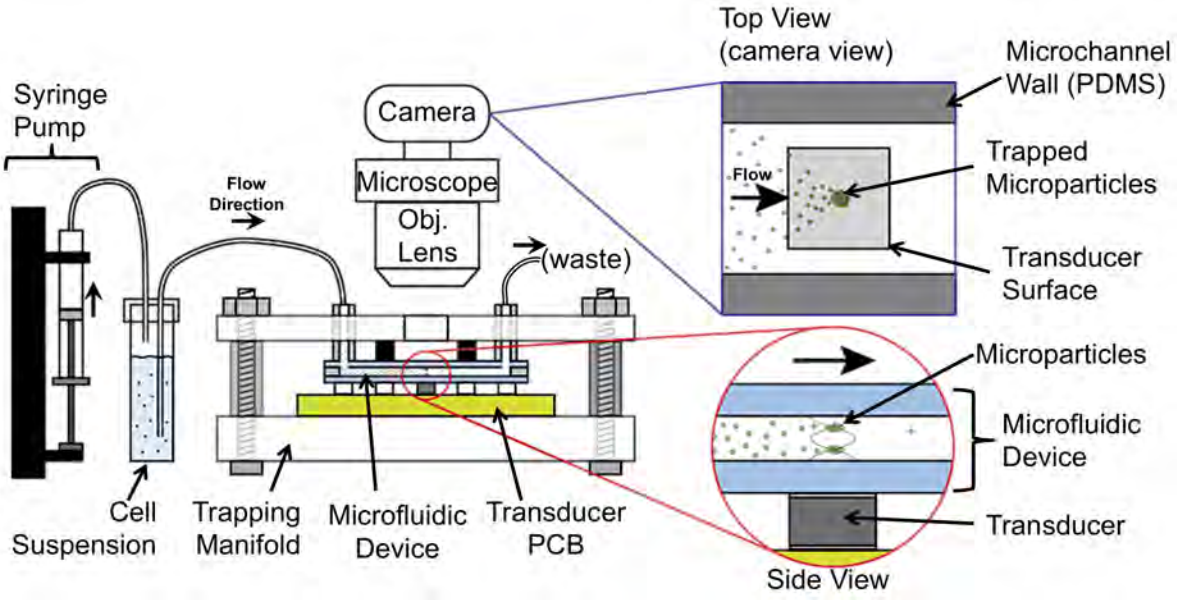

Figure 6.1: Overview of acoustic trapping apparatus.

6.3 Materials and Methods

6.3.1 Transducer Fabrication

6.3.1.1 PCB-Mounted PZT Transducers

Printed circuit boards were designed simultaneously with microfluidic devices and

clamping manifolds to generate a coherent computer model prior to fabrication. Printed circuit board patterns were designed in CorelDRAW 12 and printed on Pulsar toner transfer paper (www.pcbfx.com) with a HP LaserJet 4000 printer. The toner pattern was transferred to copper-clad circuit board (FR4 Glass Epoxy Resin, 1 oz. (0.0014" thick) copper, Philmore, Part # PCB35) using a consumer iron operated at ~135 °C. Water was used to release the toner transfer paper, and then any exposed copper (not protected by the toner mask) was etched away with persistent manual application of copper etchant (Radio Shack) with a cellulose sponge. Holes were drilled in the etched PCBs for the manifold mounting points and the transducer air backing. Next the toner mask was removed with acetone and the copper was polished with fine grit sand paper to remove oxidized copper prior to mounting of PZT elements.

PZT discs have been successfully diced into small shapes using a semiconductor wafer saw[9,10], but this equipment was not readily available so alternative and available methods were tested. PZT disks (5 MHz nominal thickness mode resonance, Steiner and Martins Inc, SM111) were diced by carefully aligning a metal cutting guide over the PZT disc and repeated scoring it using a capillary cutting stone. Manual of dicing the PZT material was both error-prone due to unpredictable ceramic breakage and it was very time consuming due to the repetitive score and level of precision required. Laser ablation, as generally described in **Chapter 4**, was used to score PZT discs for precise snapping into smaller pieces. The effects of CO_2 laser ablation on PZT has been explored previously [11], but the application and performance metrics were significantly different than those described here. The chief concern with using IR radiation to dice the PZT is that the PZT will lose its electrical polarization above a certain temperature (it's Curie

temperature). For the PZT material used in this process (7 MHz, SM111/PZT-4, Steiner and Martins Inc.), the Curie temperature was listed as roughly 250 °C. Similar to glass, bare PZT tended to crack during laser ablation, so pressure sensitive adhesive (3M, Scotch MagicTape™) was applied to the PZT disks prior to laser processing. PZT ceramic disks were scored using laser ablation (VersaLasesr 350, Universal Laser Systems Inc.; vector mode, 10% power, 5% speed, 1000 PPI) and gaps were etched into the electrodes on one side (10% power, 10% speed, 1000 PPI). Electrode gap fidelity was verified by checking the electrical connectivity across the gap. Following laser scoring and modification, the individual PZT slabs were gently snapped apart along the score lines.

Stacking of piezoelectric materials is commonplace in piezoelectric actuators, and while it significantly narrows the applicable bandwidth of the transducer, this configuration of PZT elements should also give a much stronger acoustic pressure when the entire structure is in resonance. A stack of 2 laser-processed PZT elements was constructed on a PCB identical to the single-site layout described above. The PZT polarities were matched up and the PZT elements were fastened to each other and to the PCB using conductive epoxy.

A multiplexed transducer with 4 individually addressable trapping sites was constructed via a modified fabrication scheme from the single 5 MHz transducers. Using the manual-switching device, the 4 trapping sites were powered in parallel from a single set of driving electronics. Electrical connections between the top electrode and the PCB traces were made using 25 μm diameter platinum wires that was laid in a trench etched in the PZT surface, and the trench was filled with conductive epoxy. The resistance between the PZT top electrodes and the terminal contact of the PCB was too low to be measure,

indicating a very good electrical connection despite the fine gauge wire. A manual switching device was also constructed to allow individual connection of the 4 PZT sites (in parallel) to a single BNC connector input.

An alternative PZT mounting strategy was explored where conductive (carbon-filled) silicone elastomer (Stockwell Elastomerics, 0.020, EC2040, 40D, T819) was placed between the transducer element and the PCB. PZT discs resonant at 10 MHz (Meggitt Ferroperm Piezoceramics, PZ-26 disk, 7 mm o.d., 0.20 mm thick, Part # F1260160, Product # 05/0786) with wrap-around electrodes were manually scored and snapped into roughly pieces with active regions of approximately 1 mm x 1.5 mm. The conductive silicone was shaped into a toroid and placed over the air backing hole already drilled into the PCB. The silicone and PZT were secured with a very small amount of silicone adhesive (Permatex 81730). Support posts of more conductive silicone and PZT shards were placed on the copper pads surrounding the trapping site. The microfluidic device was clamped agains the PCB, and the conductive silicone compressed and formed a self-leveling pedestal for the PZT.

6.3.2 Manifold Designs

The spacer height for the acoustic trapping manifolds was carefully established using a handheld micrometer (Anytime Tools Inc., Granada Hills, CA, USA; SKU# 203933). The 4 spacer posts were controlled to all be the same height (all were adjusted to 9.17 mm, with a measurement precision of 0.001 mm). Laser ablation rarely produces perfectly vertical holes, so through holes were cut for upright alignment posts and hex nuts and flat head machine screws were used to orient the alignment screws normal to the

PMMA base.

6.3.3 Equipment and Software

A suite of custom LabVIEW applications was developed to control the driving electronics during acoustic trapping. Instrument drivers in LabVIEW (furnished by Agilent, Tektronix, and National Instruments; respectively) were incorporated as low-level control modules. Importantly, the software was designed to log of all changes with a timestamp that can be used to accurately correlate observed phenomena (recorded on video) to the settings that caused the effects. System-wide millisecond time stamping was used to synchronize temperature measurements and parameter histories. A LabVIEW shared global variable was used to pass temperature data to the control software for active feedback control of temperature within the microchannel.

The waveform generator, oscilloscope, and amplifier circuitry were the same as described in **Chapter 5**. Oscilloscope probes (model Tektronix P2220) were used to measure the voltage on both sides of a 15 ohm resister placed in series with the PZT transducer to measure the voltage drop. The probes have a cutoff of 6 MHz when set to 1X attenuation. This resulted in much lower voltage readings at 10 MHz versus ~5.4 MHz. The 10X attenuation mode (with a reported cutoff frequency of 200 MHz) was not able to read the differential across the 15 ohm resistor with adequate resolution of the oscilloscope digitizer. The oscilloscope data acquisition program was improved to measure frequency and voltage at 3.33 Hz.

Temperature sensing electronics were the same as described in **Chapter 2**. Two measurement systems were operated simultaneously with separate DAQ cards. Forced air

cooling was used to limit remelting of hot melt adhesive used to seal around threaded thermocouples. External monitoring of temperature was implemented to reduced the amount of preparation required for microfluidic devices prior to use, and thermal grease (MG Chemicals 8615, non-electrically conductive boron nitride) was used to enhance heat flow between the microfluidic device and the thermocouple.

6.3.4 Syringe Pumps and Fluidic Connections

The syringe pumps were the same as those listed in **Chapter 5**. The key differences were the valving used in this work and addition of a stirred cell suspension tube to counteract cell settling. Microfluidic devices were connected to a pair of 4 way valves (Upchurch Scientific, Model V100T, 4.5 μL dead volume) to switch between sample infusion mode and a mode with short-circuited and connection to a nitrogen gas pneumatic line. Between cell trapping experiments, the fluidic system with rinsed with Cavicide disinfectant (or 10% bleach, if the microfluidic device was also decontaminated, to prevent PDMS swelling from isopropyl alcohol in the Cavicide) for 15 minutes via syringe pump infusion at 5 μL/min. Next, diH2O was flowed for 5 minutes at 20 μL/min.

6.3.5 Digital Video Microscopy

Optical monitoring of acoustic trapping was performed using an Olympus BXFM microscope mounted on a vibration isolation table. Epifluorescence microscopy was conducted with an HBO100 excitation source and either FITC or TRITC filter cubes. Cameras were mounted to the trinocular lens port of the microscope to document trapping experiments. Various cameras were evaluated: an analog color CCD camera

(Hitachi KP-D240) & VGA resolution USB frame grabber; a Celestron 44421 USB camera (typically acquired using the free ManyCam application for timestamping); the PixeLINK color CMOS camera described in Chapter 5; and finally a consumer camcorder (Sony HDR-CX260V) was mounted to the microscope using optics cube and rails and a 2X lens oriented for demagnification. The consumer camcorder produced either 60i or 60p videos in the AVCHD video codec (an extended variant of the standard H.264/AVC codec). Videos in 60i were typical, and these videos consisted of interlaced half frames (fields), acquired at 60 fields per second with 30 full frames captured per second. Post-processing of 60i video for particle trapping studies was conducted using the open source Avidemux (version 2.6.6) and VLC (version 2.1.4) software packages.

6.3.6 Microfluidic Acoustic Resonators

6.3.6.1 Construction

For detailed information on the fabrication of GPG microfluidic devices, please refer to Chapter 4 and Chapter 5. In brief, fluidic channels were through-cut in PDMS presented briefly here: fluidic channels were cut in sheets of silicone elastomer (HT6240, Stockwell Elastomerics, nominal thickness of ~280 μm) via laser ablation. The PDMS layers were sandwiched between glass sheets (#1 coverglass, ~150 μm for the bottom plate and #2 cover glass, ~220 μm for top plate) to create a resonant chamber.

6.3.6.2 Passivation

Previous studies by our group and others have indicated that bare glass surfaces are strong inhibitors of PCR[12,13]. Passivation of the microdevice surfaces was performed prior to cell trapping, lysis, and PCR. Covalent surface passivation was

performed using SigmaCote silanizing reagent (Sigma). During device assembly, the glass layers were treated with piranha solution to remove the anti-clumping coating applied to most coverglass types. SigmaCote is a proprietary organosilane in heptane, and the heptane quickly swells PDMS. This was problematic for 2 reasons: 1) the heptane would rapidly swell the PDMS layer of an assembled GPG device to cause distortions of the fluidic architecture, and in some cases, cracking of the glass layers due to localized swelling; and 2) solvent swelling of the PDMS layer would alter the height of the resonant cavity and thus the optimal WFG frequency. After SigmaCote treatment microfluidic devices were given at least a day at 55 °C for the heptane to evaporate (or at least evenly distribute within the entire PDMS layer). Polyethylene glycol (PEG) pre-coating and dynamic passivation have been reported to improve PCR efficiency within glass and PDMS microfluidic devices[14,15]. A working stock of 10% w/v solution (10 g per 100mL) PEG 10000 (Sigma-Aldrich) was prepared by dissolving 0.1 g per 1 mL of nuclease-free diH2O. Active debubbling of GPG devices was conducted at 5 psi for several minutes until bubbles were no longer visible.

6.3.7 Cell Culture and Handling Procedures

PC3 (ATCC® CRL1435TM) were cultured according to manufacturer guidelines. PC3 cells were counted using Beckman Coulter Z1 Coulter Particle Counter with a 100 μm aperture. Cell counts during cell passaging were typically ~= 350,000 cells (>5 um)/mL; 262,000 cells (5>size>19.8 um)/ml; 91,000 cells (>19.8 um)/mL. Removal of cell debris was performed if required by allowing the cell suspension to settle due to gravity alone for 15 minutes, and then gently pipetting up the cell pellet and adding it to new PBS buffer.

PC3 cells were labeled using a cell-permeable, blue-excitable DNA intercalating dye (Syto 11, Invitrogen). Cells fluoresced brightly after incubating for >= 15 minutes in 10 mM Syto11 (e.g., 2 uL of 5 mM syto 11 into 1 mL 1X PBS with 0.1X growth media with 35,000 cells >5 μm/mL). No washing of cells to unbound dye was required due to the large selective increase in quantum yield upon DNA binding. The extent of photobleaching depended on the incubation time (and DNA concentration in the irradiated area), but photobleaching of nuclei of stained PC3 cells was not obvious after >2 mins of illumination. To minimize photobleaching, the illumination intensity was reduced whenever possible using the microscope controls. Buccal cells were obtained by swabbing the inside of one cheek for 30 seconds, followed immediately by elution of the swab contents in 100 μL of PBS media. Cell suspensions were infused via syringe pump.

6.3.8 Ultrasonic Heating for Lysis and PCR

The temperature within the acoustic resonator was controlled by modulation of the driving frequency, the applied voltage, and the duty cycle activation. Cell lysis was achieved by first infusing lysis reagents (PrepGEM Tissue, prepared per manufacturer recommendations, ZyGEM Inc and associated entities) past trapped cells, then applying ultrasound to raise the chamber temperature to the 75 °C optimal temperature of the thermophilic protease in the lysis solution. PCR reactions were performed using diluted PCR product that had been previously amplified from *Escherichia coli* genomic DNA. The PCR master mix and pre-passivation solution consisted of the following, with final concentrations in parentheses: [PCR Buffer (1X, includes 1.5 mM $MgCl_2$), BSA (0.2 μg/μL), $MgCl_2$ (additional 0.5 mM, final conc. of 2 mM), dNTPs (0.2 mM each),

Forward and Reverse *E. coli LamB* primers[16] (0.5 μM each), PEG10000 (0.4 % w/v), PCR product (Diluted 10000-fold to just below detectable level, conc. ~8 pM), ThermoScientific Phusion Phire polymerase (0.06 U/μL)]. Thermal cycling programs for tube control reactions were identical to those described in **Chapter 5**. PCR products were analyzed with using the Agilent 2100 Bioanalyzer and microchip gel electrophoresis (DNA 1000 series II) kits.

6.4 Results and Discussion

The findings reported in this section constitute novel extensions of, and evolution of, the acoustic trapping platform described in the preceding chapter. Several factors were considered in the redesigned acoustic trapping system illustrated in Figure 6.1. The basic functional unit of the acoustic trapping system, the piezoelectric transducer, was redesigned with the goals of optimizing the contact between the microfluidic resonators and the transducer surface. The fabrication scheme for the transducer was modified to a planar, printed circuit board mounted design that was functional and rapidly fabricated with widely available materials and tools. The microfluidic acoustic resonators were characterized in greater detail. The external electrical and computer controls for the tracking system were significantly improved by detailed synchronous collection of data, improvements to the digital video microscopy methods, and by automation via a suite of custom software. The combination of pneumatic and fluidic systems provided for facile bubble management and improved introduction of cells samples to the trapping site. The phenomenon of acoustic streaming was evaluated in greater detail and demonstrated for mixing of laminar fluid streams and of cells within the acoustic trap. The most significant

novel extension presented here is the precisely monitored and controlled generation of heat using resonant ultrasound. This ultrasound-mediated heating was utilized for preparation of DNA from a human cancer cell line, and it was used to conduct PCR application within the acoustic trapping chamber. These findings suggest that a highly functional, integrated bio analytical device could be operated by a small, simple, and low-cost ceramic ultrasonic transducer.

6.4.1 Printed Circuit Board Design and Fabrication

Printed circuit board (PCB)-mounted transducers were fabricated by carefully dicing piezoelectric disks into small elements and affixing them to a pattern of electrodes on the PCB (Figure 6.2A). To present a planar surface to the glass microfluidic device, scrap pieces of the same piezoelectric material were placed on isolated copper pads that served as support columns of equal height to the transducer. A photograph of a representative PCB transducer is shown in Figure 6.2B with annotation. The raw piezoelectric transducer material did not feature wraparound electrodes, so perfectly flat electrical connections between the top electrode surface and the copper trace on the PCB were achieved with either conductive epoxy (similar to that used in **Chapter 5**) Figure 6.3A,B, or with very fine gauge (25 μm) platinum wire Figure 6.3C,D. Design iterations initially included silver conductive paint, but it was found that prolonged exposure to glycerol would cause the bond to fail.

An additional configuration of ultrasonic transducer was used where a thin conductive silicone pad was placed between the PCB copper traces and the PZT instead of conductive adhesive. This arrangement resulted in a self-leveling PZT support that

likewise resulted in good flat contact between the transducer top surface and the microfluidic device. Given that copper has a very high thermal conductivity, it is possible that this arrangement was beneficial because the relatively low thermal conductivity of the conductive silicone likely restricted heat flow from the transducer/chip into the PCB. However, the conductive silicone had low surface energy and it could not be held in place by conductive adhesive.

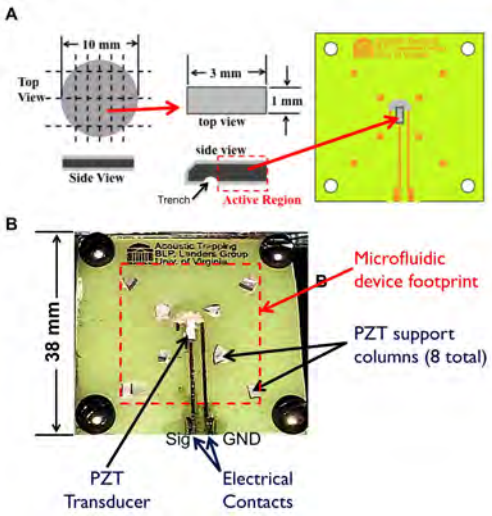

Figure 6.2. Layout of printed circuit board for ultrasonic transducer.

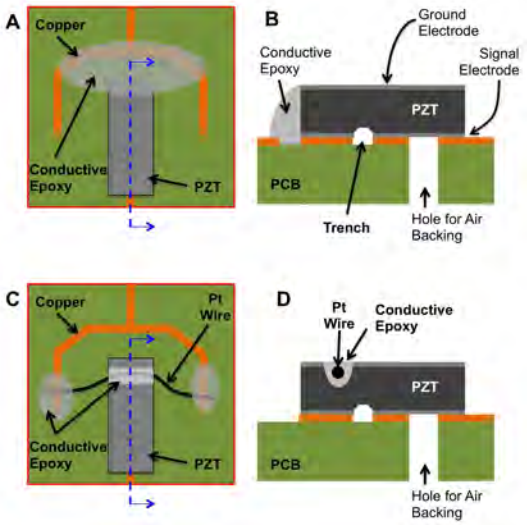

Figure 6.3. Detail of wrap-around electrode fabrication methods.

6.4.2 Design and Characterization of Microfluidic Acoustic Resonators

Glass-PDMS-glass microfluidic devices were designed specifically with high-heat applications in mind. As shown in Figure 6.4A, a special access port was made of the thermocouple wire to exit the microdevice. The beveled channel entrances that allow threading of thermocouples into a microfluidic chip were not possible in this layered design. Moreover, the silicone fluidic interconnections precluded threading thermocouples through the access holes in the top of the device. The microchannel was then sealed around the thermocouple wire. The seal proved to be a recurring problem. A

microdevice with threaded and sealed thermocouple (Figure 6.4B) allowed for insertion of a miniature (~75 μm diameter wire) thermocouple into the microfluidic chamber (Figure 6.4C). A second microfluidic device design was used that featured an etched access channel (Figure 6.4D) for removal of trapping chamber contents while bypassing the dead volume of the typical fluidic connections. The fluidic dead volume of the system was estimated by recording the time required for a dye solution to flow (as a constant volumetric flow rate) from the trapping site to the tubing outlet. For instance, a front of visible dye took 32.36 sec. when aspirated at rate at 0.6 mL/hr, so the dead volume of approximately half of the microchip volume and outlet tubing was estimated to be 6.06 μL. Both designs of GPG chip were utilized in this work for acoustic trapping and lysis, while only the design in Figure 6.4A-C was used for thermal cycling.

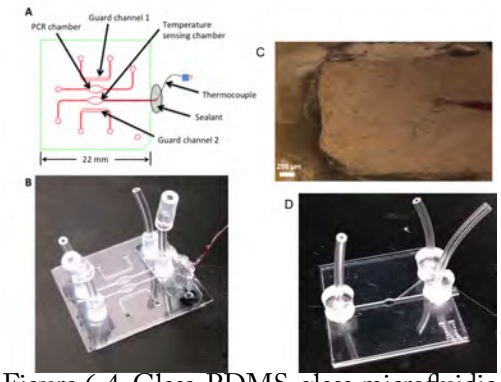

Figure 6.4. Glass-PDMS-glass microfluidic acoustic resonators.

Computer modeling of the microfluidic device in COMSOL indicated that multiple strong modes were possible in the water-filled chamber near 5 MHz (Figure 6.5A). Moreover, resonance modes with the PDMS sidewalls were also predicted (Figure 6.5B), this is corroborated by the recent used of acoustic standing waves traveling through both water and PDMS phases simultaneously[17].

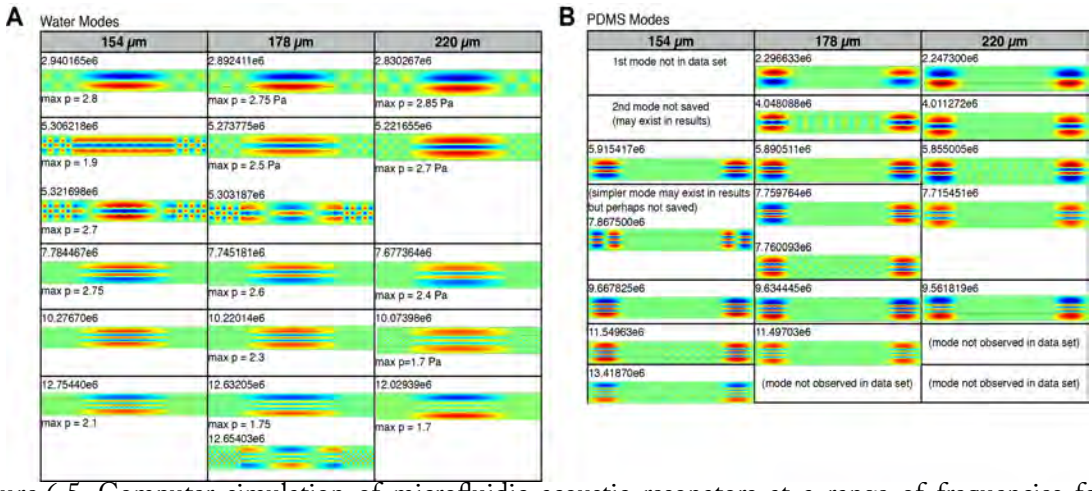

Figure 6.5. Computer simulation of microfluidic acoustic resonators at a range of frequencies for 3 thickness of the glass carrier/refelector layers.

Variability in thickness of glass used for the reflector (top plate) the carrier layer (bottom plate) layers of the GPG microdevices was assessed by measuring a random sample of coverslips (Figure 6.6). The range of coverslip thicknesses indicate that, within a given box of coverslips, coverslips can be effectively characterized by micrometer during assembly. The glass thickness were within manufacturer specifications. Ultimately, the most important resonance is the water chamber itself. Over my studies, I have observed, and published work by [3] that there is a tolerance of several hundred microns for the top glass layer. The allowable frequencies for the microfluidic resonator only strongly depend on the glass thickness when the top reflector layer has a thickness within a few kHz of the

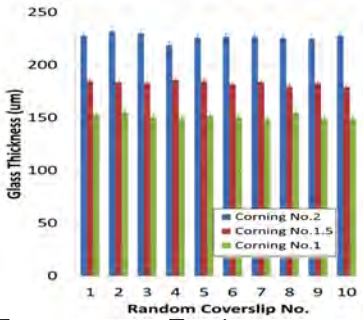

Figure 6.6. Evaluation of variation in glass layer thickness.

Table 6.1: Comparison of 3 replicate microfluidic acoustic resonators.

	Top glass layer thickness (μm)	Middle PDMS layer thickness (μm)	Bottom glass layer thickness (μm)	Optimal Frequency (MHz)
Chip1	186	287	182	5.4
Chip2	181	295	186	5.28
Chip3	181	285	182	5.4

λ/2 condition in glass[18,19]. A preliminary study of 3 GPG microdevices is summarized in Table 6.1, but the resonance characteristics were found to be significantly more complicated however, as described below.

6.4.3 Aligning Microfluidic Devices and Ultrasonic Transducers

Iterations of the acoustic trapping system were designed together – ultrasonic transducer, microfluidic device, and a manifold for aligning the parts together. Due to the fragility of the GPG microfluidic devices, the clamping force applied to the device and transducer had to be carefully controlled. A trapping manifold was designed with four alignment pins, four rigid steel spacers of equal height, and a clamping part with a deformable pad that applied a slight downward pressure on the microfluidic device. The manifold used in the majority of this work is described in Figure 6.7A-E. when the microfluidic device was placed on the transducer, and the hex nuts were tightened down against the spacer, the

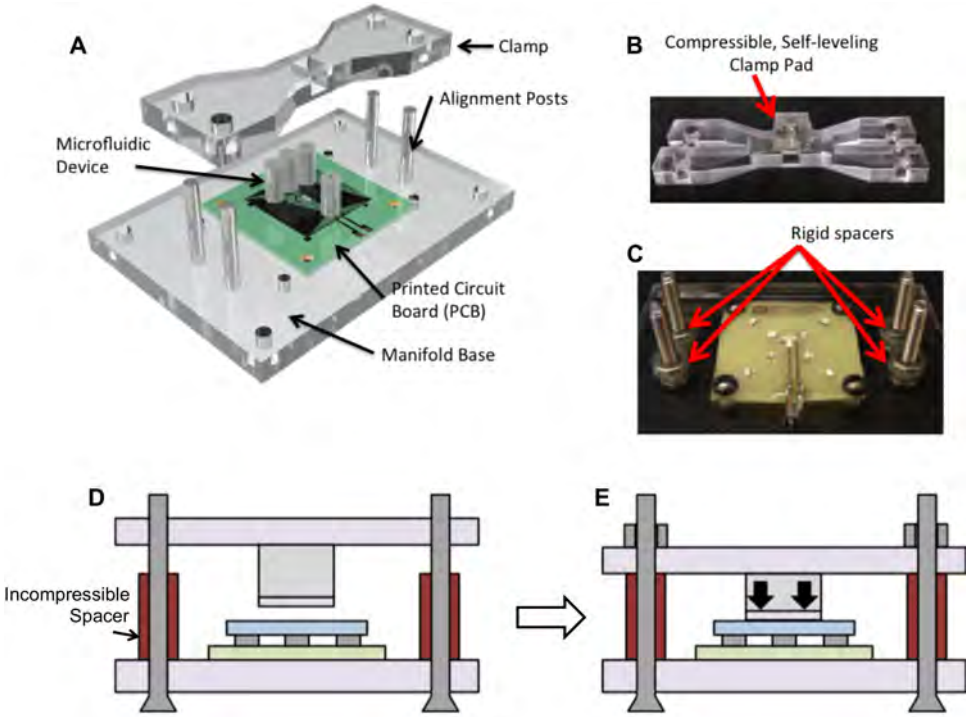

Figure 6.7. Alignment and clamping manifold for interfacing microfluidic devices and ultrasonic transducers.

microfluidic device was held in place firmly but without breakage. Optical access to the acoustic trapping chamber was afforded by a window cut into the clamping part. The microfluidic device and its associated fluidic connections, as well as the PCB and its associated electrical connections, were readily securely to the manifold baseplate for safe portability of these fragile and precisely-aligned components. Computer modeling system components allowed for maximal compatibility between the system components ,once fabricated, and an iterative design process was followed for troubleshooting and improvements.

6.4.4 Driving Electronics and LabVIEW Programs for Automated Control

The configuration of test equipment and custom computer control software allowed for flexible and autonomous operation of the acoustic trapping system. The system components (Figure 6.8A) was extended with a simple method of monitoring the power consumption of the ultrasonic transducer - the voltage drop across a resistor connected in series with the PZT was monitored using the oscilloscope (Figure 6.8B). A resistor value of 15 ohms was found to allow sufficient heating. Empirically determined maximum rates of data collection were 10 Hz for temperature and 3.33 Hz for readings of frequency and

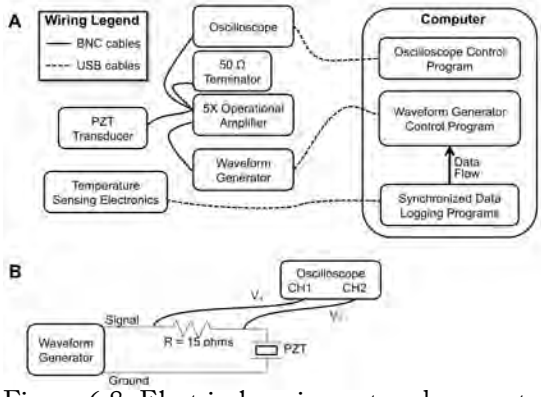

Figure 6.8. Electrical equipment and computer control schema.

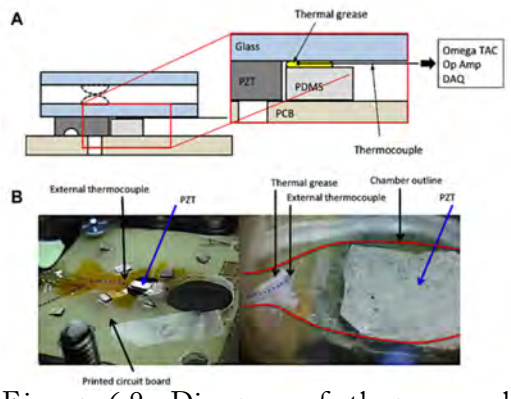

Figure 6.9. Diagram of thermocouple placement within the microchamber and against the microdevice exterior.

voltage drop across the resistor by the oscilloscope; the waveform generator was controlled asynchronously on demand. Both manual and automatic control was implemented, with automated control achievable through a scripting engine complete with feedback control of temperature as measured by thermocouples (Figure 6.9).

6.4.5 Digital video microscopy

Digital video was acquired through the microscope using a mounted consumer camcorder (Figure 6.10) that provided enough sensitivity and temporal resolution to capture movements of individual cells when Syto 11 fluorescence stain was used (Figure 6.11). With the recent release of the H.264 codec (and the Sony AVCHD implementation thereof), real-time compression of video data allows for frame rates of digital video twice that of traditional video capture rates (i.e., 29.97 frames-per-second to 59.93 frames per second) while increasing the number of pixels nearly seven-fold. While professional microscope cameras far exceed the performance specifications of this camera, a commercial grade CCD camera and hardware encoder such as this would be well suited for a portable microfluidic bioanalysis system featuring acoustic trapping. Moreover, two features proved to be unexpectedly useful during acoustic drop experiments: the ability to have an external monitor display the camera signal, and the synchronous acquisition of audio for easy notation and narration during experiments.

Figure 6.10. Incorporation of a consumer digital video camera with single cell visualization capability.

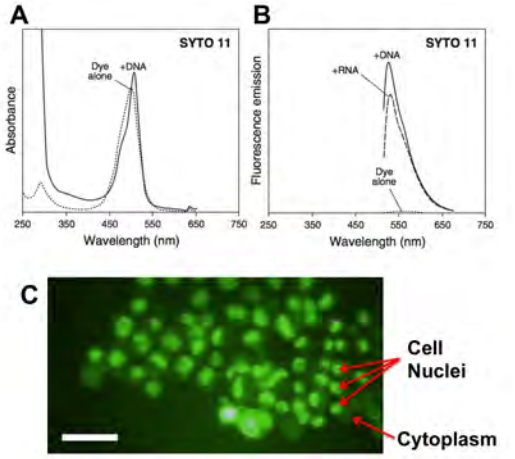

Figure 6.11. Fluorescence staining of PC3 cells with a cell-permeable DNA intercalating dye.

6.4.6 Fluidic and pneumatic connections

The rough surface of laser ablated microfluidic devices combined with gas permeability of PDMS necessitated some form of bubble suppression. A combined fluidic and pneumatic apparatus was devised (Figure 6.12A) to allow rapid switching between infusion of sample fluids and the pressurization of the microfluidic architecture with compressed nitrogen gas. Importantly, the fluidic path was "short-circuited" during pressurization by largely precluding differential pressure gradients between the 2 sides of the acoustic trapping chamber. Small air bubbles were almost inevitably present in the system when first filled with aqueous solution because numerous small

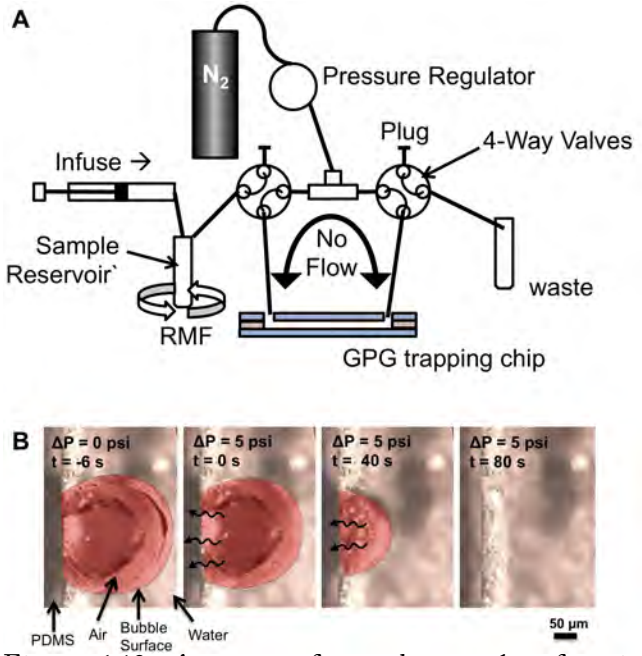

Figure 6.12. Apparatus for, and example of, active debubbling of the microfluidic chamber.

cavities in the PDMS side walls trapped micro bubbles because the advancing fluid could not readily wet such small hydrophobia pockets. Those same PDMS pockets were utilized as an exit path for trapped air, as shown in Figure 6.12B. Application of excessive pressure was problematic, however. Microchip cracking was caused by combination of laser ablation-induced cracks, chip clamping stresses, and pneumatic pressurization of the fluidic domain (10 psi often caused cracking). Nonetheless, pressurization at 5 psi was capable of both suppression of bubble growth and expulsion of bubbles.

6.4.7 Acoustic cell trapping

6.4.7.1 Evaluation of a stacked transducer prototype

During the iterative design of the acoustic trapping transducer to methods of piezoelectric element dicing were investigated. Manual dicing (Figure 6.13A) produced fairly unpredictable cleavage patterns, and thus a larger number of transducer elements had to be fashioned before a PZT block with acceptable geometry was obtained. In contrast, laser assisted ablation of piezoelectric discs produced fairly uniform blocks of PZT (Figure 6.13B). The prototype stacked PCB transducer was functional but performed worse than

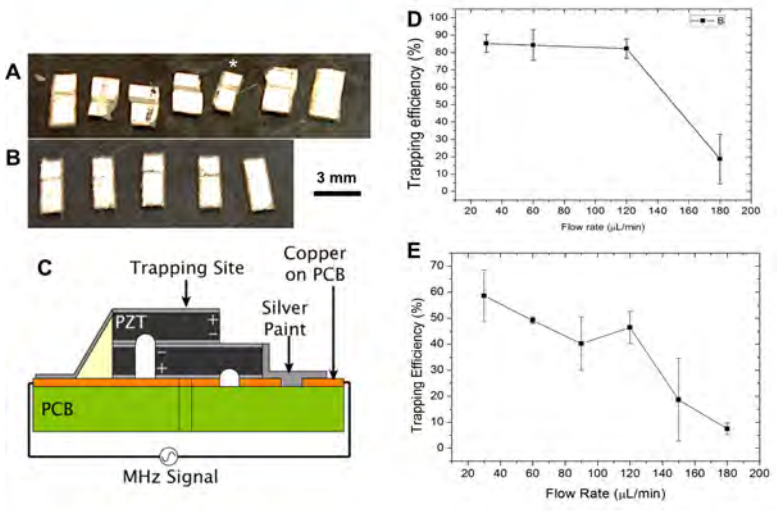

Figure 6.13. Evaluation of a prototype ultrasonic transducer based on its acoustic trapping performance.

the manually-diced single layer transducer described above (Figure 6.13C,D). Possible reasons for this degraded performance include a wider mismatch in resonant frequency of the transducer and the chip, acoustic energy losses due to impedance mismatches between the PZT material and the conductive epoxy used to bond the stack layers together, and reduced piezoelectric characteristics due to the laser ablation processing method used in its fabrication. The underlying causes of reduced performance were not investigated further because the original design was superior, but this information on the laser PZT dicing method and stacked transducer fabrication scheme are included here to better inform future researchers.

6.4.8 Acoustic Trapping of PC3 Cells

Acoustic driving studies were conducted on diluted suspensions of PC3 cancer cells. one replicate of a trap experiment is shown in Figure 6.14, where the 5 MHz transducer was used to trap PC3 cells flowing at an empirically optimized of rate up to 10 μL/min. acoustic trapping revealed that sells accumulated quickly in the pressure nodal planes (two vertical) of the ultrasonic standing wave established within the microfluidic device. interestingly the combination of incoming trajectory of cells in acoustic streaming was

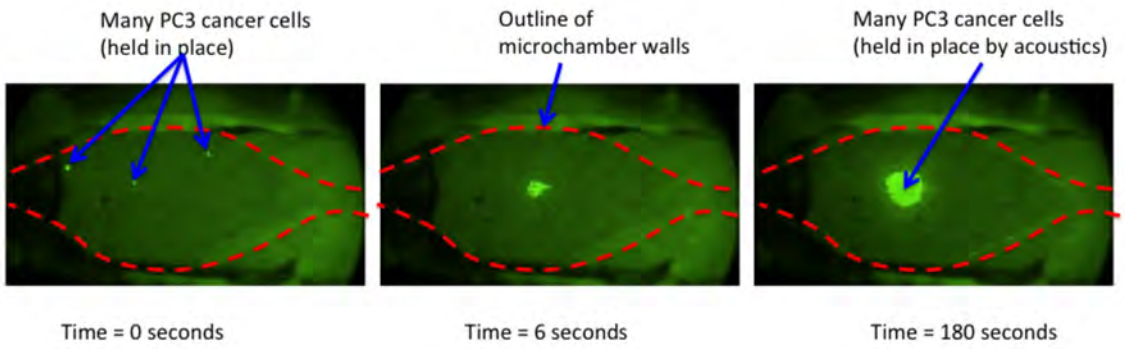

Figure 6.14. Trapping and enrichment of infused PC3 cells within the acoustic trap.

observed to deposit cells preferentially on one side of an aggregator trap cells, and this caused the cell mass to rotate in a steady clockwise pattern for an extended period of time. When the 10 MHz transducer and manifold and 20X objective were was used, it was possible to monitor the individual morphology and dynamics of cells within the acoustic trap. Trapping efficiency was initially low (~30%) while the aggregate of trapped cells was first being establish, but later the rate of acoustic trapping approached 100% as incoming cells were drawn towards the established cell cluster and retained due to secondary acoustic forces.

6.4.9 Acoustic Streaming for Microscale Mixing

Acoustic micro streaming was a nearly universal phenomenon within the GPG microfluidic acoustic resonators. This ultrasound-driven fluid flow was evaluated for promoting mixing between two parallel laminar flows. Two separate solutions of dye were infused at equal rates through a trifurcated microfluidic device Figure 6.15A (the middle channel was not used in this experiment). In absence of acoustic flow effects, the fluid level in the flowed past the trapping site with no additional mixing Figure 6.15B, but when moderate Figure 6.15C or intense Figure 6.15D ultrasound were applied the flows the evolution of a green mixed region was evident. Lastly, once the ultrasonic energy was switched off (Figure 6.15E) an unmixed, laminar flow pattern was restored.

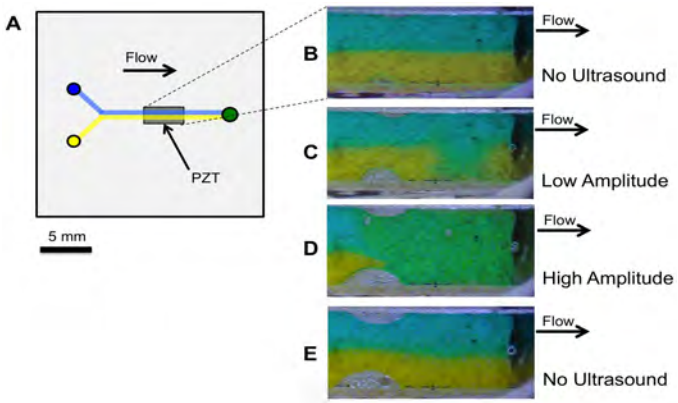

Figure 6.15. Demonstration of mixing 2 dye-containing laminar flows with acoustic microstreaming.

The same streaming vortices that were responsible for rapid mixing for fluid laminar were also effective for quickly exchanging the buffer medium surrounding cells within the acoustic trap. Streaming was a frequency dependent process, and it was observed that acoustic trapping could be conducted with little visible rotational component to trajectories of cells as they entered the device. However, when flow was stopped, the cells within the acoustic trap were able to be manipulated in chamber-scale rotational flows (Figure 6.16). This was utilized to ensure that a new buffer medium flowed past the trapped cell clusters was evenly distributed to individual cells. Microstreaming was a nearly constant phenomenon, so it is possible that the frequency shift caused the standing wave to weaken to the point that hydrodynamic forces were dominant. Following the mixing step the cells were able to be refocused. In the case of Figure 6.16, the new buffer was for cell lysis, so re-trapping may have been slower due to changes in the cell compressibility as they were attacked the detergents and protease in the lysis buffer. Rapid mixing of cells with a new buffer was useful for cell lysis experiments, but this functionality would also be useful for situations in which the cells needed to be washed. This could effectively serve as a microfluidic equivalent to the ubiquitous laboratory procedure of pelleting cells and resuspending them in new medium.

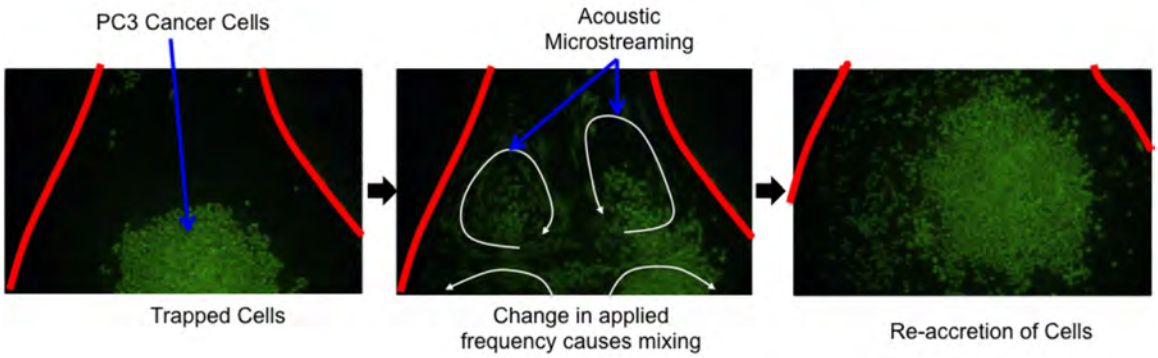

Figure 6.16. Buffer exchange and mixing via microstreaming in the acoustic trap.

6.4.10 Heating with Resonant Ultrasound

The acoustic energy of the resonant standing waves that were described above in the context of acoustic trapping was actually propagating in a lossy medium, so in addition to elastic propagation of the pressure wave some acoustic energy was absorbed and converted to heat. Empirical characterization of heating with resonant ultrasound revealed a dynamic and complex system with multiple resonant modes and rapid temperature transitions. The temperature within the microfluidic acoustic resonator strongly affected the resonant frequency, and in reciprocity, the amount of resonant acoustic energy strongly affected the production of heat. Stable temperatures were achieved when the rate of change of acoustic heat generation was close to zero and when that stable production of heat was counterbalanced by heat flow out of the resonator chamber. A variety of physical phenomena must be simultaneously considered, and the reader is invited to gradually study each physical phenomenon rather than rush to evaluate the system as a whole.

The rate of heat production was primarily determined by the intensity of acoustic energy in the microfluidic chamber and by efficiency of conversion between acoustic and thermal energy. The acoustic energy that was absorbed was converted to heat when the kinetic energy of the longitudinal pressure wave resulted in molecular rearrangements of polymers or bulk fluid movements. The conversion of acoustic energy to thermal energy is a complicated phenomenon for systems with several polymeric macromolecules (e.g., DNA, PDMS), and the specifics of the relevant physical phenomena are beyond the scope of this chapter. Note that this is an intensely studied phenomena with a variety of nonlinear physical effect that must be considered. Furthermore, ultrasonic hyperthermia

within tissue via high intensity (usually not resonant) ultrasound is an important biomedical technique[20–22]]. The devices used in this work were resonant devices filled with relaxing polymer molecules and rapid shear flows, and an empirical approach was favored to deal with the complexity of the underlying physical phenomena. The data sets generated in this work were accomplished for empirical evaluation of the effect of ultrasound on temperature.

6.4.10.1 Change in Resonant Frequency as a Function of Temperature

The resonant frequency of the device was found to be strongly temperature dependent. Achieving a self-limiting, steady-state elevated temperature (e.g., 95 °C needed to denature DNA) required time-sensitive modulation of the driving frequency to track the shift in resonant frequency with temperature. The bandwidth of the resonance peak was so narrow that if the self-sustaining resonance condition was lost the system temperature would fall precipitously.

The resonant frequency of the microchamber was found to decrease with temperature over the range of operating temperatures of approximately 50 - 98 °C. A plot of theoretical resonant frequency versus temperature Figure 6.17 shows the well known non-linear change of sound speed in water versus temperature. For example, a frequency of 5.28 MHz was used at 58 °C but heating to 95 °C

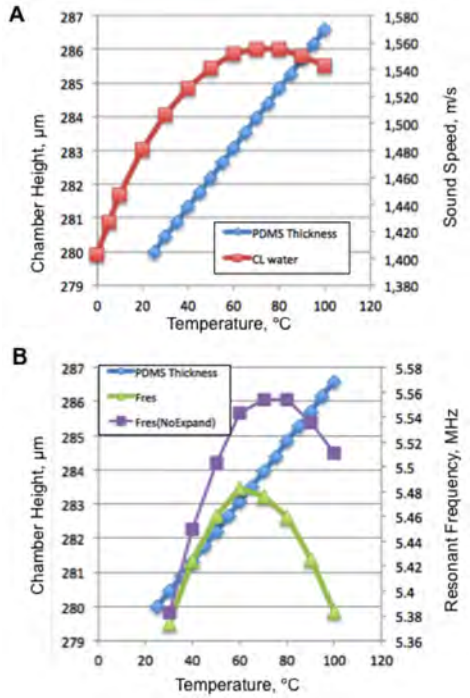

Figure 6.17. Calculated resonant frequencies as a function of temperature with and without accounting for thermal expansion of the microfluidic device.

required shifting the frequency down to 5.17 MHz. During the shift from 72 °C to 95 °C, a few steps in frequency were required (e.g., from 5.24 MHz used to hold 72 °C, to 5.22 MHz for 2 seconds to reach 82 °C, then to 5.18 MHz for 4 seconds until 94 °C was reached, then finally set to 5.17 MHz at a lower driving signal amplitude for a self-limiting temperature of 95 °C). Essentially, a ~100 kHz shift downward in signal frequency was needed to track the shift in resonance. Note that our colleagues [10] have reported a positive slope in the correlation between frequency and temperature, and while this may appear to be a discrepancy it is actually due to the shape of the sound speed versus frequency curve and a difference in which temperatures were evaluated.

6.4.10.2 Amplitude Self-Limiting Behavior

An interesting effect was observed when a shift in frequency was closer to the acoustic resonance of the system - the temperature would rapidly increase and then abruptly level off. This appears to be a form of self-attenuation. The physics of the system would definitely allow for higher temperatures (water could be boiled within the microfluidic device), but in some cases the temperature would, for instance, increase to 70 °C and hold. It was relatively insensitive to voltage, which may be because the electronics limited the driving signal or because the heat generation of transducer and resonator plateaued and an equilibrium between heat generation and heat dissipation was reached. This effect was an important aspect of temperature control by frequency modulation.

6.4.10.3 Several Resonant Modes were Observed

Layered acoustic resonators can have different resonances corresponding to individual layers[19,23]. If one layer of the structure is more resonant at the driving frequency then it will have a higher acoustic energy density than the others, and this translates to greater

heat generation in that layer. This effect was observed in 2 different ways. First, by examining the rate of change of temperature as a function of frequency while measuring the internal and external temperature; sometimes the external temperature sensor was heating up faster than the internal, which strongly suggests that heat was being preferentially generated in the glass layer or the piezoelectric transducer. Ultrasound resonance within the PDMS layer was likely at characteristic frequencies, but the lossy nature of PDMS itself may have led to stronger acoustic streaming as well. The frequency range covered by the most efficient heating (as judged by the required signal voltage) was the sharp resonance peak of the 1st harmonic vertical standing wave in the aqueous medium.

6.4.10.4 Investigation of the Effects of Temperature on Resonance

The strong temperature dependence of frequency presented experimental difficulties because an externally-controlled analog for the very localized acoustic heating would have caused significant problems. One approach would be to simply put the entire apparatus in a temperature controlled oven and scan through the control parameters at a range of temperatures. However, the integrity and characteristics of the manifold, circuit board, and microfluidic device could not be expected to withstand the temperature range of 60-95 ^{o}C; most likely the data obtained would be invalid for describing normal operating mode of the devices, but furthermore the high heat could have permanently damaged components of the apparatus.

To study the shift in system resonance as a function of temperature, acoustic heating was used to heat the device to known temperature and then apply a test condition. Two starting temperatures (58 ^{o}C and 72 ^{o}C) were chosen for pre-

equillibration points and the frequency was scanned several times to gather 3 replicates of data at each starting temperature (according to the algorithm in Figure 6.18A). The large plot of data in Figure 6.18B is from a study of ultrasonic heating versus frequency. One replicate scan for the 2 starting temperatures is shown in Figure 6.18C. The frequency of maximal heating shifted by approximately 20 kHz between 58 °C and 72 °C.

6.4.10.5 Temperature Control Strategies

The intensity of acoustic energy within the microfluidic device was controlled by modulating the electrical signal applied to the PZT transducer. Specifically, the 3 control strategies used were modulation of electrical signal amplitude, modulation the duty cycle of the applied signal, and/or modulation of how close the driving frequency was to the natural resonance of the microfluidic device. Higher signal voltages produced high temperatures in general, but some cases a voltage-independent plateau was reached where the temperature would no longer increase with increasing signal voltage. Generation of high temperatures with ultrasound required careful control of the driving frequency because the system would either drive itself out of resonance (resulting in amplitude self-limiting, possibly below the desired temperature). Alternatively, if the signal was shifted to new applied frequencies too far off resonance (and at a lower frequency than the resonance) then the system would lose resonance and the temperature would free fall to below PCR relevant temperatures.

Note that the system was not operated in perfect residence, but rather at a frequency just slightly higher due to amplitude self-limiting. Operating at resonance once the system was already at high temperatures would often result in excessive heating (e.g., to the boiling point at atmospheric pressure, or temperatures above 100 °C when the

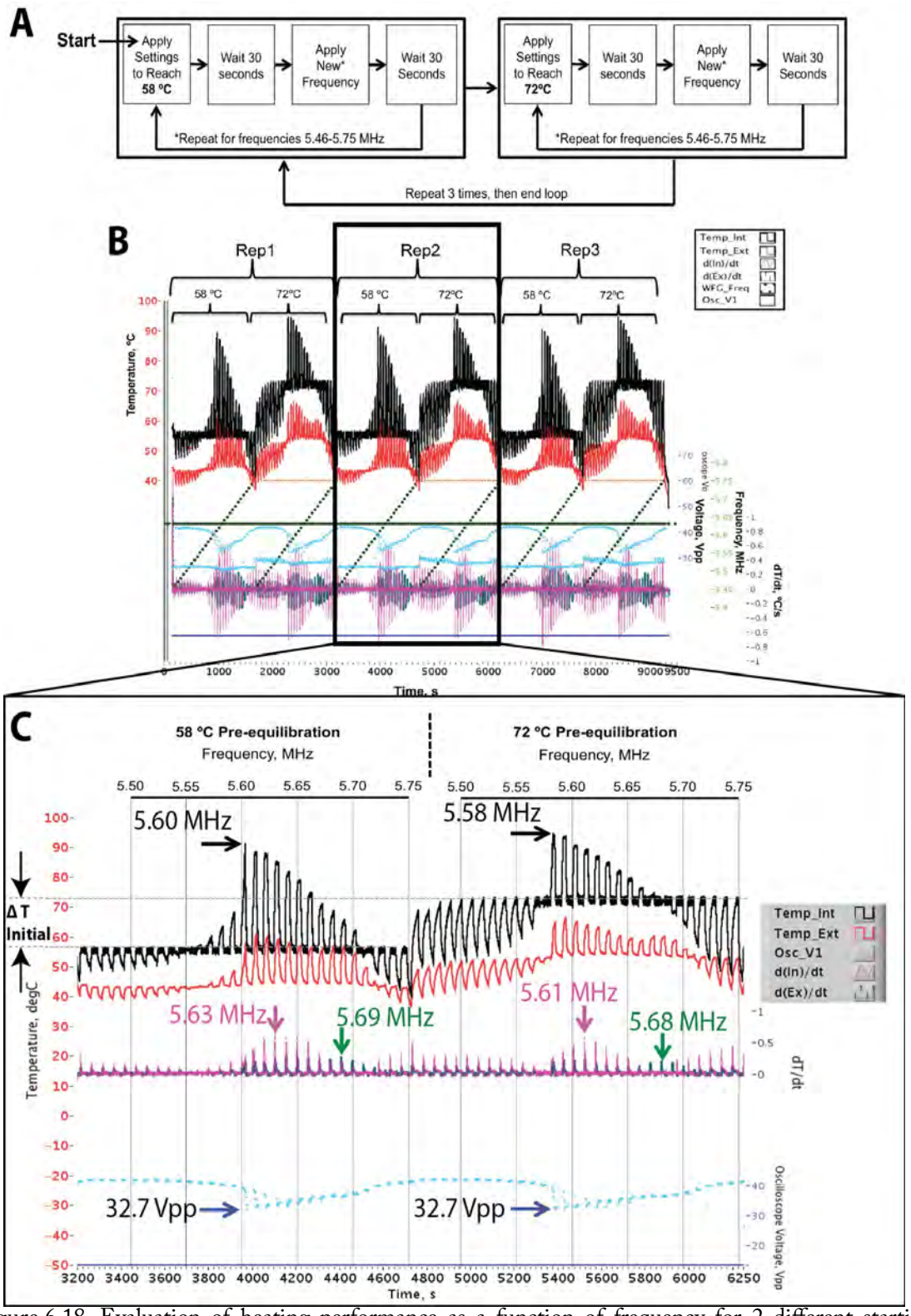

Figure 6.18. Evaluation of heating performance as a function of frequency for 2 different starting temperatures. A. Algorithm used to control waveform generator during test. B. Raw data annotated by replicate number and initial temperature. C. Annotated plot of data from the second replicate.

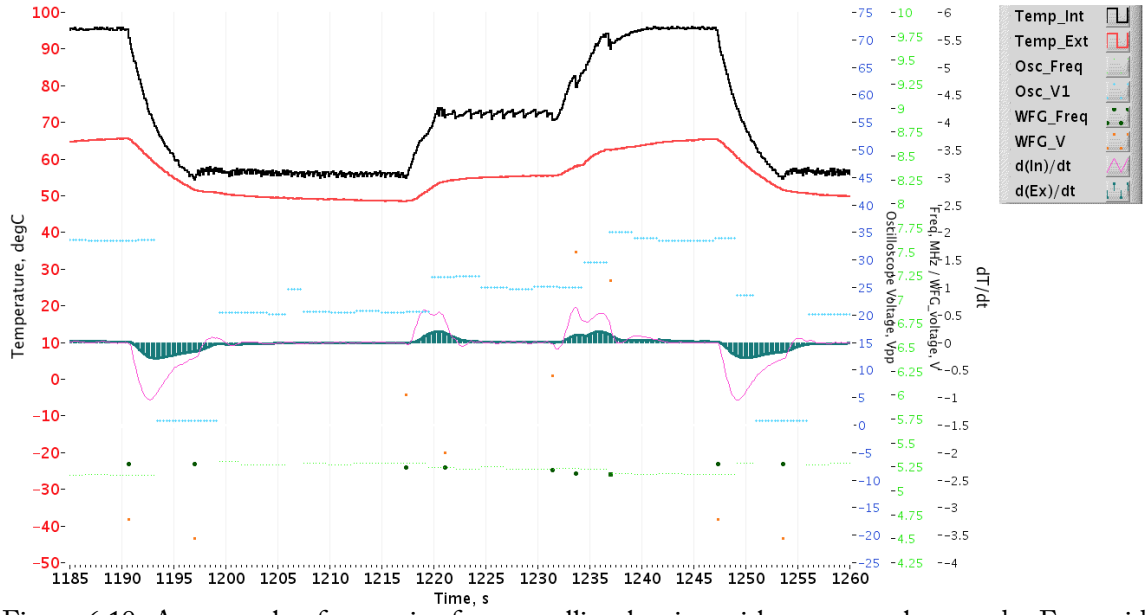

Figure 6.19: An example of strategies for controlling heating with resonant ultrasound. For rapid cooling the ultrasound was turned off for a prescribed amount of time (1190-1197 s), simple on/off duty cycle control with active feedback from an internal thermocouple was used to maintain ~55 °C (1197-1217 s), then a 2-stage heating was conducted first with higher applied voltage (1217 – 1221 s) then a lower voltage and on/off control was used to maintain 72 °C (1221 – 1231 s), finally a 3-stage heating to 95 °C was accomplished by tracking the resonant frequency (1231 – 1237 s) and ultimately utilizing the self-limiting behavior of the system to maintain 95 °C (1237 – 1247 s). This is one representative cycle out of 30.

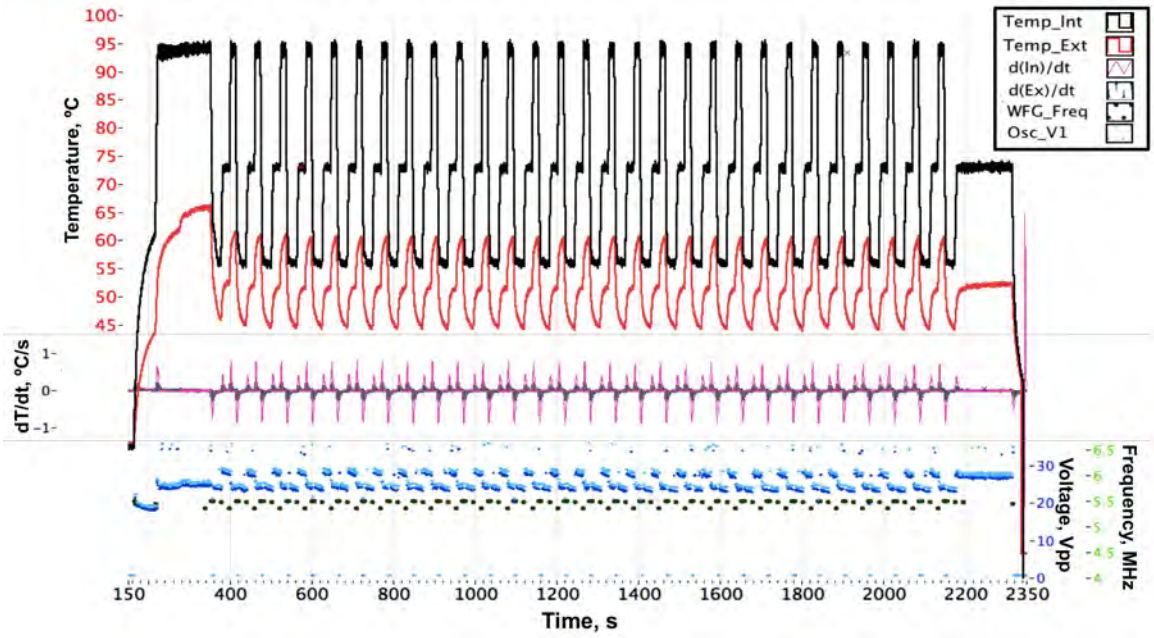

Figure 6.20. Plot of system parameters during thermal cycling for PCR via resonant acoustic heating.

system was pressured (the boiling point of water 5 psi above ambient should be 115 ºC[24])). In fact, temperature was readily modulated by how close the driving frequency was to the resonant frequency. The approximate, relative location of the resonance peak could be judged from the relationship between frequency and stable temperature. However, the true resonant frequency for the simple vertical 1st harmonic mode in the water chamber was often unknown because temperature control was more important than the amplitude of the acoustic resonance. When a hybrid control strategy of active feedback control at 55 ºC, nearly self-limiting active feedback control at 72 ºC, a multi-step self-limiting ascent to 95 ºC, and a no-ultrasound "free fall" cooling from 95 to 55 ºC was utilized (such as the thermal cycle shown in Error: Reference source not found). An optimized thermal cycling profile obtained with this hybrid control strategy is shown in Figure 6.20. Representative heating and cooling rates were +4.74±0.29 ºC/s 55 - 72 ºC, +4.44±0.49 ºC/s for 72 - 95 ºC transitions, and -6.30±0.25 ºC/s for 95 - 55 ºC transitions (this same data is visualized in Figure 6.21. The thermal control with resonant ultrasound was ultimately well within known tolerances for simple, monoplex PCR reactions.

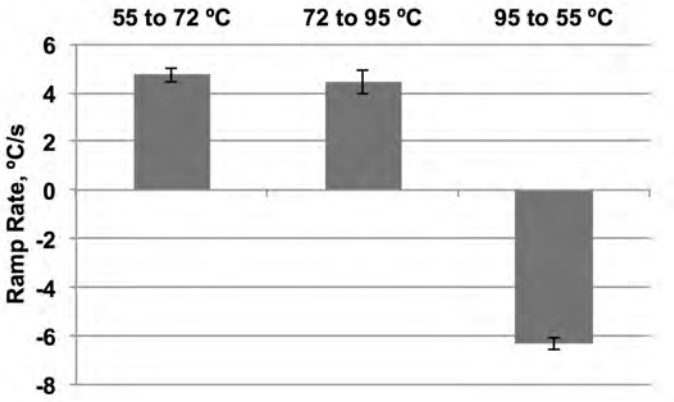

Figure 6.21: Ultrasound-mediated thermal ramping of internal chamber temperature evaluated for 3 replicate cycles.

6.4.10.6 Thermal Control During Acoustic Trapping

Thermal control during trapping was a concern because the reduced intensity of the acoustic standing wave from thermal drift directly impact trapping forces. Luckily, for the

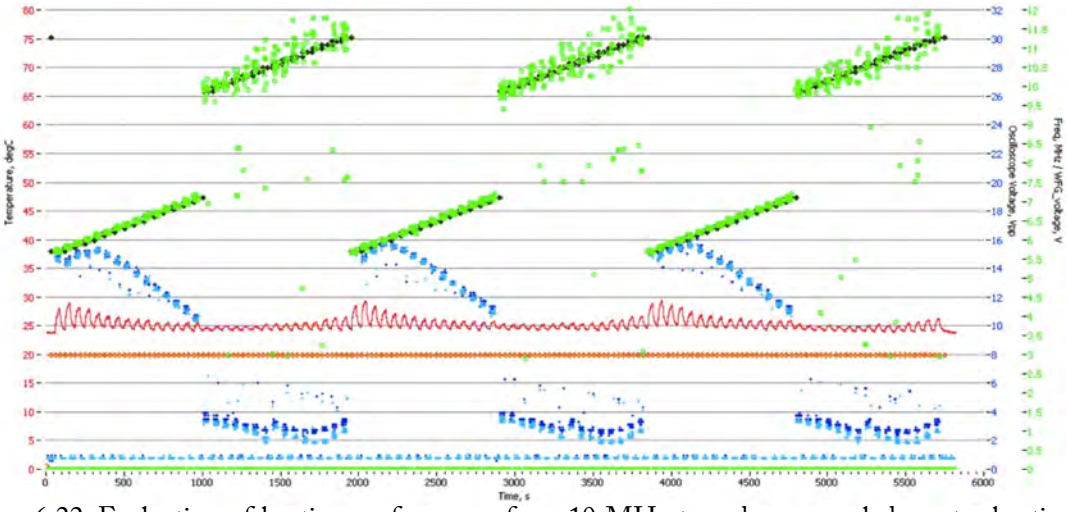

Figure 6.22. Evaluation of heating performance for a 10 MHz transducer revealed greater heating at frequencies near the second vertical mode in the water-filled chamber.

10 MHz transducer configuration, it was found that less heat was produced near the transducers optimal frequency of 10 MHz, but that heating could still be accomplished by lowering the frequency (Figure 6.22). Trapping was most effective at 10.088 MHz while heating was most effective at approximately 5.5 MHz This phenomenon was utilized for switchable heating during subsequent experiments of integration between trapping and cell lysis.

6.4.11 Combined Acoustic Trapping and Cell Lysis

6.4.11.1 Lysis of Epithelial Cells

Fluorescence microscopy was used to monitor the packing of a mixture of buccal (check) cells and fluorescent beads. Ultrasound was applied in a 2-step manner to first trap cells and beads together, and then to activate the thermophilic protease (Figure 6.23A). The initial packing of cells and beads was more spread out as seen in the microscopy images (Figure 6.23B) and as diagrammed (Figure 6.23C), which indicated the presence of intact cells between the beads. After prolonged incubation at elevated temperature, the beads

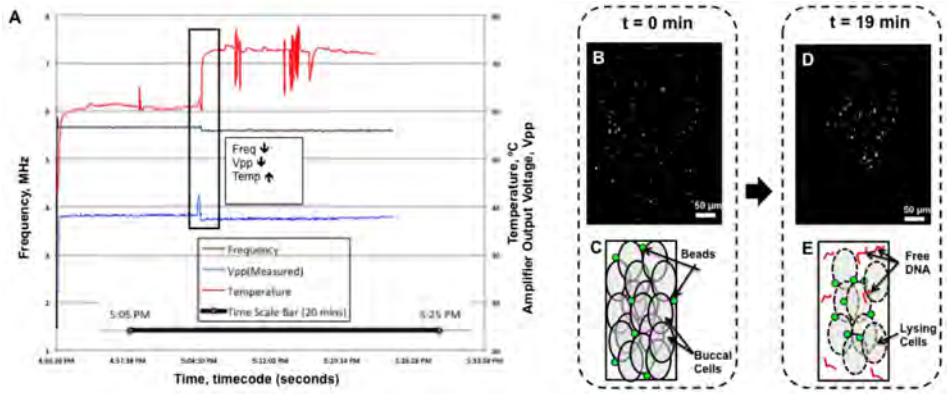

Figure 6.23. Thermally-induced lysis of buccal cells when co-mingled with fluorescent beads.

were packed closer together as a result of cell lysis (Figure 6.23D,E).

6.4.11.2 Lysis of PC3 cells

Acoustic cell trapping was integrated with enzyme-mediated liquid extraction (LE) of nucleic acids from the cells in the same microchamber. Acoustic trapping of PC3 cells was first conducted (Figure 6.24A), then a cell lysis solution was infused past the trapped cells at low temperature. To initiate cell lysis, the ultrasonic standing wave was modulated to heat the chamber contents to approximately 75 °C for several minutes.

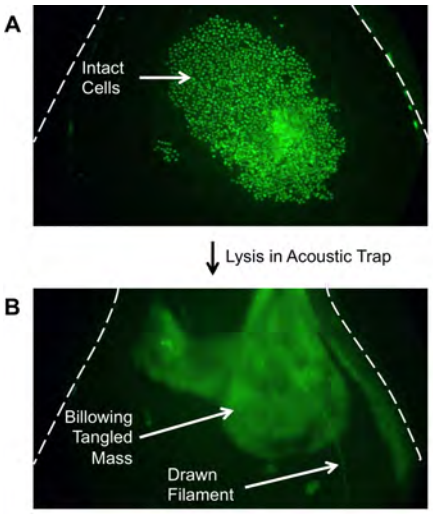

Figure 6.24. Thermally-induced lysis of PC3 cancer cells within the acoustic trap and subsequent behavior of liberated nucleic acids.

Interestingly, the liberated nucleic acids were not always evenly dispersed in the chamber following lysis, but instead formed obvious clumps and strands due to the complex motion of the acoustic microstreaming after prolonged ultrasound-mediated manipulation in the acoustic trap (Figure 6.24B). When the cell clusters were simply

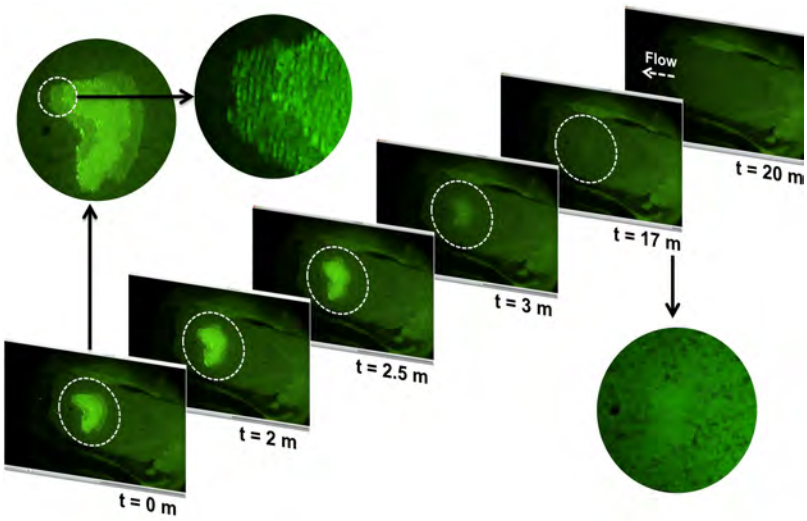

Figure 6.25. Example of preparative integration of trapping and lysis.

held in place within the acoustic trap and subjected to lysis conditions, planar discs of glowing cell debris (including nucleic acids) were obtained (Figure 6.25). In some cases these DNA-containing clusters would adsorb to the microchannels on their way out of the chip, and passivate of hydrodynamic flow focusing may be needed to prevent this. The discs of aggregated material maintained their mechanical integrity after release from the wall by a surfactant solution (documented via video microscopy; data not shown). The quantitative yield of DNA as a function of cell input could not be evaluated due to time constraints, and these experiments are the next step in characterization of this device/phenomenon.

In some cases, individual PC3 cell (and more often their liberated nuclei) were observed lysing due to protease digestion, heat, and acoustic microstreaming. One such event is depicted in the first 3 panels of Figure 6.26. The DNA from the lysed cells did not disperse in solution but rather was compacted by acoustic microstreaming, and an unusually bright region was observed at the center of an hourglass-shaped

microstreaming pattern (4th panel of Figure 6.26). It is worth noting that the PC3 cell line has many chromosomal abnormalities (e.g., it has 61 instead of the usual 46 chromosomes). This DNA aggregation was unexpected based on the equilibrium solubility of DNA in absence of flow, and cellular debris was first thought to play a role.

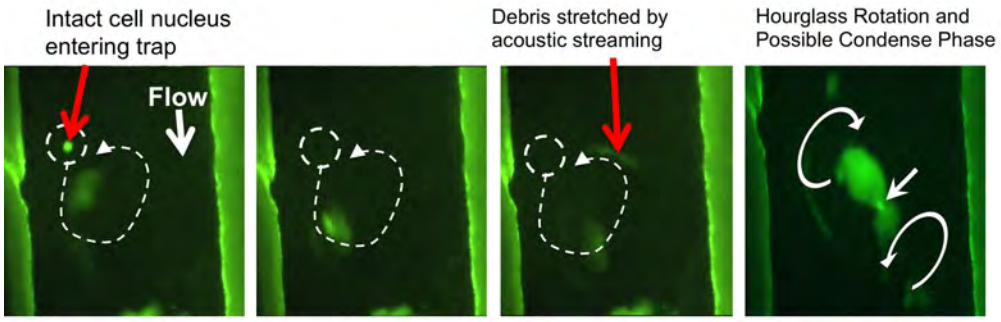

Figure 6.26. Still frames from video microscopy of individual PC3 cell nuclei lysing in the acoustic trap, followed by compaction of released nucleic acids via acoustic microstreaming.

6.4.12 Possible Confounding Phenomena for Ultrasound-mediated PCR

6.4.12.1 Aggregation of DNA as a source of PCR inhibition

Fluorescently tagged λ phage DNA, digested with EcoRI and HaeIII restriction endonucleases, appeared to form a fluorescently glowing aggregate (Figure 6.27A). Pre-purified E. coli genomic DNA stained with Syto 11 nucleic acid stain was observed in local, streaming-induced concentrations gradients and small trapped aggregates (Figure 6.27B). These findings suggest that cellular debris is not necessary for DNA aggregation in relatively low-ionic strength buffers (e.g., PCR buffer at 1X, 50 mM KCl).

The acoustic DNA aggregation appeared to reach DNA densities (as judged by fluorescent intensity) comparable to heterochromatin in an intact cell nucleus; if all of the DNA is contained in a disk that is 10 μm thick with a radius of 75 μm the volume is about 175 pL, and if the entire chamber contents were compacted down into 2 such discs the increase in concentration would be around 3000-fold (1 μL/(2*175 pL) ~=2800); the

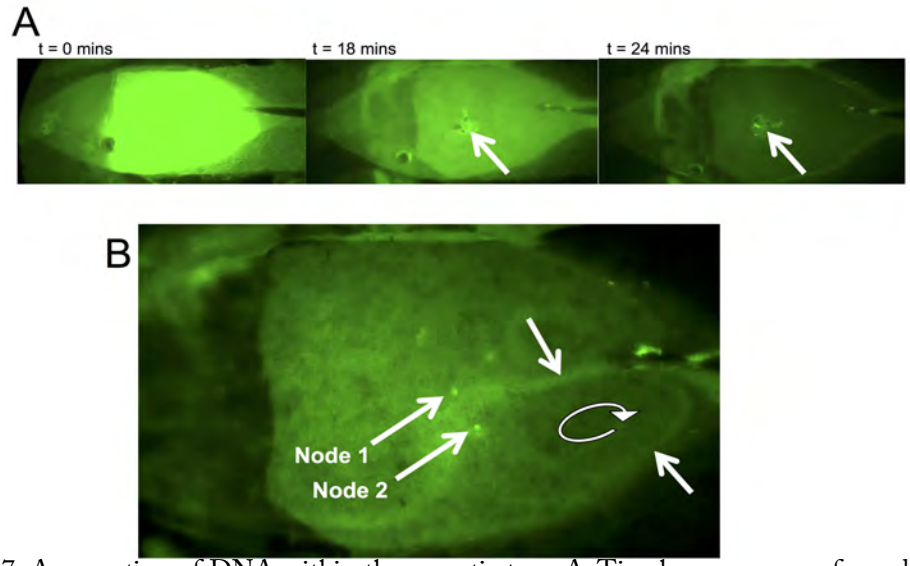

Figure 6.27: Aggregation of DNA within the acoustic trap. A. Timelapse sequence from digital video shows the progression from dispersed sample (far left) to aggregation of DNA (far right). DNA was fluorescently labeled restriction digest of lambda phage with sizes ranging from 22 kbp to approx. 150 bp. B. Streamlines in a solution of fluorescently stained E. coli genomic DNA indicate local concentration gradients due to acoustic microstreaming.

DNA clusters formed by cell lysis within the acoustic trap were shown to maintain their integrity after acoustic forces were removed, and this may be indicative of entanglement or cross-linking through hybridization between adjacent duplexes; this DNA aggregation phenomenon could be useful for concentrating nucleic acids and possibly evaluating their parameters such as length). Ultrasound was a likely inhibitor of PCR in this system, although the extent of inhibition relative to other factors and exact mechanism of this inhibition remain to be elucidated.

6.4.12.2 Evidence for Ultrasound-Promoted Polymer Adsorption

Acoustic microstreaming appeared to induce deposition of material on the glass walls of the microchamber. As the photographs in Figure 6.28 show, material was often deposited in a patterns that coincided with microbubbles locations (visible in Figure 6.27A where a small bubble in the bottom left migrated over time). Acoustic streaming has been shown

to be very intense in the vicinity of microbubbles. Shear flow induced conformational changes in the BSA, PEG, and DNA macromolecules present in the microchamber may have facilitated deposition. During prolonged acoustic trapping and lysis experiments, glowing tracks of material were observed on glass (data not shown). Fluorescent staining with a DNA-specific intercalating dye suggested this was an adsorbed band of DNA. Ultrasound-enhanced deposition of polymers onto the microdevice surface may have significantly lowered the PCR yield due to loss of template, polymerase, and/or loss of amplified product to surface adsorption.

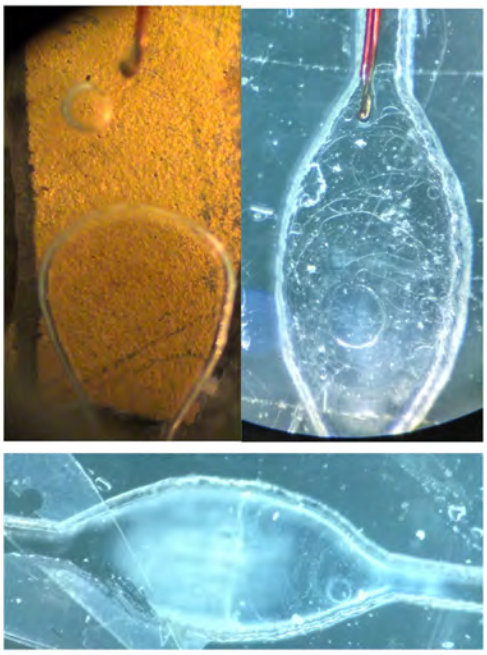

Figure 6.28. Visual evidence of ultrasound-induced adsorption of polymers near microbubbles within the acoustic trap.

6.4.12.3 Ultrasound-Mediated Thermocouple Corrosion

The thermocouple consistently corroded during ultrasound PCR. Sonochemistry has been characterized for cavitating ultrasound systems [25], and while cavitation is not expected in our system [26], this has not yet been ruled out empirically. Accelerated mass transport due to acoustic streaming may have hastened an ultrasound-independent corrosion process. A thermocouple stored in similar PCR buffer without ultrasound did not show signs of corrosion (though it was not connected to measurement electronics). The measurement electronics themselves may create a permissive condition for corrosion (e.g., by providing an electron sink), but the corrosion chemistry appears to be aqueous-

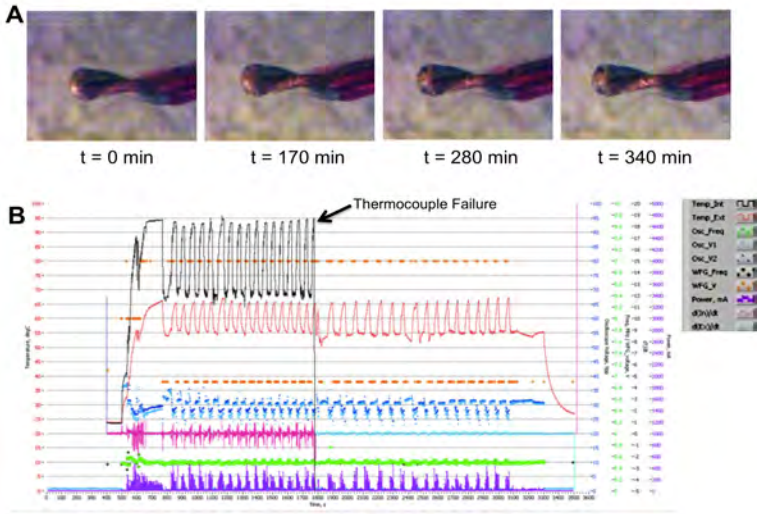

Figure 6.29. Early stages of thermocouple corrosion putatively ascribed to ultrasound exposure. A. Pitting can be seen in the copper wire of the thermocouple. B. Failure frequency occurred at high ultrasound intensity and high temperature.

based. The thermocouples were definitely corroding , and only the copper wire was degraded (or even corroded away all the way to the insulation). The thermocouple corrosion made for logistical challenges when conducting PCR, and it may have been a significant inhibitor of PCR as well.

6.4.13 Observation of Successful PCR via Ultrasound-Mediated Heating

There have been literature reports of DNA damage from non-cavitating ultrasound[27], and some macromolecular adsorption was evident (as described in section 6.4.12.2), so a solution of DNA size standard was subjected to ultrasound-mediated thermal cycling in an attempt to control for these phenomena. Figure 6.30A shows overlaid electropherogram traces for DNA size standard infused through the chip then collected (red trace) and for the same DNA solution after exposure to a typical ultrasound-mediated PCR thermal cycling program. This limited testing showed no signs of additional (post-passivation) loss of DNA to adsorption (as judged by their comparable

peak heights), nor evident DNA strand breakage (which would likely be seen as split peaks due to altered electrophoretic mobility). Importantly, the microchamber only constitutes ~10% of the volume recovered from the device, so any effect of ultrasound will be ~10-fold less pronounced than if the chamber contents could be analyzed directly. Also, the pre-purified and short (between 100 and 1600 bp) DNA size standard may not be an adequate model for genomic DNA; large DNA molecules are subject to more entanglement and possible strand breakage as the molecules are less able to reconfigure due to contrained topology (without breaking a bond in the phosophodiester backbone[28]). Nonetheless, this control experiment was relevant for the use of short linear DNA as template material for PCR.

As discussed in **Chapter 1**, the high surface area to volume ratio of microfluidic devices creates a situation where adsorption of biomolecules onto microchannel surfaces can easily be depleted those species from the aqueous volume. The PCR reaction requires several biomolecules (primarily DNA template, Taq polymerase, oligonucleotides) to combine in the liquid phase for DNA replication, and when the concentration of these key players is too low the reaction will fail to enter exponential growth[14,29]. Indeed, pre-passivation with PCR master mixture was found to be necessary for our microfluidic system. When successive fractions of master mix were infused through the device, collected, and thermal cycled a trend was evident. As Figure 6.30B shows, the peak height of PCR product in successive washes increased. Moreover, this trend was found to plateau after successive infusions of master mix, and fractions after the 3rd pre-passivation infusion showed no additional increases in peak height (data not shown). This could be due to adsorption and dispersion within the fluidic architecture. In any case, successful

amplification of PCR master mix that had been infused through the chip was indicative of sufficient surface passivation.

The possible confounding factors for PCR amplification may have been the reason for numerous failed PCR amplifications (data not shown). Once reason may have been the template choice, because interestingly, the lambda phage genome has so-called sticky ends which have been shown to cause concatemerization[30] and entanglement[31], and one hypothesis is that the shear flow from acoustic microstreaming may have caused concatemerization and condensation of lambda phage DNA to the point where it was no longer was a suitable PCR template. Genomic DNA from *E. coli* was also difficult to amplify (one success in many attempts; data not shown due to low number of replicates). The high value of genomic DNA as PCR templates certainly warrants additional study when ultrasound-mediated PCR is further developed.

To provide initial validation of ultrasound-mediated PCR, a more robust, albeit less realistic reaction recipe was utilized. This recipe used a dilution of pre-amplified PCR product for template. Moreover, a DNA-tethered polymerase (Thermo Phusion Phire) may have offset inhibition from loss of processivity due to shear flow. As Figure 6.31A shows, the peak height obtained from using PCR product as template was on the same order of magnitude as a peak amplified directly from genomic DNA. This is likely due either to a limiting condition in PCR reaction (e.g., reagent depletion ultimately curtailed amplification) or a sampling and detection upper limit of the Agilent 2100 Bioanalyzer. PCR master mix that was thermal cycled via ultrasound was shown to produce a PCR product, Figure 6.31B, which was actually diluted ~10-fold because the ~1 μL of thermal cycled microchamber contents were aspirated from the chip along with at least 9 μL of

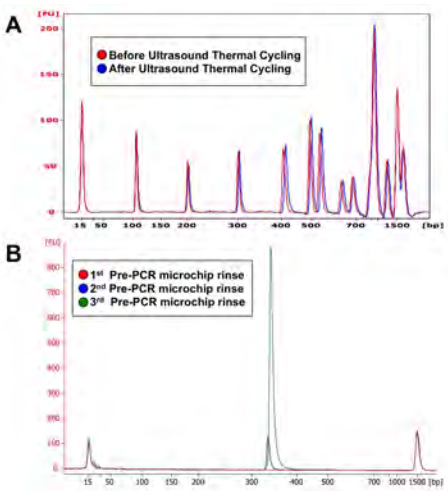

Figure 6.30. Control experiments regarding DNA shearing or adsorption and substrate inhibition by the microfluidic device.

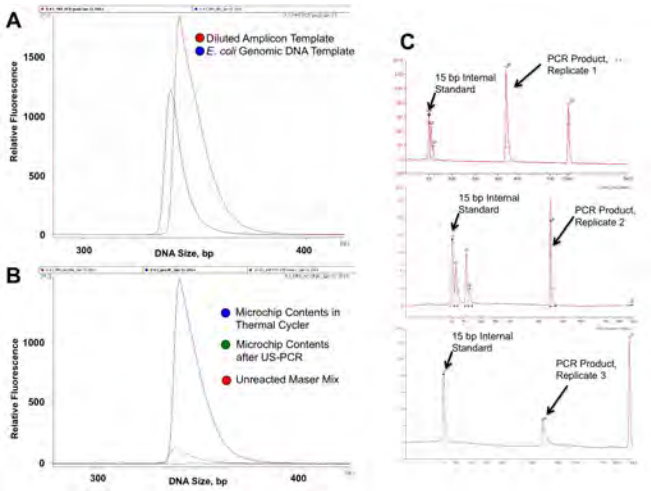

Figure 6.31. Successful amplification of PCR product via resonant ultrasonic heating, along with associated control experiments.

PCR master mix that was not thermal cycled. Importantly, unreacted PCR master mix taken from the microchip immediate prior to thermal cycling showed that no detectable product was initially present. The 3 replicates of successful PCR, Figure 6.31C, have unequivocally shown that ultrasound-mediated thermal cycling for PCR amplification was responsible for generating the expected PCR products. These data clearly show that the acoustic trapping platform was capable of ultrasound-mediated PCR amplification.

6.4.14 Possibilities of a Multi-Site PCB

Multiple trapping sites were utilized to enhance trapping efficiency by arranging the 4 trapping sites in series down the length of a single microchannel (Figure 6.32A,B). The dispersed mixture of particles must pass through 4 regions of a localized standing wave (Figure 6.32C), and at each site particles are either trapped or moved toward the nodal planes. Net trapping efficiency was visibly maximized (Figure 6.32D) when the 4 sites were operated in series for cooperative trapping.

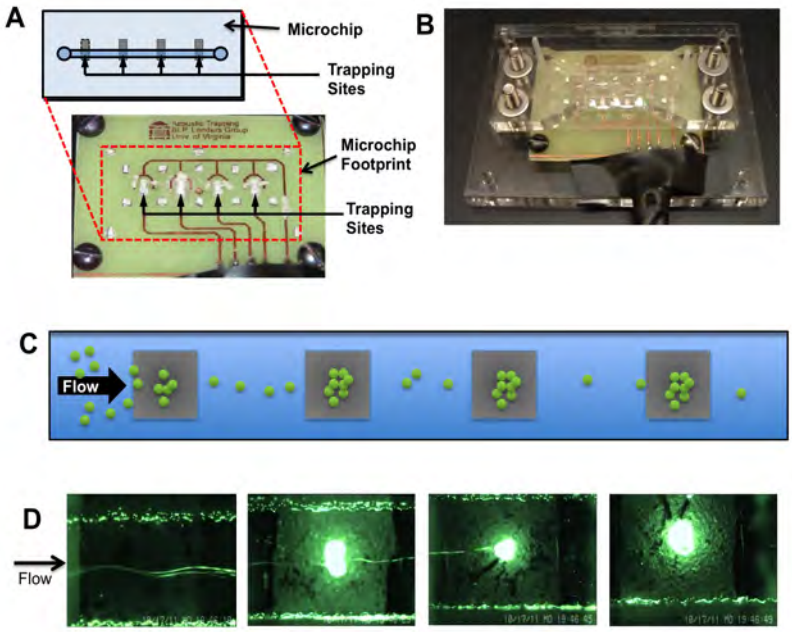

Figure 6.32. Design and preliminary evaluation of a multiplex printed circuit board transducer.

The 4 trapping sites had slightly different resonance frequencies and apparent trapping performance. Nonetheless, the range of frequencies was within 0.2 MHz, centered around the nominal 5 MHz resonance for this material. In Figure 6.32D, the left-most transducer may have been outputting a relatively weak standing wave, coupling to the microfluidic device was poor, or the microfluidic device was not in resonance. The 6 μm beads migrated to the channel center rather than trap at the first site. Based on the relatively tight distribution of observed resonant frequencies between the four sites, the simultaneous establishment of stable pressure nodes at all sites may be possible by rapidly scanning the narrow range of frequencies. Published reports by Wiklund and coworkers have shown that individual sites will "lock in" to its own frequency and maintain resonance. This is because the ring down times of ultrasonic standing waves persist over times scales on par with the scanning[32]. With respect to the current prototype, each of the transducers on the PCB were operable and capable of manipulating microparticles

through acoustic forces.

Advanced operations should be possible with this multiplexed transducer PCB through switching of the trapping sites independently and through microfluidic device design. For the serial trapping application described above, shuttling of trap contents between sites could be achieved by turning off the transducers in sequence (starting with upstream transducer first) and allowing the released trap contents to move with the hydrodynamic flow to the next trapping site. Moreover, the different functionalities described above – acoustic trapping, rapid mixing of laminar flow streams, cell lysis, and PCR – could be conducted serially with a dedicated and optimized microfluidic architecture at each site. Alternatively, the 4 sites could be operated in parallel to improve the device throughput.

6.5 Conclusions and Future Avenues of Research

The multiple functionalities of the PCB-mounted transducers could be utilized for effective (and flexible) integration of bioanalytical processes on a monolithic microfluidic device. One scenario would be a platform that would accept an incoming stream of rare, high-value cells[33] and leverage the following capabilities: acoustic trapping of cells for concentration enrichment, facile medium exchange, optical analysis of cells via epifluorescence microscopy, mixing of laminar fluid streams in a very small footprint via acoustic micro streaming, lysing of trapped cells to liberate genomic DNA (and other cellular contents such as RNA), thermal cycling for nucleic acid amplification, and (unexpectedly) apply acoustic forces to compact genomic DNA into very small volumes.

Characterization of the current platform could be improved by quantification of

DNA recovered from trapping and lysis experiments, and subsequent verification of suitability for PCR. STR profiles using post-trapping+lysis PC3 cell DNA would yield a STR profile that is characteristic of this cell line.

Resonance tracking[7,10,34]] for more accurate and automated control of resonance and heating. Improving surface passivation in hopes of reducing macromolecular deposition. Measurement of chamber temperature using ultrasound by applying resonance tracking with a validated correlation between resonant frequency and temperature. Quantitative polymerize chain reaction is a viable extension because the microscope and detection optics for fluorescence detection are already an integral part of the system. [35,36]. The DNA aggregates did act as a qualitative indicators of resonance/temperature due to reproducible decreases in fluorescence intensity when high temperatures were reached; if this intensity versus temperature were monitored closely it may be possible to quantitatively assess DNA melting.

Lastly, ultrasound has been shown to improve injection of foreign DNA into mammalian cells [1]. The effects of acoustic trapping on mammalian cells have been established in a number of studies[37–39], and conditions have been described for acoustic trapping that did not result in long term loss of viability in the cell once they were recovered from the acoustic trap. This opens the possibility of in vitro handling of cells for applications such as gene therapy or tissue engineering.

6.6 References

[1] C.M.H. Newman, T. Bettinger, Gene therapy progress and prospects: ultrasound for gene transfer., Gene Ther. 14 (2007) 465–75. doi:10.1038/sj.gt.3302925.

[2] M.H. Kershaw, J.A. Westwood, P.K. Darcy, Gene-engineered T cells for cancer therapy, Nat. Rev. Cancer. 13 (2013) 525–541.

[3] M. Evander, J. Nilsson, Acoustofluidics 20: Applications in acoustic trapping., Lab Chip. 12 (2012) 4667–76. doi:10.1039/c2lc40999b.

[4] M. Gröschl, W. Burger, B. Handl, O. Doblhoff-Dier, T. Gaida, C. Schmatz, Ultrasonic Separation of Suspended Particles - Part III: Application in Biotechnology, Acta Acust. United with Acust. 84 (1998) 815–822.

[5] J.D. Adams, C.L. Ebbesen, R. Barnkob, A.H.J. Yang, H.T. Soh, H. Bruus, High-throughput, temperature-controlled microchannel acoustophoresis device made with rapid prototyping, J. Micromechanics Microengineering. 22 (2012) 075017. doi:10.1088/0960-1317/22/7/075017.

[6] P. Augustsson, R. Barnkob, S.T. Wereley, H. Bruus, T. Laurell, Automated and temperature-controlled micro-PIV measurements enabling long-term-stable microchannel acoustophoresis characterization., Lab Chip. 11 (2011) 4152–64. doi:10.1039/c1lc20637k.

[7] K. Visvanathan, Y.B. Gianchandani, Microheaters based on ultrasonic actuation of piezoceramic elements, J. Micromechanics Microengineering. 21 (2011) 085030. doi:10.1088/0960-1317/21/8/085030.

[8] J. Kondoh, N. Shimizu, Y. Matsui, M. Sugimoto, S. Shiokawa, Development of temperature-control system for liquid droplet using surface Acoustic wave devices, Sensors Actuators A Phys. 149 (2009) 292–297. doi:10.1016/j.sna.2008.11.007.

[9] M. Evander, L. Johansson, T. Lilliehorn, J. Piskur, M. Lindvall, S. Johansson, et al., Noninvasive acoustic cell trapping in a microfluidic perfusion system for online bioassays., Anal. Chem. 79 (2007) 2984–91. doi:10.1021/ac061576v.

[10] B. Hammarström, M. Evander, J. Wahlström, J. Nilsson, Frequency tracking in acoustic trapping for improved performance stability and system surveillance., Lab Chip. 14 (2014) 1005–13. doi:10.1039/c3lc51144h.

[11] M. Knite, G. Mezinskis, L. Shebanovs, I. Pedaja, A. Sternbergs, CO2 laser-induced structure changes in lead zirconate titanate Pb(Zr0.58Ti0.42)O3 sol–gel films, Appl. Surf. Sci. 208-209 (2003) 378–381. doi:10.1016/S0169-4332(02)01408-3.

[12] C.J. Easley, J.A.C. Humphrey, J.P. Landers, Thermal isolation of microchip reaction chambers for rapid non-contact DNA amplification, J. Micromechanics Microengineering. 17 (2007) 1758–1766. doi:10.1088/0960-1317/17/9/002.

[13] C. Potrich, L. Lunelli, S. Forti, D. Vozzi, L. Pasquardini, L. Vanzetti, et al., Effect of materials for micro-electro-mechanical systems on PCR yield., Eur. Biophys. J. 39 (2010) 979–86. doi:10.1007/s00249-009-0466-5.

[14] Y. Xia, Z. Hua, O. Srivannavit, A.B. Ozel, E. Gulari, Minimizing the surface effect of PDMS–glass microchip on polymerase chain reaction by dynamic polymer passivation, J. Chem. Technol. Biotechnol. 82 (2007) 33–38. doi:10.1002/jctb.1631.

[15] J.A. Lounsbury, B.L. Poe, M. Do, J.P. Landers, Laser-ablated poly(methyl

methacrylate) microdevices for sub-microliter DNA amplification suitable for micro-total analysis systems, J. Micromechanics Microengineering. 22 (2012) 085006. doi:10.1088/0960-1317/22/8/085006.
[16] C. Ke, A.-M. Kelleher, H. Berney, M. Sheehan, A. Mathewson, Single step cell lysis/PCR detection of Escherichia coli in an independently controllable silicon microreactor, Sensors Actuators B Chem. 120 (2007) 538–544. doi:10.1016/j.snb.2006.03.019.
[17] E.J. Fong, A.C. Johnston, T. Notton, S.-Y. Jung, K.A. Rose, L.S. Weinberger, et al., Acoustic focusing with engineered node locations for high-performance microfluidic particle separation., Analyst. 139 (2014) 1192–1200. doi:10.1039/c4an00034j.
[18] M. Hill, Y. Shen, J.J. Hawkes, Modelling of layered resonators for ultrasonic separation., Ultrasonics. 40 (2002) 385–92.
[19] M. Hill, R.J. Townsend, N.R. Harris, Modelling for the robust design of layered resonators for ultrasonic particle manipulation., Ultrasonics. 48 (2008) 521–8. doi:10.1016/j.ultras.2008.06.007.
[20] V.R. Singh, M. Shriwastava, Ultrasonic Hyperthermia for Cancer Treatment., Def. Sci. J. 43 (2013) 235–241.
[21] W.L. Nyborg, Sonically produced heat in a fluid with bulk viscosity and shear viscosity., J. Acoust. Soc. Am. 80 (1986) 1133–9.
[22] T.J. Cavicchi, W.D.O. Brien, Heat generated by ultrasound in an absorbing medium 1 Re [p (2ako + j (ko Place-of-articulation information in the closure voicing of plosives, (2014) 101244–101245.
[23] M. Groschl, Ultrasonic Separation of Suspended Particles - Part I: Fundamentals, Acustica. 84 (1998) 432–447.
[24] R.C. Weast, M.J. Astle, W.H. Beyer, CRC handbook of chemistry and physics, CRC press Boca Raton, FL, 1988.
[25] C. Brett, Sonoelectrochemistry, in: A. Vives (Ed.), Piezoelectric Transducers Appl. SE - 15, Springer Berlin Heidelberg, 2008: pp. 399–411. doi:10.1007/978-3-540-77508-9_15.
[26] F. Dunn, Effects of Intense Noncavitating Ultrasound on Selected Enzymes, J. Acoust. Soc. Am. 44 (1968) 932. doi:10.1121/1.1911231.
[27] S.A. Hawley, R.M. Macleod, F. Dunn, Degredation of DNA by Intense, Noncavitating Ultrasound, J. Acoust. Soc. Am. 35 (1963) 1285–1287.
[28] T. Kondo, S. Arai, M. Kuwabara, G. Yoshii, E. Kano, Damage in DNA Irradiated with 1.2 MHz Ultrasound and Its Effect on Template Activity of DNA for RNA Synthesis, Radiat. Res. 104 (1985) 284–292. doi:10.2307/3576590.
[29] Y. Xia, Z. Hua, E. Gular, Minimizing the Surface Effect on PCR in PDMS-Glass Chips by Dynamic Passivation, 2005 Annu. …. (2005).
[30] C. Haber, D. Wirtz, Shear-induced assembly of lambda-phage DNA., Biophys. J. 79 (2000) 1530–6. doi:10.1016/S0006-3495(00)76404-6.
[31] S. Chakraborty, T. Uematsu, C. Svanberg, P. Jacobsson, J. Swenson, M. Zäch, et al., Mechanistic insight into the structure and dynamics of entangled and hydrated λ-phage DNA., J. Phys. Chem. A. 116 (2012) 4274–84. doi:10.1021/jp2108363.
[32] B. Lipkens, M. Costolo, E. Rietman, The Effect of Frequency Sweeping and Fluid

Flow on Particle Trajectories in Ultrasonic Standing Waves, IEEE Sens. J. 8 (2008) 667–677. doi:10.1109/JSEN.2008.922675.
[33] Y. Chen, P. Li, P.-H. Huang, Y. Xie, J.D. Mai, L. Wang, et al., Rare cell isolation and analysis in microfluidics., Lab Chip. 14 (2014) 626–45. doi:10.1039/c3lc90136j.
[34] M. Groschl, Ultrasonic Separation of Suspended Particles - Part II: Design and Operation of Separation Devices, Acoustica. 84 (1998) 632–642.
[35] R. Banaei Khosroushahi, H.J. Marquez, J. Martinez-Quijada, C.J. Backhouse, PDE Modeling of a Microfluidic Thermal Process for Genetic Analysis Application, J. Appl. Math. 2013 (2013) 1–12. doi:10.1155/2013/767853.
[36] C. Pfitzner, I. Schröder, C. Scheungraber, A. Dogan, I.B. Runnebaum, M. Dürst, et al., Digital-Direct-RT-PCR: a sensitive and specific method for quantification of CTC in patients with cervical carcinoma., Sci. Rep. 4 (2014) 3970. doi:10.1038/srep03970.
[37] J. Hultström, O. Manneberg, K. Dopf, H.M. Hertz, H. Brismar, M. Wiklund, Proliferation and viability of adherent cells manipulated by standing-wave ultrasound in a microfluidic chip., Ultrasound Med. Biol. 33 (2007) 145–51. doi:10.1016/j.ultrasmedbio.2006.07.024.
[38] D. Bazou, W.T. Coakley, a J. Hayes, S.K. Jackson, Long-term viability and proliferation of alginate-encapsulated 3-D HepG2 aggregates formed in an ultrasound trap., Toxicol. In Vitro. 22 (2008) 1321–31. doi:10.1016/j.tiv.2008.03.014.
[39] D. Bazou, R. Kearney, F. Mansergh, Gene Expression Analysis of Mouse Embryonic Stem Cells Following Levitation in an Ultrasound Standing Wave Trap, Ultrasound Med. …. 37 (2011) 321–330.

7 Concluding Remarks

7.1 Summary of Preceding Chapters

The unifying goal of the work presented in this thesis has been the development and improvement of integrated bioanalytical microfluidics for genetic analysis. An introductory discussion on the significance of scale was provided in **Chapter 1**, along with a discussion of commercialization of microfluidic technology. In **Chapter 2,** a genotyping assay was designed from the ground up to be inherently compatible with integrated microfluidic devices (requiring only a single PCR step, and utilizing unlabeled primers which could be readily adapted to a variety of separation and detection systems). **Chapter 3** describes the knowledge transfer and equipment upkeep of instrumentation for microchip electrophoresis with laser induced fluorescence detection. The design and rapid manufacturing of microfluidic devices using laser ablation was covered in **Chapter 4**, and a number of functional microfluidic devices (i.e., for acoustic trapping, for active fluidic control, and for directed cell culture) were fabricated using a widely available CO_2 laser engraving instrument. The development and characterization of a microfluidic system for acoustic trapping was the topic of **Chapter 5**. A bench-top method for fabricating ultrasonic transducers was presented, that were the result of an iterative design process[1,2] for interrelated components (i.e., microfluidic devices and ultrasonic transducers, and manifolds to precisely couple the two). A functional platform for acoustic trapping and enrichment of bacterial pathogens was demonstrated.

Finally, the acoustic trapping platform was refined and automated in **Chapter 6**, and a novel extension of the trapping platform was described. Acoustic resonance in

glass-PDMS-glass microfluidic devices was modulated to control the density of acoustic energy in the device, and in effect to control the rate of heat production due to absorption of ultrasound. Heating with resonant ultrasound was applied to in situ integration of acoustic cell trapping with thermally-activated cell lysis. Furthermore, polymer dynamics and rheology of DNA molecules within the acoustic resonator were found to induce concentration gradients of DNA in microstreaming and the compaction of DNA into aggregates in the nodal planes of the ultrasonic standing wave. Once the thermal control of the microchamber temperature was within tolerances of PCR a short DNA template was successfully amplified by thermal cycling with resonant ultrasound.

7.2 Potential Future Applications of Microfluidic Technologies

7.2.1 Distributed Fabrication for Biomedical Devices

Data with low signal to noise (e.g., low phenotypic penetrance of underlying genetic diseases) has been of little clinical utility, but advances in computational tools[3] may enable extraction of useful bioanalytical data from large amount of "noisy" bioanalytical data. To give a hypothetical example, the levels of a certain protein biomarker may only be indicative of disease in 30% of patients, but when hundreds of biomarkers are assessed simultaneously for a large number of patients, latent correlations between biomarkers and their true biological functions are likely to be revealed. Microfluidic technologies could constitute a widely deployable first line of testing. The performance of these first line testing devices may not match the that of expensive specialized equipment (e.g., as found in the central laboratory of a hospital), but their immediacy and widespread implementation may offer clinical utility.

The logistics of manufacturing and deploying microfluidic devices have been intensively studied[4–6] and inexpensive consumables for microfluidic technologies has been recognized as essential to their success in emerging markets such developing nations and point-of-care testing. Moreover, rapid prototyping methods for microfluidic devices are valuable because they enable broader development and deployment of microfluidic technologies. For instance, 3D printed microfluidics (e.g., [7]), as well as the chemical reaction containers [8], optical components [9], detection systems [10] may enable stakeholders in a bioanalytical testing to build their own platforms. End-users can build their own devices in an open source model for conventional method replacement[11] or microfluidic-specific functionalities[12], both of which utilize a range of microfluidic processes[13].

The laser fabrication processes described in **Chapter 4** are a contribution to the growing trend of rapid prototyping and the use of low cost materials. Researchers at both large and small institutions in many parts of the world have access to CO_2 laser engraving equipment. For instance, laser engraving instruments are often found in non-engineering academic environments such as architecture departments, where they have gained broad popularity for constructing physical scale models of buildings. The careful evaluation of instrument operation parameters in Chapter 4 reconciles the non-idealities of a mechanical stage (e.g., drive belt slippage, limited resolution of control electronics digitizer) with achievable microfluidic feature quality. The sharing of fabrication parameters that are easily adopted by researchers outside the niche of microfluidics may allow for wider adoption of microfluidic technologies by lowering the barriers to evaluating them. For instance, a researcher who specializes in cell biology (challenging

enough as it is due to the complexities of biological systems[14]) may want to study individual cells with microfluidics, but investing substantial time and a significant part of the current research budget is not an option. This hypothetical researcher could evaluate a microfluidic platform via low-cost and rapid microfluidic device prototyping. In some cases microfluidic methods may work well enough to enable collection of preliminary data for funding applications, or to warrant study of a new hypothesis entirely through new capabilities. It is worth noting that this distributed, open source model would likely encourage collaboration rather than obviate it. Proprietary commercial systems have logistical and legal advantages (e.g., commercial availability, quality traceability for forensic testing). Moreover, specialized fabrication facilities will remain essential to technology advancement and can improve collaboration[15].

7.2.2 Cell Modification Technologies

Microfluidic technologies will likely be the tools of choice for future technologies such as gene therapy and synthetic biology. When working with individual or a few cells, the precision handling that microfluidic devices can offer allows the cells to handled and modified in a controlled environment. A conceptual analogy is presented in Figure 7.2, which explores the relationship between the sizes of objects and the workshops in which they are created. The working environment must be larger than the object being worked on as well as all of the necessary tools. Granted, this traditional view of manufacturing may be challenged in the future with self-assembled or 3D printed objects, but when an existing object must be modified or repaired this workshop:workpiece size correlation may be unavoidable. Mammalian cells are generally on the order of 20 μm in diameter

(BNID 103788, [16]), so micro- or nano-scale spaces[17] are a good fit for them.

A few specialized cell types in mammals behave as somewhat autonomous agents (e.g., CD4+ T cells of the immune system), and may be metaphorized as machines consisting of functioning components. In this vein, editing the genome of a cell is the same as replacing a part in an automobile engine or reprogramming a computer. [This reductionist view is not meant to misinform[18] or trivialize the remarkable nature of our biology: extreme caution must be taken as this technology is developed. Bioethisists, policy makers and humanity at large have some important decisions to make in the near future[19,20]. Human gene therapy has faced tragic miscalculations and technical challenges[21], but hope remains for highly predictable and targeted therapies[22][23][24].] The promise of cell-based therapies for improving human health[25] should not (and will not) be ignored in the decades to come. Conventional laboratory procedures for cell-based therapies include manipulation, monitoring, and

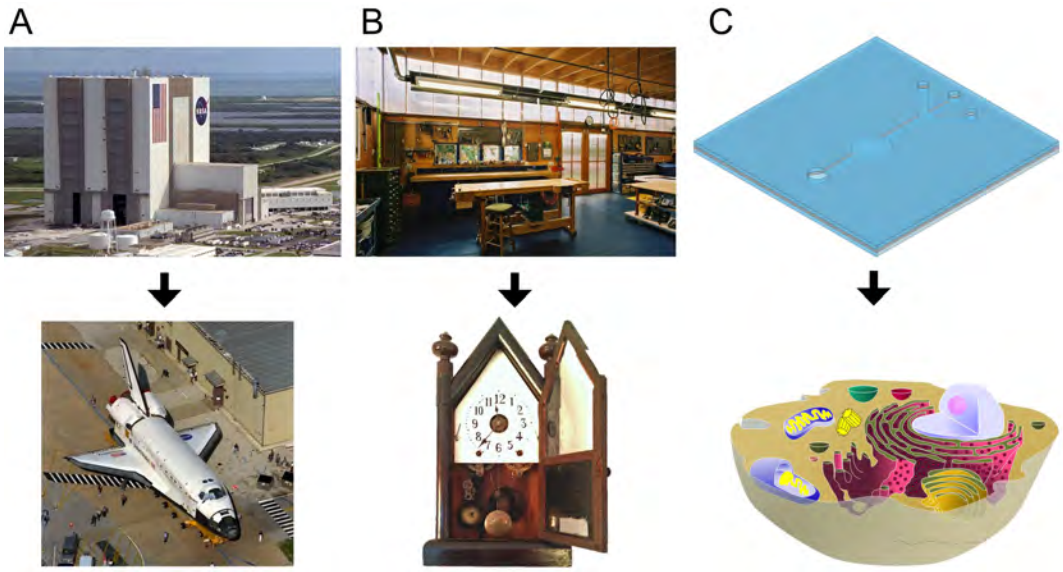

Figure 7.1. Comparison between workshop spaces and the items they produce. A. The NASA Vehicle Assembly Building[31] is one of the largest buildings in the world by volume (160 m tall x 218 m long x 157.9 m wide). This enornity is needed to enclose spacecraft during their construction. B. A traditional workworking workshop and a wooden. C. A microfluidic device (e.g., this glass-PDMS-glass device is 22 x 22 x 0.5 mm) used to manipulate a mammalian cell on the order of 20 microns in diameter.

recovery of cells by highly trained technicians, and these procedures will be expensive or impossible to scale up adequately. Microfluidic technologies will likely be essential for widespread adoption of cell-based therapies: the cost and logistics of conventional methods would become intractable, but integrated microfluidic technology could feasibly offer comparable capabilities at significantly lower cost.

The acoustic cell trapping and handling platform described in **Chapters 5 and 6** may be useful for next-generation cell handling techniques because it offers precise, gentle, and non-contact methods for handling cells. Acoustic trapping devices have already been utilized for tissue engineering[26] and temporary handling of cells without loss of viability[27,28]. Moreover, the ultrasound used for trapping, while potentially non-lethal to cells, has been shown to permeabilize cells to allow for rapid transport of macromolecules[29], small molecules into or out of cells (Figure 7.2). Implementation of a microfluidic system for cell modification with clinical utility is a challenging task, but

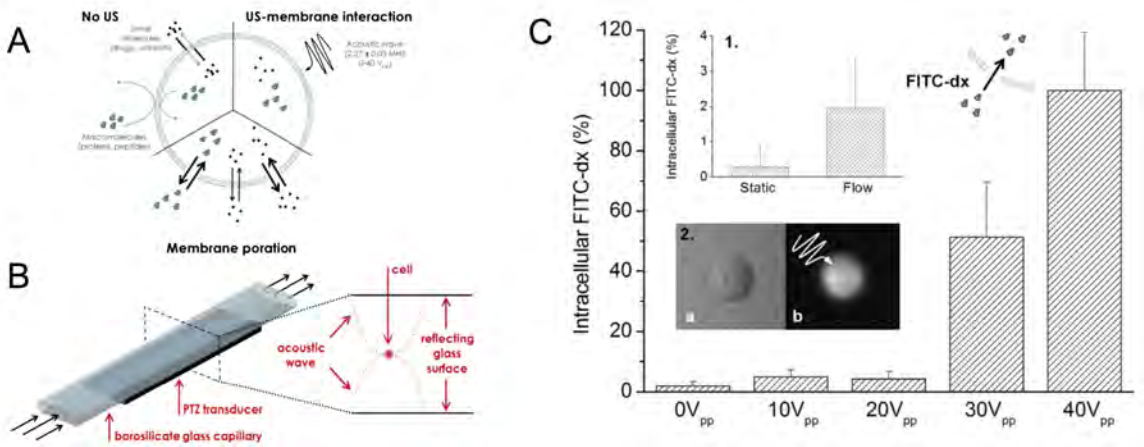

Figure 7.2. Example of applicability of microfluidic ultrasonics standing waves to gene therapy. A. Ultrasound has been shown to permeabilize the cell membrane of cells passing through an ultrasonic standing wave, allowing otherwise impermeable macromolecules such as DNA and proteins to enter (or exit) the cell. B. Diagram of apparatus used by Carugo *et al.* to expose cells to ultrasonic standing waves. C. Results of a cell permeabilization experiment where fluorescently labelled dextran (FITC-dx), a size-eqivalent analog to DNA and proteins, was taken up by cells when exposed to a strong ultrasonic standing wave. Inset 1 indicates that permeabilization by flow perturbations were very minor. Inset 2 shows a cell with intracellular fluorescent FITC-dx that was introduced via sonoporation. (Adapted from [29])

the necessary technologies already exist separately. Microfluidic devices may be able to seamlessly integrate a complicated workflow for cell trapping, addition of reagents (e.g., virus particles for gene transfection), optical evaluation of the cells, and gentle recovery so that the modified cells can be reintroduced to the patient. The choice of gene therapy targets and ultimate safety of the procedure are well beyond the scope of this dissertation. However, the low cost and deployable methods for acoustic cell trapping may facilitate research into the safety of advanced cell handling techniques by lowing the cost and time barriers to preforming experiments.

7.3 Final Thoughts

Ultimately, the original research described in this dissertation had the central goal of improving microfluidic tools for genetic and cellular biotechnology. The chapters above represent an attempt to improve the bioanalytical processes of cell handling, nucleic acid extraction, PCR assay design and implementation, PCR product separations, and interpretation of data for genetic analysis. The practical matters of commercializing microfluidic systems have proven to be non-trivial[2,4,30], yet continued development is warranted. Microfluidic devices have the *potential* to conserve precious reagents and samples, speed up bioanalysis, facillitate large-scale multiplexing, enable new technologies through unique physics, and integrate a variety of bioanalytical processes in one device. Just as computer hardware and software have co-developed to achieve what was previously impossible, microfluidic technologies will co-evolve with bioanalytical and biotechnological techniques to substantially improve human health and well-being in the decades ahead.

7.4 References

[1] A.E. Herr, Disruptive by design: a perspective on engineering in analytical chemistry., Anal. Chem. 85 (2013) 7622–8. doi:10.1021/ac4010887.

[2] A. Ríos, M. Zougagh, M. Avila, Miniaturization through lab-on-a-chip: utopia or reality for routine laboratories? A review., Anal. Chim. Acta. 740 (2012) 1–11. doi:10.1016/j.aca.2012.06.024.

[3] T.B. Murdoch, A.S. Detsky, The inevitable application of big data to health care., JAMA. 309 (2013) 1351–2. doi:10.1001/jama.2013.393.

[4] C.D. Chin, V. Linder, S.K. Sia, Commercialization of microfluidic point-of-care diagnostic devices., Lab Chip. 12 (2012) 2118–34. doi:10.1039/c2lc21204h.

[5] P. Yager, T. Edwards, E. Fu, K. Helton, K. Nelson, M.R. Tam, et al., Microfluidic diagnostic technologies for global public health., Nature. 442 (2006) 412–8. doi:10.1038/nature05064.

[6] A.K. Ellerbee, S.T. Phillips, A.C. Siegel, K. a Mirica, A.W. Martinez, P. Striehl, et al., Quantifying colorimetric assays in paper-based microfluidic devices by measuring the transmission of light through paper., Anal. Chem. 81 (2009) 8447–52. doi:10.1021/ac901307q.

[7] J.L. Erkal, A. Selimovic, B.C. Gross, S.Y. Lockwood, E. Walton, S. McNamara, et al., 3D Printed Microfluidic Devices with Integrated Versatile and Reusable Electrodes, Lab Chip. (2014). doi:10.1039/c4lc00171k.

[8] P.J. Kitson, M.D. Symes, V. Dragone, L. Cronin, Combining 3D printing and liquid handling to produce user-friendly reactionware for chemical synthesis and purification, Chem. Sci. 4 (2013) 3099. doi:10.1039/c3sc51253c.

[9] C. Zhang, N.C. Anzalone, R.P. Faria, J.M. Pearce, Open-source 3D-printable optics equipment., PLoS One. 8 (2013) e59840. doi:10.1371/journal.pone.0059840.

[10] G.C. Anzalone, A.G. Glover, J.M. Pearce, Open-source colorimeter., Sensors (Basel). 13 (2013) 5338–46. doi:10.3390/s130405338.

[11] J.M. Pearce, Materials science. Building research equipment with free, open-source hardware., Science. 337 (2012) 1303–4. doi:10.1126/science.1228183.

[12] J.E. Trachtenberg, P.M. Mountziaris, J.S. Miller, M. Wettergreen, F.K. Kasper, A.G. Mikos, Open-source three-dimensional printing of biodegradable polymer scaffolds for tissue engineering, J. Biomed. Mater. Res. Part A. (2014) n/a–n/a. doi:10.1002/jbm.a.35108.

[13] D. Mark, F. von Stetten, R. Zengerle, Microfluidic Apps for off-the-shelf instruments., Lab Chip. 12 (2012) 2464–8. doi:10.1039/c2lc00043a.

[14] I.C. Baianu, Complex Systems Theory and Biodynamics, PediaPress: Mainz, Germany, 2009.

[15] K. Panikowska, A. Tiwari, J.R. Alcock, Towards service-orientation—the state of service thoughts in the microfluidic domain, Int. J. Adv. Manuf. Technol. 56 (2011) 135–142. doi:10.1007/s00170-011-3171-3.

[16] R. Milo, P. Jorgensen, U. Moran, G. Weber, M. Springer, BioNumbers--the database of key numbers in molecular and cell biology., Nucleic Acids Res. 38 (2010) D750–3. doi:10.1093/nar/gkp889.

[17] S. Lindström, H. Andersson-Svahn, Overview of single-cell analyses: microdevices and applications., Lab Chip. 10 (2010) 3363–72. doi:10.1039/c0lc00150c.

[18] E. Pauwels, Communication: Mind the metaphor., Nature. 500 (2013) 523–4. doi:10.1038/500523a.

[19] J.C. Venter, Life at the Speed of Light: From the Double Helix to the Dawn of Digital Life (Google eBook), Hachette UK, 2013.

[20] G.M. Church, E. Regis, Regenesis: How Synthetic Biology Will Reinvent Nature and Ourselves (Google eBook), Basic Books, 2012.

[21] P.P. Denèfle, Introduction to gene therapy: a clinical aftermath., Methods Mol. Biol. 737 (2011) 27–44. doi:10.1007/978-1-61779-095-9_2.

[22] M. a Kay, State-of-the-art gene-based therapies: the road ahead., Nat. Rev. Genet. 12 (2011) 316–28. doi:10.1038/nrg2971.

[23] S.Q. Tsai, N. Wyvekens, C. Khayter, J. a Foden, V. Thapar, D. Reyon, et al., Dimeric CRISPR RNA-guided FokI nucleases for highly specific genome editing, Nat. Biotechnol. (2014). doi:10.1038/nbt.2908.

[24] M.H. Kershaw, J. a Westwood, P.K. Darcy, Gene-engineered T cells for cancer therapy, Nat. Rev. Cancer. 13 (2013) 525–541. doi:10.1038/nrc3565.

[25] L. Naldini, Ex vivo gene transfer and correction for cell-based therapies., Nat. Rev. Genet. 12 (2011) 301–15. doi:10.1038/nrg2985.

[26] D. Bazou, W.T. Coakley, a J. Hayes, S.K. Jackson, Long-term viability and proliferation of alginate-encapsulated 3-D HepG2 aggregates formed in an ultrasound trap., Toxicol. In Vitro. 22 (2008). doi:10.1016/j.tiv.2008.03.014.

[27] J. Hultström, O. Manneberg, K. Dopf, H.M. Hertz, H. Brismar, M. Wiklund, Proliferation and viability of adherent cells manipulated by standing-wave ultrasound in a microfluidic chip., Ultrasound Med. Biol. 33 (2007) 145–51. doi:10.1016/j.ultrasmedbio.2006.07.024.

[28] D. Bazou, R. Kearney, F. Mansergh, Gene Expression Analysis of Mouse Embryonic Stem Cells Following Levitation in an Ultrasound Standing Wave Trap, Ultrasound Med. …. 37 (2011) 321–330.

[29] D. Carugo, D.N. Ankrett, P. Glynne-Jones, L. Capretto, R.J. Boltryk, X. Zhang, et al., Contrast agent-free sonoporation: The use of an ultrasonic standing wave microfluidic system for the delivery of pharmaceutical agents., Biomicrofluidics. 5 (2011) 44108–4410815. doi:10.1063/1.3660352.

[30] L. Kim, Overview of the Microfluidic Diagnostics Commercial Landscape, in: G. Jenkins, C.D. Mansfield (Eds.), Microfluid. Diagnostics SE - 5, Humana Press, Totowa, NJ, 2013: pp. 65–83. doi:10.1007/978-1-62703-134-9.

[31] J.R. Wilson, D.K. Vaughan, E. Naylor, R.G. Voss, Analysis of Space Shuttle ground operations, Simulation. 38 (1982) 187–203.